INVESTIGATION OF SURFACE ENGINEERING AND MONITORING FOR RELIABLE WIND TURBINE GEARBOXES

A thesis submitted to
The University of Birmingham
for the degree of
DOCTOR OF PHILOSOPHY

by

JUN ZHOU

[redacted]

Supervisors: Dr. Mayorkinos Papaelias
Prof. Hanshan Dong,

School of Metallurgy and Materials
College of Engineering and Physical Sciences
The University of Birmingham

Abstract

Most industrial wind turbine models use gearboxes to convert the slow rotation of the wind-driven rotor to the high-speed rotation required by the generator. Although industrial wind turbines are designed to operate for at least 20-25 years, gearboxes rarely survive more than 7 years without serious refurbishment or replacement. Most gearbox failures are attributed to gear and bearing damages.

This study has made key contributions towards a substantial step-change in the reliability of wind turbine gearboxes. First of all, the root cause of failure of gearbox components retrieved from the field has been analysed. Secondly, the failure mechanisms identified from the root-cause analysis have been clearly verified using Finite Element Analysis (FEA) simulations. Subsequently, based on the identification and verification of failure mechanisms, appropriate advanced surface engineering methodologies coupled with an improved methodology of condition monitoring for wind turbine gearbox components have been developed.

Root cause analysis of failures occurring in wind turbine gearbox components is essential and of paramount importance in pertinently and successfully improving gearbox reliability. One failed bearing, a damaged spherical roller, several broken gear teeth and gear-related debris particles from various gearbox stages have been retrieved from the field. Observation, investigation and metallurgical failure analysis were carried out thoroughly on the materials of these failed gearbox components. In the end, the main root failure causes of these components were deduced to be the extremely high stresses due to the combined effects of misalignment, coarse non-metallic inclusions, and inadequate or inconsistent lubrication.

In order to validate the failure causes identified from failed wind turbine gearbox components, Finite Element Analysis was carried out. The simulation of stress distribution on wind turbine gearbox components indicates that extreme high input torque, poor and variable lubrication

quality (i.e. high friction) and misalignment significantly increase the contact stress, which prompt the initiation and development of failures. In addition, crack initiation caused by the coarse inclusions and subsequent propagation was also successfully simulated.

After the root cause of wind turbine gearbox failures has been successfully identified and verified, duplex surface systems have been designed to prevent the life-limiting damages relevantly. On the duplex surface systems Diamond Like Carbon (DLC) coating was deposited on carburised EN36 and nitrided EN40BT steel, which possesses extremely low friction coefficient (0.16), high surface hardness (11.43 GPa), enough load-bearing capacity, compressive residual stresses and inside toughness increasing the resistance to the high contact stresses due to high input torque, poor lubrication quality and unavoidable misalignment.

To develop an advanced condition monitoring methodology in order to evaluate damage evolution in wind turbine gearbox components, the relationship between the surface/subsurface defect development and acoustic emission (AE) and vibration signals has been studied. Wheel samples were tested against WC wheel using a rolling-sliding wear tester. The acoustic emission and vibration signals generated during the wear tests were recorded and analysed. The evolution of wheel damage was found to be much sensitively and closely interrelated with the AE signals. While the vibration spectrum only significantly changed after severe and visible damage formed on the surface of the tested wheel samples.

Acknowledgements

I would like to express my sincere gratitude to my supervisors, Dr Mayorkinos Papaelias, Prof. Hanshan Dong, and Dr Xiaoying Li, for their invaluable advice, guidance and supervision throughout my study at University of Birmingham.

I also wish to express my appreciation to all my colleagues in the School of Metallurgy and Materials for their time and effort in helping, encouraging, and assisting me, especially to Dr Arash Amini, Dr Nikolaos Angelopoulos, Dr Qi Chen, Dr Yangchun Dong, Dr Zheng Huang, Mr Xiaochao Ji, Mr Valter Luiz Jantara Junior, Dr Qiongxi Liu, Mr Shaojun Qi, Mr Shengrun Shi, Miss Chang Shu, Dr Linhai Tian, Dr Fei Wang, Dr Xiqian Wang, Miss Yana Liang, Dr Zhenxue Zhang.

I would also like to take the opportunity to thank all the faculty and staff in the School of Metallurgy and Materials for their help, support and cooperation during my study.

I would also like to thank the European Commission's 'Seventh Framework Programme for Research (FP7)' and the University of Birmingham for the financial support.

Finally, I would like to thank my family and dear friends, who are the most important to me, for their constant love and support.

ABBREVIATIONS AND ACRONYMS

AE	Acoustic Emission
ASPN	Active Screen Plasma Nitriding
AGMA	American Gear Manufacturers Association
BSE	Back Scattered Electron
COF	Coefficient of Friction
CAD	Computer-Aided Design
CMS	Condition Monitoring System
CF	Crest Factor
DLC	Diamond Like Carbon
DCPN	Direct Current Plasma Nitriding
EDS or EDX	Energy Dispersive X-Ray Spectroscopy
XFEM	eXtended Finite Element Method
FFT	Fast Fourier Transform
FEA	Finite Element Analysis
GMF	Gear Mesh Frequency
GDOES	Glow Discharge Optical Emission Spectrometry
HAWT	Horizontal Axis Wind Turbine
LCOE	Levelised Cost of Electricity
LBC	Load Bearing Capacity
MARSE	Measured Area under the Rectified Signal Envelope
O&M	Operating and Maintenance
RCF	Rolling Contact Fatigue
RMS	Root Mean Square

SEM	Scanning Electron Microscope
STFT	Short Time Fourier Transform
SK	Spectral Kurtosis
VAR	Vacuum Arc Re-Melting
VIM	Vacuum Induction Melting
WEC	White Etching Crack
XRD	X-Ray Diffraction

PUBLICATIONS

[1] J Zhou, S Roshanmanesh, F Hayati, V Jantara Junior, T Wang, S Hajiabady, X Y Li, H Basoalto, H Dong and M Papaelias, Improving the reliability of industrial multi-MW wind turbines, Insight - Non-Destructive Testing and Condition Monitoring 59(4):189-195, April 2017

[2] J Zhou, S Roshanmanesh, F Hayati, V Jantara Junior, T Wang, S Hajiabady, X Y Li, H Basoalto, H Dong and M Papaelias, Increasing the reliability of industrial multi-MW wind turbines, NDT 2016-55th Annual Conference of the British Institute of Non-Destructive Testing, 2016, Nottingham, UK

[3] V Jantara Junior, J Zhou, S Roshanmanesh, F Hayati, S Hajiabady, X Y Li, H Dong and M Papaelias, Evaluation of damage mechanics of industrial wind turbine gearboxes, Insight - Non-Destructive Testing and Condition Monitoring 59(8), August 2017

Table of Contents

CHAPTER 1: INTRODUCTION AND PROJECT OBJECTIVES

1.1 The industrial need

Global warming poses a serious threat to humanity and possibly to the planet as we know it, due to the rapid and at extremely large scale consumption of fossil fuels based on coal, oil and natural gas. Replacing fossil fuels with renewable energy sources can significantly reduce greenhouse gas emissions (Peter Musgrove, 2010). In recent years, wind power has become the world's fastest growing renewable energy source (Bin Lu et al., 2009). Wind energy conversion to electricity using industrial-scale wind turbines with power ratings up to several MW has greatly reduced the cost of renewable energy generation putting it into direct competition with conventional fossil fuel-based electricity production (Peter Musgrove, 2010).

The global wind energy industry has grown at a strong pace in recent decades with the total installed capacity worldwide having reached almost 500 GW (Global Wind Energy Council GWEC, 2017). At the same time, the power rating of industrial wind turbines has also grown substantially with some models, such as the Vestas V-164, being able to produce up to 9 MW (MHI Vestas Offshore Wind, 2017). Most industrial wind turbine models use gearboxes to convert the slow rotation of the rotor to high-speed rotation in the generator in order to enable the production of electricity at the required grid frequency. Although direct drive wind turbines are also available, these tend to use a much larger number of rare earth magnets rendering their nacelles heavier and involving more complex power electronics than the geared models. Also, the wind turbine blades tend to suffer from higher stresses due to the higher rotational speed of the rotor required by these models to operate efficiently.

One of the biggest challenges faced by the wind energy industry is the low reliability of wind turbine gearboxes. Although industrial wind turbines are designed to operate for at least 20-25 years, gearboxes rarely survive more than 7 years without serious refurbishment or

replacement (B.H. Chudnovsky, 2017). In the case of offshore wind turbines, the gearbox has been proven to be the Achilles heel of these industrial power generation systems due to the constantly variable high loads experienced in offshore wind farm locations. The high level of turbulence coupled with load variability can cause the initiation and subsequent propagation of damage, eventually resulting in gearbox failure occurring as early as a few months after commissioning (K Stadler and A Studenrauch, 2013).

Most gearbox failures are attributed to gear and bearing defects. In addition, wind turbine gearboxes are difficult to achieve, especially for those in offshore wind farms. To avoid unpredictable gearbox failures and assess the overall status of individual gears and bearings during operation remotely, it is necessary that condition monitoring systems (CMS) are used (TW Verbruggen, 2003). Wind turbine gearbox CMS are commonly based on vibration analysis. Such CMS are capable of continuously monitoring the performance and operation of industrial wind turbine gearboxes in real time by assessing the acquired vibration signature characteristics (Anoop Prakash Verma, 2012).

Although CMS can offer information regarding the condition of the gearbox, they cannot prevent defects from initiating and subsequently propagating. Therefore, it is important to apply appropriate surface engineering processes, which can mitigate or eliminate the life-limiting problems currently faced by wind turbine gearbox designers.

1.2 Aims and objectives

The key aim of this study has been to contribute towards a substantial step-change in the efficiency and reliability of wind turbine gearboxes. In order to achieve this, the root cause of failure of gearbox components retrieved from the field has been analysed by observation,

whilst the stress field of gearbox components has been simulated and failure mechanisms have been verified using Finite Element Analysis (FEA) simulations. The microscopic characterisation of failed components retrieved from the field coupled with the FEA simulations carried out have enabled a better understanding of the factors limiting the operational lifetime of wind turbine gearbox components under operational conditions. This has subsequently allowed the relevant development of appropriate advanced component surface systems and condition monitoring methodology that can be applied in order to enhance performance and reliability of in-service gearboxes.

The key scientific and technological objectives of the present study can be summarised as follows:

1) To observe and examine the failed gears and bearings removed from in-service industrial wind turbine gearboxes provided by wind farm operators involved in this study, and to identify the root cause of failure as well as the overall failure mechanisms involved

2) To analyse the effects of identified failure-related factors on stress distribution and crack development in meshing gears using Finite Element Analysis (FEA) simulations, thus to verify the root failure cause of the gearbox components from the field

3) To relevantly improve the properties and performance of wind turbine gearbox components by developing appropriate advanced duplex surface treatment processes that combine plasma surface hardening and low-friction self-lubricating composite coatings in order to mitigate the effects of failure-leading factors (e.g. poor lubrication and unavoidable misalignment) on the contact stress and prevent premature failures increasing the lifetime of gearbox

4) To study the performance of the developed duplex surface systems using an Amsler wheel-against-wheel rolling-sliding wear tester simulating the contact conditions of gears and bearings

5) To conduct vibration analysis and acoustic emission tests at the same time of the rolling-sliding test, then to perform detailed failure analysis and signal analysis, studying the relationship between the AE/vibration signals and damage evolution, for accurate monitoring degradation of gearbox components.

1.3 Thesis structure

The present thesis consists of six chapters as discussed next.

Chapter 1 provides an introduction to the current challenges faced in wind turbine gearbox technology and the need to address them in the foreseeable future. Chapter 2 provides a comprehensive literature review of the materials currently used for manufacturing gearbox components (bearings and gears), the surface engineering techniques currently used and possible state-of-the-art alternatives, the types of failure mechanisms and modes experienced in wind turbine gearboxes, FE techniques for simulating the loading conditions and damage mechanisms, and the methodologies available in remotely monitoring the health of the gearbox during operation. Chapter 3 describes the experimental methodologies used during the study for the characterisation of samples retrieved from the field as well as samples tested under laboratory conditions, the surface engineering techniques used to improve the wear and fatigue resistance of the reference materials considered, the wear tests carried out using an Amsler rolling contact machine, combined with acoustic emission and vibration monitoring techniques, and the FE simulations carried out to validate the observations made on the

retrieved and laboratory tested samples. Chapter 4 presents the results on the root failure cause analysis of field samples, FE simulation coupled with the findings of the characterisation of the surface treated samples. Chapter 5 presents the key results of the wear tests performed and evaluation of damage evolution and the mechanisms that resulted in failure. Finally, Chapter 6 provides a summary of the main conclusions drawn from the results of this study and presents a realistic plan for future work in this research area.

CHAPTER 2: LITERATURE REVIEW

This chapter reviews the rapid development of wind energy industry, introduced the most widely installed gearbox-driven wind turbines, stating the importance of utilising gearboxes in wind turbines. It also summarises the common materials used for manufacturing gearbox components, failure types, and failure mechanisms involved. The state-of-art methods to assess and prevent wind turbine gearbox damage initiation and propagation are reviewed, including simulation, condition monitoring and surface engineering.

2.1 Wind energy and wind turbine types

2.1.1 Wind energy

The effects of global warming are gradually manifesting themselves more evidently, over wider regions and longer periods of time. One of the main reasons behind the gradual rise in average global temperatures has been the large scale and almost uncontrollable burning of fossil fuels over the past two centuries. Replacing fossil fuels with renewable energy sources can significantly reduce greenhouse gas emissions and help gradually mitigate the effects of global warming before climate reaches a possible tipping point (Peter Musgrove, 2010). Wind power has become one of the world's fastest growing renewable energy sources with tens of thousands of large-scale industrial wind turbines installed around the world (REN21, 2016). Larger and more efficient wind turbines have contributed to the significant reduction of the power production costs associated with wind energy (Peter Musgrove, 2010). The global wind energy industry has increased continuously over the last four decades, as shown in Figure 2.1.1-1, with wind farms being built onshore and offshore. Despite offshore wind farms facing more technical challenges in comparison with onshore ones, they are becoming more and more common (see Figure 2.1.1-2). Although the total cumulative global wind energy capacity installed offshore is currently limited (around 15 GW), its contribution to the energy

mix of the UK, Denmark and Germany is gradually gaining significance. Despite the fact that offshore wind projects are relatively fewer in comparison with those built onshore, offshore wind farms tend to be very large involving wind turbine modes with power ratings above 3 MW. Building offshore wind farms has great advantages. First of all, wind farms do not compete for land which may also be required for other uses such as farming or housing. Secondly, wind energy resources tend to be better offshore allowing generally higher annual capacity factors than most onshore projects. Thirdly, it is normally easier to get planning and construction permission although care needs to paid that the wind farm location does not interfere with normal maritime traffic. Finally, the environmental impact tends to be smaller although the exact effects to marine life is yet to be accurately quantified since available data to date are somewhat limited (Tony Burton et al., 2011).

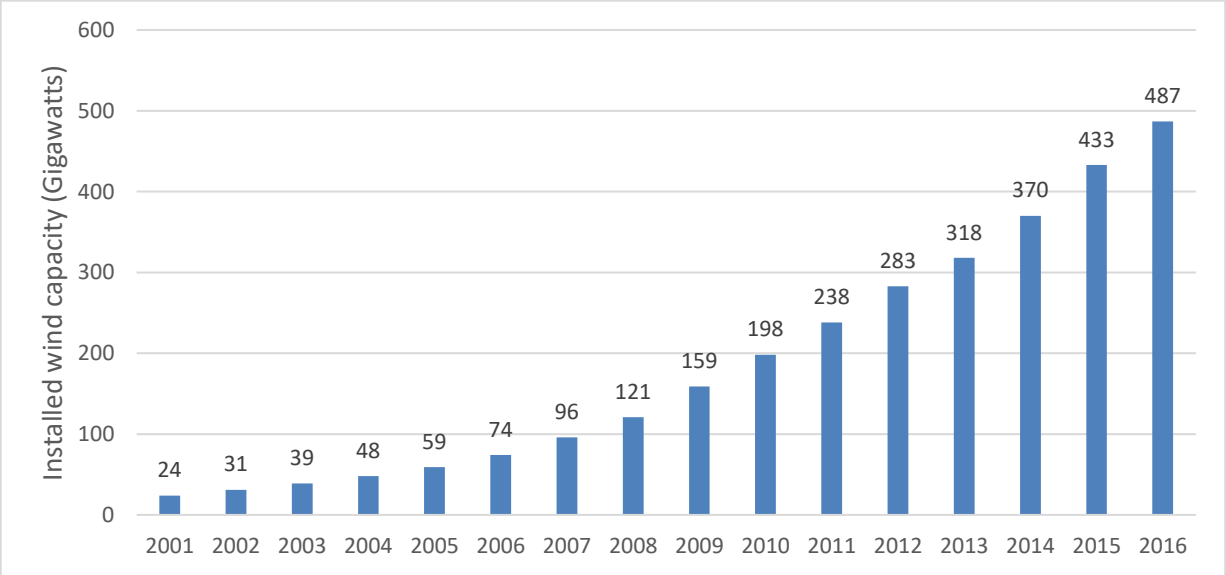

Figure 2.1.1-1 Global total installed capacity of wind power, 2001-2016 (Global Wind Energy Council GWEC, 2017)

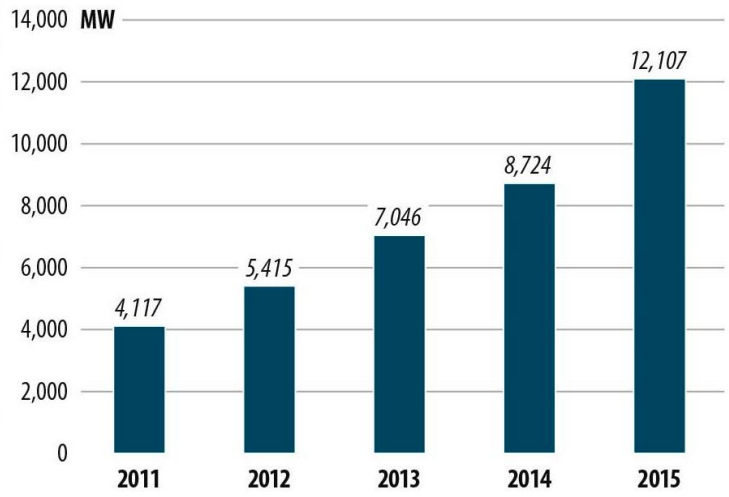

Figure 2.1.1-2 Global cumulative offshore wind installations, 2011-2015 (Global Wind Energy Council GWEC, 2017)

2.1.2 Wind turbine types

Industrial multi-MW wind turbines convert the kinetic energy of wind into electricity. The main designs and different configurations of wind turbines can be categorised based on the operational axis, the presence of a gearbox or not, the number of blades and the direction of the rotor (downwind or upwind) (Jesús María Pinar Pérez et al., 2013). The majority of industrial wind turbines tend to be based on the three-blade geared horizontal axis design.

Modern industrial multi-MW wind turbines can produce significant amounts of power once the wind speed reaches the rated velocity for the model. Most industrial wind turbines will start producing electricity at wind speeds of 3-4 m/s (cut-in speed). The rated wind speed is normally around 12-13 m/s. The cut-off speed is normally around 25 m/s and is necessary to avoid catastrophic damage of the wind turbine load bearing components, particularly the blades at very windy conditions. Multi-MW wind turbines thanks to their higher power output achieve lower cost per MWh of electric energy generated, in comparison with small and medium-scale turbines with power ratings up to 500 kW (John F Hall et al., 2011, REN21,

2016). Therefore the trend in commercial wind turbines is to increase their physical size and power rating in order to produce as much energy as possible from a single device (REN21, 2016).

As mentioned earlier the majority of modern large-scale wind turbines are typically 3-bladed horizontal-axis machines which can be either direct-drive or geared (David A. Spera, 2009) as shown in Figure 2.1.2-1. Figure 2.1.2-2 illustrates the main components that typical industrial wind turbines consist of including the rotor hub, main shaft, gearbox or speed multiplier, braking mechanisms (located on either side of the gearbox), generator (to produce power at frequencies of 50 or 60 Hz), yaw system, lubrication system, anemometry and auxiliary motors and pumps (Office of Energy Efficiency and Renewable Energy, 2006). When the wind turbine is in operation, the wind-driven rotor and the main shaft to which it is connected rotate at relatively low speed between 8-25 r/min depending on the wind turbine size. The,gearbox increases the turbine shaft speed to the required rotational speed for the generator to operate to 1100-1500 r/min (EERE DOE, 2010).

Figure 2.1.2-1 Schematic diagram of a horizontal axis wind turbine (Alan Fraser, 2002)

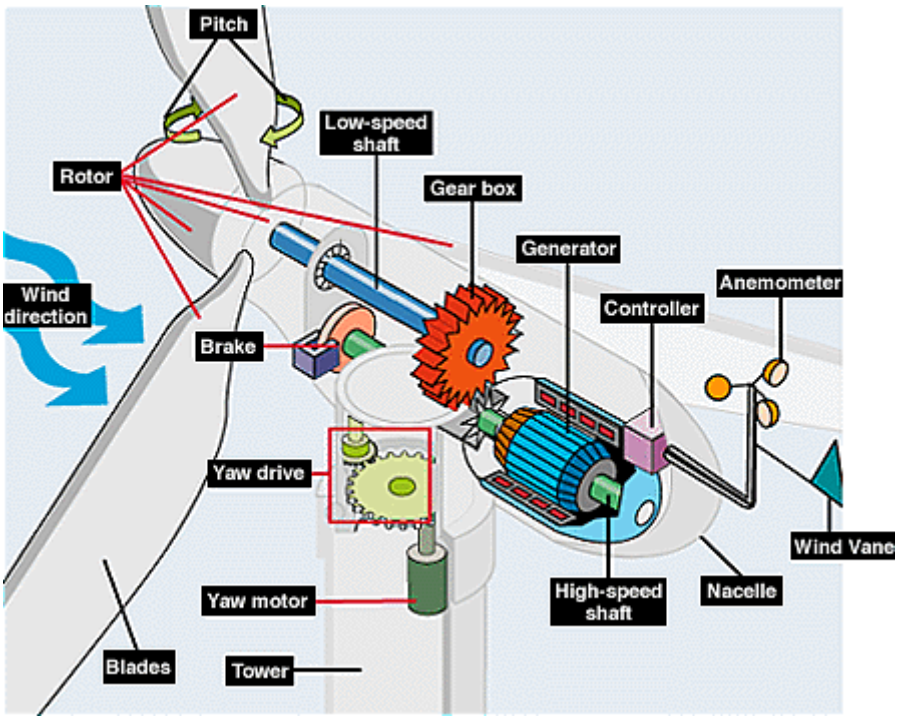

Figure 2.1.2-2 Representative configuration of drive trains in geared large-scale wind turbines (Office of Energy Efficiency and Renewable Energy, 2006)

As already mentioned earlier, most industrial-scale wind turbines use gearboxes to convert the slow rotation of the rotor to high speed rotation in the generator. Meanwhile, the reliability of gearboxes is yet to be optimised. Therefore, direct-drive wind turbine models have been developed removing the need of gearboxes in order to avoid costly gearbox failures. The main advantage of utilising gearboxes is a significant saving in generator size and thus the total weight and cost of a wind turbine is generally lower (Jan Helsen et al., 2011). In addition to that, rotors of large-scale onshore wind turbines with gearboxes can turn at relatively low shaft speeds in order to maintain an optimum tip-speed ratio (tip forward speed divided by free-stream wind speed) balancing the efficiency and the generated noise (David A. Spera, 2009). However G Bywaters et al. (2004) observed that direct–drive trains for large-scale wind turbines have attracted increased commercial support, because of their simplicity, quiet operation, better efficiency, and most importantly avoidance of costly gearbox failures. Due to

the slow shaft speed, direct-drive generators tend to be bulky and heavy due to the number of magnets required to produce electricity. To be competitive with relatively light gearbox-driven generators, designers of direct-drive power trains must employ innovative measures to reduce the size, weight, and cost of the generator. Several manufacturers have introduced large-scale direct-drive generators with ratings from 500 kW to 8 MW. However, gearbox-based wind turbine models remain the dominant design with approximately 75% of all wind turbines installed being geared (Javier Serrano‐González and Roberto Lacal‐Arántegui, 2016). Although direct-drive wind turbines avoid gearbox failures, in practice, they do not seem to have a lower failure rate in comparison with gearbox-driven ones. For larger direct-drive turbines, the failure rate for generators is at least double that of the gearbox-driven ones (PJ Tavner et al., 2006).

As wind turbines become larger and achieve higher power ratings, the rotor speed required to produce electricity is gradually reduced. However, the decreasing rotor speed simultaneously leads to an increase in both rotor torques into the gearbox and gearbox speed-up ratios (David A. Spera, 2009). Higher input torques and speed-up ratios of gearboxes would make reliability worse. Therefore, studying and improving the reliability of gearbox components is of great importance to the wind energy industry.

2.2 Wind-turbine gearbox and failure modes

2.2.1 The wind turbine gearbox

In order to increase the reliability of wind turbine gearboxes, it is important to understand them. In a gearbox-driven Horizontal Axis Wind Turbine (HAWT), the gearbox multiplies the rotor shaft rotational speed to the speed required for the generator in order to enable

production of electricity at 50 or 60 Hz (David A. Spera, 2009), it also reduces torque with the same ratio (Jan Helsen et al., 2011). For HAWT rated between 300 KW and 5 MW, the speed-increasing gearbox has a step-up ratio (equal to the generator shaft speed divided by the turbine shaft speed) from 31 to 125, depending on the design (Tony Burton et al., 2011). These large step-ups are normally achieved by three separate stages with ratios between 3 and 5 each (Tony Burton et al., 2011, David A. Spera, 2009). Parallel-shaft, epicyclic (planetary), and hybrid designs are used in gearboxes (Figure 2.2.1-1). The vast majority of all commercial wind turbines employ gearboxes using planetary gears in combination with parallel, helical, or spur gears despite that parallel-shaft gearboxes are more readily available than epicyclic units and cost less (David A. Spera, 2009). The reason for this is that planetary gears allow gearboxes to be smaller, lighter, producing lower noise levels, and more efficient. The most important factors in the planetary gearbox design are load sharing among the planet gears and load distribution on the gear tooth flank (Jeong Gil Kim et al., 2011). Gearbox failures are predominantly related to bearing and gear failures (David A. Spera, 2009).

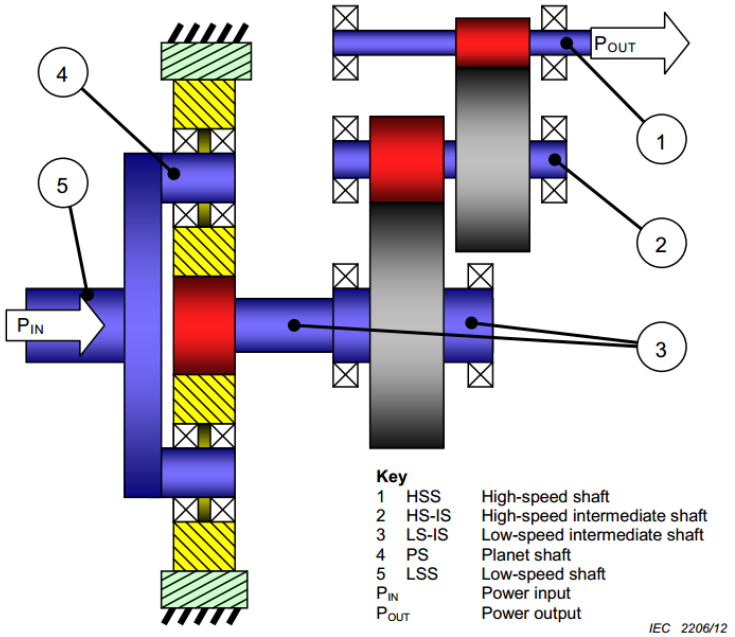

Figure 2.2.1-1 Shaft designation in 3-stage gearboxes with one planet stage (IEC, 2012)

The gear ratio, Gear Mesh Frequency (GMF) and linear speed of simple parallel-shaft gearbox is mathematically described as (Ralph T Buscarello, 1985):

$$Gear\ ratio\ =\ \frac{\omega_{driving}}{\omega_{driven}} = \pm\ \frac{N_{driven}}{N_{driving}} \qquad Equation\ 1$$

$$GMF\ (cycles\ per\ minute) =\ shaft\ synchronous\ speed\ (r/min) \times N \qquad Equation\ 2$$

$$Linear\ speed\ V\ (m/s) =\ \omega\ (rad/s) \times \frac{D}{2}(m) = \frac{1}{2} \times \omega \times module \times N \qquad Equation\ 3$$

Where ω is the angular velocity, N is the number of teeth and D the diameter.

In a planetary gear set (Figure 2.2.1-2), the ring is fixed (i.e. ω_R=0) and the carrier is the input. The planet speed relative to the carrier is (ω_P - ω_C), the sun speed relative to the carrier is (ω_S - ω_C), and the ring speed relative to the carrier is (ω_R - ω_C) = - ω_C. Then it can be expressed similar to simple parallel-shaft set,

$$\frac{\Omega_P - \omega_C}{\omega_S - \omega_C} = -\frac{N_S}{N_P} \qquad Equation\ 4$$

and

$$\frac{\omega_P - \omega_C}{-\omega_C} = \frac{N_R}{N_P} \qquad Equation\ 5$$

So the gear ratio

$$R_G\ = \frac{\omega_C}{\omega_S} = \frac{N_S}{N_R + N_s} \qquad Equation\ 6$$

and the

$$GMF = \omega_C \times (N_R + N_S) \qquad Equation\ 7$$

The torque T that is applied to the gear is given as (Gitin M Maitra, 1994, cited by Elon J Terrell et al., 2012)

$$T = \frac{P}{\omega} \qquad Equation\ 8$$

Where P is the transmitted power and ω is the angular speed.

The Hertzian compression stress between a pair of spur gear teeth in contact at the pitch point is given by (Tony Burton et al., 2011)

$$\sigma_C = \sqrt{\frac{F_t}{bd_1}\frac{E}{\pi(1-v^2)}\frac{u+1}{u}\frac{1}{sin\,\alpha\,cos\,\alpha}} \qquad Equation\ 9$$

Where F_t is the force between the gear teeth at right angles to the line joining the gear centres, b is the gear face width, d_1 is the pinion pitch diameter, u is the gear ratio (greater than unity), α is the angle at which the force acts between the gears (pressure angle), and is usually 20° - 25°.

The maximum bending stress at the tooth root is given by (Tony Burton et al., 2011)

$$\sigma_B = \frac{F_t h}{\frac{1}{6}bt^2}K_S \qquad Equation\ 10$$

Where h is the maximum height of single tooth contact above the critical root section, t is the tooth thickness at the critical root section, K_S is a factor to allow for stress concentration at the root.

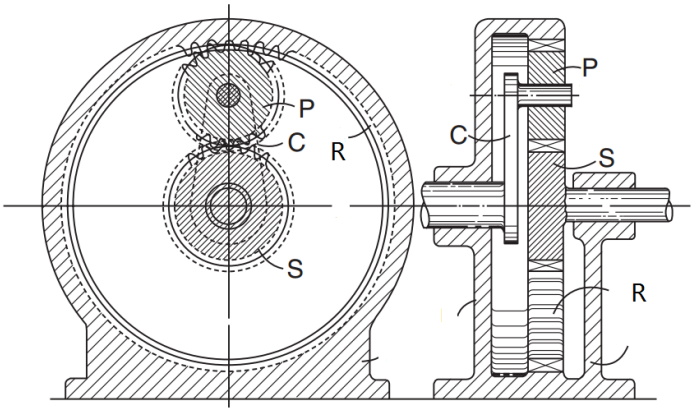

Figure 2.2.1-2 Planetary gear set (Thomas Kenneth Garrett et al., 2000)

On wind turbine gearboxes, the typical Hertzian stresses are between 1034 and 2068 MPa. For bending stresses, the values range from 345 to 483 MPa. The peak stresses (e.g. due to braking events) have been reported to be four to ten times greater than the nominal stresses (R. Errichello et al., 1994).

In rolling bearings, the contact area and stress distribution is shown in Figure 2.2.1-3 and Figure 2.2.1-4 respectively. As it can be seen from the Figure 2.2.1-4 (b), with the increase of depth, the shearing stress τ_{45} increases quickly from 0 to its maximum value at a critical depth, z, beyond which, τ_{45} keeps decreasing slowly. The maximum shearing stress τ_{max} is related to the bearing life and it is proportional to the maximum Hertz stress S_{max}, as

$$\tau_{max} = k_1 S_{max} \qquad Equation\ 11$$

For ball bearings, as it can be observed from Figure 2.2.1-4 (b), the constant k_1 equals to 0.32. For roller bearings, k_1 equals to 0.30 (Erwin V Zaretsky, 2012).

Load and unloaded zones exist in operating rolling element bearings. In the load zone, rollers work in desirable conditions involving high traction forces and good alignment. In the unloaded zone, the traction forces are inadequate and consequently the rollers have high slide-to-roll ratios. Moreover, they are misaligned up to a certain degree. An instantaneous torque

reversal on shaft, for instance, could relocate the load zone of the bearing suddenly. Thus, higher contact stresses are applied to misaligned and high slide-to-roll ratio rollers (Michael N Kotzalas and Gary L Doll, 2010).

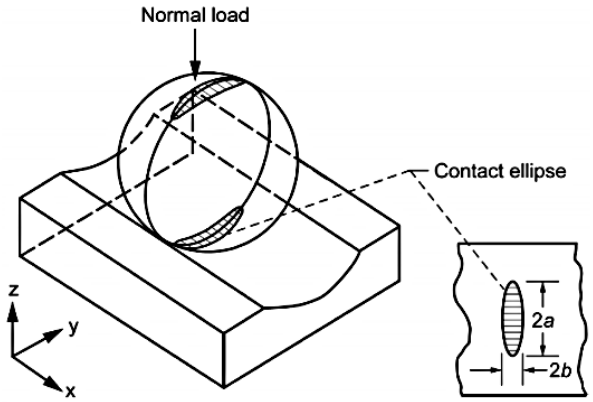

Figure 2.2.1-3 Sketch of a ball on a bearing race showing their contact ellipse (Erwin V Zaretsky, 2012)

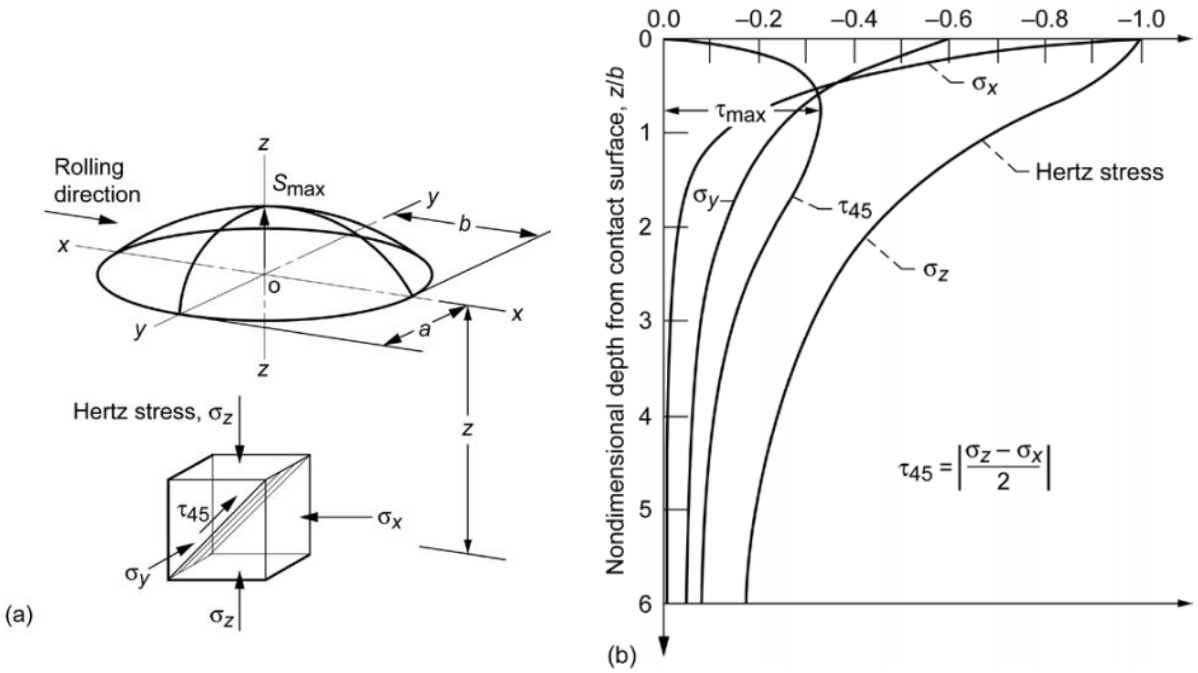

Figure 2.2.1-4 (a) Stresses on the ball (S_{max} is the maximum Hertz stress), and (b) stress distribution under the contact surface (Erwin V Zaretsky, 2012)

2.2.2 Rolling bearing materials

Steel grades used for manufacturing bearings are primarily produced via the double vacuum processing method VIM-VAR. This production process combines vacuum induction melting (VIM) with vacuum arc re-melting (VAR). Compared with air-melting processes, the vacuum-based production process significantly reduces the amount of hard oxide inclusions, entrapped gases and trace elements in the bearing steel (Erwin V Zaretsky, 1986). Hence, this helps achieve a longer lifetime for bearings operating under harsh conditions. High cleanliness of bearing steels is necessary. It is widely known that oxide inclusions can cause premature failure of the bearings by concentrating local stresses and initiating cracking (Erwin V Zaretsky, 2012).

The majority of bearing materials are based on high C steel grades which have been through-hardened. The C content in such steel grades is >0.8 in wt%. Alternatively low C steels or carburised grade steels with C content<0.2 in wt% are also used (Xiaolan Ai and Charles Moyer, 2001).

The most widely used high C steels are required to achieve high surface hardness which is greater than 58 HRC (653 HV) at working temperature, or 60 HRC (697 HV) at room temperature, aiming to ensure the bearings can survive their intended design lifetime under in-service conditions. The hardness requirements can be met using the through hardening method which is based on quenching and low temperature tempering between 160 and 280 ˚C of the steel alloy. The reason for through hardening is that the bearing design lifetime which is ultimately limited by rolling contact fatigue is expected to be longer when hardness is higher (Erwin V Zaretsky, 2012, Xiaolan Ai and Charles Moyer, 2001, HKDH Bhadeshia, 2012). The relationship between hardness and expected bearing design lifetime provided that the

bearing is well designed, assembled and lubricated, and not overloaded, has been expressed by Erwin V Zaretsky (1986) as

$$L_{10} = e^{m[(RC)_T - 60]} \left(\frac{C}{P}\right)^p \qquad Equation\ 12$$

Where L_{10} is the bearing theoretical life that 90% of the bearing population should survive at the working load P. m is a hardness-life exponent and its typical value is 0.1, $(RC)_T$ is the Rockwell C hardness at working temperature, C is the critical load under which the 90% bearing population could survive with 1 million inner-race revolutions, p is a load-life exponent and equals to 3 for ball bearings and 10/3 for other roller bearings (Erwin V Zaretsky, 2012). With regards to the effect of hardness difference between bearing roller elements and raceways on the bearing lifetime, their relationship is illustrated in Figure 2.2.2-1, which suggests that if the rolling elements were just up to 10% (60-80 HV) harder than the raceway, the bearings' service lifetime would be much higher than if the hardness difference between the raceway and rollers was different (Michael J Neale, 1995). To ensure high C steels (through-hardened steels) exhibit sufficient hardenability (hardenability indicates how deep the steel can be hardened), alloying elements such as Cr, Mn, Si and/or Mo are required to be present in the chemical composition (Xiaolan Ai and Charles Moyer, 2001). However, the total percentage of alloying elements in the bearing steels should be low, <3 wt%, in order to obtain a high resistance to rolling contact fatigue (HKDH Bhadeshia, 2012). Erwin V Zaretsky et al. (1981) observed that the bearing steels containing a higher proportion of alloying elements exhibited lower contact fatigue life. Typical high C steels used by the bearing-manufacturing industry are listed in Figure 2.2.2-2.

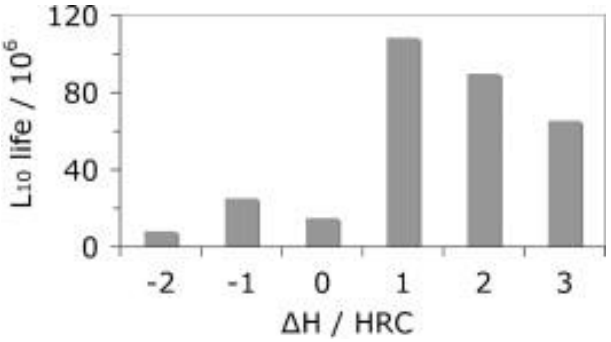

Figure 2.2.2-1 The effect of hardness difference between the rolling element and the raceway on the fatigue life of bearings made of 52100 steel. The raceway hardness was 63 HRC. The bearings were tested under a radial load of 5871 N, using mineral oil as lubricant (Michael J Neale, 1995).

	Chemical Composition (%)							
Grade	C	Si	Mn	Cr	Mo	P	S	Application
ASTM-A295(50100)	0.98–1.10	0.15–0.35	0.25–0.45	0.40–0.60	≤0.10	≤0.025	≤0.025	Not commonly
ASTM-A295 (51100)	0.98–1.10	0.15–0.35	0.25–0.45	0.90–1.15	≤0.10	≤0.025	≤0.025	used
JIS-G4805 (SUJ1)	0.95–1.10	0.15–0.35	≤0.50	0.90–1.20	—	≤0.025	≤0.025	
ASTM-A295-94 (52100)	0.98–1.10	0.15–0.35	0.25–0.45	1.30–1.60	≤0.10	≤0.025	≤0.025	Typical steels for
ASTM-A535-85 (52100)	0.95–1.10	0.15–0.35	0.25–0.45	1.30–1.60	≤0.10	≤0.015	≤0.015	small and
BS-535A99	0.95–1.10	0.10–0.35	0.40–0.70	1.20–1.60	—	≤0.025	≤0.025	medium-size
DIN-100Cr6	0.90–1.05	0.15–0.35	0.25–0.40	1.40–1.65	0.30	≤0.025	≤0.025	bearings
JIS-G4805 (SUJ2)	0.95–1.10	0.15–0.35	≤0.50	1.30–1.60	—	≤0.025	≤0.025	
NF-100C6	0.95–1.10	0.15–0.35	0.20–0.40	1.35–1.60	≤0.08	≤0.030	≤0.025	
ASTM-A485-89 grade 1	0.90–1.05	0.45–0.75	0.95–1.25	0.90–1.20	≤0.10	≤0.025	≤0.025	Used for large-size
ASTM-A485-89 grade 2	0.85–1.00	0.50–0.80	1.40–1.70	1.40–1.80	≤0.10	≤0.025	≤0.025	bearings
JIS-G4805 (SUJ3)	0.95–1.10	0.40–0.70	0.90–1.15	0.90–1.20	—	≤0.025	≤0.025	
ASTM-A485-89 grade 3	0.95–1.10	0.15–0.35	0.65–0.90	1.10–1.50	0.20–0.30	≤0.025	≤0.025	Used for ultra-
ASTM-A485-89 grade 4	0.95–1.10	0.15–0.35	1.05–1.35	1.10–1.50	0.45–0.60	≤0.025	≤0.025	large-size
JIS-G4805 (SUJ5)	0.95–1.10	0.40–0.70	0.90–1.15	0.90–1.20	0.10–0.25	≤0.025	≤0.025	bearings

Figure 2.2.2-2 Chemical composition of high-carbon bearing steels (Xiaolan Ai and Charles Moyer, 2001)

Low C steels are used to manufacture bearings which not only require high surface hardness, but also satisfactory fracture toughness. Satisfactory fracture toughness can prevent rapid growth of a crack that has initiated, but normally it is inversely proportional to hardness. Bearings manufactured from low C steels can obtain a ductile core and hard surface via surface hardening process, such as carburising, followed by quenching and tempering (Erwin V Zaretsky, 2012). Case hardening also introduces compressive stresses into the surface,

which enables improved fatigue resistance (Dalenda Jeddi and Henri-Paul Lieurade, 2010, P Zhang et al., 2011), giving surface-hardened raceways higher resistance to the initiation of surface defects (e.g. indentations) than through-hardened (Daniel Nelias et al., 2005). The hardenability of low C steels can be increased with Ni, Cr, Mn and Mo (Xiaolan Ai and Charles Moyer, 2001). Fracture toughness can be increased by adding Ni or by reducing C content. The C content also influences the hardness, while Ni improves the steel's toughness without affecting hardness (Erwin V Zaretsky, 2012). Typical low C bearing steels are shown in Figure 2.2.2-3.

The operating temperature should also be considered when choosing the right bearing steel. It is known that steel hardness will drop sharply if the material is heated to temperature close to or higher than its tempering temperature. Therefore, normal bearings should not operate at temperature close to their tempering temperature, which is between 160 and 280 °C. For special elevated temperature conditions, bearing steels with high-temperature hardness should be adopted, as shown in Figure 2.2.2-4. For roller bearings operating at a temperature lower than 150 °C, through-hardened AISI 52100, and case-hardened AISI 8620 and AISI 9310 are recommended as manufacturing materials of choice. For operating temperatures that are higher than 150 °C, through-hardened AISI M-50 and case-hardened AISI M50 NiL are the recommended grades instead (Erwin V Zaretsky, 2012).

Grade	Chemical Composition (%) C	Si	Mn	Ni	Cr	Mo	P	S	Application
ASTM-A534-90 (5120H)	0.17–0.23	0.15–0.35	0.60–1.00	—	0.60–1.00	—	≤0.035	≤0.040	Used for small-size bearings
ASTM-A534-90 (4118H)	0.17–0.23	0.15–0.35	0.60–1.00	—	0.30–0.70	0.08–0.15	≤0.035	≤0.040	
ASTM-A534-90 (8620H)	0.17–0.23	0.15–0.35	0.60–0.95	0.35–0.75	0.35–0.65	0.15–0.25	≤0.035	≤0.040	
DIN 20NiCrMo2	0.23	0.35	0.90	0.70	0.60	0.25	≤0.025	≤0.025	
JIS-G4052/4103 (SCr420H)	0.17–0.23	0.15–0.35	0.55–0.90	—	0.85–1.25	—	≤0.030	≤0.030	
JIS-G4052/4103 (SCM420H)	0.17–0.23	0.15–0.35	0.55–0.90	—	0.85–1.25	0.15–0.35	≤0.030	≤0.030	
JIS-G4052/4103 (SNCM220H)	0.17–0.23	0.15–0.35	0.60–0.95	0.35–0.75	0.35–0.65	0.15–0.30	≤0.030	≤0.030	
ASTM-A534-90 (4320H)	0.17–0.23	0.15–0.35	0.40–0.70	1.55–2.00	0.35–0.65	0.20–0.30	≤0.035	≤0.040	Used for medium-size bearings
JIS-G4052/4103 (SNCM420)	0.17–0.23	0.15–0.35	0.40–0.70	1.55–2.00	0.35–0.65	0.15–0.30	≤0.030	≤0.030	
ASTM-A534-90 (9310H)	0.07–0.13	0.15–0.35	0.40–0.70	2.95–3.55	1.00–1.45	0.08–0.15	≤0.035	≤0.040	Used for large-size bearings
JIS-G4052/4103 (SNCM815)	0.12–0.18	0.15–0.35	0.30–0.60	4.00–4.50	0.70–1.00	0.15–0.30	≤0.030	≤0.030	

Figure 2.2.2−3 Composition of carburising-grade bearing steels (Xiaolan Ai and Charles Moyer, 2001)

Grade	Chemical Composition (%) C	Si	Mn	Ni	Cr	Mo	W	V	Co	Temperature Limits (°C)	Applications
M-50	0.82	≤0.25	0.25	≤0.10	4.12	4.25	≤0.25	1.00	≤0.25	420	Used for high-temperature bearings
M-50-NiL	0.15	0.18	0.15	3.50	4.00	4.00	—	1.00	≤0.25	315	
CBS-1000	0.15	0.50	0.50	3.00	1.05	4.50	—	0.38		314–425	
CBS-600	0.19	1.10	0.55	—	1.45	1.00	—	—	—	230–315	
TBS-600	1.03	1.03	0.70	—	1.45	0.30	—	—	—	315	
VASCO X-2	0.22	0.90	0.30	—	5.00	1.40	1.35	0.45	—	380	
M-10	0.87	0.25	0.25	—	4.00	8.00	0.75	1.90	—	430	
M-1	0.83	0.30	0.30	—	3.75	8.50	1.75	1.15	—	480	
M-2	0.83	0.30	0.30	—	4.15	5.00	6.15	1.85	—	380	
SKH4	0.78	≤0.40	≤0.40	—	4.15	—	18.00	1.25	10.00	450	
440-C	1.10	≤1.00	≤1.00	≤0.60	17.00	≤0.75	—	—	—	200	Used for high-temperature and corrosion-resistant bearings
BG-42	1.15	0.30	0.50	—	14.50	4.00	—	1.20	—	480	
ASM 5749	1.15	0.21	0.12	0.10	4.13	4.80	1.40	1.08	7.81	480	

Figure 2.2.2-4 Chemical Composition of Special Bearing Steels (Xiaolan Ai and Charles Moyer, 2001)

For the bearing manufacturing industry, spheroidisation treatment is important for bearing steel alloys as it significantly affects the material's microstructure. One of the main bearing

production methods includes hot forging (Murat Arbak et al., 2005). Bearing manufacturers use hot forging processes to roughly turn steel into the desired shape before machining. But the forged parts consisting of fine pearlite are too hard to conduct the subsequent machining processing. Therefore, softening treatment or spheroidisation annealing is carried out after forging, making lamellar cementite relatively spherical and coarse. This results in a lower steel hardness, enhancing machinability. Another reason to carry out spheroidisation is to mitigate the pro-eutectoid cementite, i.e. the secondary cementite $(Fe_3C)_{II}$ networks at the prior austenite grain boundaries in the hot-rolled high C hypereutectoid bearing steel, which form due to the insufficient cooling speed. The $(Fe_3C)_{II}$ networks are undesirable since they are brittle and result in decreased rolling contact fatigue lifetime of the bearing steel (HKDH Bhadeshia, 2012, S Chattopadhyay and CM Sellars, 1982, Petra Gembalova et al., 2007). After spheroidising, spheroidised cementite carbides are dispersed in the ferrite matrix within the steel's microstructure. Combined with hardening treatment (quenching and tempering) after machining, the whole heat treatment process (spheroidising + hardening) leads to a final steel microstructure of evenly dispersed fine residual and precipitated carbides with martensite (Wenwen Song et al., 2014). This fine microstructure is desirable for satisfactory performance of bearings, such as higher resistance to wear and fatigue (K Monma et al., 1968, HKDH Bhadeshia, 2012). Specially, higher C content in the steels could give more initial nucleation sites for spheroidisation, thus promoting this process. In addition to C, higher Cr content in the steel could also significantly facilitate the spheroidisation process. The presence of Cr reduces the interlayer distance of pearlite, rendering the starting of cementite spheroidising easier (NV Luzginova et al., 2008, HKDH Bhadeshia, 2012). Some of the Cr will be absorbed into the spheroidised carbides, enhancing the thermodynamic stability of the cementite carbides in the subsequent heat treatment (HKDH Bhadeshia, 2012).

2.2.3 Gear materials

Power transmission gears are usually manufactured from ferrous alloys (Gerald D Lindell and Daniel H Herring, 2007). According to the international standards for wind-turbine gearboxes, e.g. IEC 61400-4 (IEC, 2012) or ANSI/AGMA/AWEA 6006-A03 (ANSI/AGMA/AWEA, 2004), all wind-turbine gears are required to be made from grade 2 material in ANSI/AGMA 2001-D04 (ANSI/AGMA, 2004) or grade MQ material in ISO 6336-5(ISO, 2003). Therefore, industrial wind turbine gears are widely made of CrNiMo low alloy steels like SAE 4320, SAE 4820, SAE 9310 and 18CrNiMo7-6 (Mike LaPlante, 2009). These steels are all carburising grades with a basic C content of around 0.2 in wt%. Carburising is widely applied to gears to improve fatigue strength and wear resistance. Moreover, heavy duty gears are mostly carburised, since case hardened steels can handle more load than through hardened steels. After carburising and post-heat treatment, the surface hardness of gear tooth is required to be in the range between 660 and 800 HV. The reduction of surface hardness in the outer 0.1 mm of the case should be less than 40 HV. The corresponding case depth for gears with different normal module is shown in Figure 2.2.3-1 (ISO, 2003). After case hardening, it is ideal to keep the core hardness of gear tooth around 30-40 HRC to avoid tooth breakage (Gerald D Lindell and Daniel H Herring, 2007).

Replacing carburising with nitriding in gear treatment has great potential. This is due to the fact that the treating temperature of the nitriding technique is lower than that of carburising. Carburising, nitriding and other surface treatment technologies are comprehensively reviewed in section 2.5.3.

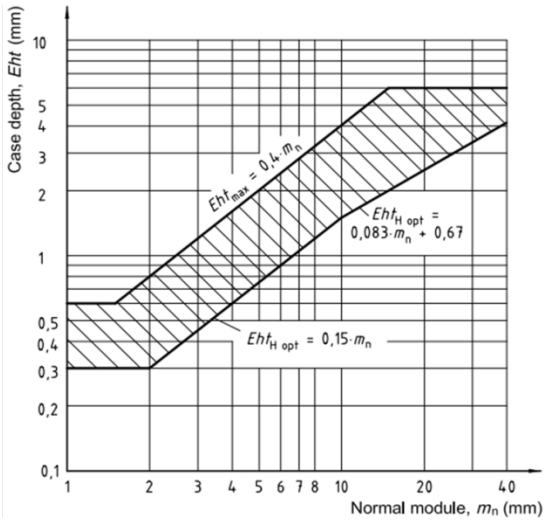

Figure 2.2.3-1 Recommended case depth for carburised gears with different module (ISO, 2003)

2.2.4 Wind turbine gearbox failure

Among the various components of the wind turbine drive-train, the gearbox is the most critical with respect to maintenance requirement (Michael R Wilkinson et al., 2007). In large-scale industrial wind turbines, the gearbox represents a significant part of the overall procurement cost of the wind turbine. It is also among the subsystems of the wind turbine currently posing the most serious technical challenges (RW Hyers et al., 2006). Although wind turbine gearboxes are designed to operate for 20-25 years, they rarely survive more than 7-8 years without serious refurbishment or replacement. It is generally acceptable that an onshore wind turbine may need three or four times to have its gearbox repaired or even replaced during its entire lifetime. In the case of offshore wind turbines, gearbox reliability has been causing concern due to the high variable loads experienced which lead to premature failures as early as one year after commissioning (K Stadler and A Studenrauch, 2013). The availability of onshore wind turbines has reached 95-98%, while for offshore wind turbines, the average availability is only 80-85% (K Smolders et al., 2010). In addition, the gearbox is the component with the longest downtime per failure, mainly due to the difficulties arising

from taking the necessary spare parts to where they are required and removing the old gearbox from the nacelle (Jesús María Pinar Pérez et al., 2013). Thus, particularly for offshore wind farms, gearbox maintenance costs are a major contributor to the resulting higher Levelised Cost of Electricity (LCOE) in comparison with onshore wind farms.

Operating and Maintenance (O&M) costs of onshore wind farms normally do not exceed 20-25% of the overall LCOE. However, in the case of offshore wind farms, O&M costs can be as high as 40% of LCOE and even higher (Dolf Gielen, 2012, IEA-ETSAP and IRENA, 2016). Therefore, there are still significant technical issues that are yet to be resolved, especially in the case of offshore wind turbine models.

2.2.4.1 Types of gearbox failure

Gear tooth damage and bearing faults in wind-turbine gearboxes are both common (Bin Lu et al., 2009). It has been found that most gearbox failures do not initiate as gear failures or gear-tooth design deficiencies. The majority of wind turbine gearbox failures appear to initiate in gearbox bearings instead (Michael R Wilkinson et al., 2007, Walt Musial et al., 2007). The observed failures appear to start at several specific bearing locations under certain conditions, which may later advance into the gear teeth as bearing debris and excess clearances cause surface wear and misalignments. Among all bearings in a gearbox, the planet bearings, the intermediate shaft bearings and high-speed shaft bearings tend to fail more frequently and at higher rates (Walt Musial et al., 2007). In the case of gears, damage tends to be greater in the low-speed stage, especially in the sun pinion gear (Mark Michaud et al., 2011).

The failure modes typically observed include rolling contact fatigue (e.g. micro-pitting and macro-pitting), scuffing, false brinelling, fretting corrosion, white etching area, and cracking (A Greco et al., 2013, Michael N Kotzalas and Gary L Doll, 2010, Peter Julian Blau et al.,

2010, Erwin V Zaretsky, 2012, Erick S Alley and Richard W Neu, 2010, Farshid Sadeghi et al., 2009). Between these different failure modes, one type may influence the others.

1) Micro-/Macro-pitting is a surface damage mode caused by rolling contact fatigue. Compared with the original mirror-like surface, the micro-pitted area scatters light and exhibits a frosted or light grey appearance, so micro-pitting is also named as frosting (P Davoli et al., 2007). Micro-pitting is commonly a precursor of larger surface failure, such as macro-pitting. But macro-pitting could also occur without the precursor of micro-pitting (A Greco et al., 2013). Micro/Macro-pitting normally initiates from some crack nuclei or stress raisers, e.g. indentations or asperities in the surface, or inclusions in the subsurface region. It subsequently grows and forms crack networks at a shallow angle to the surface, causing flaking and leaving micro-/macro-pits after the cracks have reached a critical depth (Farshid Sadeghi et al., 2009). Apart from the material's inherent mechanical properties (such as hardness and cleanliness), other factors that influence micro-/macro-pitting include surface finish, lubricant, load, temperature, speed and the ratio of slide to roll. Among these factors, contact pressure has the greatest effect on micro-pitting initiation, and speed and slide-to-roll ratio are the most critical factors of micro-pitting propagation (Adrian Oila and SJ Bull, 2005). Higher slide-to-roll ratio in rolling-sliding contact would significantly increase friction. It is known that friction coefficient of pure rolling is only about 1~2%, while the friction coefficient can be as high as 10% if sliding friction occurs. Therefore, higher slide-roll ratio could generate higher shear and tensile stresses, causing maximum contact stresses closer to the surface. These contact stresses can accelerate the initiation and propagation of micro-/macro-pits (Figure 2.2.4-1) (Shizhu Wen and Ping Huang, 2012). In addition, higher friction from higher slide-to-roll ratio leads to raising the surface temperature, thus deteriorating the properties of the material and lubricant, i.e. reducing the lubricant viscosity and material

hardness, subsequently prompting development of micro-/macro-pitting (Adrian Oila and SJ Bull, 2005). In bearings, micro-/macro-pitting is typically prompted by skidding (a combination of rolling and sliding motion) between the rollers and the raceway during unsteady operation, such as rapid acceleration or deceleration (A Greco et al., 2013). In wind turbine gearboxes, high-speed shaft bearings operating under relatively low loads and high speeds, are prone to skidding. Thus, they are more inclined towards micro-pitting than other gearbox bearings (Sharad Jain, 2013).

Theoretically, in order to retard the micro-pitting initiation and propagation, it is necessary to reduce stress raisers, contact pressure and friction force or introduce compressive residual stresses. Other possible ways of retarding micro-pitting are to improve material cleanliness, lubricant film thickness and surface finish, and avoid overload and misalignment, increase the surface hardness and adopt low-friction DLC coatings (FAG, 2001, Adrian Oila and SJ Bull, 2005).

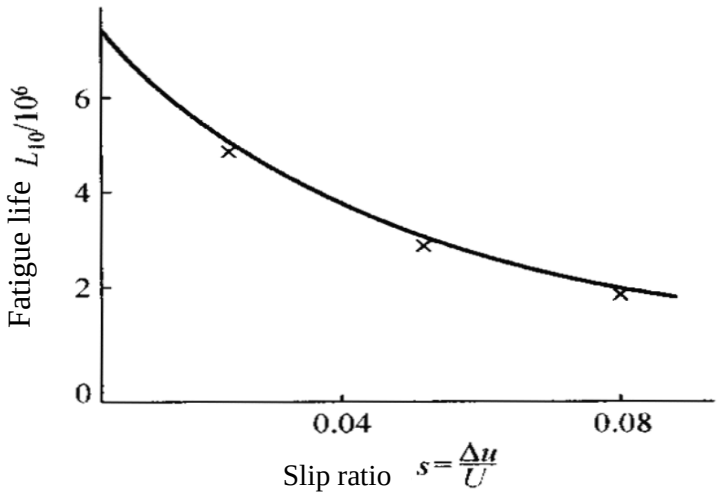

Figure 2.2.4-1 The effect of slip ratio (slide-to-roll ratio) on the fatigue life. $\Delta \boldsymbol{u} = \boldsymbol{u_1} - \boldsymbol{u_2}$ & $\boldsymbol{U} = \frac{\boldsymbol{u_1}+\boldsymbol{u_2}}{\boldsymbol{2}}$, where $\mathbf{u}_1$ and $\mathbf{u}_2$ is the linear speed of each contact part, **U** is the entrainment velocity (Shizhu Wen and Ping Huang, 2012)

2) Scuffing surface damage occurs in gears or bearings due to severe adhesion or adhesive wear in metal-to-metal contact area where lubrication is inadequate. Starvation of lubrication leads to direct asperity contact (i.e. metal-to-metal contact) and local frictional heating between the friction pair. As a consequence of this, attractive atomic forces between the real contact regions (i.e. the contacting asperities), can lead to 'welding' of the contacting asperities together, causing adhesion. Then high normal contact pressure and frictional shear stress could strengthen the local material of contacting asperities through plastic deformation, increasing the area of asperity junction (G. Stachowiak and A.W. Batchelor, 2013). Subsequently, the movement of the friction pair can tear the 'welded' and cold-worked asperity material away from one friction body and transform it to the other one. Therefore, the smooth as-machined surface of the gear teeth or bearing is disrupted and roughened, displaying signs of strong adhesion and adhesive wear (G. Stachowiak and A.W. Batchelor, 2013). Scuffing often leads to modification of the component profile, thus increasing vibration or shock during operation of gears and bearings (NOVEXA, 2017). Therefore, scuffing may act as a precursor to more severe wear, contact fatigue-related defects and cracking. Scuffing is commonly observed in field failures, while an extensive lubrication can slow down or even stop this type of damage (A Greco et al., 2013, Tibor E Tallian, 1992, NOVEXA, 2017).

3) Fretting wear is a common issue for some bearing and gear components in pitch and yaw systems which experience only a small range of rapid motion or structure-borne vibration. This condition causes the lubricant to be constantly squeezed out from the contact area making it difficult to replenish it. Thus metal-to-metal contact is allowed resulting in the superficial protective oxide layers to be rapidly removed and regenerated (A Greco et al., 2013, Michael N Kotzalas and Gary L Doll, 2010, Robert Errichello, 2004, Gary Doll, 2011).

At the early stages of fretting wear, the wear mechanism is mild adhesion and wear debris is mainly composed of magnetite (Fe_3O_4). The surface damage at this early stage is also called as false brinelling. As the wear debris accumulates it reaches a certain level at which it totally inhibits lubrication between the contact area. Consequently, this leads to the oxide layer being broken causing wear due to severe adhesion. Fretting corrosion involves high wear rates, generating very fine haematite (Fe_2O_3) powder debris, which is reddish-brown in colour (Michael N Kotzalas and Gary L Doll, 2010).

Surface damage due to fretting wear acts as stress concentrator, thus prompting other failure modes such as rolling contact fatigue (HKDH Bhadeshia, 2012). It was reported that the material loss caused by fretting corrosion could be reduced by increased material hardness (Paland EG, 1982, HKDH Bhadeshia, 2012).

4) Microstructural alteration (i.e. the 'white etching area' or 'butterfly crack') commonly appears as a crack on a bearing surface or crater on bearing and gear surfaces. It is a type of rolling contact damage formed under cyclic loading conditions. However, it is unlike conventional rolling contact fatigue. White etching crack (WEC) may be a result of multiple factors, including hydrogen-induced embrittlement from lubricant decomposition or water contamination, and low-temperature recrystallisation mechanically induced from high cycle extreme loading applied to highly stressed and slipping regions, e.g. around non-metallic inclusions (A Greco et al., 2013). The initiation and propagation of WECs around inclusions can be replicated by applying simultaneous compound load (i.e. normal impact load plus sliding) of 2.5 GPa on bearing steel for about 1 million cycles (T Bruce et al., 2016). WECs have also initiated at inclusions which are present between 30 and 800 μm below the contact surface of twin steel wheels through rolling contact fatigue tests under the maximum contact pressure of 2.15 GPa (M-H Evans et al., 2013). WEC is uncommon in steels with significant

amounts of austenite phase, which may absorb the energy and transform into martensite first due to stress induced phase transformation. WEC is one of the most critical and least understood failure modes experienced in wind turbine gearboxes. It has been found to be much more prevalent in the wind industry than in other applications.

2.2.4.2 Gearbox failure mechanisms

The contact and bending stresses are the source of failure in helical gears. As to the bearings, their lifetime is ultimately limited by failures due to contact stress, such as rolling contact fatigue. In order to assure high gearbox reliability for wind turbines, materials, lubrication and design parameters must be considered. The misalignment caused by the own weight of large wind turbine components, the extremely unusual variable operating loading conditions, the poor lubrication conditions and inadequate material cleanliness are deemed to be responsible for wind turbine gearbox failures.

1) In order to handle the large amount of torque wind turbine gearbox components need to be massive. The heavy gearbox sub-components can generate flexing of the gearbox casings and shafts, causing unavoidable misalignment of the gear mesh and bearings (Michael N Kotzalas and Gary L Doll, 2010). The misalignment results in a non-uniform load distribution on gear and bearing surface, with perhaps very little or no load on one side and a larger edge load on the other. Such poor load distribution conditions might increase local stresses at the overloaded side that are higher than the allowable limits, thus, leading to premature failures, e.g. contact fatigue and severe wear (MA Hotait et al., 2007).

2) Another reason for gearbox failures in wind turbines is the random wind speed causing highly variable dynamic load characteristics, involving transient loading events, which can arise from sudden wind gusts and emergency stops.

The torque level in a wind turbine gearbox will vary between zero and the rated torque, depending on the wind speed. In the case of fixed-speed pitch regulated wind turbines, due to the slow pitch response, excursions above the rated torque can occur. Temporary torque fluctuations will excite drive train resonances, causing relocation of the load zone of bearings, leading to axial skidding and impact on the overstressed rollers.

Moreover, even when wind is not driving the rotor, small-amplitude vibrations of driving systems can still arise by unstable wind conditions, leading to fretting wear of the gearbox components (Tony Burton et al., 2011, Michael N Kotzalas and Gary L Doll, 2010, Doug Herr Dave Heidenreich, 2012). P Tavner et al. (2010) investigated the influence of weather and wind turbine location on gearbox failure rates and downtime. They demonstrated that a significant cross-correlation exists between the failure rate and wind conditions.

In addition, when connecting or disconnecting the generators to the power grid, gearboxes will experience rapid transient acceleration and torsional variation. For example, a torque trace of main shaft was recorded with the torque monitor during a grid disconnect event as shown in Figure 2.2.4-2. In the beginning, the torque (indicated by the solid red trace line) slightly fluctuated around the rated torque (indicated by the interrupted blue trace). Once the wind turbine has been disconnected from the power grid, the shaft rotational speed (green line) decreased and significant torsional reversals started. When the torque continually reversed across the zero-torque line, the bearing rollers were very likely skewing and skidding at the same time (Doug Herr Dave Heidenreich, 2012). Another instance is that an intermediate shaft of a 1.5 MW gearbox may rapidly accelerate from 375 to 420 rpm in 2 seconds due to premature generator engagement, hence torque reversals between negative 800 kN·m and positive 430 kN·m occurs in less than 100 milliseconds. Hence, high contact stresses and impact forces are experienced by the bearings and gears, resulting in catastrophic tooth failure,

significantly reducing roller element surface durability (J Rosinski and D Smurthwaite, 2010). In practical operation of the wind turbine, torsional reversals, due to generator engagement and disengagement to the power grid, can happen thousands of times per year (Michael N Kotzalas and Gary L Doll, 2010).

Besides, there will be occasionally much larger torques of short duration due to braking events unless the brake is fitted to the low-speed shaft. Although braking loads are infrequent and of short duration, their magnitude means that they can have a decisive effect on fatigue damage. During these transient load events, extremely high cyclic contact stresses (may exceed 3.1 GPa (Jürgen Gegner, 2011, T Bruce et al., 2016)) are experienced by the gears and bearing rollers, leading to premature failure due to micro-pitting and smearing (Tony Burton et al., 2011, Michael N Kotzalas and Gary L Doll, 2010).

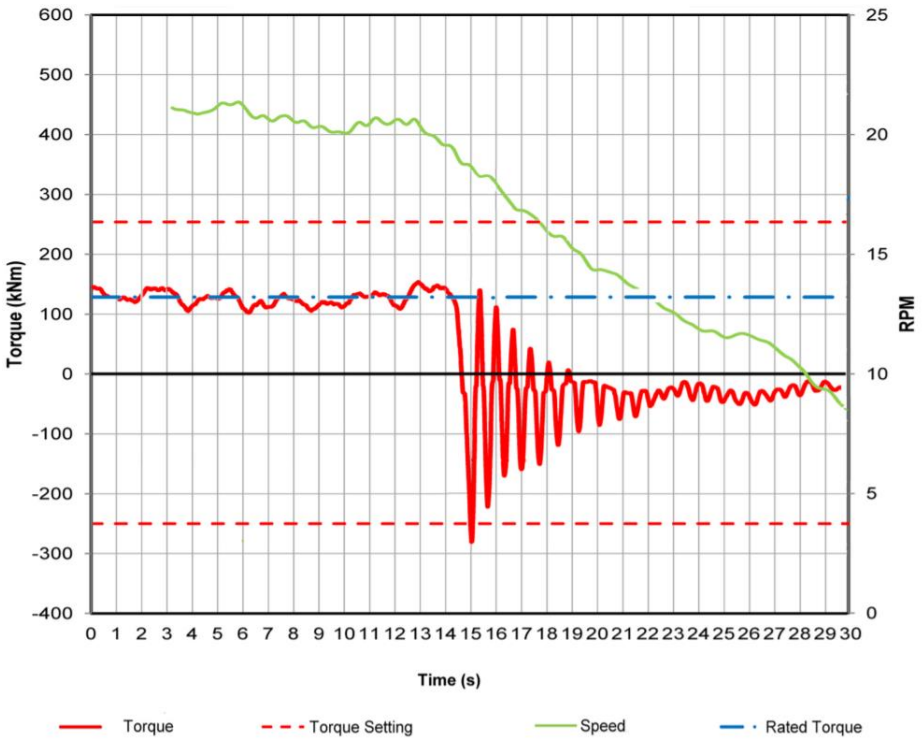

Figure 2.2.4-2 Reversing torque and the torsional vibration recorded during a grid-disconnect event (Doug Herr Dave Heidenreich, 2012)

3) Poor lubrication conditions (i.e. the cleanliness and thickness of lubricant) also contribute to failure of gearbox subcomponents. The lubricant film performs many critical functions, such as cooling, separating moving surface and carrying the load to reduce friction, protecting against wear and corrosion, and removing debris away. The first problem is the presence of contamination in the lubricant which interferes with its intended lubrication quality. The contaminants can be solid particles of dirt or wear debris, a liquid, such as water, or gaseous, such as air. Poor quality of lubrication eventually results in failure of gearboxes. For example, the hard solid particles may form three-body wear with moving component surfaces or embedded in one surface hence increasing wear rate. It was reported that in comparison with gears, rolling element bearings are more sensitive to particulate contamination. By using fine rated filters to reduce the contamination levels, improved maintenance levels (e.g. using oil monitoring) can contribute to the improvement of the lubrication reliability. Changing of lubricant or cleaning filters in time can hence improve the service lifetime of the gearbox (BKN Rao, 1996).

Another problem is the inadequate thickness of the lubricant film. The lubricant film thickness is determined by viscosity, speed and load as shown in the following formula (DM Pirro and AA Wessol, 2013).

$$T \propto \frac{\text{Viscosity} \times \text{Velocity}}{Load}$$

Micro-pitting, scuffing and smearing of bearings are caused by severe roller/raceway sliding in the area where the ratio Λ of lubricant thickness to surface roughness is low (Gary Doll, 2011). Gears and bearings in the gearbox low-speed stage rotating very slowly, normally fail to generate sufficient thick lubricants films, even with high viscosity lubricants. This results in an increasing trend for surface damage (Michael N Kotzalas and Gary L Doll, 2010). The

micro-pitting problems could be solved by increasing the specific film thickness of the operating lubricant or by using smooth component surfaces (R. Errichello et al., 1994). The recently developed super-finishing process can reduce the component roughness value by an order of magnitude to about 0.05 μm, thus significantly increasing the resistance to micro-pitting (Lane Winkelmann, 2011, Lane Winkelmann et al., 2009).

4) Coarse inclusions (e.g. the hard oxides, nitrides and residual carbides, and soft sulfides such as MnS) in steel can cause premature failure of gearbox components. Most steels produced today could be deemed very clean, but coarse non-metallic inclusions persist. Gears and bearings are designed assuming the material is ideally homogeneous and clean. However, in fact, the material is microscopically heterogeneous and contains non-metallic inclusions, deteriorating the property and shortening the lifetime of components (Erick S Alley and Richard W Neu, 2010). For example, Richard Jay Parker and Eric N Bamberger (1983) reported that large carbides negatively influenced the rolling contact fatigue life to a large extent. The classical explanation is that these inclusions cause component failure by concentrating local stress and initiating cracks, weakening the toughness and ductility of the steels because their thermal and mechanical properties are different to the surrounding matrix (L. de Campos Franceschini Canale, 2008). Specifically, micro-voids/holes were observed at the inclusion tips (TR McNelley, 1986, ZZ Yuan et al., 2006). These voids were formed during heat treatment or the component operation, through inclusion fracture or interface separation of the inclusion/matrix boundary. These voids become weak locations and act as crack nuclei. MH Evans (2012) reviewed the influence of inclusions on the initiation of the white etching area cracks. It was observed that the white etching area (where material microstructure altered) formed beside carbides and sulphides, and preferentially formed at oxides. Meanwhile, hydrogen was found at defects in the matrix surrounding Cr carbides,

MnS and Al_2O_3 inclusions. Therefore, eliminating inclusions in gearbox materials is recommended to improve the service time of wind turbine gearbox components.

As mentioned before, the gearbox is among the least reliable subsystems of the wind turbines. In this section, the common reported failure modes of wind turbine gearboxes are summarised, including rolling contact fatigue, scuffing, false brinelling, fretting corrosion and white etching cracking. The failure causes of wind turbine gearbox components (high stresses due to misalignment, variable loading conditions, poor lubrication conditions and inadequate material cleanliness) were summarised and reviewed. Considering the fact that the current failure rate of wind turbine gearboxes is still high, further research on the failure modes, failure causes and appropriate strategies is needed to understand deeper gearbox damage mechanisms, reduce wind turbine failure rate, and further lower the cost of wind power production.

2.3 Simulation of operation of gearbox components

Modelling is a powerful, straightforward and efficient method to demonstrate stress distribution in gearbox components and evaluate the effects of different factors on stress fields, which is difficult with other methods. Simulations of gear and bearing operation have been considered in a number of studies.

Raul Tharmakulasingam (2009) simulated the contact stress distribution of meshing gear teeth (friction neglected) using finite element analysis (FEA). As shown in Figure 2.3-1, the maximum stress is located at the subsurface, which is consistent with the traditional Hertz contact theory.

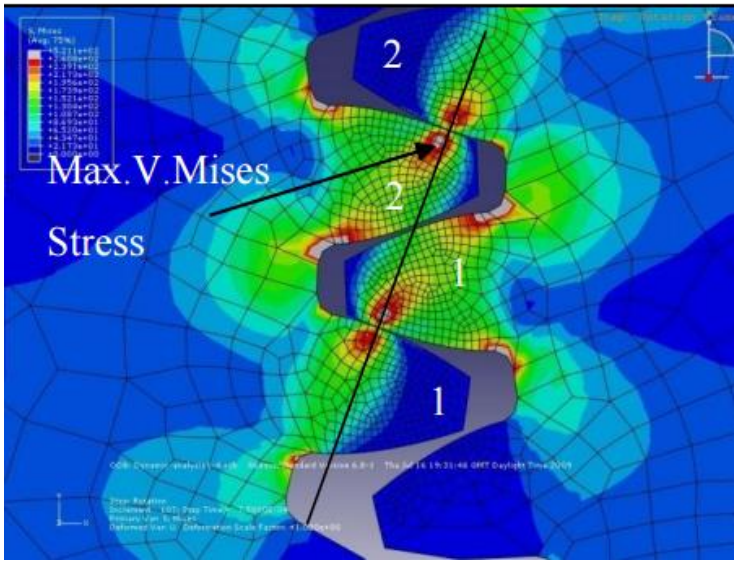

Figure 2.3-1 Contact stress distribution (friction neglected) of meshing gear teeth simulated by ABAQUS (Raul Tharmakulasingam, 2009)

Muhammad Irfan (2013) analysed the effect of radial and angular misalignments on contact stresses of wind turbine gears with a friction coefficient of 0.12 through FEA simulations. As indicated in Figure 2.3-2, the stress flow of the contacted teeth would be higher when radial misalignment and angular misalignment increase.

F Oyague (2009) carried out modelling of a wind turbine gearbox loading conditions using FEA software SIMPACK together with FAST_AD code. Under the emergency breaking condition, the planet carrier would be misaligned as shown in Figure 2.3-3. Misalignments result in uneven load distribution between the contacted planetary gears, prompting gear failures. When helical gears are adopted, the intermediate shaft would move back and forward along the axial direction during the breaking event (as shown in Figure 2.3-4) which is one of the possible reasons for bearing failures.

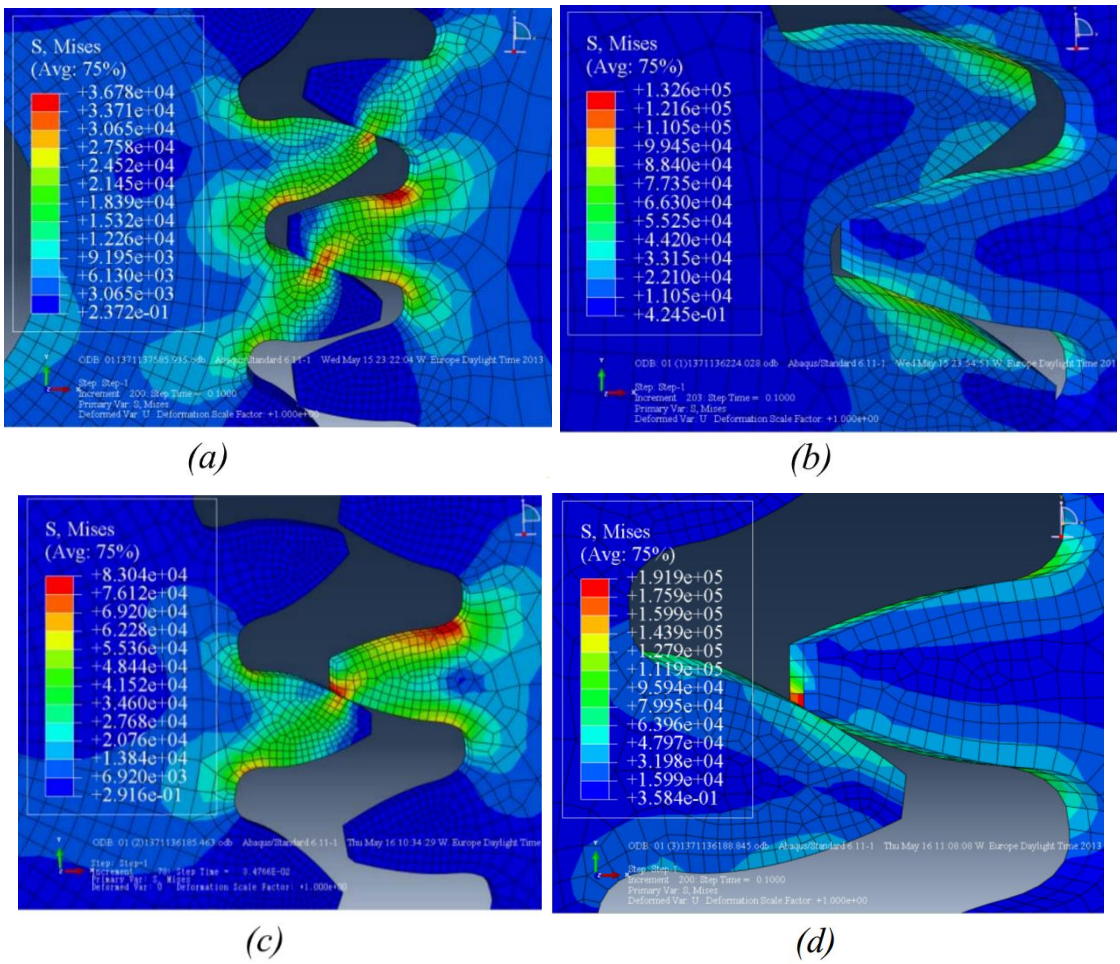

Figure 2.3-2 Stress flow of teeth contacted at (a) 0 mm radial misalignment and 0 degree angular misalignment, (b) 0 mm radial misalignment and 2 degree angular misalignment, (c) 4 mm radial misalignment and 0 degree angular misalignment, and (d) 4 mm radial misalignment and 2 degree angular misalignment (Muhammad Irfan, 2013)

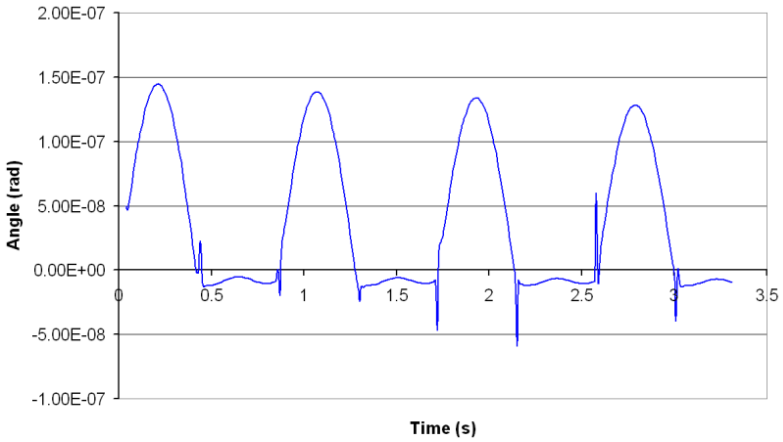

Figure 2.3-3 Angular misalignment of the planet carrier under breaking event (F Oyague, 2009)

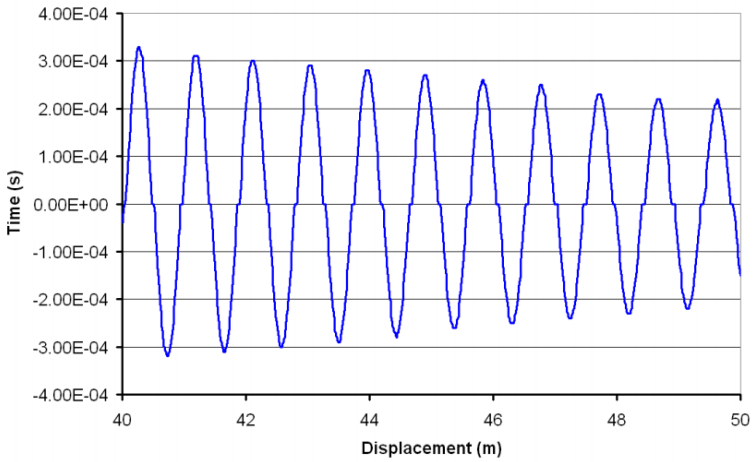

Figure 2.3-4 Axial displacement of intermediate stage shaft under breaking event (F Oyague, 2009)

Yi Guo and Robert G Parker (2010) built a two-dimensional lumped-parameter model simulating a planetary gear of a wind turbine drive train. Based on the modelling results obtained, it was concluded that tooth wedging in large planetary gears may cause tooth damage and bearing failure. The tooth wedging is a phenomenon that both the drive-side and back-side of a tooth comes into contact with other two teeth simultaneously. This phenomenon changes the load sharing among the planets, elevates their tooth loads (as shown in Figure 2.3-5) and thus boosts the planet bearing forces dramatically (as shown in Figure 2.3-6). Tooth wedging is the combined effect of gravity and bearing clearance nonlinearity (as shown in Figure 2.3-7). Tooth wedging is prone to occur in planetary gears involving a heavy component and large bearing clearance. Bearing clearance allows great translational vibration, while gravity is the dominant excitation source causing the large motions that lead to tooth wedging. Gravity disrupts the planet symmetry and thus breaks the mesh phasing rules that can reduce planetary gear vibration in selected harmonics of mesh frequency (Yi Guo and Robert G Parker, 2010).

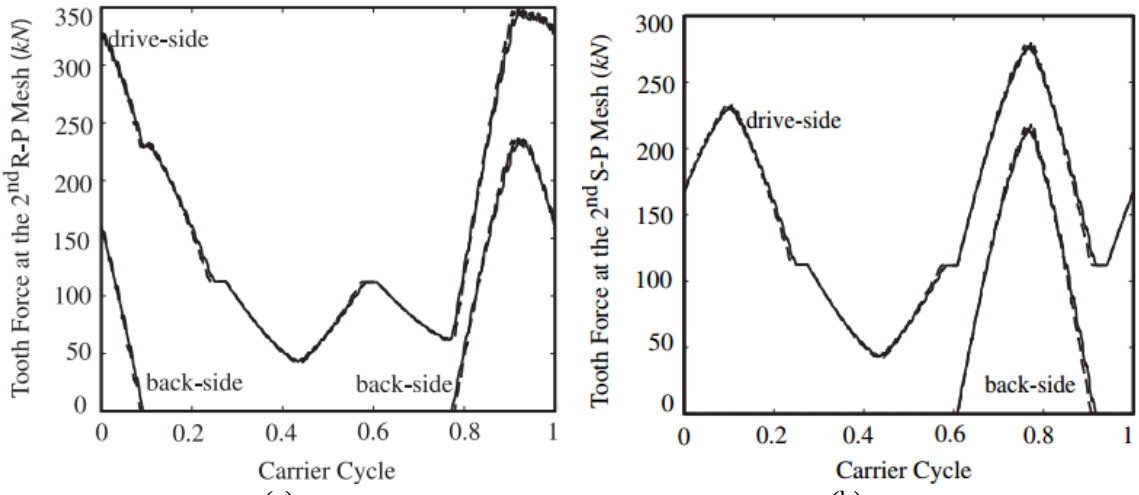

Figure 2.3-5 Drive- and back-side tooth forces at the (a) Ring-Planet mesh and (b) Sun-Planet mesh (Yi Guo and Robert G Parker, 2010)

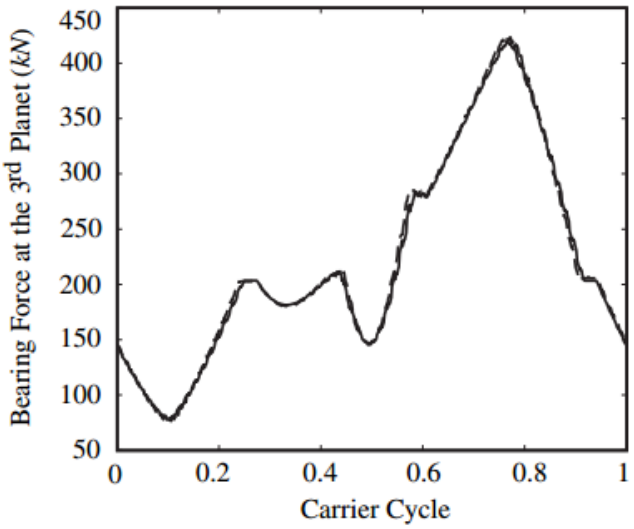

Figure 2.3-6 Bearing force at one of the planets (Yi Guo and Robert G Parker, 2010)

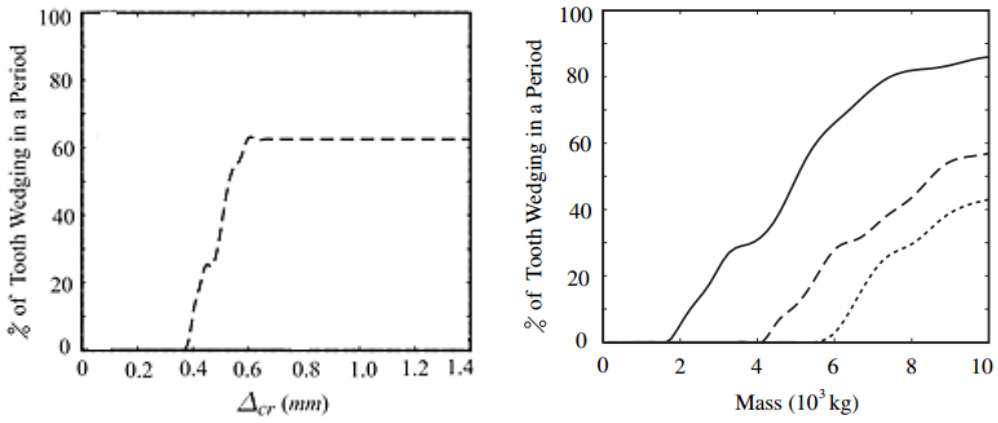

Figure 2.3-7 Extent of tooth wedging in a carrier period with a) varying bearing clearance Δcr and b) varying mass of the planetary gear components (sun (solid line), carrier (dashed line), and ring (dotted line)) (Yi Guo and Robert G Parker, 2010)

Emil Claesson (2014) developed and verified three simplified finite element models for cylindrical roller bearings using FEA software ABAQUS to simulate the loads to which the bearings are subjected.

Erick S Alley and Richard W Neu (2010) pointed out that assuming the modelled material is homogeneous and isotropic, even directly embedding inclusions in matrix material, makes the simulation results unrealistic to some extent. The authors adopted heterogeneous crystal plasticity material models instead of the homogeneous J_2 plasticity model to simulate rolling contact fatigue. They found that the former model predicts the accumulation of local strains in bearing steel more realistically.

FEA simulations have been carried out by a number of researchers studying the effects of misalignment and tooth wedging on gears. The results published have shown the significant ability of FEA methods in evaluating stress distribution. However, the effect of variable

friction coefficient on contact stress, or the effect of coarse inclusions on stress field and cracking have not been studied. These issues have been simulated in this project.

2.4 Condition monitoring of wind turbine gearboxes

Condition monitoring systems (CMS) based on vibration analysis and acoustic emission measurements, can significantly increase the reliability and reduce the O&M costs of wind turbines, by avoiding sudden and unpredictable gearbox failures. Therefore, a novel condition monitoring methodology was developed in this study.

The reduction of downtime and O&M expense associated with wind turbines is a critical issue that needs to be addressed in order to lower the price of electricity produced and make wind power more competitive with respect to conventional and other renewable energy sources (Bin Lu et al., 2009).

Poor reliability of wind turbines leads to a direct increase of the downtime and consequently O&M costs, increasing the overall cost of wind energy (Christopher A Walford, 2006, Cited by Bin Lu et al., 2009). Although larger turbines reduce the LCOE, the cost per failure is increased. It is known that the gearbox is one of the most expensive, difficult to repair and least reliable subsystems of industrial wind turbines. Unexpected failure can result in substantial unnecessary costs. Thus, improving the operational reliability of wind turbine gearboxes can significantly contribute towards the meaningful reduction of the overall O&M cost.

Wind turbines are often located in remote areas, and are hard to access (e.g. access highly depends on location, wind and weather conditions) especially in the case of offshore wind

farms. Condition monitoring and fault diagnosis of wind turbines has thus great benefit for wind farm operators (Bin Lu et al., 2009).

With good data collection and appropriate signal analysis methods, the health of wind turbines can be monitored remotely. Hence, faults can be identified early while components are operational. More efficient corrective or preventive maintenance actions can be planned and carried out in time to avoid further damage to other components or to the subsystem level, resulting in improved reliability and availability of wind turbines, and decreasing the O&M cost of wind turbines (Fausto Pedro García Márquez et al., 2012).

Central control systems, continuously monitoring the performance and operation of every wind turbine have been adopted by most modern wind farms (David A. Spera, 2009, Christopher J Crabtree et al., 2014). Fausto Pedro García Márquez et al. (2012) and WY Liu et al. (2015) reviewed vibration analysis, acoustic emission and other state-of-the-art condition monitoring techniques of wind turbines. Fausto Pedro García Márquez et al. (2012) pointed out that, in addition to the monitoring technique employed, the overall capability of a condition monitoring system depends on two basic elements; the proper type and distribution of sensors, and the associated signal processing methods utilised to extract key information from complex signals.

2.4.1 Vibration-based condition monitoring

Vibration analysis has been widely used to monitor structural and mechanical health of components in many industrial fields, including the wind energy industry. Vibration-based condition monitoring systems are currently the most popular technology adopted for monitoring wind turbine gearboxes, although they are not sufficiently sensitive for low speed components.

2.4.1.1 Principles of vibration analysis

Every dynamic system will virtually vibrate and make noise. Individual components generate distinctive vibration patterns. When mechanical defects initiate and evolve in the gearbox, the vibration spectrum will differ from that of a defect-free structure. In addition, different mechanical defects affect vibration in their unique way. These make it possible to identify gearbox faults by measuring the vibration characteristics (A. Davies, 1998, Ron Barron, 1996) .

The typical stages of vibration signal acquisition and analysis for rotating machinery are summarised in Figure 2.4.1-1. The first step of vibration analysis is to assess each machine's condition and normal level of vibration. Based on this, the acceptable level of vibration is set. Once the acceptable vibration level has been exceeded, the next step is to process and analyse the measured data using proper analysis methods. Then the problem or defect can be identified by comparing the processed vibration characteristics with the nature of the machine and the abnormal vibration with different causes (A. Davies, 1998).

In the data detection stage, the acceleration, velocity or displacement of vibration amplitude is measured, depending on the frequencies being analysed: acceleration covers frequencies from 0 to around 20 kHz, velocity covers from 0 to 2 kHz and displacement (i.e. the absolute position) covers from 0 up to 200 Hz (Ron Barron, 1996). In order to acquire satisfactory vibration measurements, appropriate sensors suitable for certain frequency range need to be chosen. For instance, position sensors are suitable for low frequencies, velocity sensors for middle frequencies, accelerometers for high frequencies and energy spectral emitted sensors for very high frequencies (TW Verbruggen, 2003). Industrial accelerometers with a broad operational frequency range (from 0.5 Hz up to 25 kHz) are normally used for wind turbine gearbox monitoring purposes.

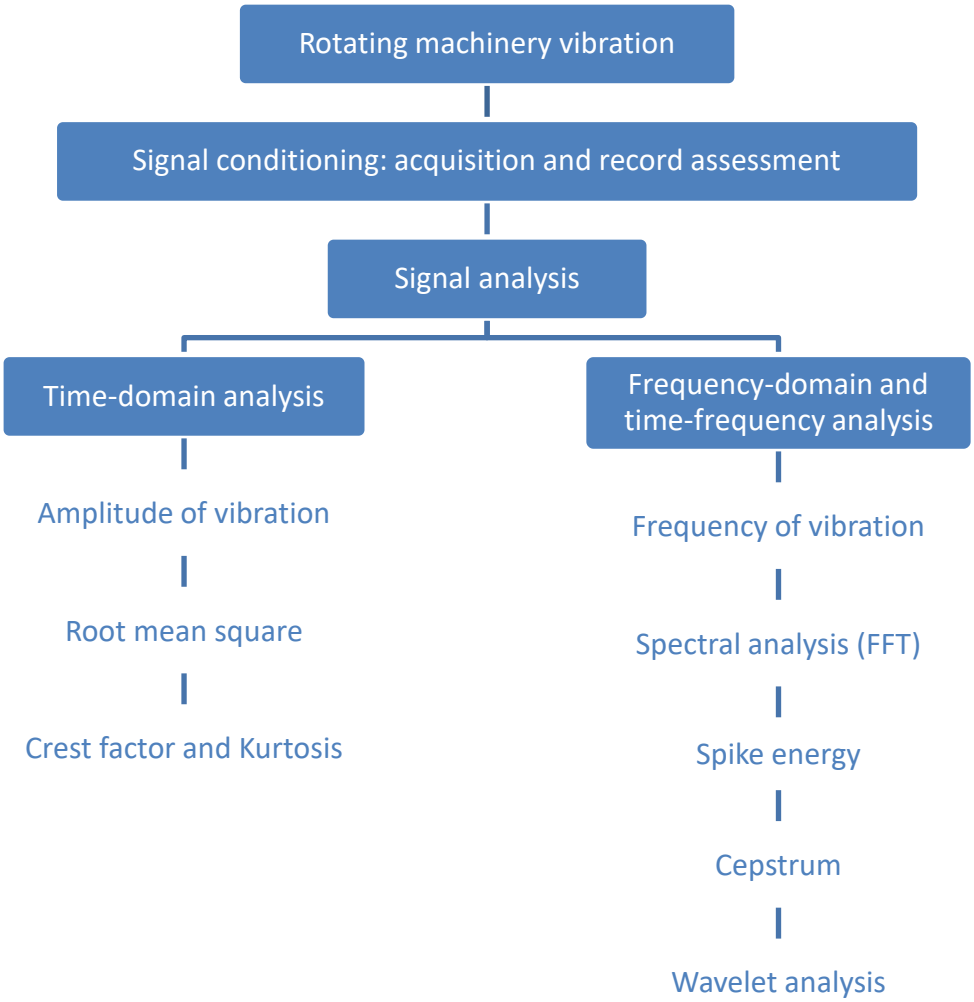

Figure 2.4.1-1 Typical stages of vibration signal acquisition and analysis (Ron Barron, 1996)

2.4.1.2 Signal processing methods

In order to analyse vibration data, a variety of signal processing methodologies can be employed in order to extract key information from the acquired complex signals (Ron Barron, 1996, Fausto Pedro García Márquez et al., 2012, A. Davies, 1998, Faris Elasha et al., 2015). Through appropriate analysis of the vibration data the diagnosis of the condition of the gearbox components becomes possible and faults that may be present can be identified. The signal processing methods can be classified into three main groups, based on time-domain analysis, frequency-domain analysis, and time-frequency-domain analysis. The time-domain

analysis includes raw vibration waveform analysis (e.g. peak-peak analysis) and statistical analysis (e.g. Moving Root Mean Square or RMS, Moving Crest Factor and Moving Kurtosis). The frequency-domain analysis includes spectral analysis (e.g. using Fast Fourier Transform FFT), spike energy (also known as the power spectrum of the signal envelope or demodulated signal) and cepstral analysis (inverse Fast Fourier Transform). Time-frequency-domain analysis includes Short Time Fourier Transform (STFT), Spectral Kurtosis (SK) and wavelet analysis. For the reliable analysis of vibration data most or all of these algorithms should be used as they are sensitive to different forms of damage.

The Root mean square (RMS) value is the square root of the mean square of the signal amplitude. For a signal f(t) in the time period T_1-T_2, its RMS is expressed as (A. Brandt, 2011)

$$\boldsymbol{RMS = \sqrt{\frac{1}{T_2 - T_1}\int_{T_1}^{T_2}[f(t)]^2 dt}} \qquad \textbf{Equation } 13$$

The RMS is trended to illustrate the vibration state change. The RMS value will increase gradually as the damage evolves further (A. Davies, 1998). Therefore, by trending the RMS value it is possible to identify the damage progression with time. However, the RMS cannot provide an indication of what the exact fault is other than that there is a fault somewhere in the gearbox.

The Crest Factor (CF) of a waveform is the ratio of its peak amplitude value to the RMS value (A. Davies, 1998). Hence the CF can be expressed as

$$\boldsymbol{CF = \frac{peak\ amplitude}{RMS}} \qquad \textbf{Equation } 14$$

The use of CF is beneficial when the signal contains several impulses. CF can help identify which peaks are related to a real defect and which are due to noise. For components in good condition, the CF value will be in the range between 2.5 to 3.5. CF values higher than 3.5

generally hint the presence of damage. CF value will increase due to strong damage-induced impulsive vibration, such as tooth breakage. Severely damaged components generating significant impulsive vibration can exhibit CF values up to around 11 (M.P. Norton and D.G. Karczub, 2003). But, for occurrence of slight incipient failure, the CF only increases marginally and it will decrease when the incipient failure develops progressively (A. Davies, 1998). CF is sensitive to significant discrete vibration impulses above the background signal. Although the corresponding RMS values will not change evidently if the duration of damage-induced impulses is short or the occurrence frequency of impulses is low, CF values will (Salem K Al-Arbi, 2012).

Kurtosis is the 4th-order statistic moment of the distribution of the signal, describing the impulsive character of the signal (F De Lorenzo and M Calabro, 2007). Kurtosis is expressed

$$\boldsymbol{K = \frac{1}{N}\sum_{i=1}^{N}\left(\frac{x_i - \mu}{\sigma}\right)^4} \qquad \textbf{Equation } 15$$

where N is the tests number, x_i is the vibration amplitude in time history, μ is the average (1st-order moment), and σ is the standard deviation (2nd-order moment) given by equation

$$\boldsymbol{\sigma = \sqrt{\frac{1}{N}\sum_{i=1}^{N}(x_i - \mu)^2}} \qquad \textbf{Equation } 16$$

Kurtosis can be trended and compared in order to determine the degree of severity of damage present (Ron Barron, 1996). For a defect-free component, the Kurtosis value is around 3. For damaged machinery, it will become greater than 4 (M.P. Norton and D.G. Karczub, 2003), indicating the increase of major signal peaks (M.P. Norton and D.G. Karczub, 2003). Similar to CF, Kurtosis is also reliable in analysing severe impulsive vibration signals (M.P. Norton and D.G. Karczub, 2003). The signal trend expressed by Kurtosis has been found to be similar to CF, but Kurtosis changes more evidently than CF, i.e. Kurtosis possesses much higher

numerical magnitude than CF (A. Davies, 1998). However, the Kurtosis algorithm is computationally far more expensive than CF.

Spectral analysis using Fast Fourier Transform (FFT) to convert the time-domain signal into frequency-domain and thus obtain its frequency spectrum (Ron Barron, 1996), is very useful in vibration analysis. Therefore, spectral analysis is widely used to identify faulty gears and bearings. It is known that mechanical parts with certain faults generate vibration at distinct frequencies. Spectral analysis can identify major frequency components (including the fundamental frequency, its harmonics and sidebands) in the vibration signal. If some frequency components in spectrum are in accordance with the symptom frequencies of certain part faults, then the fault parts can be identified (Fausto Pedro García Márquez et al., 2012, Faris Elasha et al., 2015).

The spike energy (C. Scheffer and P. Girdhar, 2004, Ron Barron, 1996) algorithm, also known as the power spectrum of the demodulated signal (Fausto Pedro García Márquez et al., 2012), enveloping or acceleration enveloping (Nathan Weller, 2004, Charlie Hatch, 2004), can be applied in order to extract the impact repetition frequencies associated with a defect present in the overall vibration signal. It can be trended to evaluate the progression of machine condition and it is able to detect bearing or gear faults very early. The spike energy method is a multiple-step process. The typical steps involved are shown in Figure 2.4.1-2. In brief, the raw vibration waveform is first high-pass or band-pass filtered. The signal is then full-wave rectified, followed by demodulation. Finally, FFT is applied to obtain the frequency spectrum of the demodulated signal as explained by C. Scheffer and P. Girdhar (2004) and Nathan Weller (2004). If defects develop, more harmonics of fundamental frequency or sidebands related to the running speed will appear in the power spectrum of the processed signal (Nathan Weller, 2004). The spectrum of the demodulated signal can be more sensitive

to defect frequencies than conventional FFT applied on the raw vibration signal. Therefore, spike energy is a particularly useful tool for monitoring rotating components in wind turbines (Charlie Hatch, 2004).

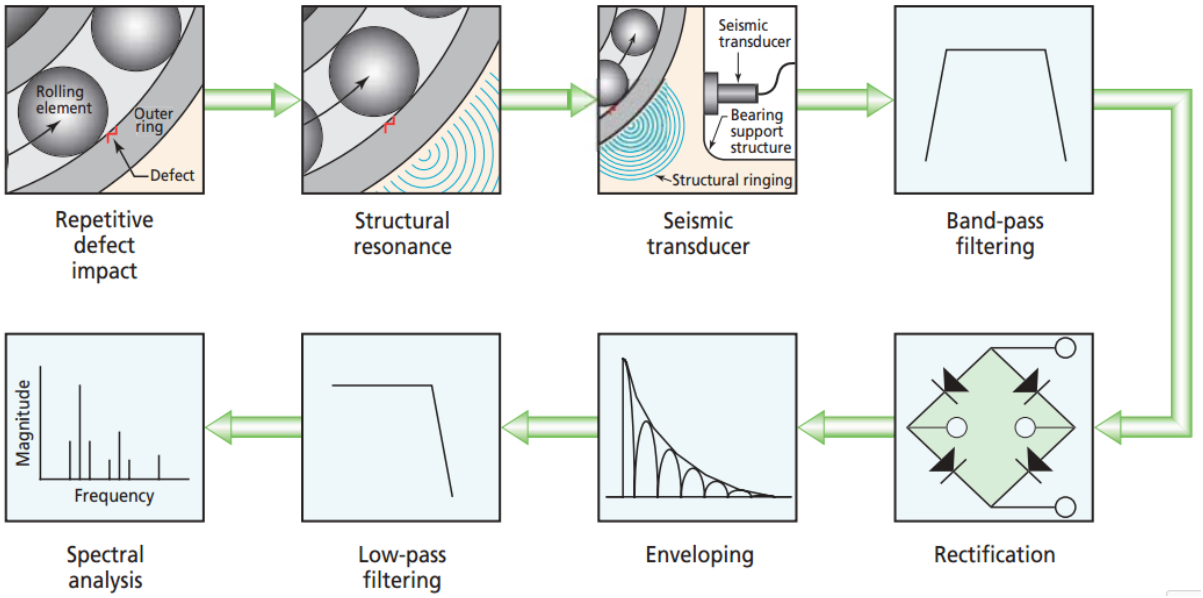

Figure 2.4.1-2 Typical steps in the implementation of enveloping (Nathan Weller, 2004)

Cepstrum analysis is the inverse Fast Fourier Transform which can clearly emphasis the periodic frequency components of the raw spectrum, such as the harmonics and sidebands (Ron Barron, 1996). It is also very useful for monitoring the progression of the system's overall health condition. For instance, the sideband level of defect-free components generally remains constant with time. If the amount and amplitude of the sidebands changes, it normally implies that defects have developed in the system (Fausto Pedro García Márquez et al., 2012).

Short time Fourier transform (STFT) is a time-frequency analysis method, which is suitable for non-stationary signals (Fausto Pedro García Márquez et al., 2012), i.e. the signal frequencies changes with respect to time. STFT utilises the concept of time window to separate the whole time-domain vibration signal into smaller sections, and then FFT applied

to obtain their power spectrum. However, STFT has an intrinsic limitation related to the window concept, which is the uncertainty principle (K. Gröchenig, 2013). If the window size is small, which means the time resolution is high, then the frequency resolution is low, and vice versa.

The Spectral Kurtosis (SK) is a statistical tool to find the serial transient components and identify their positions in the frequency domain (Jérôme Antoni, 2006). It was originally defined as the normalized fourth moment of real part of STFT (R Dwyer, 1983). Later, the definition was modified as the fourth order moment of the magnitude of STFT (C Ottonello and S Pagnan, 1994, S Pagnan et al., 1994).

Wavelet transform is also a time-frequency analysis method but more complex in nature than STFT and Spectral Kurtosis. It uses the concept of mother wavelet instead, which can be described as a brief oscillation and the mother wavelet can be flexibly stretched, squeezed and moved. Then the wavelet transform is applied to correlate a raw signal with a set of mother wavelets , without the concern of the uncertainty principle (P.S. Addison, 2017).

2.4.1.3 Vibration analysis and its limitations

Vibration-based condition monitoring systems have been used to provide early warning of structural and mechanical defects, enabling wind farm operators to carry out predictive maintenance and hence reducing downtime. Depending on the type of damage, early warning up to six months is possible (E Becker and Paul Poste, 2006).

Although vibration analysis is still the most popular technology employed for monitoring wind turbine gearboxes (Z. Hameed et al., 2009, cited by Fausto Pedro García Márquez et al., 2012), its sensitivity is reduced significantly by low rotational speeds of some components such as the main bearing or main shaft. This is due to the fact that the impact energy and

signal amplitudes associated with defects varies directly with rotational speed (David Mba and Raj BKN Rao, 2006). Moreover, unless the accelerometers used have an appropriate operational frequency range which covers the rotational frequencies of low-speed components, defects that may be present can go undetected when analysis is carried out using frequency-domain algorithms such as FFT. In addition, vibration-based CM systems lack ability to give material information.

2.4.2 Acoustic emission

The relatively low rotational speed of certain wind turbine drive train components poses technical challenges during vibration-based condition monitoring. To address these challenges, acoustic emission (AE) has attracted much attention as an alternative to vibration as well as a method capable of detecting faults earlier (Bin Lu et al., 2009).

2.4.2.1 Principles of AE testing

Acoustic emissions (AE) are transient elastic waves generated from a rapid release of strain energy caused by a deformation or damage within or on the surface of a material (David Mba and Raj BKN Rao, 2006). For instance, a tree branch emits a cracking sound before it fully breaks (Charles Hellier and Michael Shakinovsky, 2003). With proper configuration and settings, surface displacements as small as a few picometers (10^{-12} m) can be detected using piezoelectric sensors mounted on the surface of the structure being monitored. AE sources are mostly-associated with dynamic processes, including initiation and subsequent propagation of cracks, phase transformation, de-bonding, friction and so on in metals, polymers, ceramics and composites (NDT-Resource-Center, 2012).

The application of AE for monitoring rotating machinery monitoring is related to the detection and analysis of the transient elastic waves generated by the interaction of two media in relative motion. These acoustic emission waves propagate on the surface of the material as Rayleigh waves which are detectable using an AE sensor (David Mba and Raj BKN Rao, 2006). An appropriate acoustic couplant in the form of an adhesive liquid or grease is applied between the piezoelectric sensor face and the smooth structure surface. Due to the low amplitude of the electrical signals generated by the AE sensor, pre-amplifiers and amplifiers with suitably selected gains are employed to amplify the AE signals during acquisition.

AE covers a wide frequency range from 20 kHz to 1.2 MHz. Time domain waveforms associated with AE are of two types: burst shown in Figure 2.4.2-1, and continuous shown in Figure 2.4.2-2. A continuous acoustic emission signal may be a result of turbulent fluid flow in a pipe, while a burst type could be associated with the transient rolling action of meshing gears (David Mba and Raj BKN Rao, 2006). Burst signals are more useful, as they are typically associated with the presence of defects and their evolution with time. However, transient signals can also be generated by unwanted noise sources such as excessive electrical noise or friction. Continuous signals are primarily related to unwanted noise (Hartmut Vallen, 2002). Nonetheless, in monitoring rotating machinery, continuous noise is also useful, since it can contain the signals from defects present on the contact surfaces of the rotating components interacting with each other, e.g. the teeth of two different gears that are in contact as the gears rotate. Figure 2.4.2-1 indicates a typical burst AE waveform in the time domain. The waveform shows a fast rise and then a much slower decay. The rising part is formed by strong waves directly arising from the signal source. The decaying part of the signal is due to the acoustic damping caused by the structure (Charles Hellier and Michael Shakinovsky, 2003). The shape characteristics of the waveform are related to useful parameters of the signal

such as the amplitude, energy and duration (Figure 2.4.2-3), These parameters can provide valuable indications about the nature of the signal source and its severity. Therefore, they are very useful in the subsequent data interpretation process using statistical analysis tools. The size and the speed of the source influence the amount of energy and amplitude of the AE waveform detected. Hence, the AE signal amplitude is proportional to the crack velocity (Charles Hellier and Michael Shakinovsky, 2003).

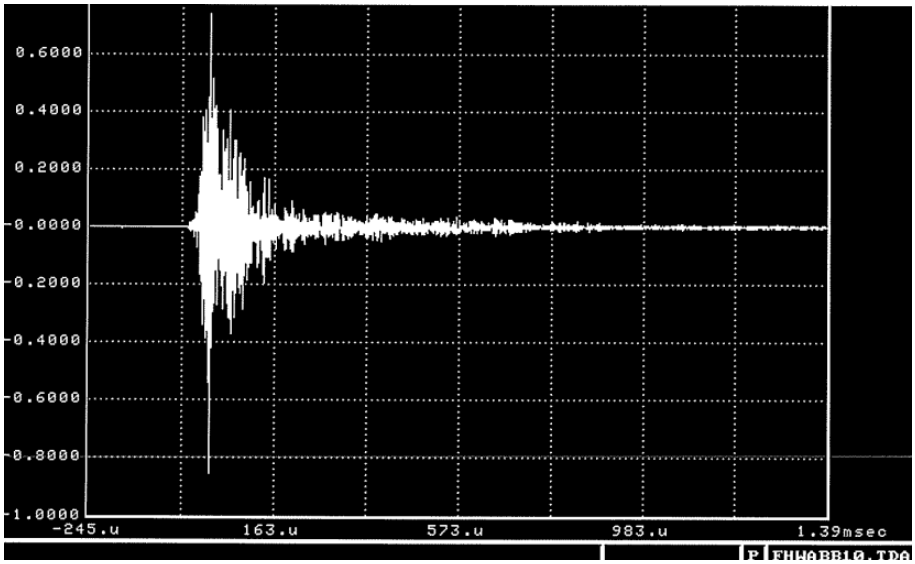

Figure 2.4.2-1 Typical burst AE waveform (Charles Hellier and Michael Shakinovsky, 2003)

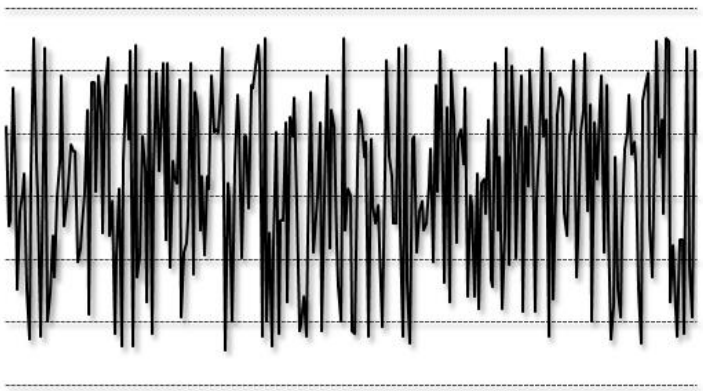

Figure 2.4.2-2 Continuous AE waveform (RETEGATE, 2017)

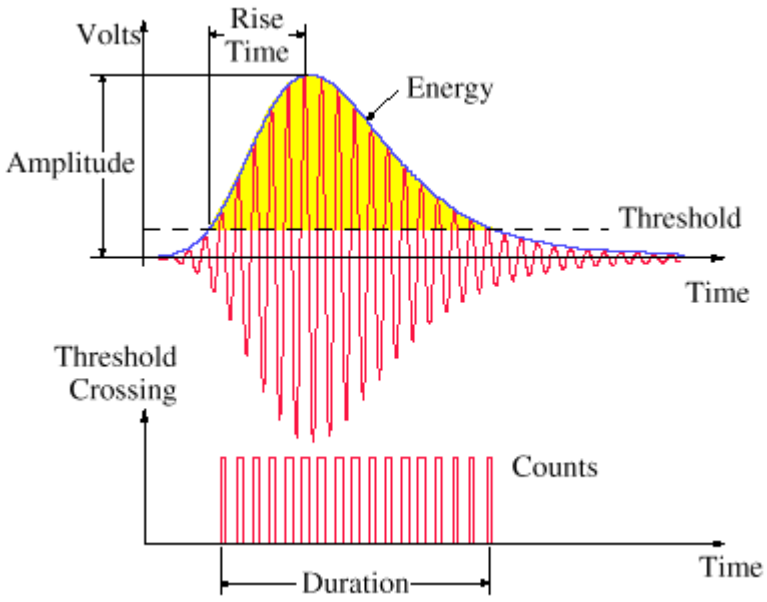

Figure 2.4.2-3 The shape characters of the burst AE waveform (Miinshiou Huang et al., 1998)

Based on the way in which the signals are recorded and analysed, AE techniques can be divided into two groups: the signal-based and the parameter-based AE signal processing methods (Christian U Grosse and Lindsay M Linzer, 2008).

In signal-based AE technique, full waveforms are recorded. The sensor signal goes through conditioning (i.e. amplification and band-pass filtering) followed by the acquisition process. Amplifiers boost the signal voltage so as it is optimised for the measurement circuitry. Along with several stages of amplification, band-pass frequency filters are adopted to attenuate low-frequency background noise (usually from noise sources with frequency lower than 100 kHz). The conditioned signals (waveforms) are collected by transient recorders and stored in the computer for further analysis. The signal-based method needs significant storage space for a large number of full signals (waveforms) to be recorded, but it can supply enough information for further statistical analysis using appropriate software tools (Christian U Grosse and

Lindsay M Linzer, 2008, Charles Hellier and Michael Shakinovsky, 2003). For the data processing and interpretation of AE waveforms, signal analysis methods based on time-domain, frequency-domain and time-frequency domain algorithms can be used as described in section 2.4.1.2.

In parameter-based AE analysis, only the key features of the signal are recorded instead of the full waveform. The conditioned signal is sent to the acquisition circuit, where it is compared with the operator-defined parameters. Whenever the signal characteristics are within the boundaries set by the operator, the signal is captured and stored, otherwise it is discarded. The first pulse marks the start of the AE hit and is used to trigger the signal measurement process. The measurement circuits are actively measuring several key features or parameters of the signal. The most commonly measured AE features are amplitude, duration, counts, counts-to-peak, rise time, RMS, MARSE energy and absolute energy. When the amplitude of the signal drops to a value which is lower than the defined threshold, the system determines that the hit has ended storing it for interpretation and evaluation together with the rest of the signals obtained using statistical tools (Charles Hellier and Michael Shakinovsky, 2003, David Mba and Raj BKN Rao, 2006). Commonly, the measured AE features are trended to evaluate the system conditions., The cumulative sum of the AE features (e.g. cumulative energy) are plotted to illustrate the trend (Rúnar Unnþórsson, 2013). The parameter-based method needs less space and is more efficient than signal-based one, but it may lose many important details and information which could be used to evaluate the nature of the defects present and their severity (Christian U Grosse and Lindsay M Linzer, 2008).

The absolute energy of an AE signal represents its true energy. It is calculated by integrating the squared voltage divided by the reference resistance of the detecting system over the duration of the AE signal. Absolute energy is measured in attojoules (aJ, 10^{-18} J). The

absolute energy is the whole energy of the AE waveform, which may also contain energy from noise sources. Thus, it is not desirable for illustrating failure evolution. However it is appropriate to monitor continuous signals, since it is independent of the threshold (MISTRAS Group Inc., 2009).

The Measured Area under the Rectified Signal Envelope (MARSE) energy is also known as signal strength, energy, relative energy, or energy release (H. Berger et al., 1992). Expressed mathematically, it is represented by the integral of the rectified voltage signal envelope above the threshold over the duration of the AE signal. Its unit is picovolt·sec (pV·s), MARSE is sensitive to both amplitude and duration (MISTRAS Group Inc., 2009).

PAC-energy is a parameter defined by Physical Acoustics Corporation (now MISTRAS Group). It is derived from the MARSE energy and is related to the gain of the AE system. Actually, it is a scaled version of MARSE energy to match the analogue AE systems with gain (Mohamed Kharrat et al., 2016). Therefore, PAC-energy shows the same trend as the MARSE energy. The unit of PAC-energy is μVolt·sec, i.e. μV·s (MISTRAS Group Inc., 2009).

2.4.2.2 AE testing of gears and bearings

Because acoustic emission (AE) is more sensitive to crack propagation and interactions of damaged surfaces that are in contact than vibration measurements (Babak Eftekharnejad and David Mba, 2009), it has gained much more attention recently. It is considered as a suitable replacement to classic vibration analysis for gearbox diagnosis, especially for early detection of pitting, cracking or other potential faults of low-speed components. Alternatively it can be used as a supplementary method to traditional vibration analysis (Bin Lu et al., 2009).

E Siores and AA Negro (1997) mounted AE sensors on the casing of a gearbox, in which some common gear failures were induced, such as excessive backlash, shaft misalignment, tooth breakage, scuffing and worn teeth. It was reported that the monitored AE parameters (i.e. root mean square, standard deviation and duration) exhibited changes which were clearly associated with the detection of the induced defects (David Mba and Raj BKN Rao, 2006). Hirofumi Sentoku (1998) also reported that AE could monitor gear teeth pitting (David Mba and Raj BKN Rao, 2006).

A Singh et al. (1996) compared the ability of AE and vibration analysis to detect gear pitting. A resonant AE sensor and an accelerometer were mounted on the gearbox housing. In a gear set with pits simulated by machining, both techniques detected the pit, but AE exhibited better signal to noise ratio. In another gear set without original pits being present, after 30 minutes of operation, pits started to develop and periodic peaks were detected by the AE sensor, while no distinguishable peak was yet collected by the accelerometer (David Mba and Raj BKN Rao, 2006).

N Tandon and S Mata (1999) not only successfully detected pits induced in gears as other researchers had done previously, but also reported that AE could detect smaller pits compared with vibration analysis.

A Singh et al. (1999) conducted gear-tooth bending testing with AE and vibration (acceleration) transducers attached on the gear. They reported that AE first detected failure-related signals when the gear had reached 90% of its final lifetime. The AE amplitude increased with crack growth while the vibration signal only changed evidently at the final stages of failure (David Mba and Raj BKN Rao, 2006).

Using AE testing, Juha Miettinen and Pentti Pataniitty (1999) successfully detected the defect within a rolling bearing at slow rotating speed between 0.5 and 5 r/min. They also conducted

some low frequency vibration measurements with data being analysed using various algorithms such as spike energy, etc. on the same faulty bearing. The lower speed limit where the defect could be detected using vibration was between 10 and 20 r/min.

K Miyachika et al. (1995) employed AE during bending fatigue testing of case-hardened or normalized gear teeth. It was found that the amplitude of the AE signal and the peak level of the frequency spectrum from the case-hardened gears were much higher than from normalized gears. In addition, the obvious increase in the AE cumulative event count and event count rate just before crack formation were observed in the case-hardened gear but not in the normalised one. Therefore, prediction of crack initiation based on AE was more likely for case hardened gear than normalized one (David Mba and Raj BKN Rao, 2006).

Though the great potential of AE in condition monitoring of gearbox components has been widely recognised, the adoption of AE by the wind energy industry has so far been limited. More in depth research and further evaluation in the field are required to enable the widespread use of AE in wind turbine gearbox monitoring.

Chee Keong Tan and David Mba (2005) discussed the effect of the lubricant temperature on the levels of AE activity. Tim Toutountzakis and David Mba (2003) observed that the AE parameters increased as the component rotating speed increased. Chee Keong Tan and David Mba (2004) reported that the effect of variation of the applied load (torque) on the AE activity (root mean square) was negligible under elastohydrodynamic lubrication condition.

To sum up, condition monitoring systems (CMS) are necessary to reduce the downtime and O&M costs of wind turbine gearboxes by detecting faults early. Vibration-based CMS is widely adopted in wind farms, but it has low sensitivity in detecting faults in low-speed components and unable to reflect component material information. Acoustic emission (AE) CMS shows great potential to complement vibration-based CMS, which has been proven by

many researchers. In this study, the relationship between the AE/vibration signals and the damage development in rolling-sliding test samples has been studied, in order to develop a novel CM methodology for wind turbine gearbox components.

2.5 Surface engineering of gearbox components

2.5.1 Surface engineering

Based on the various failure mechanisms in wind turbine gearbox components, surface engineering treatment can be adopted to eliminate or mitigate the life-limiting problems relevantly to increase the reliability. Surface engineering involves the application of traditional and innovative surface technologies and processes on engineering components and materials in order to produce a composite that possesses the combined surface and bulk properties required for a particular application which would otherwise be unattainable (T. Bell, 1987). Surface engineering technology includes the processing methods used to engineer the material surfaces, the characterisation of those surfaces, and evaluation of their performance (K. N. Strafford, Datta, P. K. and Gray, J. S., 1989). The required material surface can be engineered via surface modification and/or by application of appropriate surface coatings.

1) In surface modification (e.g. induction hardening, carburising, nitriding etc.), the case of the surface material is modified using thermal or thermochemical methods (C. Subramanian and K. N. Strafford, 1993). For instance, the widely adopted carburising method is used to diffuse C atoms into the material surface and near-surface, increasing C content to 0.56-1.10 in wt% under controlled temperature and atmosphere (Xiaolan Ai and Charles Moyer, 2001).

Similar to carburising, nitriding is a process of diffusing N atoms into the surface and near-surface of an engineering material. Traditional gas nitriding and liquid nitriding cause

environmental problems, producing thick, hard but brittle compound layers, which are usually undesirable. Plasma nitriding has provided a way to solve these problems. In direct current plasma nitriding (DCPN), a voltage is applied between the chamber and the samples in order to generate a glow discharge which provides heat to enhance solubility of nitrogen atoms in the matrix and accelerate N ions towards the surface of the sample (P. Hubbard et al., 2010b). A boost in surface hardness and reduction in wear and friction coefficient are achieved by plasma nitriding. In addition, plasma nitriding significantly improved corrosion resistance (D.C. Wen, 2009). But DCPN has some problems, such as arcing and 'edge effect', due to the bias applied on components(M. Olzon-Dionysio et al., 2010). These problems impede the wider industrial utilisations of DCPN. For instance, arcing is mainly caused by non-conductive substances, e.g. grease, oil and rust, which are very common in industrial environments. Therefore, all parts must be thoroughly cleaned to avoid severe arcing during the DCPN treatment. This may be difficult, time consuming and costly(Santiago Corujeira Gallo and Hanshan Dong, 2009). Active screen plasma nitriding (ASPN) has been conceived to solve the problems associate with DCPN. In ASPN, bias is applied between the chamber and the active screen, so the bias on components could be removed. Li, Georges et al.(2002) found that ASPN can achieve similar hardening effects compared to DCPN without the problems associated with DCPN such as the 'edge effect'.

2) In surface coating, an extra material layer is added to a component surface (C. Subramanian and K. N. Strafford, 1993). According to the coating properties, they can be classified as hard coatings and low-friction coatings.

Most hard coatings are transition metal nitrides, e.g. TiN, CrN and TiAlN. Because of their high hardness, hard coatings have been increasingly employed in various sectors of industry to protect components (e.g. cutting tools and injection moulds) from failure caused by wear,

thus leading to an increased lifetime. Meanwhile, if the introduction of hard coatings induces a high level of compressive stress at the component, the fatigue life of the component will be increased. This is particularly true for the steel substrates which are quenched and tempered, since the austenite/martensite transformation can often result in tensile stress at the treated substrate surface (N. Lecis et al., 2006).

Low-friction coatings are developed for the components used under certain conditions where lubrication is difficult to apply. Low friction coatings normally mean the coatings with coefficient of friction (COF) not higher than 0.2 (J.P. Hirvonen et al., 1996). Common low-friction coatings include PTFE, MoS_2, WS_2, graphite as well as diamond-like carbon (DLC) coatings. DLC coatings are attractive due to their good mechanical, tribological and biomedical properties (JL Endrino et al., 2008).

3) Duplex surface engineering means the sequential application of two (or more) established surface technologies to produce a surface composite with combined properties which are unobtainable through any individual surface technology(T Bell et al., 1998).

Great technical and economic benefits can be achieved via the application of duplex surface engineering. For instance, premature and unexpected failures of thin coatings are caused usually by plastic deformation of the substrate. The duplex treatment (nitriding plus coating) can be introduced to improve the load bearing capability of the coated component which is very beneficial (N. Lecis et al., 2006). For instance, J. C. A. Batista et al. (2003) reported that both (Ti,Al)N and CrN coatings on nitrided substrate displayed better fatigue resistance than those on non-nitrided substrate.

2.5.2 Surface engineering of bearings

Except traditional dominant through-hardened high C steels, bearings can also be produced using case-hardened low C steels. Case-hardened bearings made of low C steels possess both high surface hardness (higher than 58 HRC) and enough inner fracture toughness. On the contrary, the core of traditional through-hardened steel has limited fracture toughness (usually less than 24 $MPa \cdot m^{1/2}$), because the toughness is inversely proportional to the hardness of the material (Erwin V Zaretsky, 2012). Therefore, the bearing components requiring balanced core toughness and surface hardness will undergo the case-hardening process (e.g. carburising and nitriding) prior to classical hardening heat treatment. Let's consider carburising as an example. The original C content of a low C bearing steel is lower than 0.2 in wt%. Through carburisation, the C content at the surface and near-surface region can be increased up to 1.10 in wt%. Then the carburised steel is heat-treated (e.g. quenching and/or tempering). The obtained structure has a hardened surface layer for high surface damage resistance and retains sufficient fracture toughness in the ductile core material absorbing heavy shock loads and preventing crack propagation (Erwin V Zaretsky, 1992, Xiaolan Ai and Charles Moyer, 2001). In addition, most precisely controlled nitriding and carburising processes could introduce compressive residual stress into the surface of treated bearing components, thus increasing their service lifetime (Erwin V Zaretsky, 2012). For instance, A. J. Gentile and A. D. Martin (1965) reported that the endurance of a nitrided ball bearing were twice as high as that of an unnitrided one. This was due to the fact that the nitriding process introduced compressive residual stresses which could compensate for the tensile stresses applied on the bearing parts (e.g. the inner races), preventing the stress raising effects caused by non-metallic inclusions. In addition, Robert Errichello et al. (2013) reported that, according to the field experience of

wind turbine operation, carburised bearings were more durable than through-hardened bearings.

One of the coating technologies developed by bearing manufacturers is a black oxide coating called Durotect B, from Schaeffler Ltd. for its FAG cylindrical roller bearings. It is proposed that it may reduce wind turbine gearbox failures, because this mixed iron oxide coating provides increased resistance to slippage during alternated low-load conditions (Steed Webzell, 2009). However, G. L. Doll et al. (2010) and Ryan D Evans et al. (2009) reported that bearing surface with black oxide coating provided no protection against smearing and although it may delay damage onset will not eliminate the risk of micro-pitting and adhesive wear eventually.

Ryan D Evans et al. (2009) suggested another type of coating, the amorphous hydrocarbon coating with tungsten carbide dispersed in, i.e. WC/a-C:H. They performed ring-on-ring rolling/sliding contact tests to simulate the high slip contacts relevant to wind turbine gearbox bearings. The results obtained, suggest that this hard-coated surface consistently survived the harshest slip and boundary lubrication conditions. Benjamin D Leonard et al. (2009) reported this WC/a-C:H coating could reduce fretting wear effectively, even under unlubricated conditions. Meanwhile, this coating can solve micro-pitting, smearing, false brinelling and scuffing, it also give bearings improved tolerance of particulate debris (Gary Doll, 2011). A combination of isotropic super-finishing and this durable wear resistant coating (nano-crystalline WC precipitates homogeneously dispersed in an amorphous hydrocarbon matrix) applied to the rolling elements, eliminated micro-pitting, greatly reducing the risk of smearing, increasing the resistance to damage from lubricant interruption and gearbox debris, and improving fatigue life (G. L. Doll et al., 2010).

2.5.3 Surface engineering of gears

In the gear manufacturing industry, significant effort has been put in place to extend service life against wear, contact fatigue and fatigue rupture. The main technique currently employed to address these technical challenges is based on surface hardening, which is used to obtain a case with high wear resistance and enough fatigue strength on the tough, ductile and shock-resistant core material (Marco Boniardi et al., 2006). Moreover, surface coating and duplex treatment also holds great potential to improve the performance and service life-time of gears.

2.5.3.1 Carburising of gears

Carburising is already the most widely used surface hardening method for wind turbine gears, because the deep carburised layer with residual compressive stresses is crucial to contact-fatigue resistance (M Zlatanović et al., 2007). In common industrial practice, carburising takes place between 870 °C and 1010 °C, typically on alloy steels with C content of about 0.10-0.20 in wt%. The case depth varies from 0.13 to 8.25 mm (Gerald D Lindell and Daniel H Herring, 2007). In the international standard ISO 6336-5:2003 for carburised gears (ISO, 2003), the recommended surface C content is between 0.65 and 0.90 in wt% and surface hardness between 660 and 800 HV. The suggested thickness of hardened layer for gears with different modules is shown in Figure 2.5.3-1.

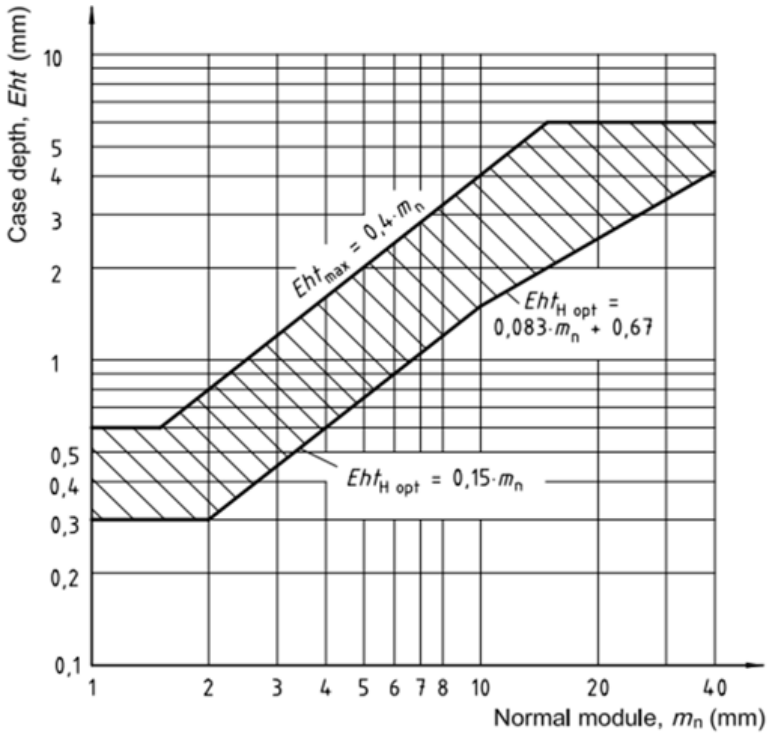

Figure 2.5.3-1 Recommended harden layer thickness for carburised gears with different modules (ISO, 2003)

Atmosphere carburising is the standard processing method used in the present gear industry. In atmosphere carburising, the steel parts are heated in carrier gas, containing approximately 20% CO, 40% H_2 and 40% N_2, to austenitizing temperature. The carrier gas, neither carburising, nor decarburising the steel, is generated from a methanol (CH_3OH)/nitrogen mixture or natural gas (containing 90-95% CH_4) and nitrogen mixture. The enriching gas, usually natural gas or propane (C_3H_8), is added to the carrier gas atmosphere to perform carburising. Atmosphere carburising possesses many advantages, e.g. low investment cost, high volume output and adequate process control and troubleshooting. However, the atmosphere carburised gears may need large material allowance for post operations due to accuracy and finish requirements. In addition to that, the cases are usually non-uniform throughout the gear geometry (Gerald D Lindell and Daniel H Herring, 2007).

Low pressure carburising (LPC) has great potential for future utilisation. LPC is done at 3-20 Torr which is far below the atmospheric pressure 760 Torr, using acetylene (C_2H_2), propane, cyclohexane (C_6H_{12}), etc. During heating stage, steel surface is cleaned and the low pressure makes carbon transfer to steel surface faster. Meanwhile, the distortion is less and the case is more uniform. Nevertheless, the investment cost is high and part cleanliness is much critical (Gerald D Lindell and Daniel H Herring, 2007).

To meet the requirements of modern wind turbines (e.g. more reliable and cheaper), innovative surface treatment is needed and some improved techniques have been developed.

2.5.3.2 Nitriding and other surface hardening of gears

It is possible to replace carburising with nitriding in gear treatment. The influence of carburising and nitriding on gear failures was analysed and the alternative nitriding treatment to solve the challenges faced was considered by Marco Boniardi et al. (2006). Firstly, though the effective depth of nitrided layer is lower, the adverse effect of low case depth of nitrided gear on fatigue resistance can be made up by its higher superficial hardness (Marco Boniardi et al., 2006, Gerald D Lindell and Daniel H Herring, 2007). Secondly, compared with carburising, nitriding can also induce compressive residual stress (Bojan Podgornik and Jože Vižintin, 2001) due to precipitation effect. Thirdly, nitriding can be conducted typically at the temperature range of 495-565 °C which is lower than the tempering temperature. Thus higher hardness can be reached without great deformation. M Zlatanović et al. (2007) also reported pulse plasma surface treatment of wind turbine gears which consists of plasma nitriding and subsequent post-treatment, improved the fatigue, wear and corrosion resistance.

Induction heating then quenching is another method commonly used in heat treating of gears. In contrast to carburising and nitriding, induction hardening does not require heating the whole component. Accurately controlled induction heat treatment systems can selectively heat

and harden specific areas of gear teeth and bearing races producing the required metallurgical properties with minimum shape resulting in manufacturing of high quality parts that directly affect the service lifetime of wind turbine gearbox components. Immediately after induction hardening, stress relieving or tempering is required to prevent cracking. The main drawbacks of induction heating are its complexity and high cost, especially for large-size components (E Kečkováa et al., 2008, G Doyon et al., 2009, Gerald D Lindell and Daniel H Herring, 2007, Valery Rudnev et al., 2003).

Electrochemical boriding in coordination with the use of nano-colloidal lubricant additives was applied on flat gear steel samples by A Greco et al. (2011). The borided surfaces enhanced the mechanical properties of the surface layer, leading to improved wear resistance. But the high treatment temperature (around 950 °C), the formation of very brittle FeB layer and the very high cost of boriding (five to six times higher than carburising and nitriding) may limit the adoption of the boriding process (A Erdemir et al., 2012).

Except tempering, some other post-hardening processes, e.g. Sub-Zero treatment and shot peening, may be conducted on hardened gears. Sub-Zero treatment is cooling parts in the temperature range of -85 °C and -195 °C, to transform retained austenite and increase the hardness and dimensional stability. Shot peening is to bombard the gear surface with small spherical media, in order to induce a residual compressive stress on the gear surface (Gerald D Lindell and Daniel H Herring, 2007).

2.5.3.3 Surface coating of gears

Except surface modification, surface coating may also be used to improve the gear properties.

Two self-lubricating DLC coatings, Graphit-iC (GiC) and Dymon-iC (DiC), are highly likely to be adopted in wind turbine gearboxes. Both GiC and DiC coatings possess high hardness

1200-2500 HV0.05, friction coefficient lower than 0.1 and low wear rate of about $10^{-17}m^3/Nm$. Above all, both of them can withstand contact pressures higher than 3.4 GPa (SK Field et al., 2004, S Yang et al., 2000). It has been reported that the wear performance of DiC is unstable and strongly depends on the environmental conditions (J Stallard et al., 2004). GiC coating can exhibit low wear rates in air, water and oil conditions, while DiC coating failed rapidly when tested in water, although DiC exhibits lower wear rates than GiC in air and oil (J Stallard et al., 2004). Graphit-iC is a dense, non-crystalline, hydrogen-free carbon (a-C), electrically conducting coating with sp^2 bonding. Dymon-iC is an amorphous, electrically insulating, hydrogenated carbon coating (a-C:H) with a significant proportion of sp^3 bonding. When they are sliding with a counterpart, a low friction transfer film will be formed as a third body between the carbon-based coatings and their counterpart (SK Field et al., 2004). For example, DiC coating is metastable and hydrogenated (a-C:H) containing sp^2 and sp^3 bonds. During sliding with the counterpart, the movement of two bodies will cause a friction-induced local annealing at real contact area. As a result, the sp^3 bonds will be destabilised and hydrogen will be released, forming a lubricious graphite-like transfer film. Because of the formation of transfer film, a-C:H coatings possess low friction coefficient (Y Liu et al., 1996b). Similarly, a thin layer of amorphous GiC coating surface will turn into a crystalline graphite layer with very low friction (DG Teer, 2001).

As it was mentioned earlier, duplex treatment (i.e. the combination of two or more surface techniques) can achieve more technical and economic benefits than single treatment (surface modification or coating alone) (JCA Batista et al., 2003, N Lecis et al., 2006, T Bell et al., 1998). As for wind turbine gearboxes, M Zlatanović et al. (2007) mentioned some possible duplex surface treatments which combined diffusion and deposition processes, such as plasma nitriding, plasma enhanced magnetron sputtering and solid-lubricating coatings. Therefore,

developing innovative duplex surface systems for wind-turbine gearbox components may achieve the desired properties and improve gearbox reliability.

2.6 Summary

Most industrial-scale wind turbines are based on geared three-blade horizontal axis design. One of the challenges faced by the wind energy industry and academia is the unacceptably low reliability and high downtime of wind turbines. Especially, the gearbox is among the least reliable subsystems and leads to the longest downtime per failure. Nearly all gearbox failures are related to the defects and damage of bearings and gears, particularly planetary and high-speed gears.

Most reported failures relate to rolling contact fatigue (e.g. micro-pitting and macro-pitting), scuffing, false brinelling, fretting corrosion and white etching area. The possible reasons for these failures are misalignment, adverse operating loading conditions, poor lubrication and inadequate material cleanliness. Current results are still inadequate to fully understand and reduce these failures. Therefore, the first crucial task of this study is to thoroughly examine the failed bearings and gears to identify the root cause. Secondly, finite element analysis simulation has been adopted in this study to analyse and better understand the stress distribution and verify the failure root cause of gearbox components.

Although various single surface treatment methods have been developed for wind turbine gearbox components, such as nitriding and black oxide coating, duplex surface treatment show superior potential than single surface treatment methods. Thus, the third task of this study is to design and evaluate an advanced duplex surface system for bearings and gears to against the identified and verified life-limiting problems. Nonetheless, it is important to acknowledge that lubrication variability can be a considerable problem which is not

straightforward to address through further improvement of wear and fatigue resistance of the materials alone. Poor lubrication quality will always lead to damage initiation at an early stage which will subsequent propagate with time even the lubrication consistency has improved.

The vibration analysis is widely used in condition monitoring of wind turbines, but its limitations in low speed applications and lack of material information need acoustic emission test to complement to vibration related methods. The qualitative relationship between AE and vibration signals and rolling contact fatigue development is studied in this project to get better understanding which can be used for diagnostic purposes and damage detection. However, the evaluation of the severity and prediction of the remaining lifetime remain more complicated issues that are yet to be resolved particularly due to the operational conditions of wind turbine gearboxes involving variable loads, changes in lubrication quality and instantaneous misalignments which can result in extremely high contact stresses.

CHAPTER 3: EXPERIMENTAL STUDIES

The aim of this study has been to improve the reliability of wind turbine gearboxes. The diagram in Figure 3-1 illustrates the research methodology employed during this project.

To obtain information and identify the root cause of failure of received bearings and gears, observation, metallographic analysis and characterisation were performed using optical microscopy, SEM/EDS, XRD and so on.

Finite element analysis (FEA) can accurately, clearly demonstrate stress distribution. Therefore, FEA simulation software has been adopted in this study to analyse and better understand the effects of observed suspicious factors on stress field of wind turbine gearbox components and verify the failure root cause identified by observation.

In order to mitigate the identified and verified life-limiting problems, advanced duplex surface systems for bearings and gears have been designed and produced relevantly to improve the resistance to higher stress level due to the identified failure causes. The duplex systems were designed combining carburising/DCPN/ASPN and DLC coating. The properties of designed surface systems, such as low friction and high load bearing capacity, were systematically evaluated using nano-indentation, micro-indentation, Raman spectroscopy, profilometry, micro-scratching and wear testing.

Detection of early-stage defects in components can prevent catastrophic failures of the system. Therefore, the relationship between AE/vibration signals and rolling contact fatigue evolution has been studied by combining AE/vibration test systems with the rolling-sliding wear tester.

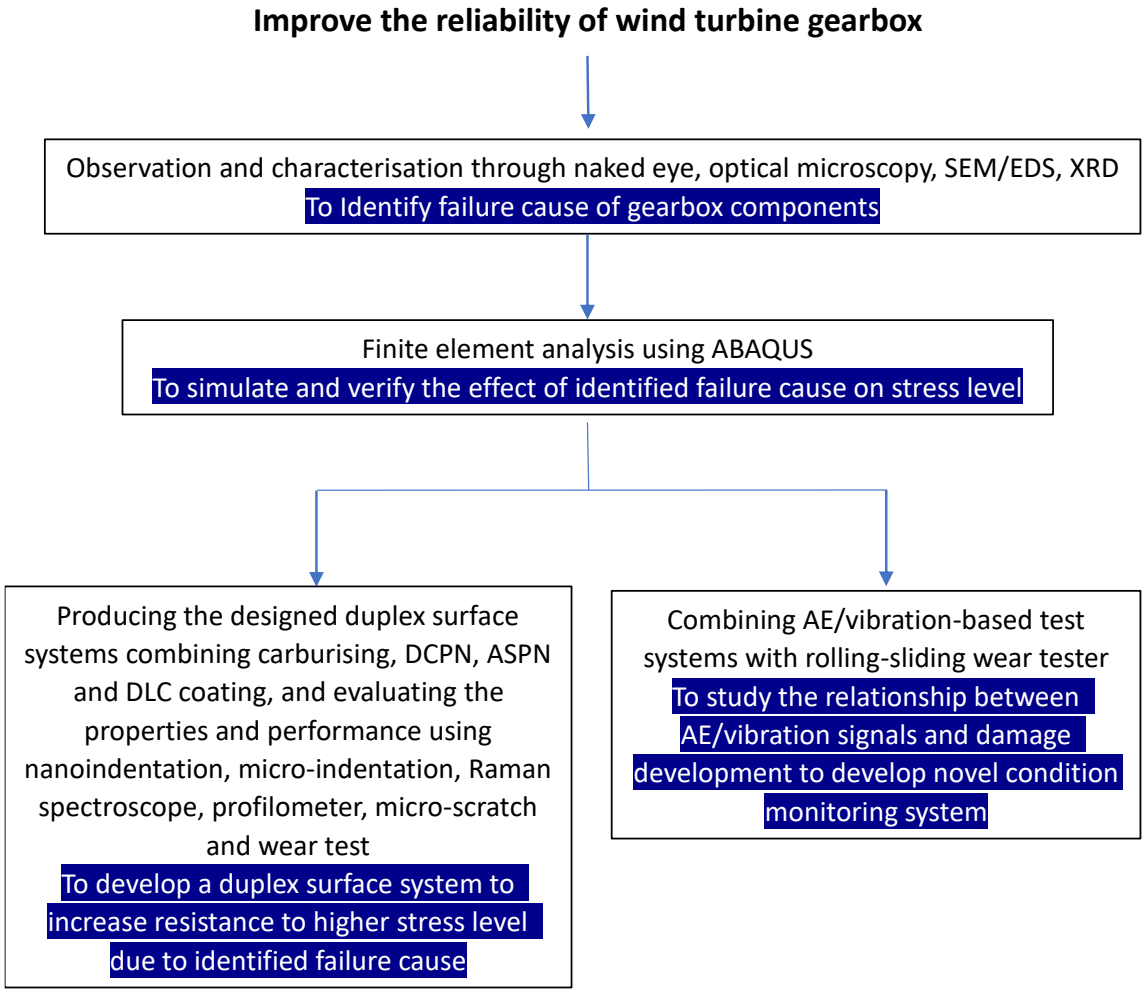

Figure 3-1 The systematic diagram illustrating research methodology for the aim and objectives

3.1 Material observation and characterisation

3.1.1. Microstructure observation and characterisation

Optical microscopy (metallography) and Scanning Electron Microscopy (SEM) (morphology, microstructure and layer structure) were used for the microstructural characterisation of the materials considered in this study. All samples prior to observing their microstructure under optical microscope and SEM, were etched using 2% nital (mixture of nitric acid and ethanol) (P. Hubbard et al., 2010a).

The optical microstructural observation was performed using a ZEISS Axioskop 2 MAT Mot optical microscope equipped with an AxioCam MR digital camera.

Philips XL-30 (LaB6), Jeol 6060 and Jeol 7000F SEMs with Oxford Inca EDS were used in both secondary and backscattered modes with an accelerating voltage of 20 kV and a working distance of 10 mm.

3.1.2. Composition and phase analysis

A Glow Discharge Optical Emission Spectrometry (GDOES) GDA 650 HR manufactured by Spectruma Analytik GmbH was used to obtain the content-depth profiles of the samples considered.

The Oxford Inca EDS system on SEM was used to conduct the elemental analysis and mapping of samples.

The phase constitution of samples was analysed using an X-Ray Diffractometer with a Cu-$K_\alpha 1$ radiation (λ=1.540560Å) at incident angles 2θ in the range of 0° and 120°. The obtained XRD patterns were analysed with the 'Match!' and 'HighScore' phase identification programme.

3.2 Simulation using Finite Element Method

In order to study the effects of misalignment, input torque, friction coefficient and coarse inclusions on stress field in meshing gears inside the wind-turbine gearboxes, and to verify the observed failure causes of wind turbine gearbox components, finite element analysis was conducted using ABAQUS. ABAQUS is a powerful finite element base software for 2D and 3D simulations. In order to simulate the stress field of rolling-sliding movement, a workflow

of different modules, namely Part, Property, Assembly, Steps, Interaction, Mesh, Load, Job and Visualisation was employed.

Firstly, the components were built directly in the Part module. Alternatively, the components can be built in other CAD software (e.g. SOLIDWORKS) and subsequently be imported into the Part module of ABAQUS. Then in the Property module, the material properties were defined and applied to the corresponding section and region of the parts. In the Assembly module, the individual parts were assembled to the contact position. In the Steps module, different analysis modes can be defined for the simulation, such as static general, dynamic implicit and dynamic explicit. In the Interaction module, their contact mode is set, and other related factors (e.g. the friction coefficient) were also defined. After that, the torque, rotating speed and other boundary conditions were set in the Load module. In the Mesh module, the components were divided into small elements (the Hexahedron element C3D8I was used to mesh the components). At last, in the Job module, the job was submitted for computation. The results were observed in the Visualisation module.

3.3 Surface treatment and evaluation

3.3.1 Materials and treatment process

EN36 carburising steel and EN40BT nitriding steel have been procured and used as the substrate materials for surface treatment of this study.

EN36 (655M13) is a case hardening steel specifically designed for carburising to produce a very hard case with a strong core. It is commonly called Nickel Steel. Its high nickel content produces a high level of hardenability. EN36 was widely used for large case carburised

marine gears (Christian Scholz, 2013, Manan Kulshreshtha, 2013). Its chemical composition is shown in Table 3.3-1.

EN40BT is a Cr-Mo low alloy steel, suitable for nitriding, supplied in the hardened and high-temperature tempered condition. It exhibits good toughness and ductility. The relatively low temperature of the nitriding process promises minimum effects on the EN40BT microstructure. This steel is suited for applications that require excellent wear resistance and high fatigue strength, such as shafts, gearwheels, drills and spindles (West-Yorkshire-Steel-Ltd, 2012b). Its chemical composition is shown in Table 3.3-2.

Table 3.3-1 The chemical composition of EN36 (West-Yorkshire-Steel-Ltd, 2012a)

Analysis composition %		C	Si	Mn	P	S	Ni	Cr
EN36	min.	0.12	0.10	0.30	-	-	0.60	3.00
	max.	0.28	0.35	0.60	0.05	0.05	1.10	3.75

Table 3.3-2 The chemical composition of EN40BT (West-Yorkshire-Steel-Ltd, 2012b)

Analysis composition %		C	Si	Mn	P	S	Cr	Mo	Ni
EN40BT	min.	0.20	0.10	0.40	-	-	2.90	0.40	-
	max.	0.30	0.35	0.65	0.05	0.05	3.50	0.70	0.40

Before surface treatment, EN36 and EN40BT samples were cut, ground, polished and cleaned.

The atmosphere carburising treatment of EN36 was performed by S. C. PLASMATERM S.A. with the appreciable help of Professor Zoltan Kolozsvary. Atmosphere carburising was performed at a temperature of 920 – 930 °C, followed by hot oil quenching in a sealed quench furnace. The carburised samples were then low-temperature tempered at 200 ˚C for 2 hours to reduce the quenching-induced residual stress. This is a common heat treatment after quenching.

The EN40BT was surface hardened by direct current plasma nitriding (DCPN) and active-screen plasma nitriding (ASPN). Two series of treatments were designed (as shown in Table 3.3-3) to investigate the temperature and time effect on the nitriding of EN40BT, in order to identify the optimum nitriding conditions for EN40BT to form a hardened case with satisfactory hardness and thickness. The plasma nitriding treatment was carried out in a KLÖCKNER IONON GMBH plasma nitriding machine at the School of Metallurgy and Materials of the University of Birmingham. The furnace was heated up to the treatment temperature in a H_2 atmosphere. The nitriding process was carried out in an atmosphere of 25 % N_2 and 75 % H_2 mixture. The configurations of DCPN and ASPN are shown in Figure 3.3-1 and Figure 3.3-2 respectively.

Table 3.3-3 Sample code and nitriding parameters for direct current and active screen plasma nitriding of EN40BT steel

	Sample code for DCPN	Sample code for ASPN	Temperature (°C)	Time (hour)
Temperature effect	DCPN530-20	ASPN530-20	530	20
	DCPN550-20	ASPN550-20	550	20
	DCPN570-20	ASPN570-20	570	20
Time effect	DCPN-530-20	ASPN530-20	530	20
	DCPN530-40	ASPN530-40	530	40
	DCPN530-60	ASPN530-60	530	60

The low friction DLC coating chosen for this project was the WC/a-C:H coating, i.e. a mixture of WC and hydrogenated diamond-like carbon (a-C:H). Before coating was deposited, the carburised and nitrided substrate was repolished. The WC/a-C:H coating, traded under the tradename BALINIT® C, was deposited by Oerlikon Balzers Coating UK Ltd. According to the specifications, BALINIT® C belongs to low-friction coatings, with a friction coefficient of 0.1-0.2. This coating is ideal for low lubrication and even dry running applications. It is

mainly used to reduce adhesive wear, surface fatigue and tribo-oxidation. Its maximum service temperature is 300 ˚C (Oerlikon-Balzers, 2017).

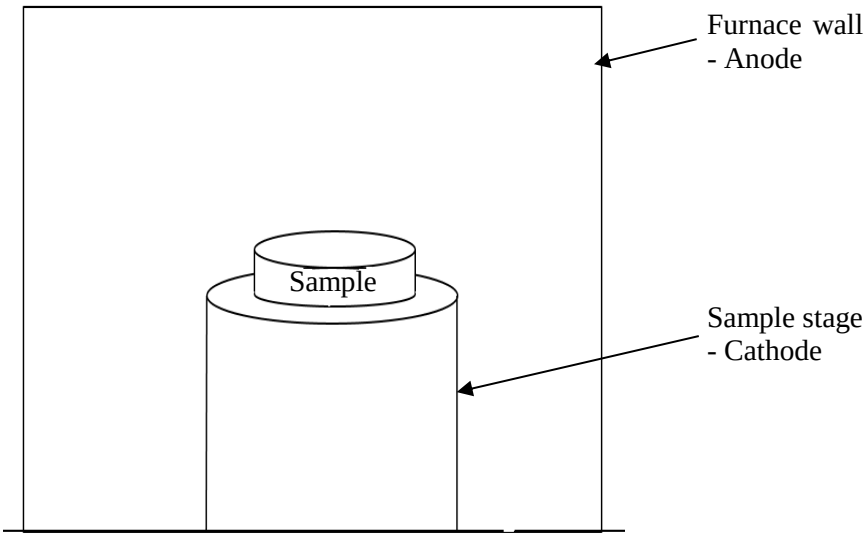

Figure 3.3-1 Schematic configuration of direct-current plasma nitriding

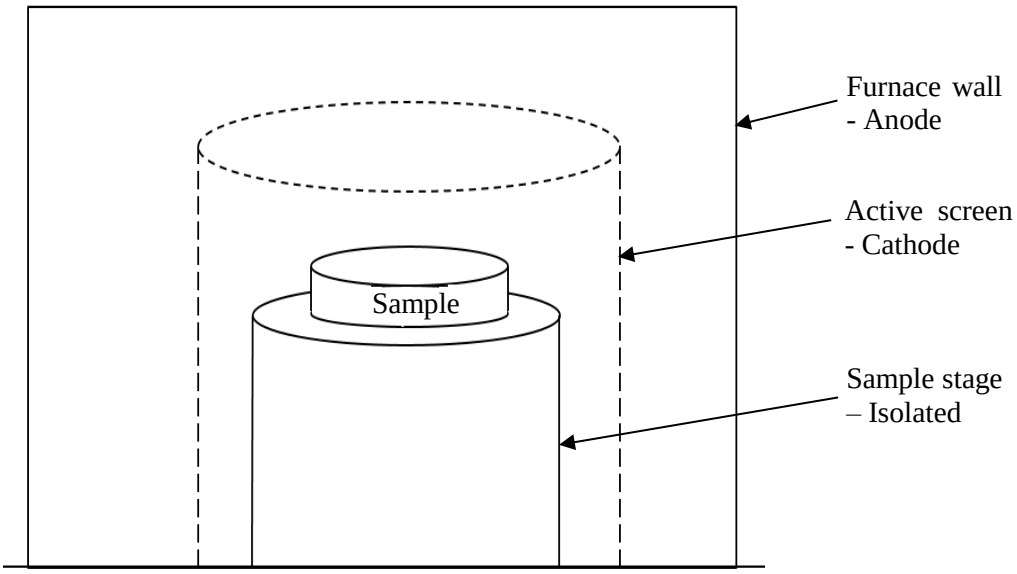

Figure 3.3-2 Sketch of active-screen plasma nitriding configuration

3.3.2 Properties evaluation

Mechanical and tribological properties were evaluated using Raman spectroscope (for sp^2 and sp^3 clusters) nanoindentation (for hardness and modulus), micro-indentation (for micro-hardness and loading bearing capacity), profilometer (for surface roughness and wear loss), micro-scratch (for bonding strength), reciprocating wear test (for coefficient of friction) and rotating/sliding wear test (for wear resistance).

Nanoindentation was used to sensitively evaluate the hardness and Young's modulus of coatings without the effect of the substrate. To produce reliable results, 50 points were indented in each sample with the maximum load of 50mN using the NanoTest^{TM} machine. Then the load-unload curves (e.g. Figure 3.3.2-1) of each indentation were collected and processed using the software provided. The obtained data were analysed statistically and validated.

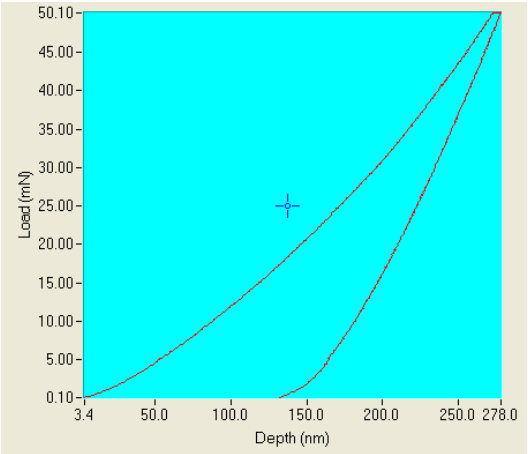

Figure 3.3.2-1 A loading-unloading curve of a nanoindentation

The structure (sp^2 and sp^3 clusters) of DLC coating was analysed using a laser Raman spectroscope which is composed of the Renishaw InVia reflex spectrometer and a confocal microscope with a ×20 objective. The monochromatic excitation laser for Raman scattering

has a wavelength of 488 nm and its power is about 2 MW. The sample was measured in an Instec HCS621V cell with an argon gas flow of 100 mL/min at 1 bar.

A Vickers indenter of Mitutoyo MVK-H1 micro-hardness tester was used to evaluate the microhardness of the designed surfaces and to determine the depth distribution of micro-hardness of hardened samples. In addition, the load bearing capacity of the designed surfaces was assessed by making indents with Vickers indenter on sample surfaces under a series of loads ranging from 0.025 kg to 1 kg and observing any cracks within and around the indents under SEM.

The surface roughness of samples was measured using the AMBIOS XP-200 3D profilometer.

Scratch tests were carried out to evaluate the bonding of a coating to the substrate and the damage resistance of surface systems designed. Single pass scratch was generated with a spherical Rockwell diamond indenter with a tip radius of 200 μm under continuous progressive load from 10 to 60 N. The loading rate was 100 N/min and the linear velocity of the indenter was 10 mm/min. The friction and its first derivative were recorded. To protect the test apparatus, the maximum friction force was set at 30 N higher than which the test would be stopped.

The Phoenix Tribology TE79 MULTI-AXIS TRIBOMETER was used to evaluate the coefficient of friction (COF). COF of all sample surfaces were measured at room temperature under a constant load of 10N reciprocating against a WC/Co pin ball of 12.7mm in diameter for 100 strokes (5mm in length) at 0.4 mm/s.

Tribological properties of wheel samples were evaluated using a TypeA135 Amsler wheel-against-wheel rolling-sliding wear test machine (Figure 3.3.2-2). The lower specimen can rotate in two stages of speeds: Speed I=200 r/min and Speed II=400 r/min. The upper wheel

specimen can rotate at I=180 and II=360 r/min. Speed I and II were used for unlubricated (dry) and lubricated (oil) tests respectively. Specimen wheels made of steels have the same geometry and size (Figure 3.3.2-3). Hence, the slip ratio $\frac{V_L - V_U}{\frac{1}{2}(V_L + V_U)}$ was about 10.5 %, where V_L and V_U are the cylindrical speed of the lower and upper wheel respectively.

Before each test, both wheels were degreased with acetone using an ultrasonic machine for 5 minutes and weighed using a digital balance with the precision of 0.1 mg. For lubricated tests, Shell Universal Engine Oil of 15W-40 was filled into the tank under the lower wheel, letting the lower part of the lower sample was dipped in the oil. During testing, the oil was brought into the contacting zone by the lower wheel to lubricate the wheel pair. Fresh oil was used for each pair. The test was carried out semi-continuously. After a certain period, the test was stopped and the specimen wheels were observed and weighed after ultrasonic cleaning in acetone. Extra care was taken as much as possible to ensure the wheel was put back close to the original arrangement and position.

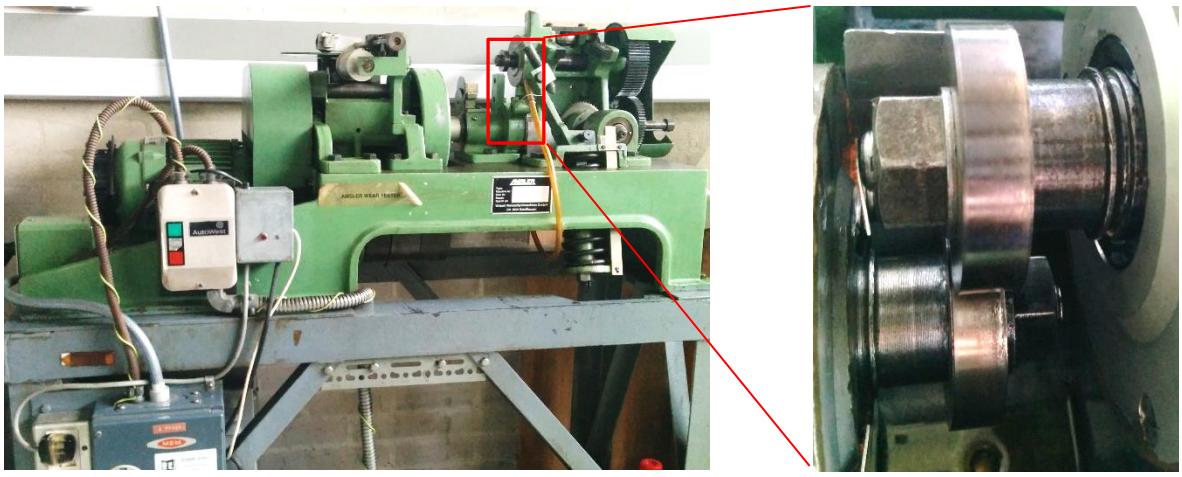

Figure 3.3.2-2 Amsler rolling-sliding wear testing machine and wheel samples arrangement

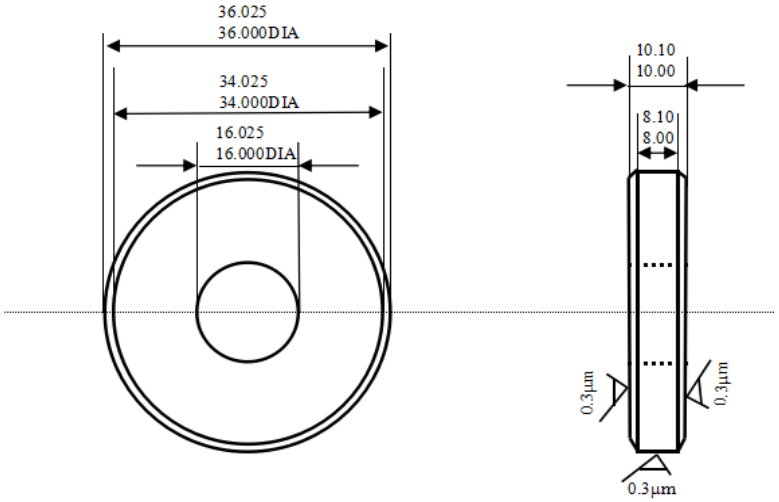

- All surfaces, except chamfer, must be square and parallel
- Circumference to be concentric with bore to within 0.012
- All dimensions in mm
- Surface finish except otherwise stated to be 0.5µm

Figure 3.3.2-3 Specimen size of steel wheel for Amsler rolling-sliding wear tests

3.4 Condition monitoring and signal analysis method

Acoustic emission and vibration analysis were conducted during the Amsler rolling-sliding wear testing when steel wheels (as shown in Figure 3.3.2-3) were rubbing against a WC/Co wheel (as shown in Figure 3.4-1). Based on the size of the two wheels and their rotating speed, the slip ratio was about 0.734. Applied load was 90 kg, thus original contact stress was about 4.34 GPa.

The vibration analysis equipment (as shown in Figure 3.4-2) consists of an industrial computer, one 0.5 Hz – 25 kHz Wilcoxon accelerometer, a Vibrametrics twelve-channel accelerometer power supply, an Agilent decoupling module and an Agilent 2531A four-channel data acquisition module capable of acquiring data up to 2M samples/s (single-channel mode). The accelerometer was attached near the top wheel shaft (as shown in Figure 3.4-3(a)). Data acquisition was carried out during tests using a customised data logger written in

Labview by Dr Zheng Huang from the School of Metallurgy and Materials of the University of Birmingham. The vibration data acquired were subsequently analysed using Matlab.

The acoustic emission system consists of an industrial computer, one 150-700 kHz Physical Acoustic Corporation (PAC) R50α AE sensor and a PAC pre-amplifier (as shown in Figure 3.4-2). The AE signals were collected and analysed using the commercial PAC AE system. The AE sensor is attached on the outside face of the oil tank using Araldite (as shown in Figure 3.4-3). The gain of the preamplifier is 40 dB. The unit of AE amplitude is dB, relative to 1 microvolt at the preamplifier input with a 40-dB preamp. Pencil-lead break test succeeded proving the AE transmission path feasible.

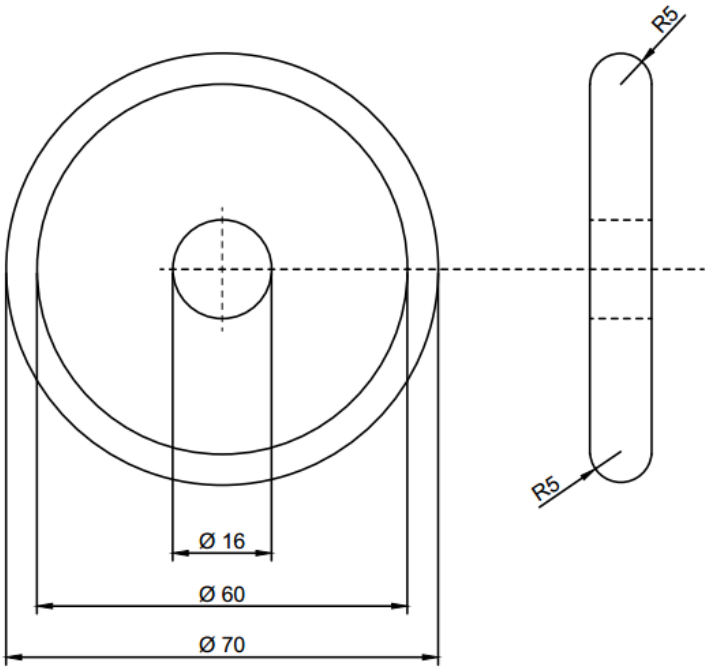

Figure 3.4-1 Specimen size of WC/Co wheel for rolling-sliding tests

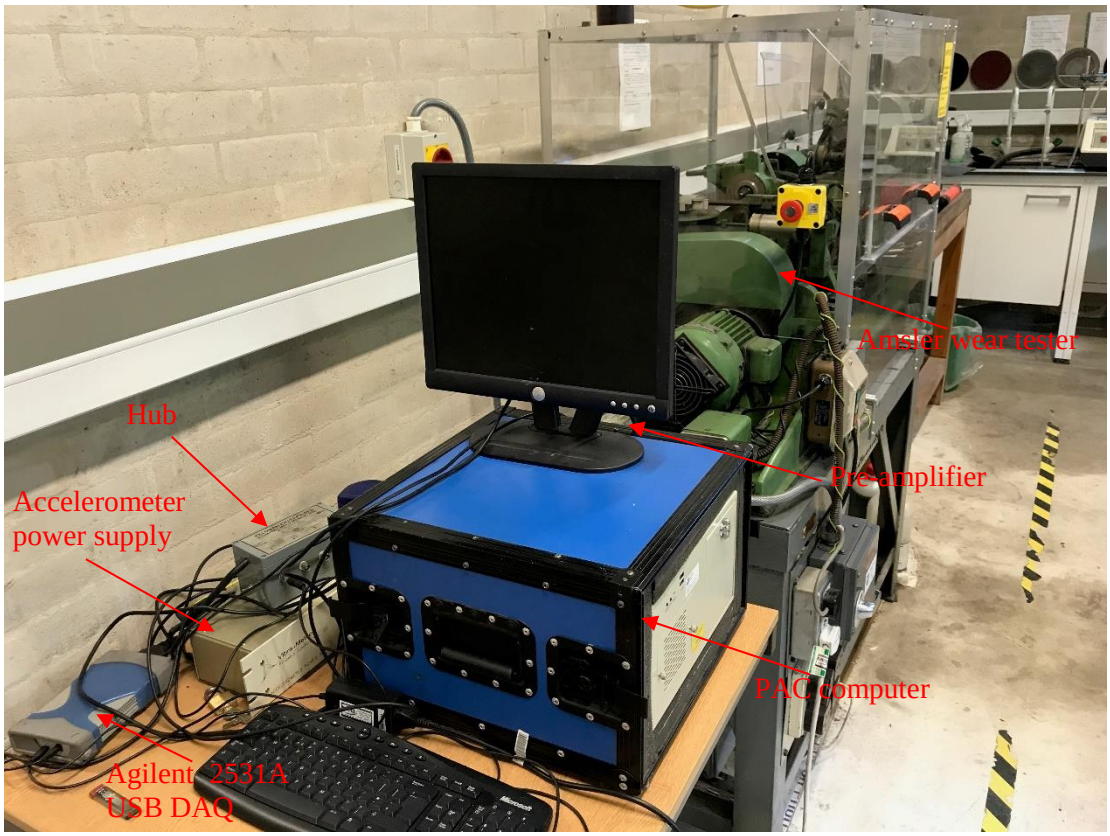

Figure 3.4-2 Vibration test and AE analysis equipment combined with the rolling-sliding wear tester

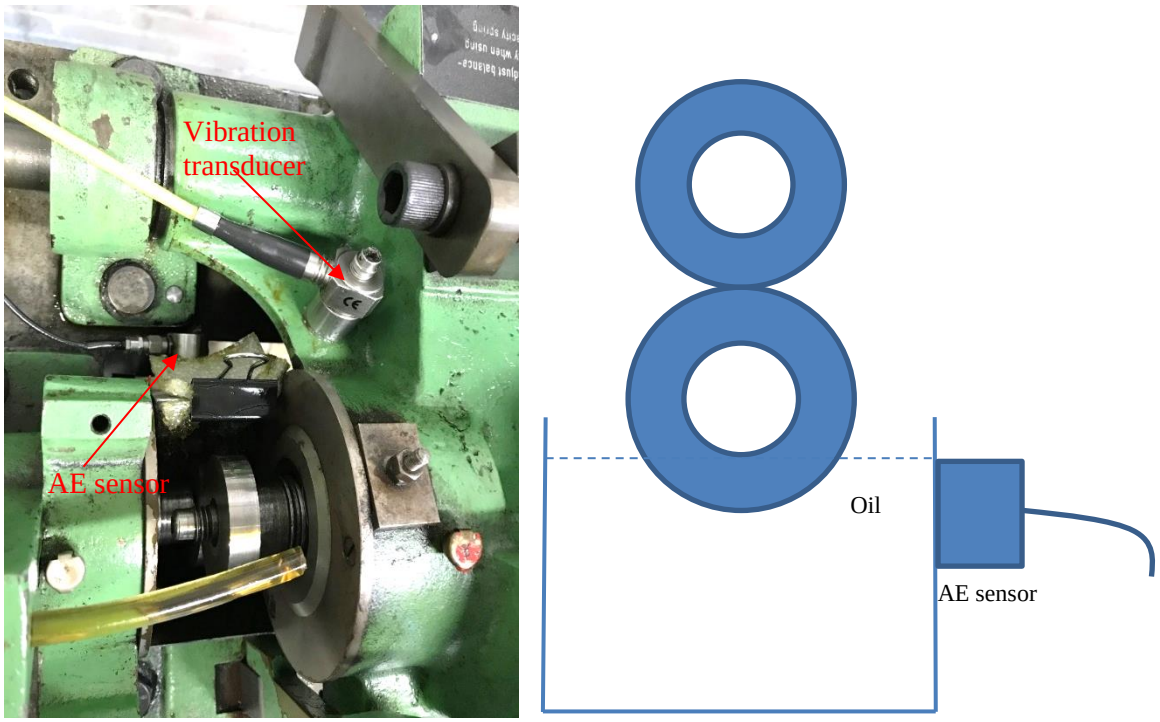

(a) (b)

Figure 3.4-3 (a) the position of the Vibration and AE sensors, (b) sketch of transmission path for AE signal, i.e. wheel → oil → tank wall → AE sensor

3.5 Summary

Observation and characterisation have been conducted on received damaged bearings and gears using optical microscopy, SEM/EDS, and XRD to identify the root failure cause. FEA simulations have been performed to analyse the effects of observed factors on the stress field of wind turbine gearbox components and verify the failure root cause identified by observation. After the root cause of failures were verified, advanced duplex surface systems for bearings and gears were produced relevantly combining carburising, DCPN, ASPN and DLC coating to mitigate the life-limiting problems via increasing the resistance to higher stress level due to the identified failure causes. The properties of designed surface systems were systematically evaluated using nano-indentation, micro-indentation, Raman spectroscopy, profilometry, micro-scratch and wear test. Finally, the relationship between AE/vibration signals and rolling contact fatigue evolution has been studied by combining AE/vibration test systems with the rolling-sliding wear tester, aiming to develop a novel condition monitoring methodology to detect defects in the early stage.

CHAPTER 4: ROOT FAILURE CAUSE ANALYSIS, FEA SIMULATION, AND DUPLEX SURFACE SYSTEMS FOR WIND TURBINE GEARBOX COMPONENTS

In order to contribute to the improvement of the reliability of wind turbine gearboxes, systematic work has been performed in this study.

First of all, the root cause of failure of gearbox components retrieved from the field has been evaluated. This is essential and of paramount importance in pertinently and successfully reducing gearbox failure rates. Observation, investigation and metallurgical failure analysis were carried out on the materials of these failed gearbox components. The main root failure causes of these components were deduced to be the extremely high stresses arising from the combined effects of misalignment, coarse non-metallic inclusions, and inadequate or inconsistent lubrication.

Secondly, the failure mechanisms identified from the root-cause analysis have been clearly verified using Finite Element Analysis (FEA) simulations. In order to validate the failure causes identified from failed wind turbine gearbox components, FEA simulations were carried out. The simulation of stress distribution on wind turbine gearbox components indicates that extreme high input torque, poor and variable lubrication quality (i.e. high friction) and misalignment significantly increase the contact stress, prompting the initiation and subsequent development of faults. In addition, crack initiation caused by stress concentration around coarse inclusions and subsequent propagation was also successfully simulated.

Subsequently, based on the identification and verification of failure mechanisms, appropriate advanced duplex surface systems have been designed to prevent the life-limiting damages of gearbox components relevantly. The duplex surface systems were Diamond Like Carbon (DLC) coating deposited on carburised EN36 and nitrided EN40BT steel, which possess extremely low friction coefficient (to deal with high friction due to inadequate lubrication),

high surface hardness, enough load-bearing capacity, compressive residual stresses and inside toughness (to resist higher stress level raised by misalignment and high load).

4.1 Root failure cause analysis of field samples

Root cause analysis of failures occurring in wind turbine gearbox components is essential and of paramount importance in improving gearbox design and reliability. Failed rolling elements from various wind turbine gearbox stages have been retrieved from the field to identify the failure causes. More specifically, the failed samples obtained from the field and examined in the laboratory include one failed high-speed shaft bearing, a spherical roller, several broken gear teeth and gear-related debris.

Observation, investigation and metallurgical failure analysis were carried out on the materials of these failed gearbox components. In the end, the root failure causes of these components were deduced to be high stresses due to combined effects of misalignment, coarse non-metallic inclusions, and inadequate or inconsistent lubrication.

4.1.1 High-speed shaft bearing and a spherical roller from planetary gear bearing

A failed high-speed shaft bearing and a single spherical roller were retrieved from wind turbines after failure had been identified by maintenance crew members. The single roller is from the planetary gear bearing of the low-speed stage of the gearbox. As mentioned earlier, the majority of wind turbine gearbox failures have been found to initiate from the planet bearings, the intermediate shaft bearings and high-speed shaft bearings (Walt Musial et al., 2007). Hence, identification of the root failure cause of the bearing can contribute to the identification of the root failure cause for the entire gearbox affected.

4.1.1.1 High-speed shaft bearing

It is known that high-speed shaft bearing is among the gearbox components with the highest failure rate. Thus, a failed high-speed shaft bearing is received from project partner for root cause analysis to reduce the failure rate.

The failed high-speed shaft bearing (as shown in Figure 4.1.1-1) was used to hold the high-speed shaft of the wind turbine gearbox rotating at about 1100 r/min. The model of the failed high-speed shaft bearing considered herewith was FAG NU222E-M1; this is a cylindrical roller bearing with single row, straight bore, removable inner ring, brass cage, 110 mm inside diameter, 200 mm outside diameter and 38mm width. It is a non-locating bearing with two ribs/flanges on the outer ring, none on the inner ring, allowing outer and inner rings to be axially displaced relative to each other from the central position. Its removable inner ring allows lubrication to take place. The operational temperature range of this bearing is between -30 and +150 °C (Hong-Kong-Bearing-Company, 2017).

Figure 4.1.1-1 The front and side view of the whole bearing for high-speed stage

The retrieved bearing had been deemed to have failed due to micro-pitting and macro-pitting that had occurred in its roller surface, inner ring raceway and outer ring raceway. Once pits had formed and had been detected, the bearing had to be replaced. If the bearing was allowed to remain in-service rotational response would give rise to significant vibrations and noise, whilst possible eventual structural failure of the bearing sub-parts could result in catastrophic failure of the gearbox (W Glaeser, 1996, T Davidson, 1999). The bearing seats including the axial mating surfaces, inner ring bore, and outer ring outside diameter, had been observed to be generally in good conditions.

After the bearing had been disassembled, the rollers, cage, inner race and outer race it consisted of were examined individually. According to the investigation, some contributing factors to the high contact stress and stress concentration which led to surface damage of the rolling components were identified. Firstly, misalignment is thought to have affected the bearing during operation. This conclusion with respect to misalignment can be deduced due to the presence of uneven macro-pitting which is seen to be higher at one edge than the other of the rollers, inner race and outer race. Secondly, a large amount of coarse non-metallic inclusions was observed in the microstructure of the steel grade used for manufacturing this particular bearing. In addition, some of the inclusions seem to be related to the micro-/macro-cracks observed on the surface of the retrieved sample. Thirdly, some indentations caused by hard debris travelling through the rolling elements with the circulation of the lubricant were observed in the outer ring raceway. This indicates that the lubricant cleanliness was not satisfactory. Fourthly, separated raceway discolouration due to local surface overheating was observed, indicating severe roller skidding in the bearing. Lastly, a great number of big wear debris were found embedded in the cage surface which could not be removed by lubricant, thus forming severe three-body wear.

4.1.1.1.1 Cylindrical rollers

Each of the cylindrical rollers were visually checked. All of them were observed to have accumulated identical type of damage of similar severity (Figure 4.1.1-2). From the cylindrical rollers, one of them was randomly selected for more in-depth observation and investigation.

The photograph of the roller considered is shown in Figure 4.1.1-3. It is firstly noticed that the surface of the roller has been severely damaged exhibiting clear signs of micro-pitting and macro-pitting. The micro-pitted surface scatters light and exhibits a frosted or grey appearance (P Davoli et al., 2007). In addition, the extent of surface damage on one side is different to the other side (as shown in the SEM images in Figure 4.1.1-3). This finding is in accordance with the misalignment giving rise to uneven wear of the bearing raceways (see section 4.1.1.1.3 & 4.1.1.1.4). Most micro-pits are distributed on the left part of the roller rather than on the right side. However, on the opposite right side, more macro-pitting is clearly observable in comparison with the left side. Normally macro-pitting is the secondary failure mode initiated by micro-pitting, because micro-pits can cause stress concentration and resulting in bigger chunks of material breaking off. Therefore, it can be concluded that micro-pitting was the primary failure mode of the roller. The right side of the roller suffered higher stress than the left side at some point during the service lifetime of the bearing (RL Errichello, 2012). This also means that the resistance to rolling contact fatigue and load bearing capacity of the roller surface is insufficient for its working condition, especially in the presence of misalignment effects causing much higher contact stresses.

Figure 4.1.1-2 All the rollers are severely damaged

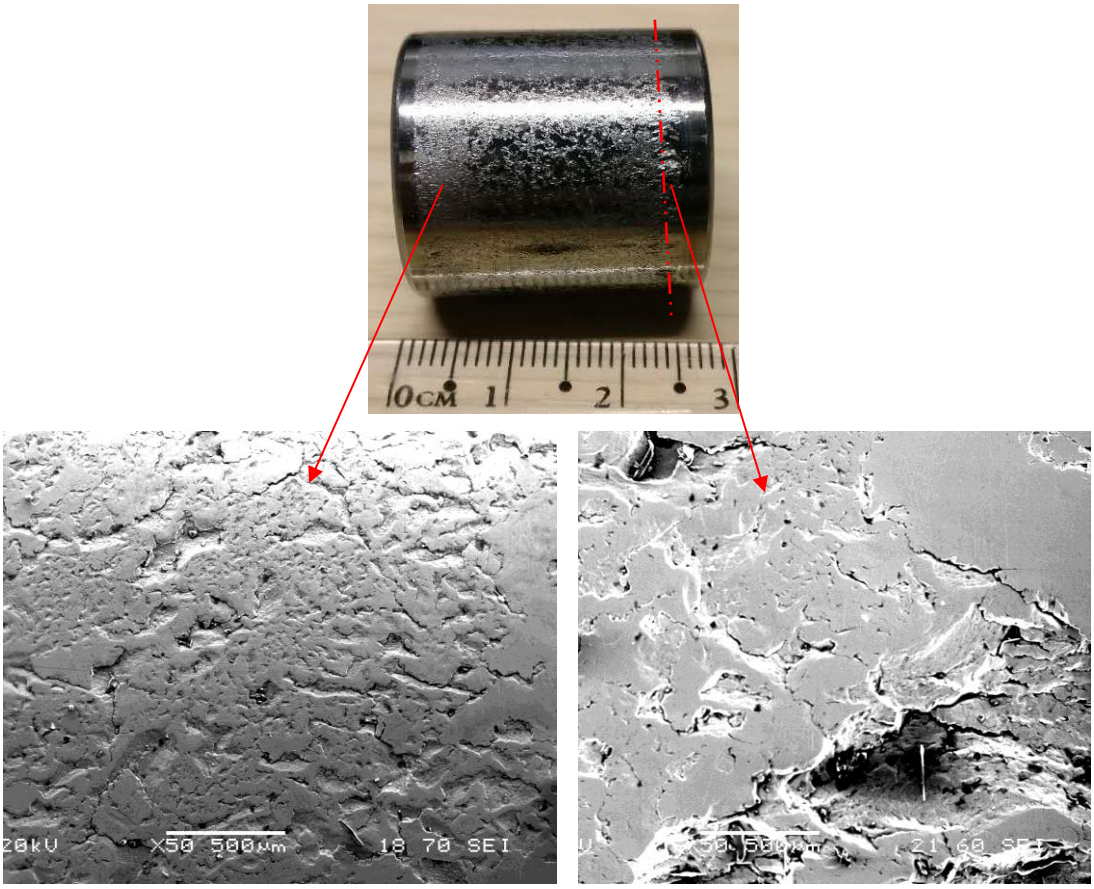

Figure 4.1.1-3 The surface of the rollers is damaged in the form of macro-pitting and micro-pitting, and the surface morphology of the left side is different to the right side.

Figure 4.1.1-4 shows a high-magnification SEM micrograph of the surface of the roller affected by micro-pitting damage. The bottom of a micro-pit crater, has a rough surface which is typically caused due to ductile fatigue crack propagation (RL Errichello, 2012). As

indicated in Figure 4.1.1-4, the featheredge of the pit has formed at the back of the micro-pit crater, having a white colour appearance under SEM. This is due to the edge effect, i.e. the emission of secondary electrons is enhanced at the edges of the samples, resulting in brighter appearance in the SEM micrograph image obtained (Bob Hafner, 2007). The formation of the featheredge is caused by plastic flow of material over the crater rim (RL Errichello, 2012). The surface outside micro-pits are mostly smooth and featureless. It is noticed that the direction of the micro-pits in rollers is non-uniform. According to RL Errichello (2012) the nonuniform sliding directions in rolling-element bearing components leads to the random direction of the micro-pits.

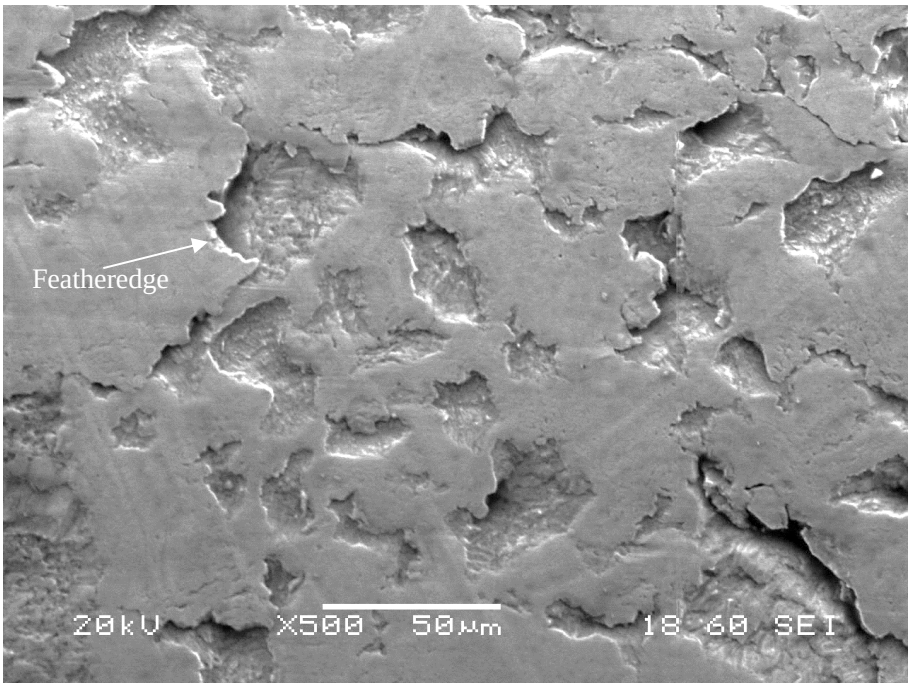

Figure 4.1.1-4 SEM image of micro-pitting on cylindrical roller surface

Figure 4.1.1-5 shows the back-scattered-electron (BSE) image and EDX analysis of the roller surface. Firstly, Spectrum 1 indicates that the roller is made of steel with a Cr content of around 1.71 in wt%, Si 0.17 in wt%, Mn 0.69 in wt% and C 2.22 in wt%. Because of the C contamination in the SEM chamber (e.g. from pump oil), the tested C value is commonly

higher than the real value, so the actual C content in the steel examined should be less than 2.22 in wt%. The compositions of the steel from which the rollers were manufactured was measured using EDS. The EDS findings place the steel used within the limits reported in the relevant standards for bearings (Xiaolan Ai and Charles Moyer, 2001). Also, some areas in the BSE image appear brighter than the rest of the sample. This suggests that elements heavier than Fe exist on the roller surface. Elements with higher atomic number can generate more BSEs than elements with lower atomic numbers, hence resulting in a brighter region in the micrograph obtained. Cu has been detected on the brighter areas of roller surface through EDS analysis. Since it is known that the cage is made of soft brass, this would suggest that some material had been transferred from the surface of the cage to the roller while the bearing was still in service. The composition of cage has been analysed using EDS as shown in Figure 4.1.1-20 of section 4.1.1.1.2.

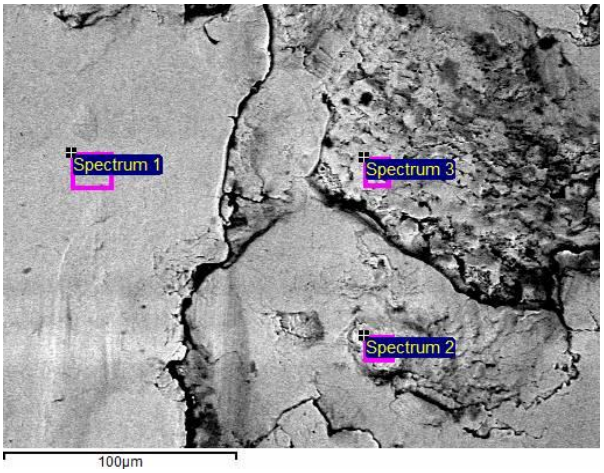

Spectrum/weight%	C	Si	Cr	Mn	Fe	Cu
1	2.22	0.17	1.71	0.69	95.20	
2	3.56	0.19	1.37	0.39	93.33	1.16
3	4.42	0.22	1.44	0.41	92.69	0.81

Figure 4.1.1-5 The back-scattered-electron image and EDX results of the roller surface, indicating the roller is made of steel and copper is detected on the surface

To see the cross-section of the rolling contact fatigue damage, the roller was cut perpendicularly to its axis through the red dash line shown in Figure 4.1.1-3. Figure 4.1.1-6 shows the back-scattered micrograph of the cross-section, with some typical micro-pits and macro-pits being clearly present in the roller. As it can be seen in Figure 4.1.1-6, the micro-/macro-crack depth/angle to surface are 92.9 μm/26.6º, 73.4 μm/17.7º, 299.5 μm/17.5º and 195.1 μm/30.7º respectively for crack a, b, c and d. Among them, it is worth noticing that the crack can be as deep as about 300 microns, indicating the fracture toughness in the subsurface area is insufficient. It is known that the rolling contact fatigue cracks can be surface (i.e. pitting) or subsurface initiated (i.e. spalling) (Farshid Sadeghi et al., 2009). The surface-initiated micro-pits normally originate from indents, scratches or cracks. The sub-surface ones initiate from micro-cracks usually initiating from inclusions. In this roller, no coarse inclusion was observed in the micro-/macro-cracks observed as shown in Figure 4.1.1-7. Some short cracks originating at the surface were observed. Therefore, it is possible to conclude that these micro-pits initiated at the surface rather than subsurface. W Glaeser (1996) reported that surface-initiating micro-pits are more common than sub-surface-initiating ones. Surface-originating fatigue cracks are highly related to high tangential force sustained. According to the direction of propagation of these cracks, which is from upper right to lower left, it is known that the dominant friction direction is from left to right, based on the relationship observed and explained by D. Nélias et al. (1999). The sliding-induced tractive force can cause shear stresses at surface geometrical discontinuities and the shallow area below them, e.g. surface asperities, grinding marks and idents. The shear stresses can lead to local plastic deformation, giving rise to tensile residual stresses. After the critical number of contact cycles has been exceeded micro-cracks initiated. Cracks will subsequently continue propagating at an angle between 15º and 30º with respect to the surface axis. During the propagation, the

crack will branch up. someone of the branches will eventually propagate towards the surface. When a critical depth has been reached, a fragment of material will break off, leaving a micro-pit behind it (D. Nélias et al., 1999, Shuangwen Sheng, 2010).

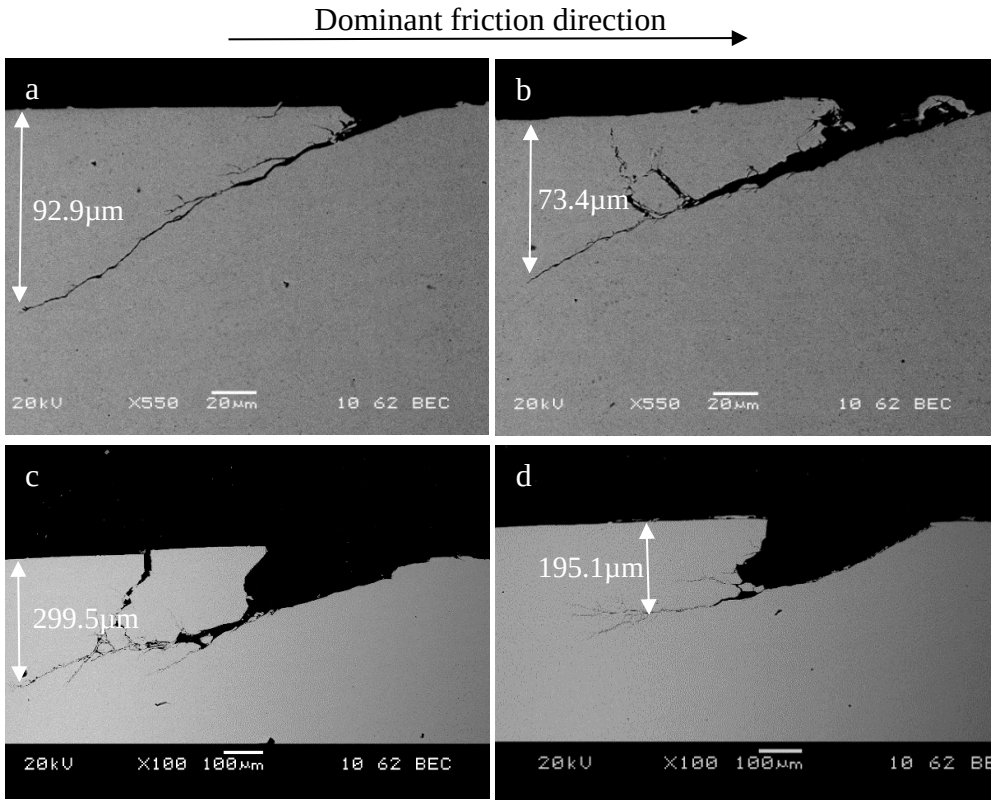

Figure 4.1.1-6 Cross section of typical micro-/macro-pitting cracks on the roller

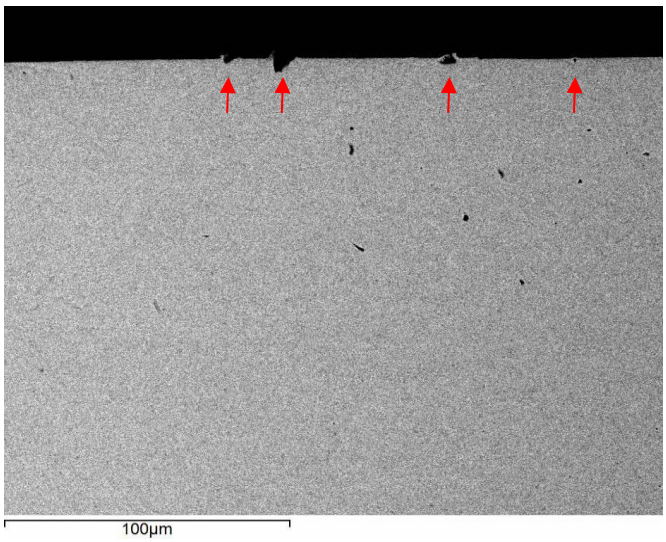

Figure 4.1.1-7 Rolling contact fatigue initiated at roller surface as arrowed

Except of these typical rolling contact fatigue pits shown in Figure 4.1.1-6, some unusual micro-pits were also observed. For instance, in Figure 4.1.1-8, the direction of crack C is from upper left to lower right, which is opposite to the direction of the other cracks. This suggests that crack C is likely to have been caused by another force opposite to the dominant friction force. The crack depth/angle to the surface of crack A, B and C are 33.7 μm/20.6º, 37.2 μm/18.2º and 24.3 μm/30.3º respectively. In Figure 4.1.1-9, the small initial part of the crack on the right has an angle of 41.8º to the surface, but the following main part of the crack changed direction and became parallel to the roller surface at a depth of 23.5 μm below the surface. The explanation is that if the subsurface crack entered a sufficiently strong compressive stress field in the proximity area of the subsurface, then its propagation direction would change dramatically causing it to propagate parallel to the surface without breaking the surface.

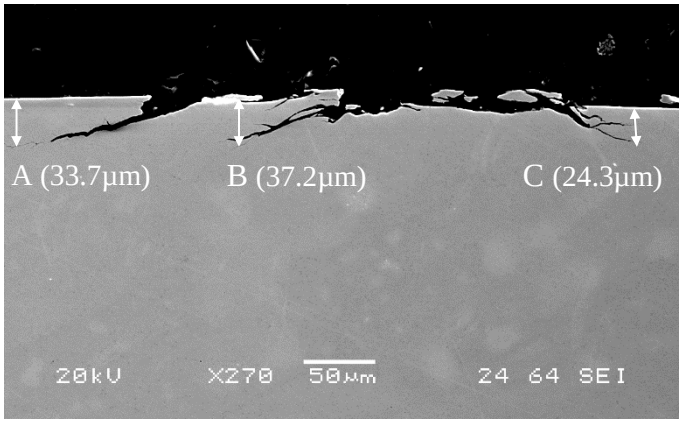

Figure 4.1.1-8 Crack C has a different propagation direction with A and B on the roller

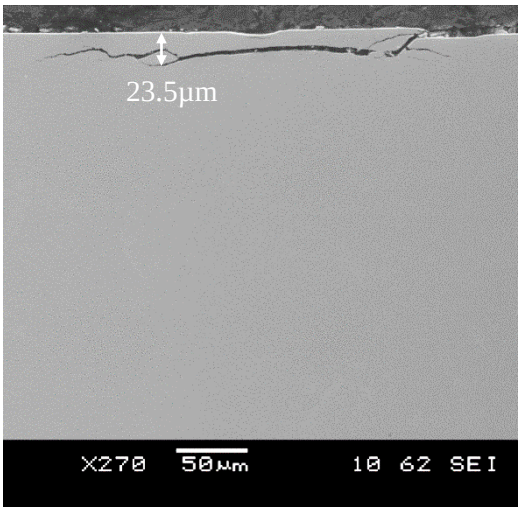

Figure 4.1.1-9 One crack propagated parallel to the surface on the roller

Although the surface fatigue cracks in the roller were considered to have initiated from surface defects instead of sub-surface inclusions, it is still important to notice that some coarse non-metallic inclusions are present in the steel from which the roller was manufactured. The inclusions were observed in the surface and sub-surface areas of the roller, including SiC (Figure 4.1.1-10), Al_2O_3 (Figure 4.1.1-11), and $MgO{\cdot}Al_2O_3$ (Figure 4.1.1-12). The sources of SiC inclusion could be related to the material that the refractory brick of furnace is made of, or the deoxidizing agent used for steel making. SiC is one of the most widely used refractory materials in steel-making furnace, because of its high thermal stability, good thermal conductivity, shock resistance, and high enough chemical stability (R. Amavis, 1990). Also, SiC may be used during the steel making process, in order to de-oxidise steel and adjust the content of C and Si (Pierre-Marie Cabanne, 2006, Electro-Abrasives, 2015, Miller-and-Company LLC, 2015). The common Al_2O_3 inclusion is the de-oxidising product in the steel arising when Al is used as de-oxidising agent. Moreover, alumina could even form in the steel melt with less than about 200 ppm Al present if the steel melt had been mainly deoxidised using Si (Joo Hyun Park, 2007). With respect to the $MgO{\cdot}Al_2O_3$ inclusion, there are two possible reasons behind its presence. In some cases, $MgO{\cdot}Al_2O_3$, an inclusion with spinel

crystal structure, could form in steel. This has also been reported by other researchers (Shufeng Yang et al., 2010, Neslihan Dogan et al., 2015, Joo Hyun Park, 2007). Since MgO is widely adopted for desulfurization of steel, some retained MgO in the ladle slag may be present after the desulfurisation step, The MgO present may react with dissolved aluminium in liquid steel to form $MgO \cdot Al_2O_3$ inclusion (Chris Pistorius et al., 2011, Obinna Adaba, 2015). It is also possible that $MgO \cdot Al_2O_3$ inclusions arise from the refractory material used in the steel-making process (Raymond P Racher et al., 2004).

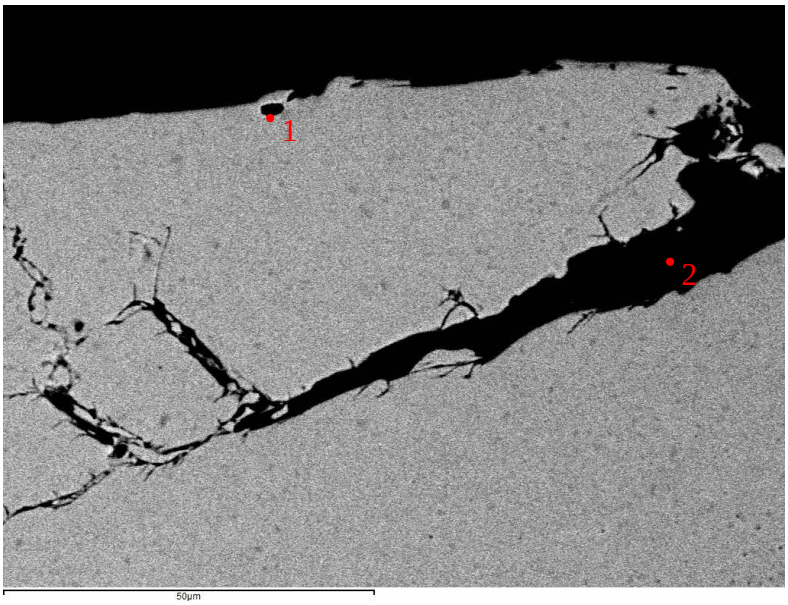

Spectrum (W%)	C	O	Si	S	Cr	Fe	Comment
1	14.53		31.78		0.72	52.97	SiC
2	91.54	3.57	0.41	0.71		3.78	Bakelite

Figure 4.1.1-10 Back-scattered-electron image of a crack and a SiC particle was detected in roller surface through EDS analysis

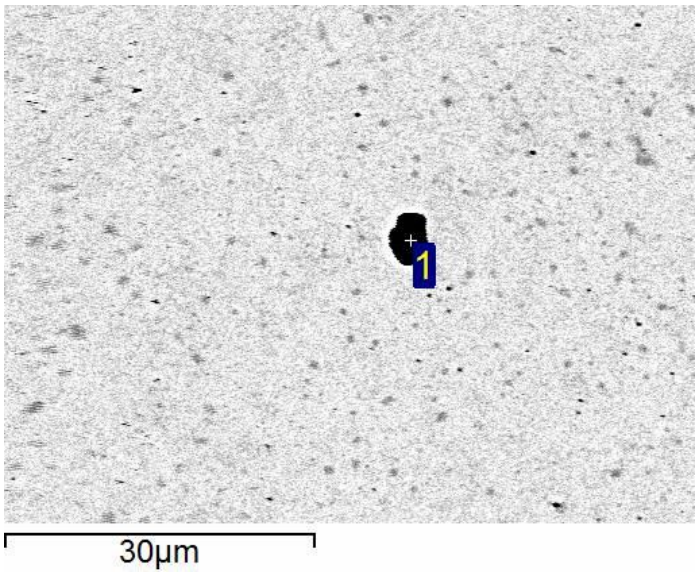

Spectrum (W%)	C	O	Mg	Al	Ca	Cr	Mn	Fe	Comment
1	4.19	13.64	4.44	36.79	6.34	0.58	5.79	28.22	Al_2O_3

Figure 4.1.1-11 Back-scattered-electron image and the EDS results of a coarse Al_2O_3 inclusion particle in roller subsurface

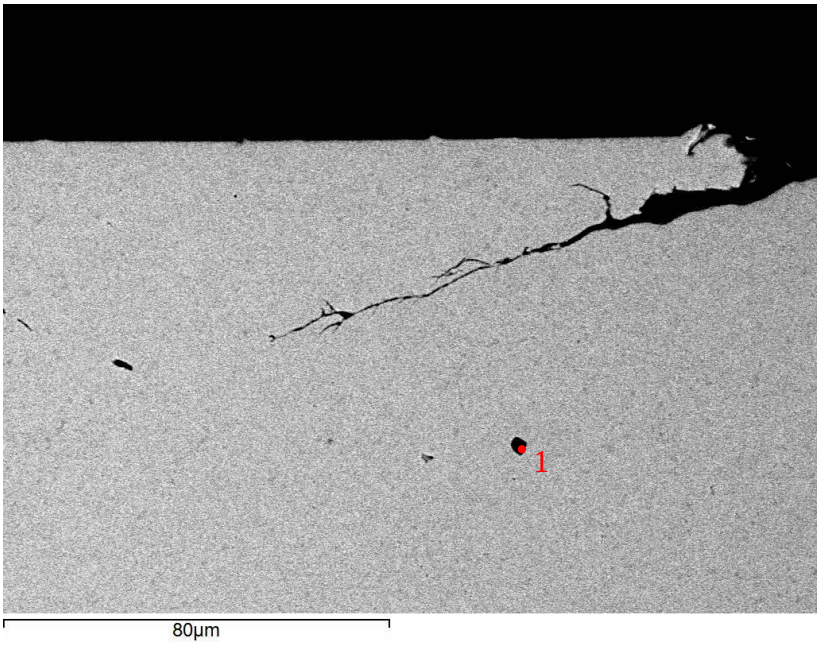

Spectrum (W%)	C	O	Mg	Al	Fe	Comment
1	5.40	16.82	10.19	33.85	33.74	$MgO \cdot Al_2O_3$

Figure 4.1.1-12 Back-scattered-electron image and the EDS results of a coarse $MgO \cdot Al_2O_3$ inclusion particle in roller subsurface

Despite the presence of coarse inclusions, fine well-dispersed spheroidised carbides were observed under high magnification back-scattered-electron microscopy carried out on the polished but not etched roller sample (Figure 4.1.1-13). The sample was subsequently etched using 2% nital. Figure 4.1.1−14 shows the optical micrograph obtained at a magnification of 500×. Figure 4.1.1-15 shows the SEM micrograph of the etched microstructure of the roller cross-section. They both show a typical tempered martensite microstructure containing dispersed spheroidised fine carbides (spheroidite). The findings are in accordance with the results of the back-scattered-electron microscopy (Figure 4.1.1-13). In addition, the EDS analysis presented in Figure 4.1.1-15 revealed that the carbides are rich in Cr and Fe. These carbide particles are possibly formed because of the spheroidisation annealing process and their composition is likely to be M_3C (M=Fe/Cr) (H Fu et al., 2017). The presence of the fine uniformly dispersed carbides in the microstructure is desirable since it improves the fatigue damage resistance of the bearing. Hence, carbide refinement treatment is commonly conducted on bearing steel after machining. One of the usual methods is spheroidisation followed by quenching and tempering heat treatment (Philip K Pearson and Thorn W Dickinson, 1988, CA Stickels, 1974, Jaromir Dlouhy et al., 2014, Wenwen Song et al., 2014, HKDH Bhadeshia, 2012).

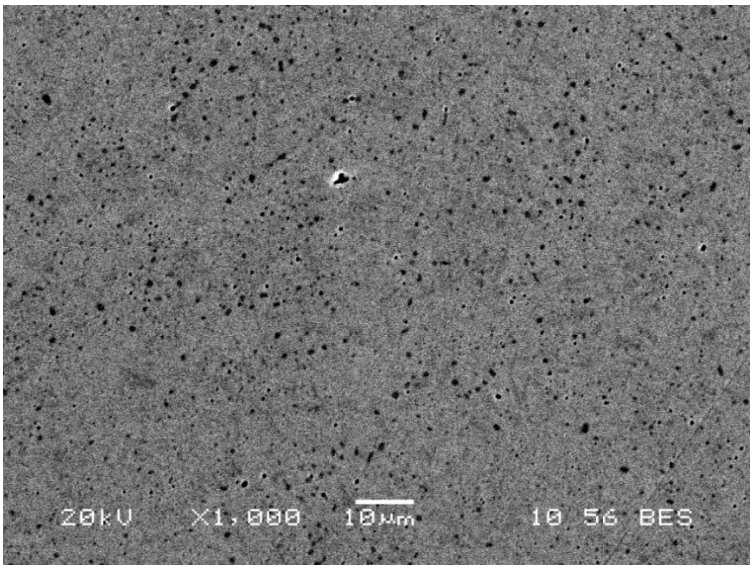

Figure 4.1.1-13 Back-scattered-electron image shows dispersed carbide (the black dots) in the roller material

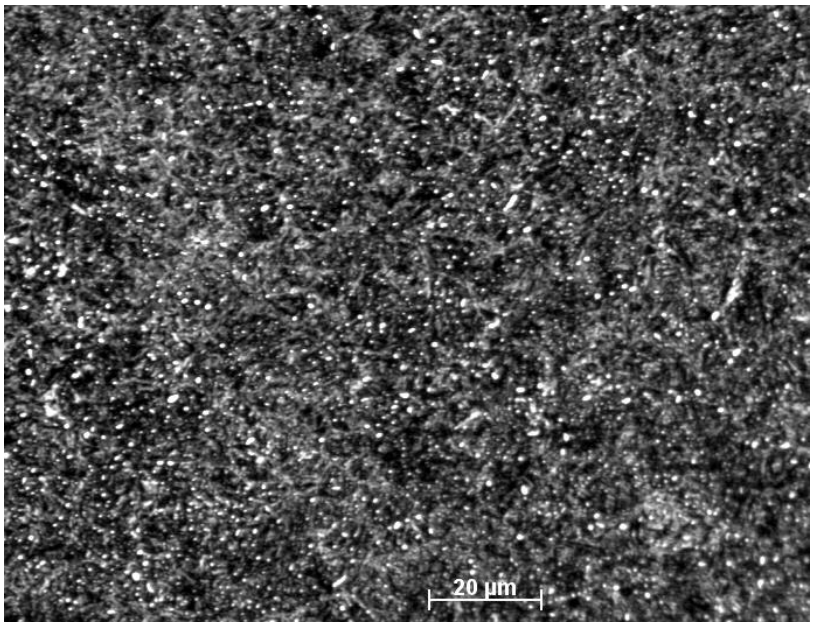

Figure 4.1.1−14 Metallography of the roller microstructure, composed of tempered martensite and dispersed spheroidised fine carbides (2% natal, 500×)

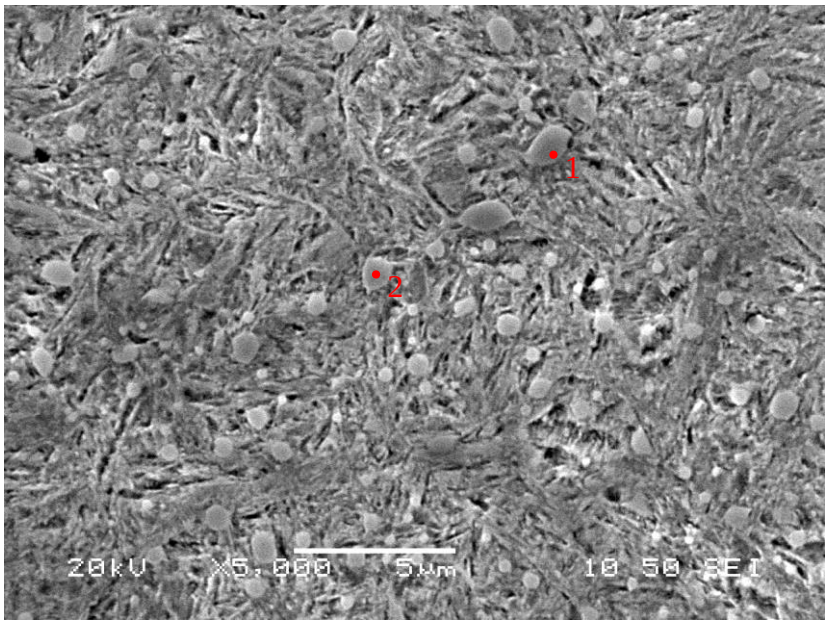

Spectrum/Weight%	C	Cr	Fe	Comment
1	21.36	8.77	69.87	Cr/Fe enriched carbide
2	20.94	10.14	68.92	Cr/Fe enriched carbide

Figure 4.1.1-15 SEM image and EDS analysis of the spherical carbide in roller

The hardness profile of the roller is shown in Figure 4.1.1-16. The surface hardness is slightly higher than the hardness of the subsurface and deeper areas. The hardness increase in the roller surface may be the result of work hardening effect during service loading (HKDH Bhadeshia, 2012). Below a depth of 20 μm, the hardness value is relatively constant up to a depth of 3 mm. Therefore, the rollers were likely through hardened before commissioning. One of the disadvantages of the through-hardened steels is that they do not possess enough fracture toughness in the subsurface and core area. Thus, the steel alloy does not exhibit enough fatigue resistance to prevent surface cracks from propagating into deeper area. Fatigue performance can be improved by using case hardened steel. Case hardened steels combine a hardened surface and tough core at the same time. The average hardness of the roller between 30 μm and 3000 μm is 706.50 ± 18.09 HV0.05 which meets the minimum hardness requirements 60 HRC (about 693 HV) (Erwin V Zaretsky, 2012). In addition, the micro-

hardness measured value are in agreement with the tempered martensitic microstructure observed. The hardness of the low-temperature tempered martensite (between 150 and 250 ˚C) is in the range of 650 HV to 850 HV (RA Grange et al., 1977). The XRD analysis carried out on the sample from the roller material shown in Figure 4.1.1-17, revealed only peaks for α'-Fe phase, which is possibly generated from the tempered martensite phase observed in the micrographs obtained.

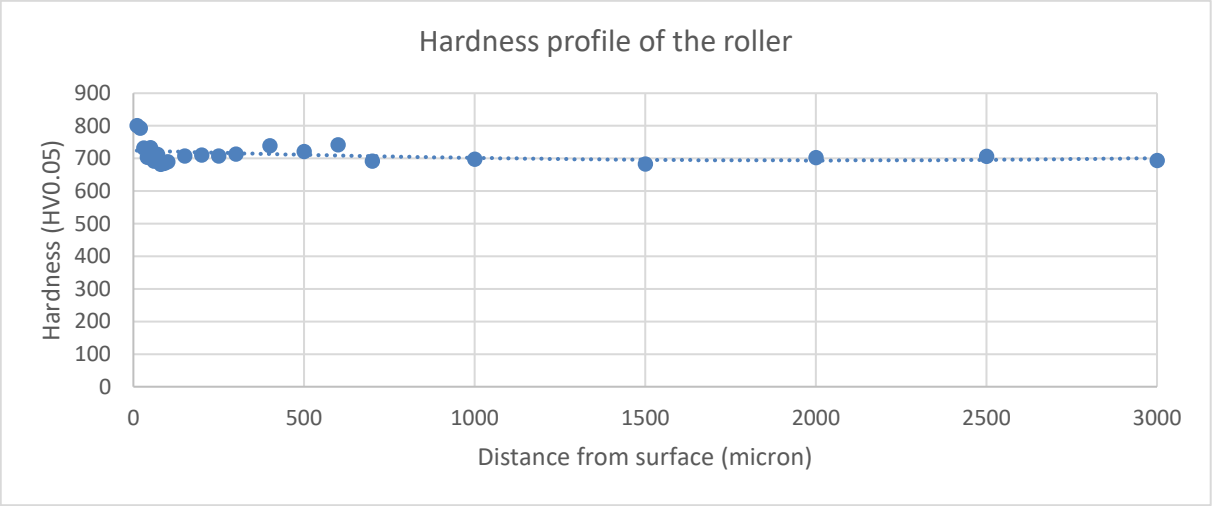

Figure 4.1.1-16 The hardness profile of the roller proving the roller was through hardened before service. The average hardness of the roller between 30 µm and 3000 µm is 706.50 ± 18.09 HV0.05

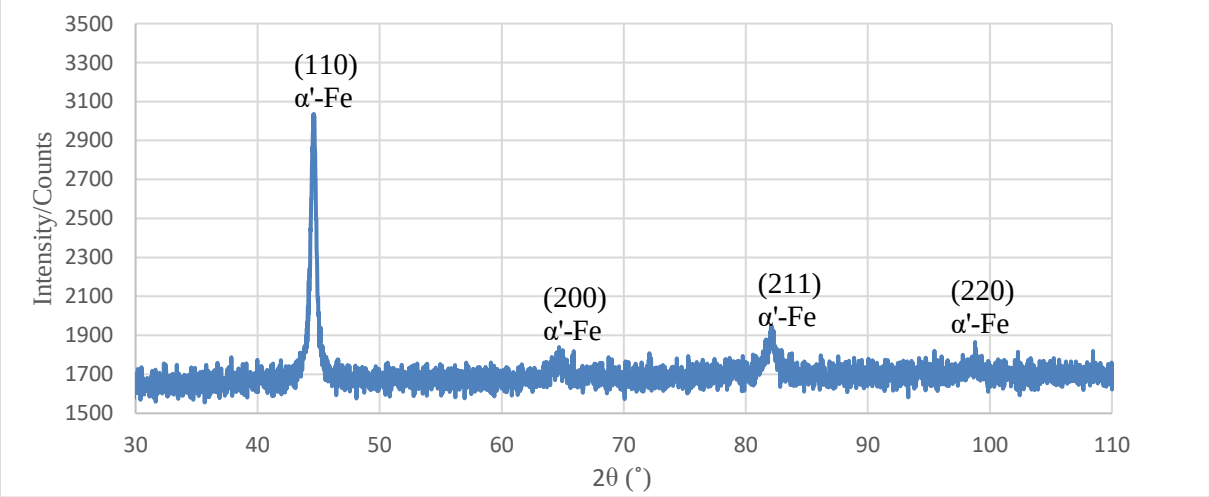

Figure 4.1.1-17 XRD pattern showing the main phase of the roller

To sum up, the microstructure of roller material is tempered martensite with dispersed fine carbides and some inclusions, specifically SiC, Al_2O_3 and $MgO \cdot Al_2O_3$. The hardness of the rollers has been measured to be 706 HV in average, which is relatively low and just reaches the lowest hardness level required by the bearing industry. The mechanisms that have led to the failure of the rollers have been identified to be micro-pitting and macro-pitting. In addition, most of the rollers show more severe surface damage at one end side than the other one, which is clearly evidence of misalignment effects. Misaligned rollers suffered uneven distribution of contact stress over the surface, leading to local stress concentration, and subsequently prompting the initiation and propagation of rolling contact fatigue in the contact area.

4.1.1.1.2 Bearing cage

Commonly, cages of medium and large roller bearings are made of soft brass. The function of the cage (also named as separator or retainer) of a rolling bearing is to equally separate the rollers and maintain their position (Avraham Harnoy, 2002). Hence, the cage is in contact with the rollers. The contact surface of cage has been observed as part of the investigation of the failure causes of the bearing.

The photograph of the bearing cage with yellow colour is displayed in Figure 4.1.1-18. For the convenient observation of the cage, concave surface which is in contact with the rollers, i.e. the part highlighted by the framed area in Figure 4.1.1-18 was cut off from the cage. The photograph of the concave roller-cage contact surface of the removed part is shown in Figure 4.1.1-19. It can be seen that the surface condition is really poor. Observation by naked eye reveals white shinning particles on the roller-cage contact surface of the yellow cage part. Also, the distribution of the white particles is uneven. The number of the white shinning particles increased from the area A to the area B (A & B are shown in Figure 4.1.1-19).

Except from the presence of the aforementioned white particles, it can be easily seen that the surface morphology of area B is different from the other area.

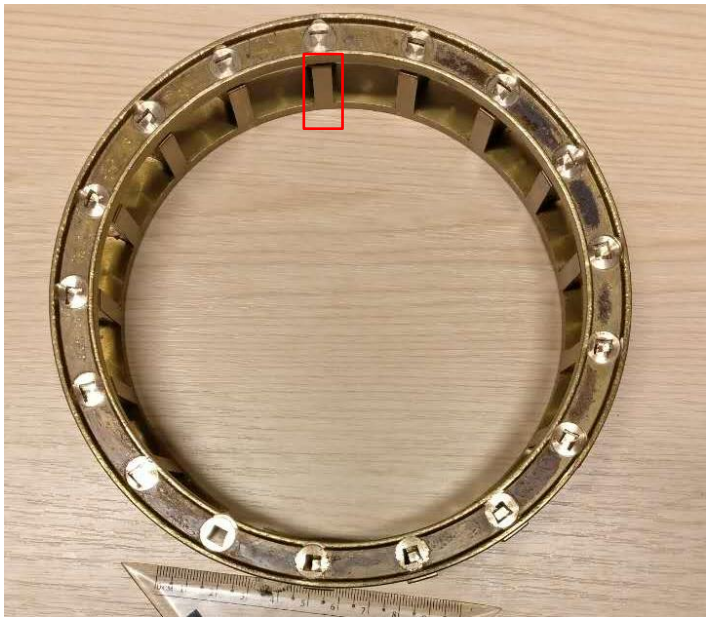

Figure 4.1.1-18 The cage of the shaft bearing of the high-speed stage

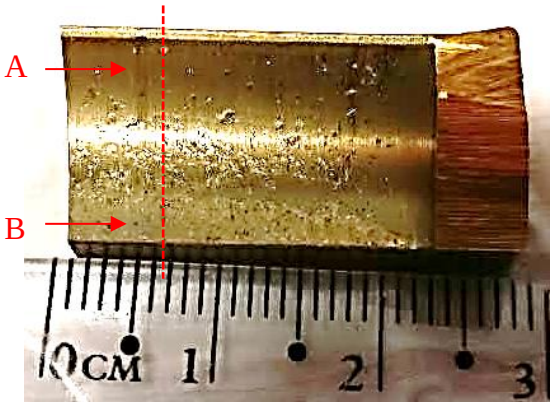

Figure 4.1.1-19 The worn concave surface of the cage

The SEM backscattered electron micrographs and the EDS results of the area A and B are shown in Figure 4.1.1-20 and Figure 4.1.1-21 respectively.

In area A (Figure 4.1.1-20), most of surface is covered by scratches in the same direction which were possibly produced by machining. Also, two larger and several smaller indents can be seen on the surface. Apart from that, one darker particle (with approximate dimensions of

180 µm × 130 µm) was discovered to be embedded in the matrix material. Based on backscattered electron microscopy, the darker particle has been identified to be mostly composed of lighter elements compared with surrounding material. Following from the results of EDX analysis, the darker particle has similar composition to that of the roller steel. Hence, it has quite likely broken off from the steel roller. The EDX results also suggest that the whiter matrix material is proved brass alloy, containing Cu and Zn. The micro-hardness of the brass cage was tested and the average value is only 108.73±1.67 HV0.05, while the average hardness of the roller is as high as 706.50 ± 18.09 HV0.05. Therefore, any roller fragments breaking off can very easily cause indents or be embedded in the surface of soft brass cage.

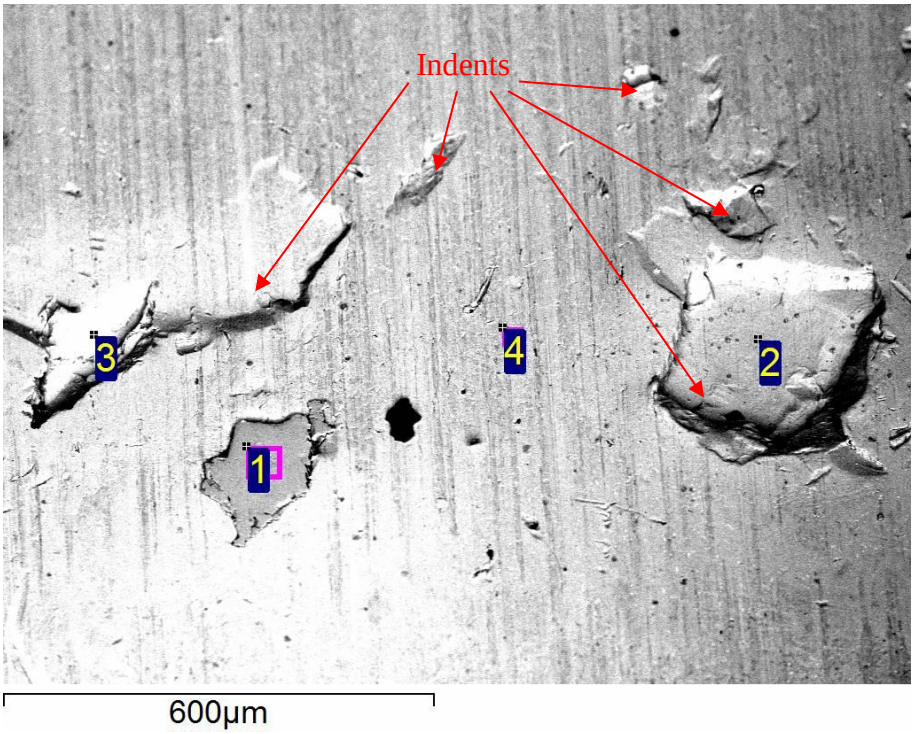

Spectrum / Weight%	C	O	P	S	Cr	Fe	Cu	Zn	Comment
1	3.87				1.42	94.72			Steel debris
2	5.35	1.20	0.51				55.54	37.40	Brass
3	5.46	0.76		0.40		0.43	57.26	35.68	Brass
4	10.30	1.14	0.52	0.81			53.05	34.17	Brass

Figure 4.1.1-20 Back-scattered electron image and EDS analysis of area A of the cage worn surface

In the area B (Figure 4.1.1-21), more roller debris is embedded. The average size of the debris particles observes is bigger than those seen in area A. The largest embedded steel debris particle in Figure 4.1.1-21 has been measured to be about 450 µm × 260 µm, which makes it observable even by the naked eye. Due to the large number of indentations made by the large and hard roller fragments, the matrix brass is so severely plastically deformed that all scratches from the machining have disappeared.

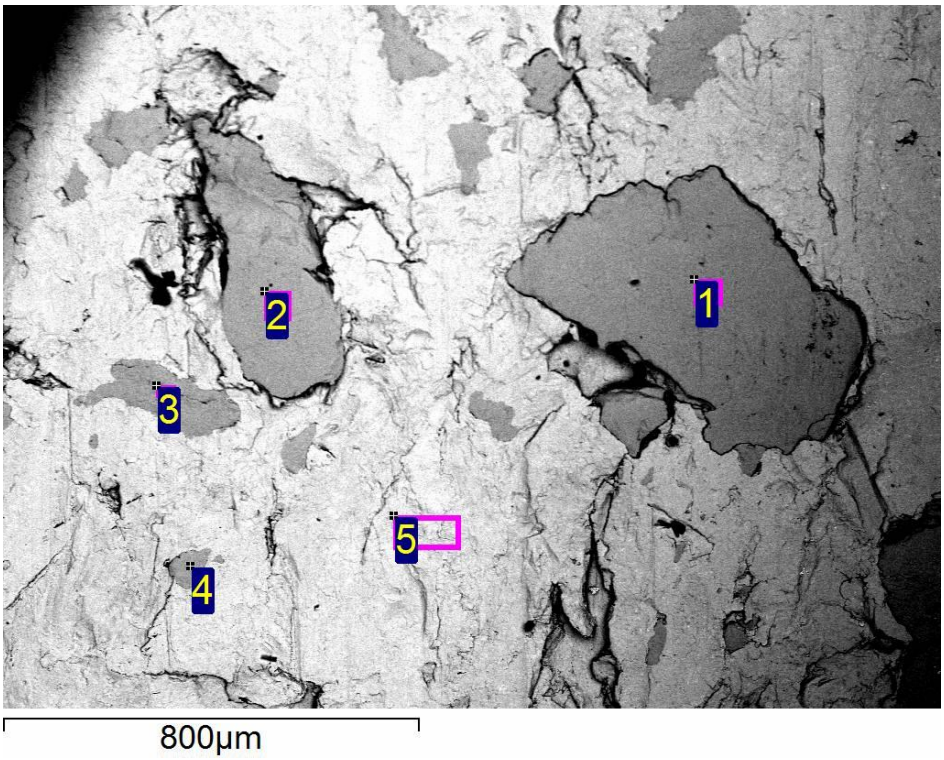

Spectrum / Weight%	C	O	P	Cr	Mn	Fe	Cu	Zn	Comment
1	1.41			1.41		97.18			Steel debris
2	1.52			1.47	0.63	96.37			Steel debris
3	2.22		0.36	1.48		95.94			Steel debris
4	2.13			2.00		95.87			Steel debris
5	3.25	0.66					57.74	38.35	Brass

Figure 4.1.1-21 Back-scattered electron image and EDS analysis of area B of the cage worn surface

To observe the cross-section of the cage part, the sample was cut along the red dash line as shown in Figure 4.1.1-19. The photograph of the cut cross-section is shown in Figure 4.1.1-22.

In the framed area in Figure 4.1.1-22, a particle embedded in the cage surface is observed under SEM. The backscattered-electron micrograph and the EDS analysis of the embedded particle is shown in Figure 4.1.1-23. The results from both techniques indicate that the embedded particle is a steel fragment which has most likely broken off from the rollers. In addition to that, small cracks can be seen in the steel fragment. The penetration depth of the fragment is at least about 15.3 micron from the cage surface.

One of the lubricant's functions is to remove wear debris from the contact area to prevent debris concentration. But when the large and hard roller fragments are embedded in the soft brass cage, it is impossible for the lubricant to remove them. Moreover, due to the hard debris remaining as third-body components between the roller and cage, the wear rate is accelerated (Jennifer A Kleinhans et al., 2009). The mechanism is that the hard third-body embedded in the soft material can act like the asperities of a hard material(Timothy M Wright and Stuart B Goodman, 2001, Seppo S Santavirta et al., 1999). In this case, rubbing with the roller surface and increasing the contact stress, causes removal of more roller material in its path and promotes the acceleration of the wear rate of the rollers. The original intention of adopting soft material for manufacturing the cage is to prevent the rollers from adhesive wear or abrasive wear which arises from rubbing with a cage made from material with similar or higher hardness. However, third-body wear occurred instead, due to the low hardness of brass cage.

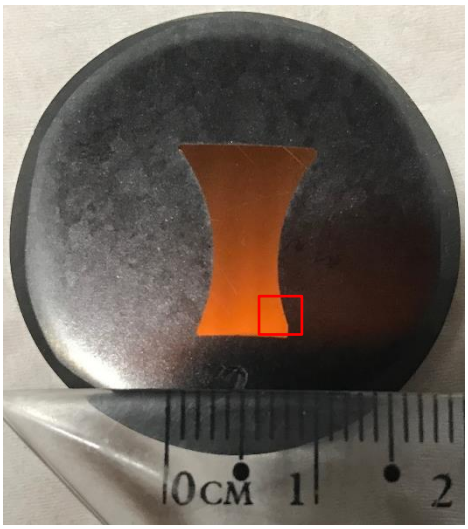

Figure 4.1.1-22 Cross section of the part removed from brass cage

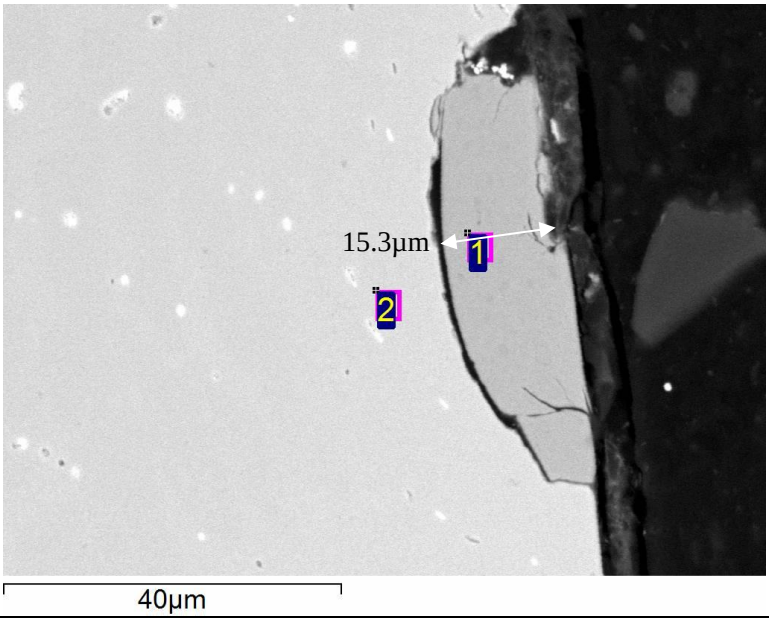

Spectrum (W%)	C	Si	Cr	Mn	Fe	Cu	Zn	Comment
1	2.19	0.31	1.33	0.50	94.96	0.72		Steel
2	2.39				1.38	58.97	37.25	Brass

Figure 4.1.1-23 Back-scattered-electron image of one steel fragment embedded in the brass cage surface and the EDS results

In summary, it has been found that large and hard steel fragments broke off from rollers caused indents and were embedded in the surface of soft brass cage. When the hard roller fragments are embedded in the soft brass cage, it is impossible for the lubricant to remove

them. Moreover, the embedded hard debris remaining as third-body components between the roller and cage, rubbing with the roller surface and increasing the contact stress, caused removal of more roller material in its path and promoted the micro-pitting formation of the rollers.

4.1.1.1.3 The inner race

In the bearing, the cylindrical rollers are in contact with the inner ring raceway. Therefore, surface damage may occur in the inner race. The inner race has been observed to identify the root cause of the bearing failure.

The front and side view of the inner race is shown in Figure 4.1.1-24. On the entire surface of the inner ring raceway (see Figure 4.1.1-25), macro-pitting and micro-pitting are identified, same failure mode as observed in the roller surface. In the middle part of the raceway, area II, the surface damage mode observed is related to micro-pitting. At each end of the raceway, areas I and III, the damage is more severe than the middle area II, as larger fragment of material has broken off resulting in macro-pitting. The macro-pitting damage at the ends of the raceway is thought to have followed micro-pitting damage in the raceway (RL Errichello, 2012). The explanation is that the micro-pitting reduced the contact area between the roller surface and the raceway, leading to higher contact stresses, especially at the ends of the rollers (Geometric Stress Concentration), eventually causing macro-pitting at the raceway. Moreover, it is noticed that the macro-pitting damage on the right-side area III is more severe than the left side I. This hints the effect of misalignment in the shaft connected to this particular component. Misalignment effects are important issues for materials used to manufacture the components of the gearbox and drive-train in general. This is due to the fact that

misalignment dramatically increases the contact stress levels, accelerating material wear and fatigue leading to premature failure due to micro-pitting and macro-pitting.

Figure 4.1.1-24 The front and side view of the inner race

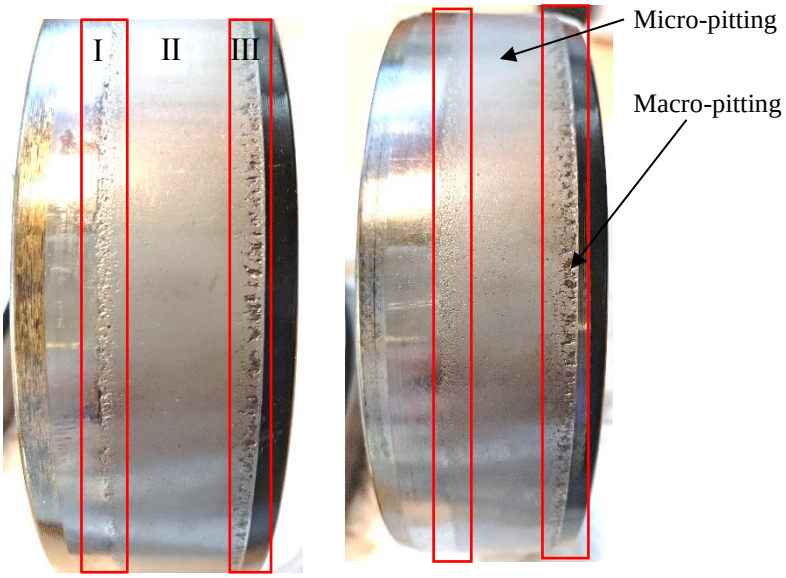

(a) (b)

Figure 4.1.1-25 Macro-pitting and micro-pitting are observed on the surface of inner ring raceway, (b) is the back side of (a). The surface damage at the end of raceway I & III (macro-pitting) is more serious than the middle part II (micro-pitting or frosting). Moreover, the macro-pitting damage on the right side III is severer than the left side I.

For the purpose of convenient observation and testing, a small piece of the inner race was cut off along the radial direction as shown in Figure 4.1.1-26. Figure 4.1.1-27, Figure 4.1.1-28 and Figure 4.1.1-29 show the SEM micrographs obtained from the areas I, II and III of the inner race, respectively. It can be seen that area II is affected by micro-pitting. Both areas I and III are affected by macro-pitting. The macro-pits in area III are much larger than those in area I.

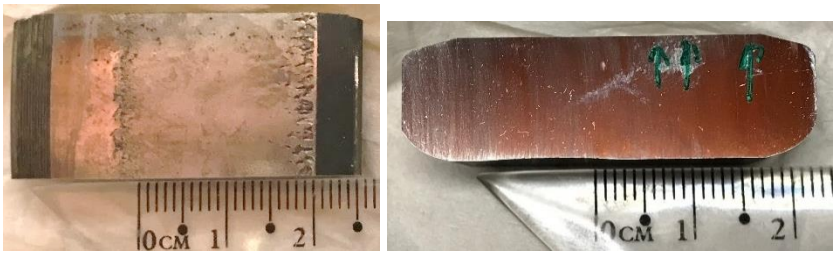

Figure 4.1.1-26 The raceway and the cross section of a small piece cut from the inner race for observation and test

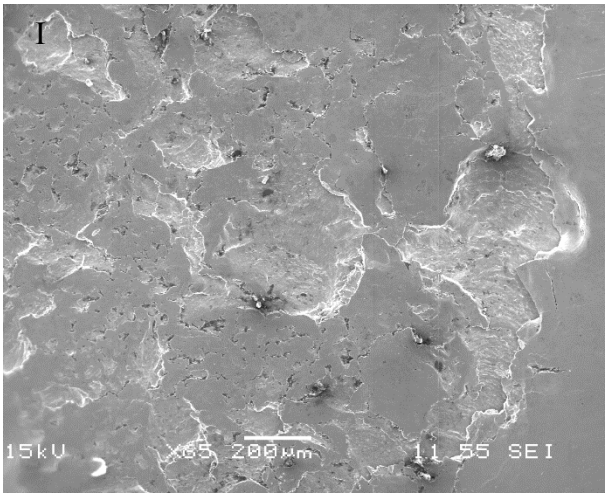

Figure 4.1.1-27 The SEM image of the area I of the inner race shows the area is macro-pitted

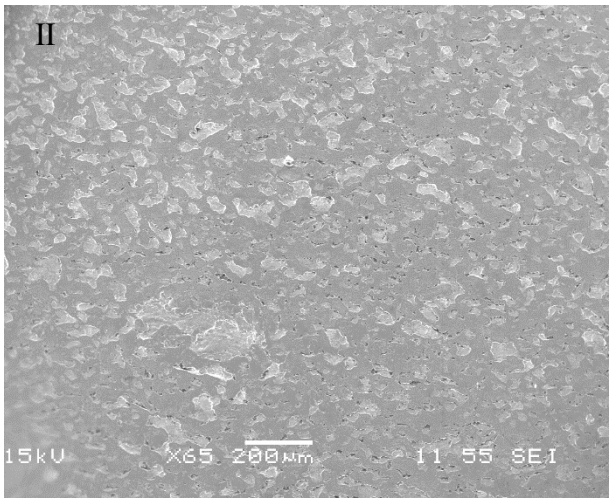

Figure 4.1.1-28 The SEM image of the area II of the inner race shows the middle area is micro-pitted

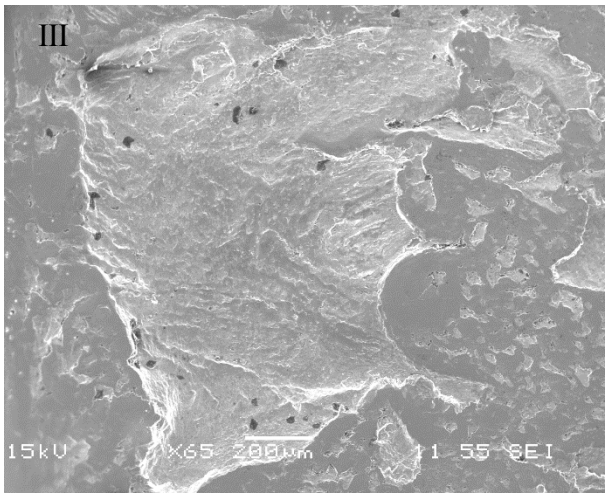

Figure 4.1.1-29 The SEM image of the area III of the inner race shows the area is macro-pitted, and these pits are bigger than those in area I

In the subsurface of the cross-section of the inner race, a large number of non-metallic inclusions, such as MnS, MnS surrounded Al_2O_3 (i.e. Al_2O_3+MnS), and SiC are observed. Some cracks are observed to have initiated from the SiC inclusions. MnS inclusions and MnS surrounded Al_2O_3 inclusions can be seen in Figure 4.1.1-30, Figure 4.1.1-31 and Figure 4.1.1-32. However, none of these subsurface MnS or Al_2O_3+MnS inclusions are related to the surface micro- or macro-cracks.

The formation mechanism of MnS surrounded Al_2O_3 is that the Al_2O_3 particles form first during the cooling stage. They act as the nuclei around which MnS solidifies later. SiC inclusions are shown in Figure 4.1.1-32, Figure 4.1.1-33 and Figure 4.1.1-34. It is worth noticing that the SiC inclusion in Figure 4.1.1-32 is connected to a pit. A crack is seen propagating through a SiC inclusion in Figure 4.1.1-33. Therefore, it is possible that some of the surface fatigue cracks in the inner race have initiated from subsurface inclusions, while others have initiated from the surface.

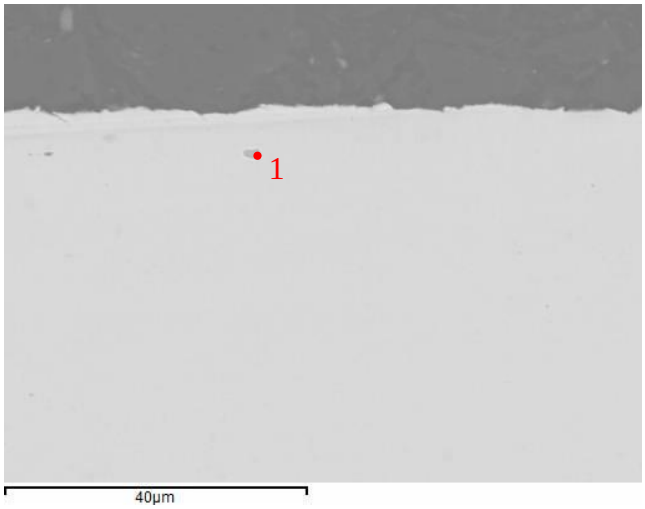

Spectrum (W%)	C	S	Ca	Cr	Mn	Fe	Comment
1	3.30	23.00	5.72	0.66	40.20	27.12	MnS

Figure 4.1.1-30 Back-scattered-electron image and the EDS results of a coarse MnS inclusion particle in inner race subsurface

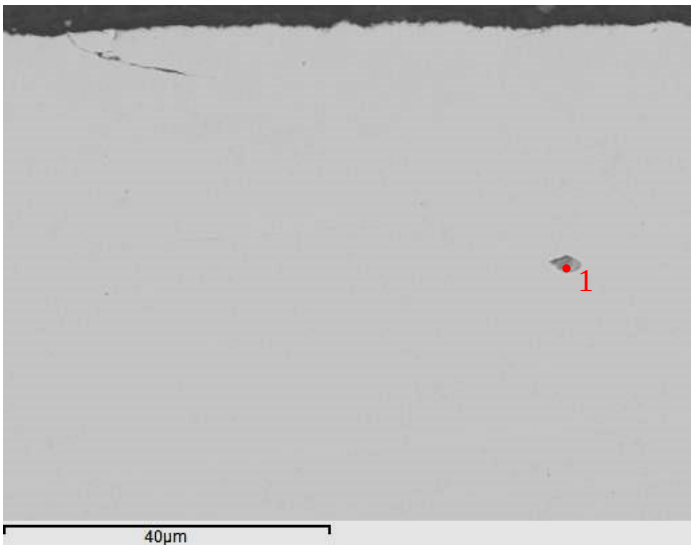

Spectrum (W%)	C	O	Mg	Al	S	Ca	Mn	Fe	Comment
1	4.21	5.42	1.85	14.52	19.21	3.85	32.02	18.93	Al_2O_3+MnS

Figure 4.1.1-31 Back-scattered-electron image and the EDS results of a coarse MnS surrounded Al_2O_3 inclusion particle in inner race subsurface

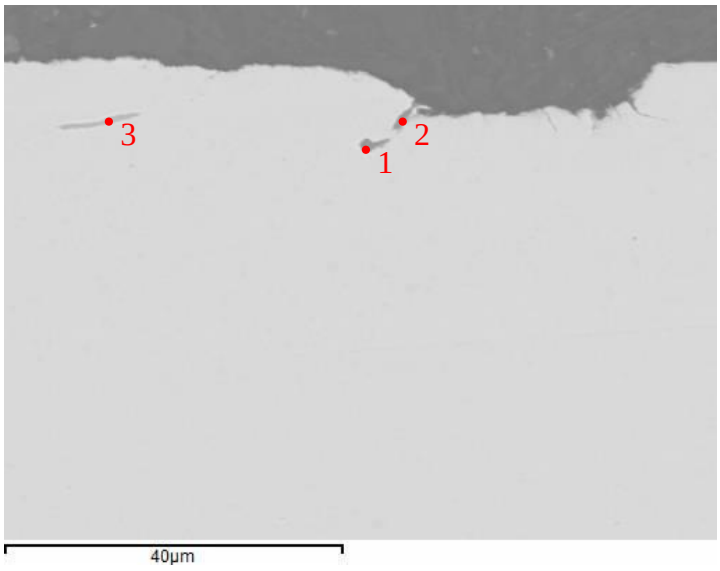

Spectrum (W%)	C	O	Si	S	Cr	Mn	Fe	Comment
1	16.97		46.03		0.94		36.07	SiC
2	15.46	1.77	46.62		0.75		35.41	SiC
3	2.85			22.09	0.90	47.66	26.49	MnS

Figure 4.1.1-32 Back-scattered-electron image and the EDS results of two SiC inclusion particles and a stripe MnS inclusion particle in inner race subsurface

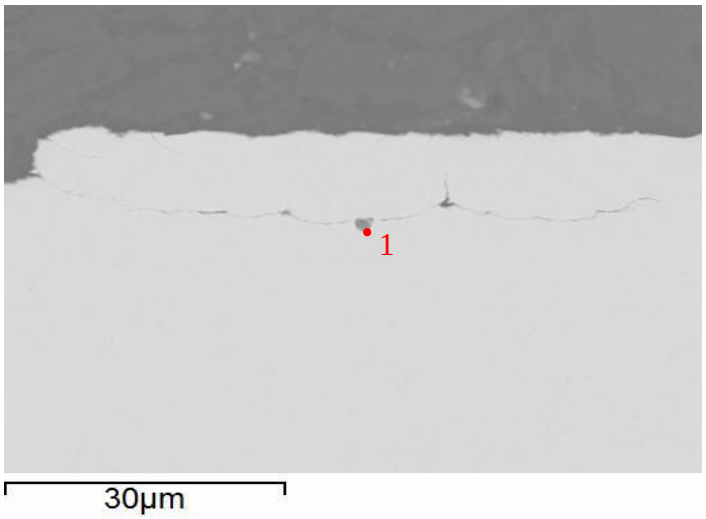

Spectrum (W%)	C	Si	Fe	Comment
1	23.13	50.42	26.45	SiC

Figure 4.1.1-33 Back-scattered-electron image and the EDS results of a coarse SiC inclusion particle in inner race subsurface

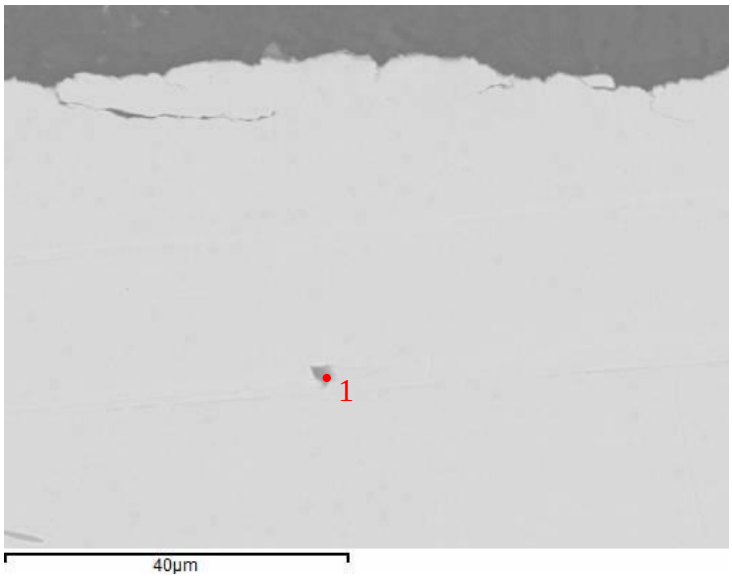

Spectrum (W%)	C	Si	Cr	Fe	Comment
1	16.39	40.84	0.93	41.84	SiC

Figure 4.1.1-34 Back-scattered-electron image and the EDS results of a coarse SiC inclusion particle in inner race subsurface

The hardness profile of the inner race is shown in Figure 4.1.1-35. It can be seen that the hardness value is relatively constant from the raceway surface up to a depth of 3 mm. Therefore, the inner race was possibly through hardened by quenching and tempering during

manufacturing. The average hardness of the inner race material is 757.76 ± 19.17 HV0.05 which meets the minimum hardness requirements 60 Rockwell C (about 697 HV) (Erwin V Zaretsky, 2012). The XRD analysis of the inner race material is shown in Figure 4.1.1−36. Only peaks of α'-Fe are observed. Figure 4.1.1-37 is the micrograph at a magnification of 500x of the inner race steel material after being etched with 2% nital. The microstructure observed consists of tempered martensite with fine dispersed spheroidised carbides.

The SEM image of the etched sample and the EDS analysis of the carbide (Figure 4.1.1-38) revealed the same microstructure whilst the carbide was found to be rich in Cr and Fe content. The microstructure observed is in agreement with the micro-hardness measurement and XRD analysis of the inner race.

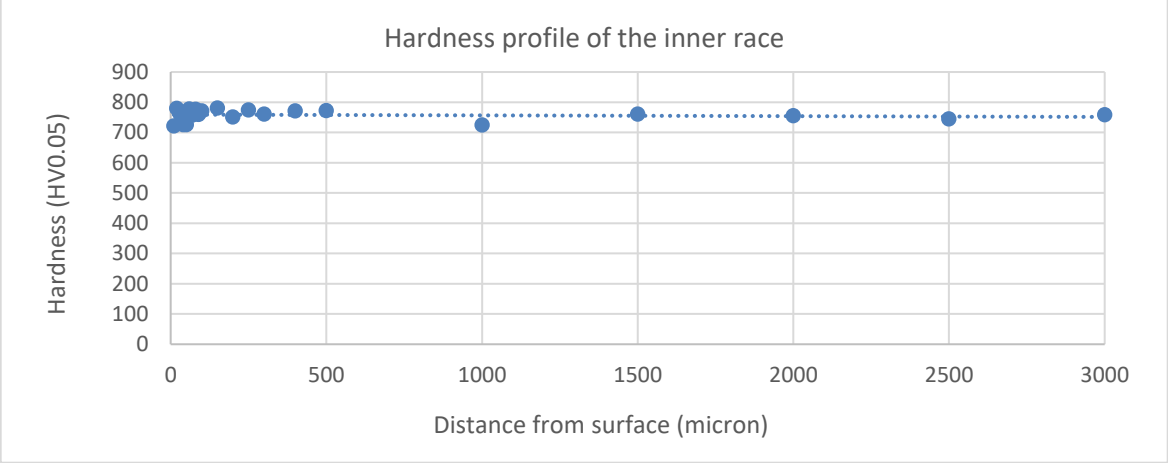

Figure 4.1.1-35 The hardness profile of the inner race suggesting the inner race is possibly through hardened. The average hardness of the inner race material is 757.76 ± 19.17 HV0.05

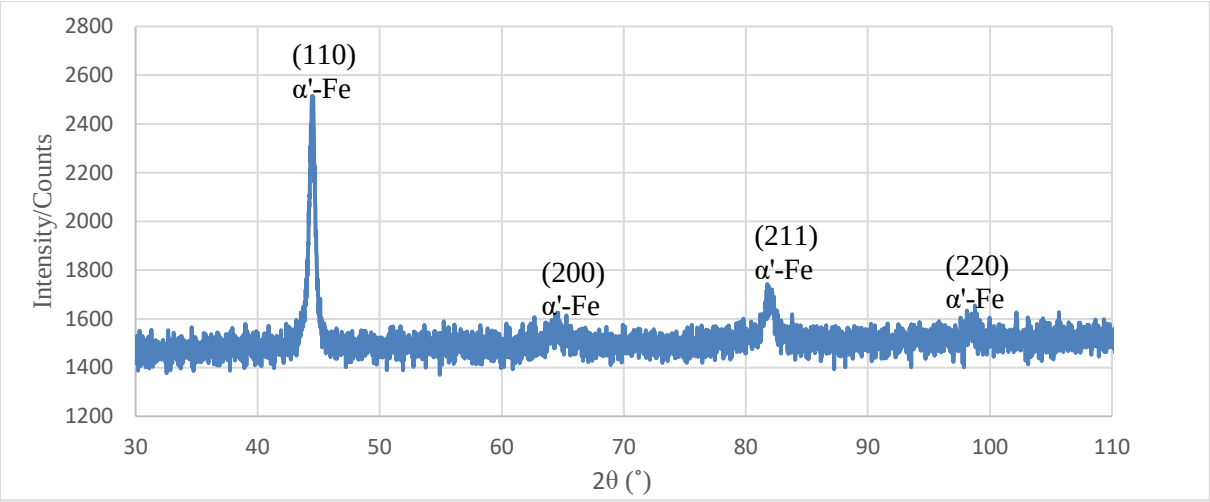

Figure 4.1.1−36 XRD pattern showing the main phase of the inner race steel

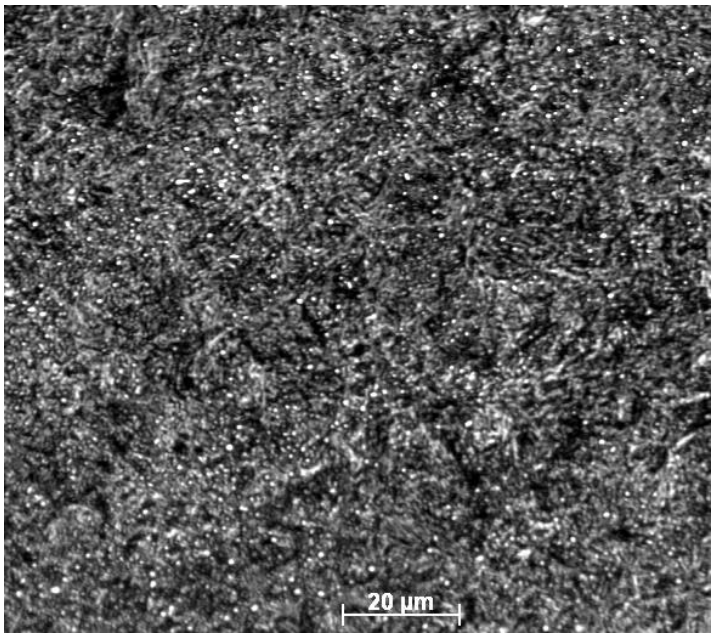

Figure 4.1.1-37 Metallography of the inner race microstructure, composed of tempered martensite and dispersed spheroidised fine carbides (2% natal, 500×)

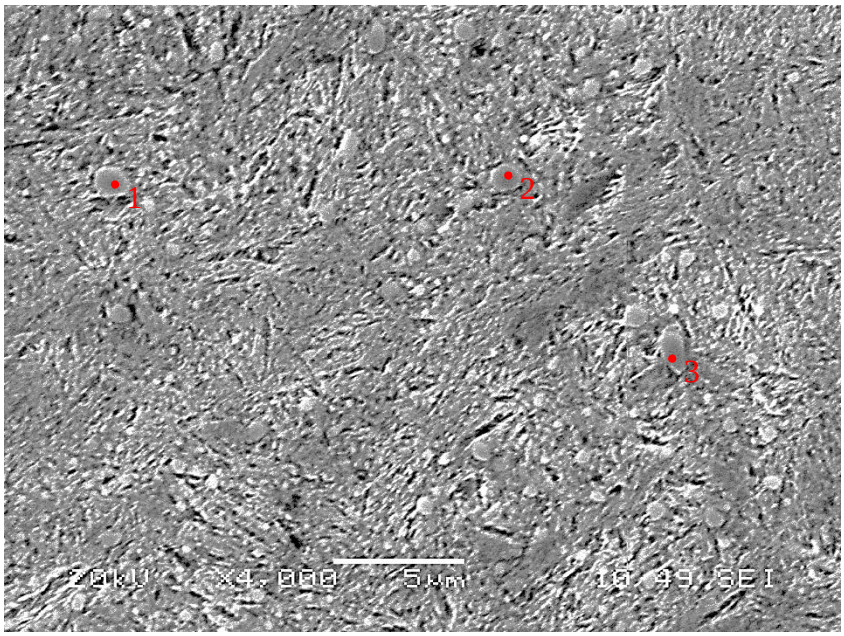

Spectrum/weight%	C	Cr	Fe	Comment
1	20.14	12.24	67.62	Cr/Fe enriched carbide
2	22.40	7.76	69.85	Cr/Fe enriched carbide
3	23.60	10.97	65.43	Cr/Fe enriched carbide

Figure 4.1.1-38 SEM image and EDS analysis of the spherical carbide particles in inner race

In summary, the microstructure of the inner race material consists of tempered martensite with fine dispersed spheroidised carbides present. The average hardness of the inner race material is 757.76 ± 19.17 HV0.05 which meets the minimum hardness requirements of 697 HV. Rolling contact fatigue damages macro-/micro-pitting has been observed in the entire raceway. Misalignment and non-metallic inclusion SiC are very likely to have contributed to the surface damage of the inner race observed by causing local stress concentration.

4.1.1.1.4 Outer race

The cylindrical rollers rotate on the outer ring raceway, making it possible for surface damage to occur in the outer race. Therefore, the outer ring raceway has been investigated in order to identify the root cause of failure of the bearing.

Initially visual observation was conducted on the outer race of the bearing being investigated. As indicated in Figure 4.1.1-39, micro-pitting, macro-pitting, separated shades and small indentations can be seen in the outer ring raceway. Compared with the shiny undamaged area, the micro-pitting area can be easily identified from its light grey colour, occupying more than one third of the total area of the outer race (Figure 4.1.1-39). As indicated in Figure 4.1.1-39 and more clearly in Figure 4.1.1-40, the relatively larger macro-pits occur along one edge of the micro-pitted area. In addition, several separated light brown and dark grey shades can be easily distinguished in the micro-pitted surface. Under closer observation, a large number of small indentations can be identified at the end of the micro-pitted area, as shown in Figure 4.1.1-39 and Figure 4.1.1-41.

Only about one third of the outer ring raceway surface is damaged. This suggests that the loading is unevenly distributed along the outer race, and the damaged region can be used as an indicator of the load distribution (load zone) of the bearing. The macro-pitting on one edge of the outer race proves the existence of severe angular misalignment in the bearing once again. It indicates misalignment is a critical issue which did affect the bearing under examination. The indentations found adjacent to the micro-pitted area could act as surface stress raisers, subsequently prompting the initiation and growth of micro-pits. These indentations were thought to have been caused by harder debris, suggesting that the cleanliness of the lubricant was poor (FAG, 2001). The light brown and dark grey shades, i.e. the raceway discolouration, were mainly a result of chemical reactions between the steel and the lubricant when the local

temperature exceeded 80 °C. These surface shades appear very frequently in the loading zone, having no negative effect on the bearing service life themselves (FAG, 2001). However, they give clues to local surface heating due to severe sliding friction between the rollers and the outer race, which could cause degradation of the properties of the lubricant and steel. However, the local surface temperature is unlikely to have been too high. Hence, the degradation effect was very likely limited since no steel deformation was observed inside the shadow area.

Figure 4.1.1-39 In the outer ring raceway, grey micro-pitted area (i.e. frosting), macro-pitting damage, separated light brown and dark grey shades, and small indentations were identified

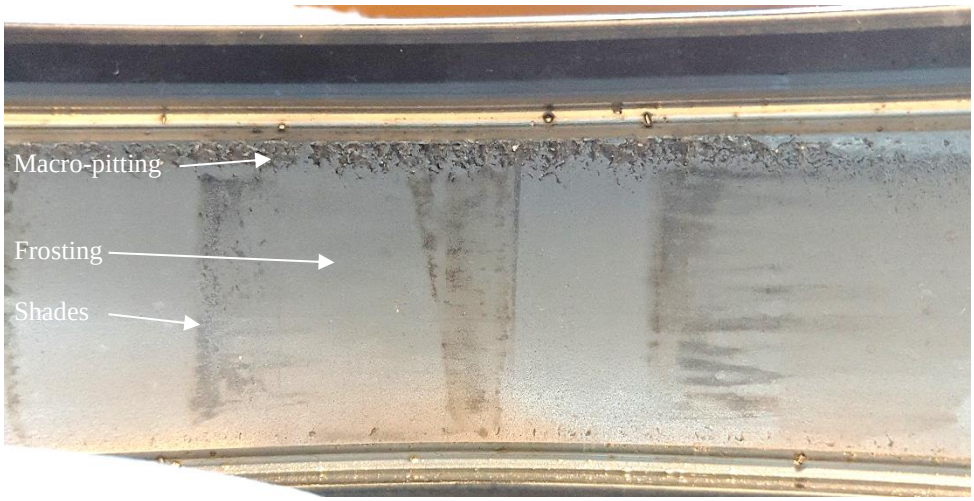

Figure 4.1.1-40 Closer observation of the main damaged area in the outer ring raceway

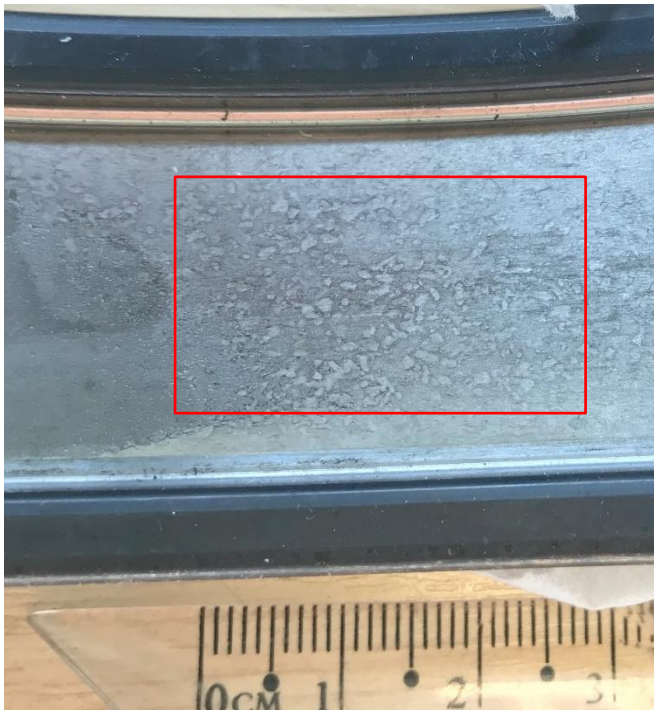

Figure 4.1.1-41 Closer observation of the small indentations by wear debris in the raceway, as framed

One section of the outer race was cut off from the main body for further examination as shown in Figure 4.1.1-42. The surface morphology of the damaged outer ring raceway observed under SEM is shown in Figure 4.1.1-43. It illustrates more clearly than visual checking that micro-pitting exists in the left end and in the middle of the raceway. Macro-pitting can be seen at the right end of the raceway. In the cross-section, a large number of elongated MnS and Al_2O_3+MnS inclusions were observed, as shown in Figure 4.1.1-44, Figure 4.1.1-45 and Figure 4.1.1-46. Almost every inclusion lies parallel to the raceway surface. The top MnS inclusion in Figure 4.1.1-44 is very close to the raceway surface and it connects with the micro-pit. It is very likely that the micro-crack initiated from this inclusion and subsequently the micro-pit formed. Other MnS inclusions in Figure 4.1.1-44, Figure 4.1.1-45 and Figure 4.1.1-46 are seen deeper from the surface of the outer race. Thus, deeper

MnS inclusions have no effect on the surface damage but can influence subsequent crack propagation.

The hardness profile of the outer race is shown in Figure 4.1.1-47. The hardness value is relatively constant from the raceway surface to a depth of up to 3 mm. Therefore, the outer race was very likely through hardened during manufacturing. The average hardness of the outer race material is 723.66 ± 11.36 HV0.05 which satisfies the hardness requirements of 60 Rockwell C (about 697 HV) (Erwin V Zaretsky, 2012).

The main phase of the outer race material was analysed using XRD as shown in Figure 4.1.1-48. The XRD analysis revealed peaks of α'-Fe phase without any clear peaks of any other phases.

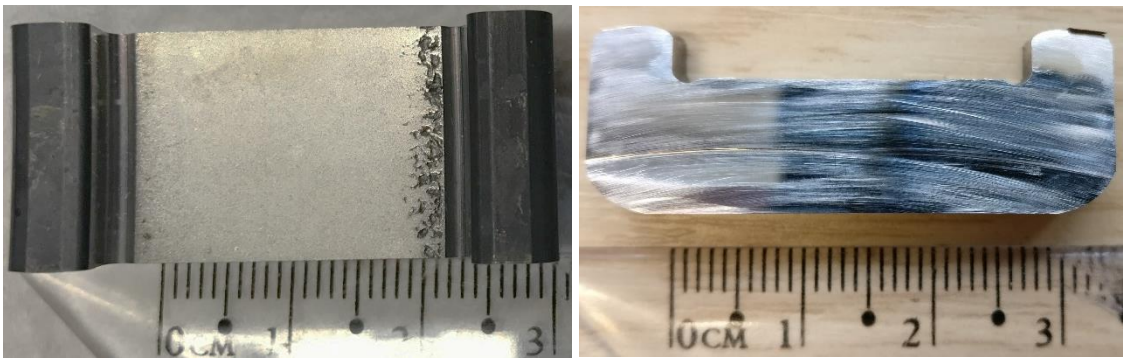

(a) (b)

Figure 4.1.1-42 (a) The outer ring raceway surface and (b) the cross section of a small piece cut from the outer race

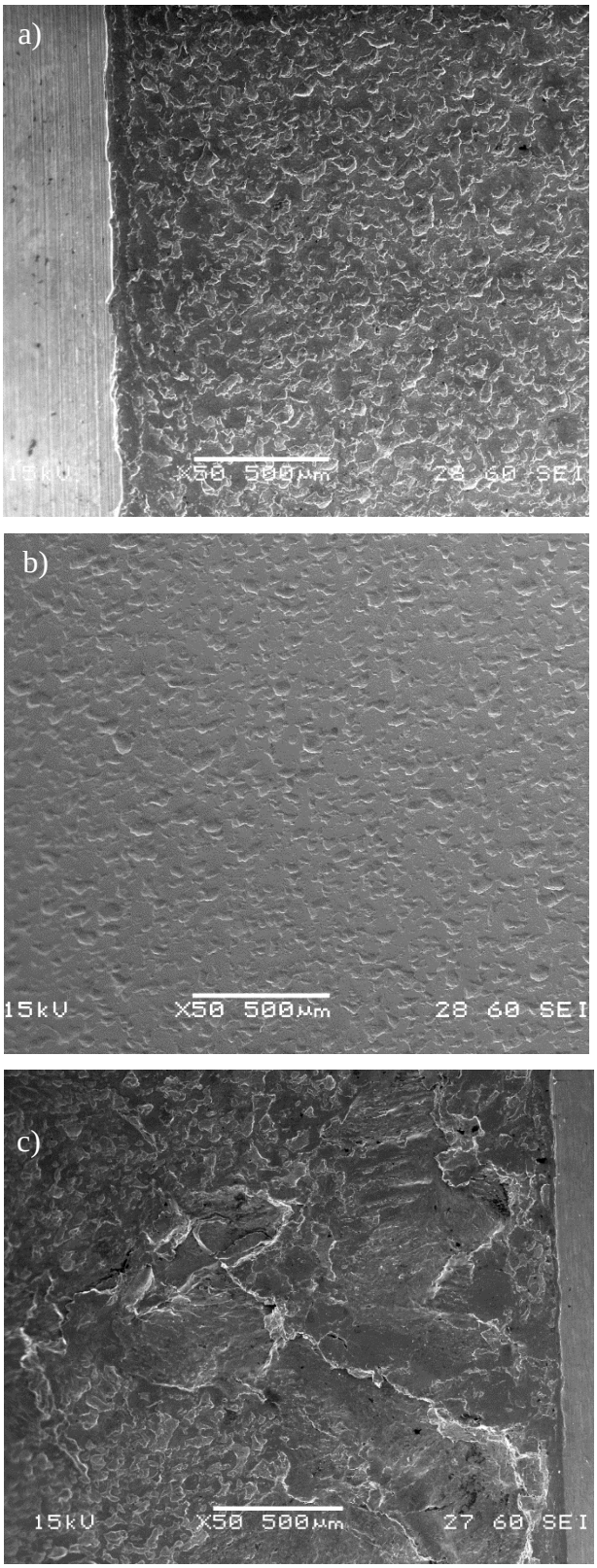

Figure 4.1.1-43 SEM images showing the surface damage of the outer ring raceway, a) micro-pitting in the left end of the raceway, b) also micro-pitting in the middle, and c) macro-pitting in the right end

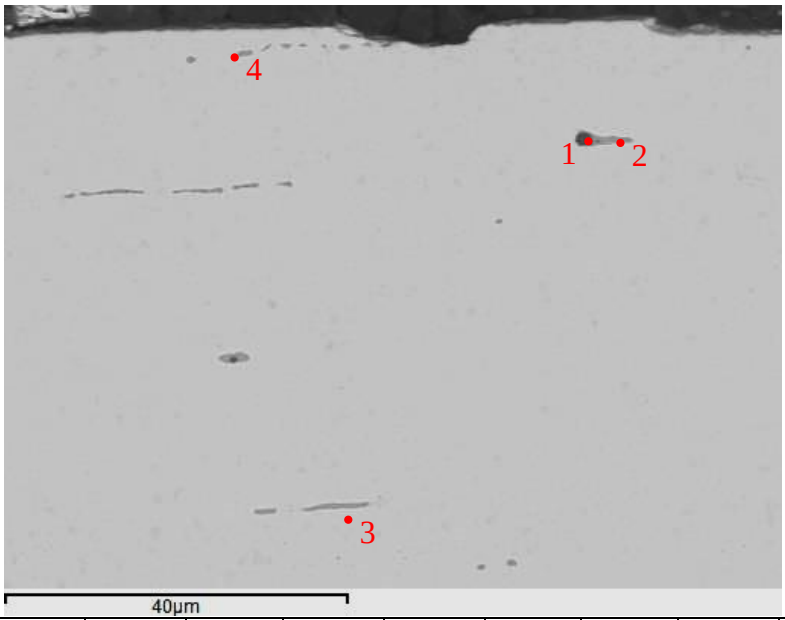

Spectrum (W%)	C	O	Mg	Al	S	Ca	Cr	Mn	Fe	Comment
1	5.87	21.76	1.81	51.60	6.00			5.98	6.98	Al_2O_3
2	2.78		1.49		26.39	1.50		49.39	18.46	MnS
3	2.36				20.55		0.94	47.25	28.89	MnS
4	3.15				21.11		1.74	46.90	27.10	MnS

Figure 4.1.1-44 Back-scattered-electron image of some inclusions and the EDS results indicating two stripe MnS inclusions and a coarse Al_2O_3 particle surrounded by MnS inclusion in outer race subsurface

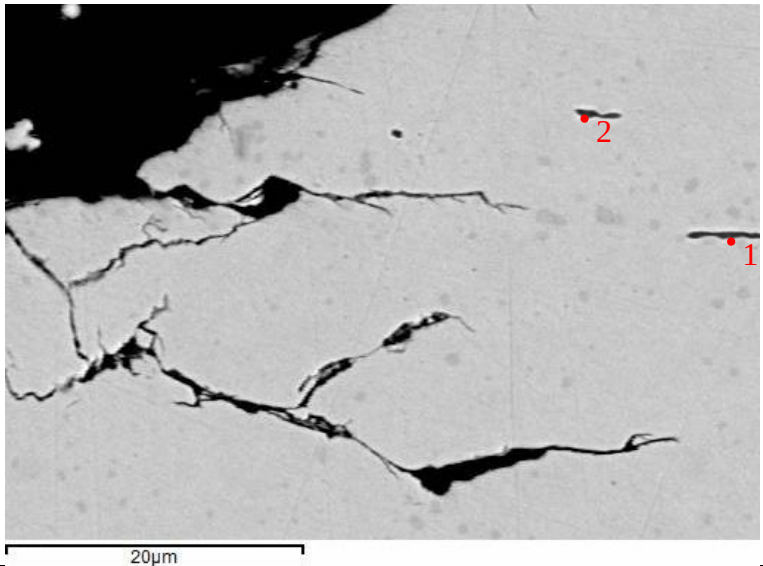

Spectrum (W%)	C	S	Cr	Mn	Fe	Comment
1	3.36	16.67	1.20	38.38	40.39	MnS
2	4.16	15.91	1.07	37.97	40.88	MnS

Figure 4.1.1-45 Back-scattered-electron image and the EDS results of two stripe MnS inclusion particles in outer race subsurface

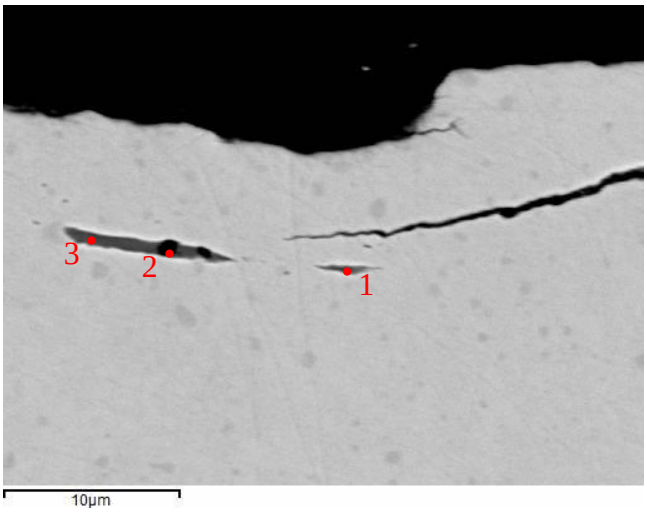

Spectrum (W%)	C	O	Al	S	Cr	Mn	Fe	Comment
1	2.73			8.82	1.11	23.94	63.39	MnS
2	3.89	8.04	20.71	14.85		30.47	22.04	Al_2O_3+MnS
3	3.20			23.94	1.07	50.50	31.29	MnS

Figure 4.1.1-46 Back-scattered-electron image and the EDS results of a stripe MnS inclusion and a coarse Al_2O_3 inclusion particle surrounded by a stripe MnS inclusion in outer race subsurface

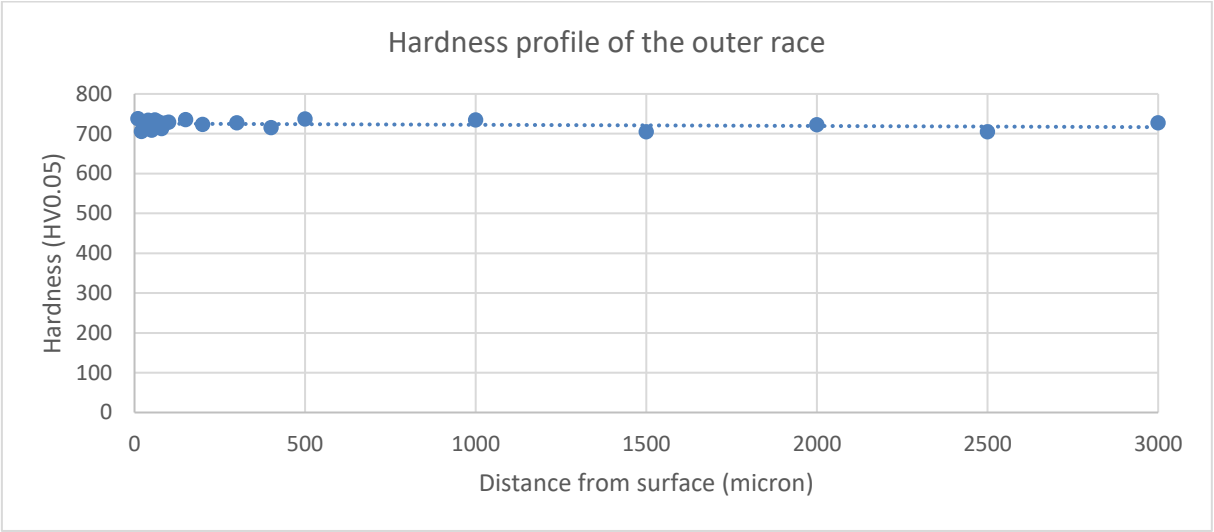

Figure 4.1.1-47 The hardness profile of the outer race suggesting the outer race is very likely through hardened. The average hardness of the outer race material is 723.66 ± 11.36 HV0.05

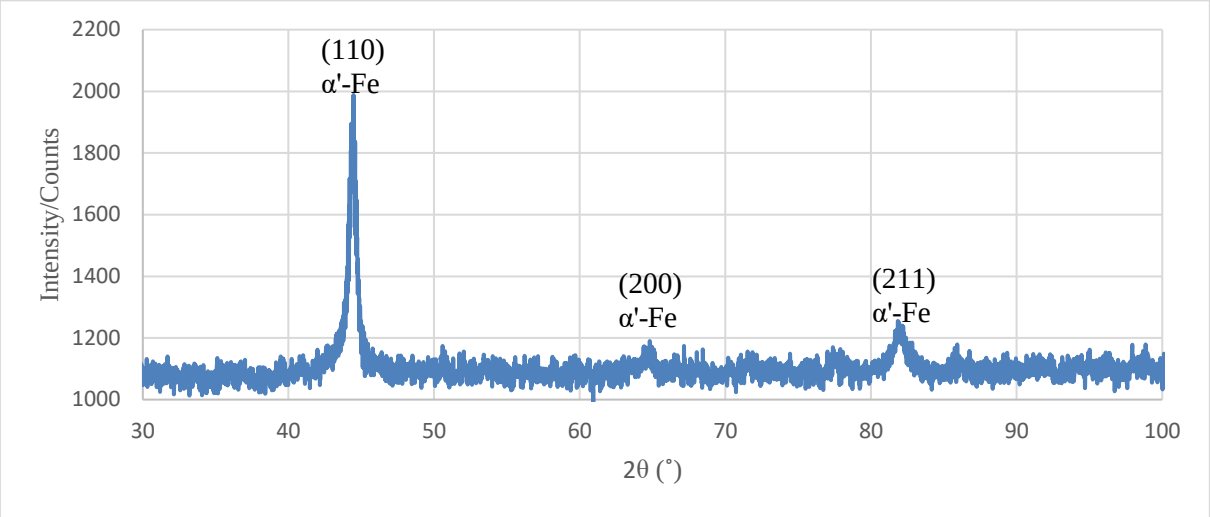

Figure 4.1.1-48 XRD pattern of the outer race steel showing the main phase is α'-Fe

Figure 4.1.1-49 shows the micrograph of the outer race section at a magnification of 500× after etching using nital. The microstructure observed appears to be that of tempered martensite with fine dispersed spheroidised carbides. This is similar to the microstructure observed in the rollers and inner race. The SEM micrographs of the etched sample and the EDS analysis (Figure 4.1.1-50) revealed that the spherical carbides dispersed in tempered martensite matrix are rich in Cr/Fe. The microstructure observed is in agreement with the measured micro-hardness values and the XRD analysis of the outer race. In addition to that, large amount of MnS inclusions were also observed in the etched sample (Figure 4.1.1-51), and some of the MnS inclusions are in conjunction with the carbides which were framed in the Figure 4.1.1-51.

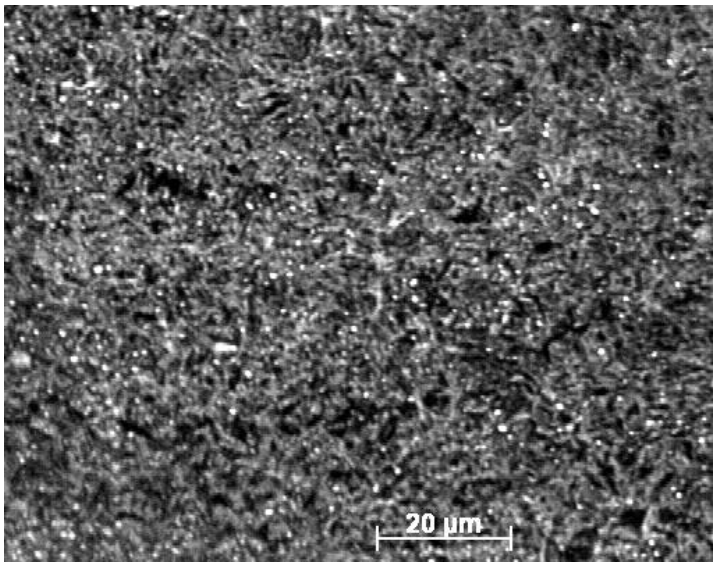

Figure 4.1.1-49 Metallography of the outer race microstructure, composed of tempered martensite and dispersed spheroidised fine carbides (2% natal, 500×)

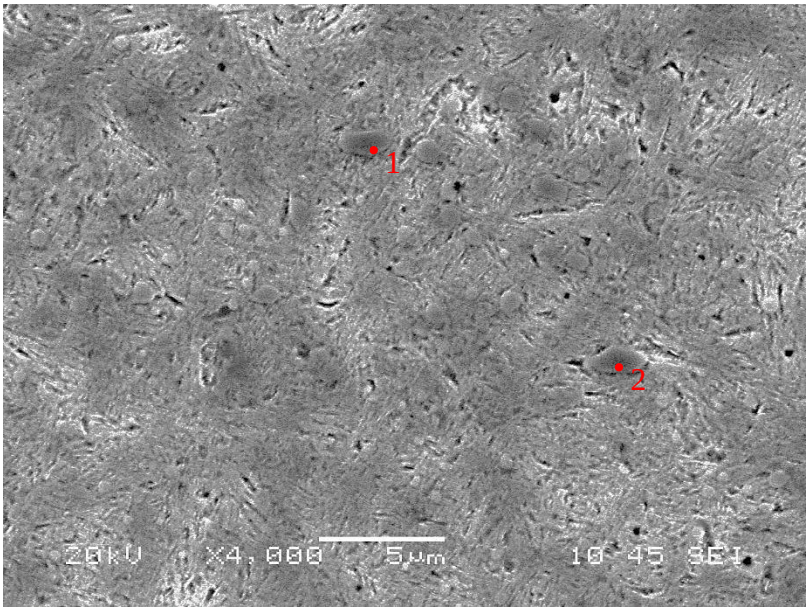

Spectrum/weight%	C	Cr	Fe	Comment
1	19.03	14.87	66.10	Cr/Fe enriched carbide
2	22.92	12.70	64.38	Cr/Fe enriched carbide

Figure 4.1.1-50 SEM image and EDS analysis of the spherical carbide particles in outer race

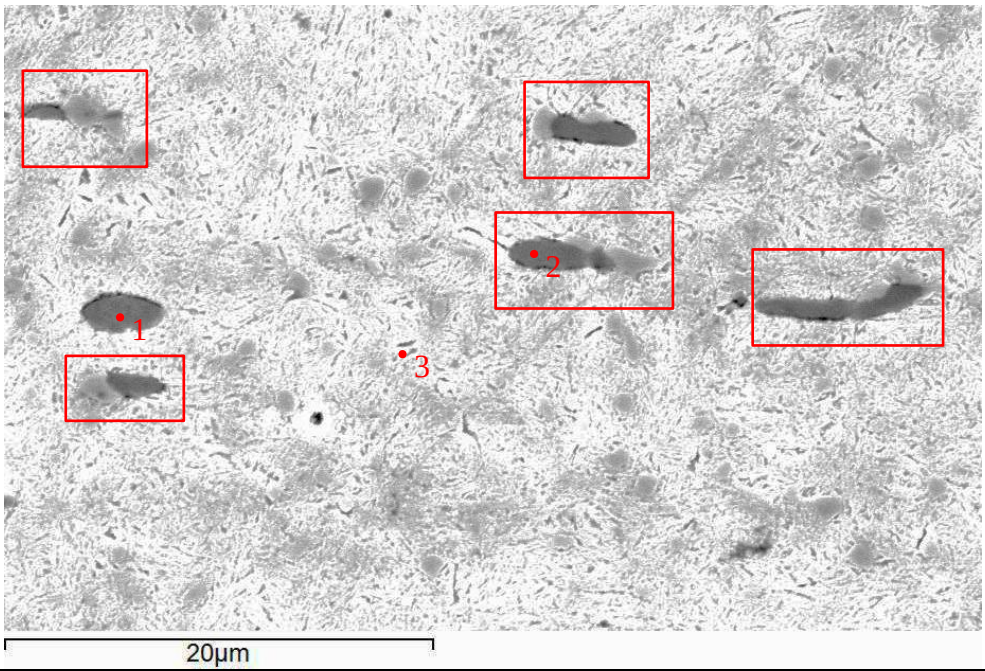

Spectrum/weight%	C	S	Cr	Mn	Fe	Comment
1	4.81	25.55	0.79	53.22	15.63	MnS
2	5.11	20.90	2.36	42.96	28.66	MnS
3	2.89		2.53	0.48	94.09	Matrix

Figure 4.1.1-51 SEM image and EDS analysis of the MnS particles in outer race, some carbides can also be seen. Some of the MnS inclusions are in conjunction with the carbides as framed

To sum up, the microstructure of the outer race material appears to be that of tempered martensite with fine dispersed spheroidised carbides. This is similar to the microstructure of the rollers and inner race. The average hardness of the outer race material is 723.66 ± 11.36 HV0.05 which satisfies the hardness requirements of 697 HV. Surface damage such as micro-pitting, macro-pitting, separated shades and small indentations were identified in the outer ring raceway. The observed surface damage was deemed to have been caused due to the combined effects of excessive contact stresses and stress concentration due to misalignment, the coarse MnS inclusions present, and lubrication variability.

4.1.1.1.5 Summary

The high-speed shaft bearing has been thoroughly observed and examined. It has been found that the bearing steels have been spheroidising annealed and through-hardened using quenching and low temperature tempering heat treatment. This resulted in a uniform microstructure of tempered martensite with dispersed fine carbides present in the matrix. The hardness of rollers, inner and outer race has been measured to be 706, 757 and 723 HV respectively in average, which is relatively low and just reaches the lowest hardness level of the bearing industry. Moreover, the roller hardness is lower than the race, but for the purpose of maximum bearing lifetime, roller hardness is expected to be up to 10 % higher than the race hardness (Michael J Neale, 1995).

The failure of this bearing has been caused by micro-pitting and macro-pitting. In addition, the inner/outer races and most of the rollers show more severe surface damage at one end side than the other one, which is clearly evidence of misalignment effects. Whenever the load is no longer evenly distributed over the full width of the bearing components, together with the coarse non-metallic inclusions close to the contacting surface and the indentations in the raceway surface, local stresses would rise substantially resulting in localised surface fatigue damage. The magnitude of the contact pressure has the greatest effect on micro-pitting initiation. In addition, roller skidding and lubricant contaminated by debris can induce further surface damage to accumulate. After the material starts flaking, an increase in radial clearance of the bearing can occur, further contributing to the failure of the whole bearing and possibly gears (Shuangwen Sheng, 2010). It also needs to be taken into account that, a great number of hard wear particles are embedded in the soft cage surface. These embedded wear particles cannot be removed by the lubricant, forming severe three-body wear leading to further acceleration of the surface damage rate to some extent.

Therefore, to increase the bearing service lifetime under much higher stress levels than expected caused by misalignment effects which can be difficult to avoid, improving the material hardness, steel cleanliness and lubrication quality can be helpful. Through-hardened steel could also be changed to case-hardened steel for their beneficial compressive residual stress. In addition, WC dispersed DLC coating (WC/a-C:H) could be adopted to increase the bearing's resistance to micro-pitting.

4.1.1.2 Examination of a spherical roller from planetary bearing

It is known that wind turbine gearbox failures frequently initiate from the planet bearings. Therefore, a damaged planetary bearing roller has been investigated to identify the causes of its failure.

The damaged large spherical roller retrieved from the planetary bearing at the low-speed stage of the gearbox was shown in Figure 4.1.1-52(a). Firstly, unaided visual inspection was carried out on the whole surface area of the spherical roller. The roller surface exhibited different surface finish, texture and colour from that of a freshly machined steel surface, due to unsteady rolling/sliding under high cyclic load conditions. According to the preliminary visual examination (Figure 4.1.1-52(b)), several discrete macro-pits of various sizes and mild adhesive wear area were observed, especially in the central area. Among the observed surface defects, big craters due to macro-pitting were deemed to be the main failure mode.

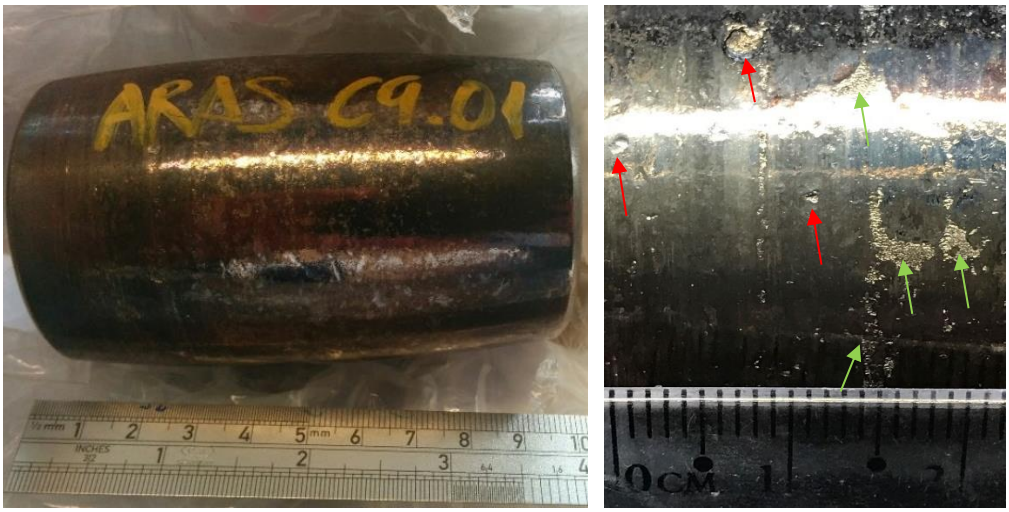

(a) (b)

Figure 4.1.1-52 Photos of the spherical roller, a) over look of the whole roller, and b) close look of the roller surface, discrete craters (red arrow) and mild adhesive wear area (green arrow) were identified

The SEM micrograph of one large crater is shown in Figure 4.1.1-53. The dimensions of the crater can be seen to exceed 3 mm × 3 mm. The dominant friction direction is indicated in the figure based on the position of leading-edge and the featheredge of the crater. The bottom of the large crater shown in Figure 4.1.1-54 is relatively smooth, implying brittle crack propagation.

Then the roller was cut-off through the big crater to check its cross-section. The cross-section of the big crater is shown in Figure 4.1.1-55, which indicates the big crater was composed of several small craters. The crack further left possibly initiated due to the stress concentration caused by the presence of the adjacent crater. The crack is very likely to cause fracture soon, causing further growth of the crater.

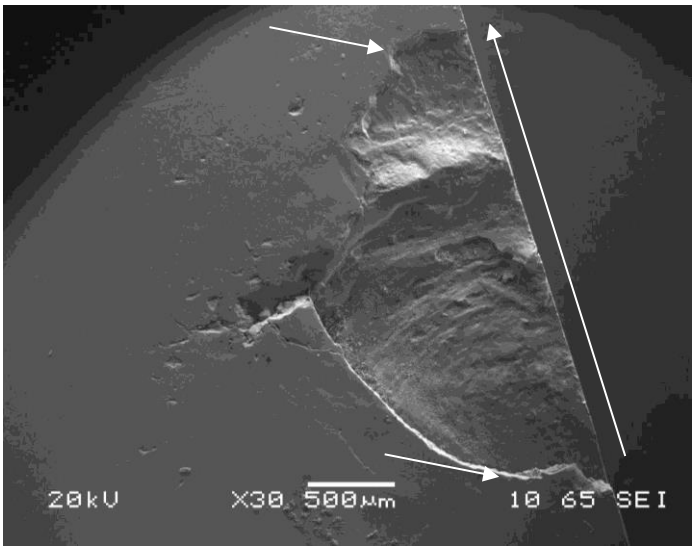

Figure 4.1.1-53 SEM image of the half big crater in spherical roller surface

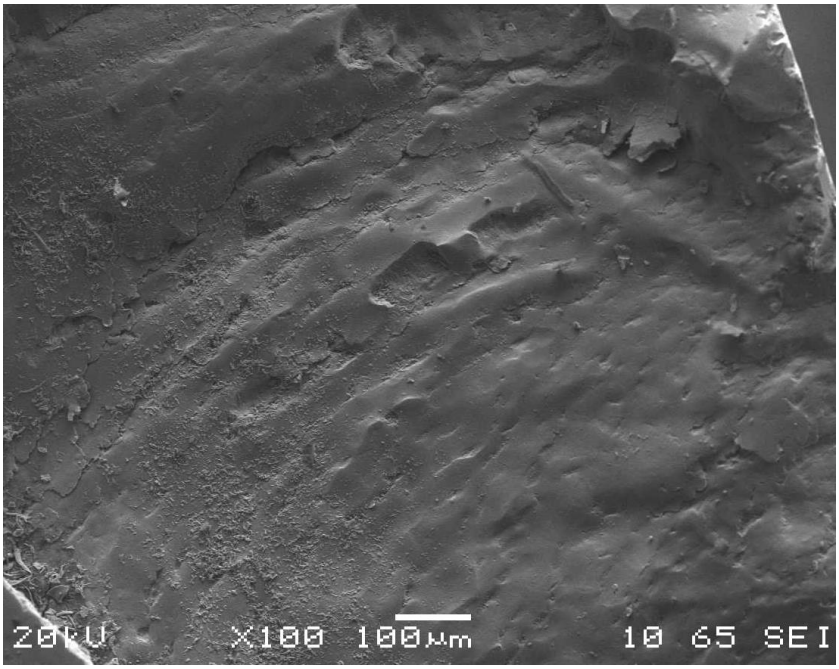

Figure 4.1.1-54 The floor of the big crater is smooth

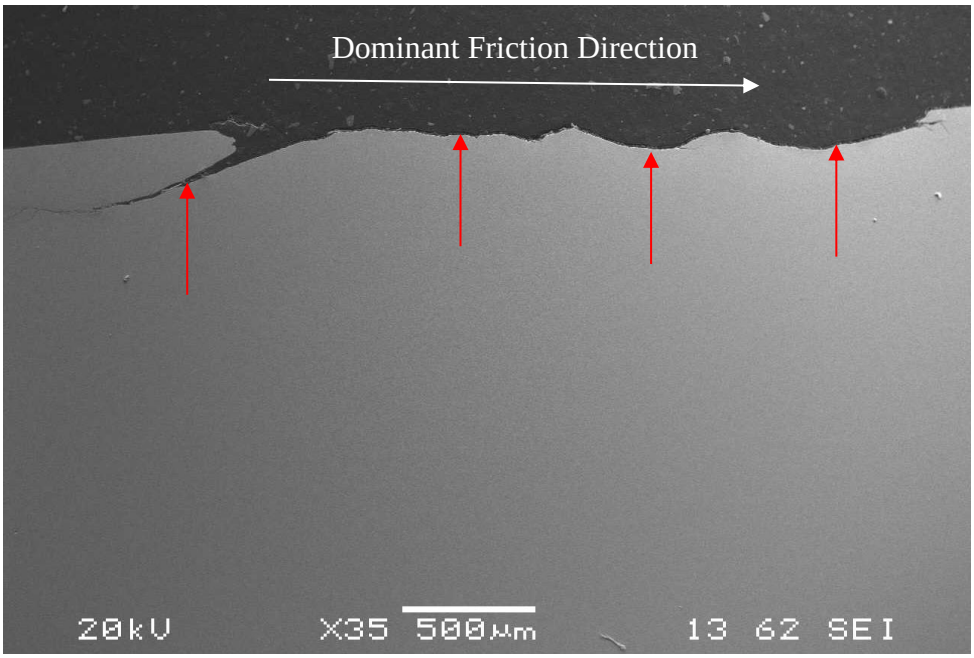

Figure 4.1.1-55 The cross section of the big crater in the roller surface, indicating it is composed of several small craters as arrowed

The EDS results of the roller material (Figure 4.1.1-56) indicate a high C steel alloyed with Cr, Mn and Si. The compositions measured by EDS are within the norms of commonly used bearing steel (Xiaolan Ai and Charles Moyer, 2001). In the back-scattered electron micrograph shown in Figure 4.1.1-57, fine well-dispersed spheroidised carbides (spheroidite) were observed, meaning the spherical roller has been spheroidising annealed. No non-metallic inclusions were observed, meaning that the cleanliness of the roller material is high. In the SEM micrograph of the etched roller material shown Figure 4.1.1-58, a microstructure consisting of tempered martensite and spheroidised carbides can be clearly observed. The XRD pattern of the roller material (Figure 4.1.1-59) only shows peaks of α'-Fe phase arising from the martensite present. From the hardness-depth profile of the roller cross-section (Figure 4.1.1-60), it can be concluded that the roller material has been through-hardened using quenching and tempering heat treatment processing. The hardness is constant from surface to

core, with an average value of 784.26±23.69 HV0.05. The average hardness value measured is within the limits set by the ISO hardness requirements of 60 Rockwell C (about 697 HV).

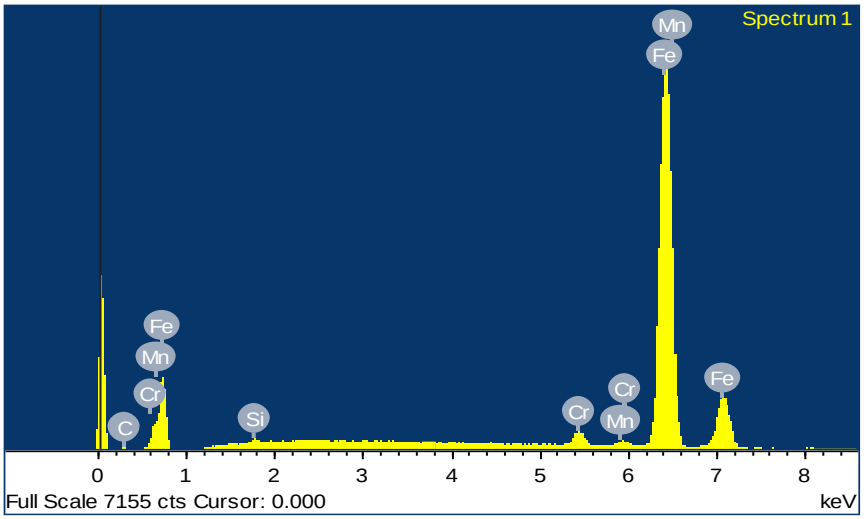

C	Si	Cr	Mn	Fe
1.72	0.25	1.85	0.75	95.43

Figure 4.1.1-56 EDS results of the roller material

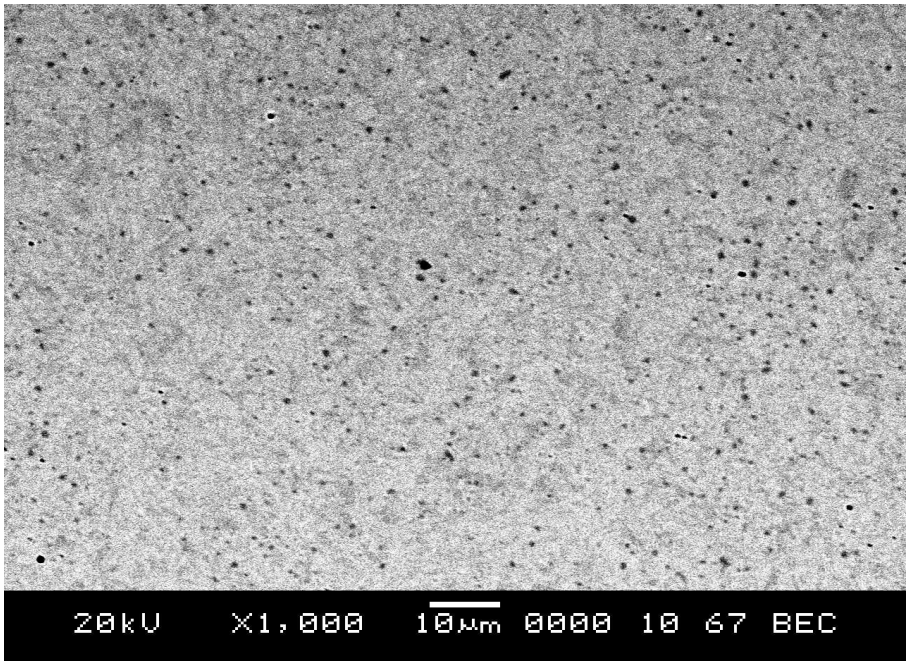

Figure 4.1.1-57 Back-scatted-electron image of the roller material

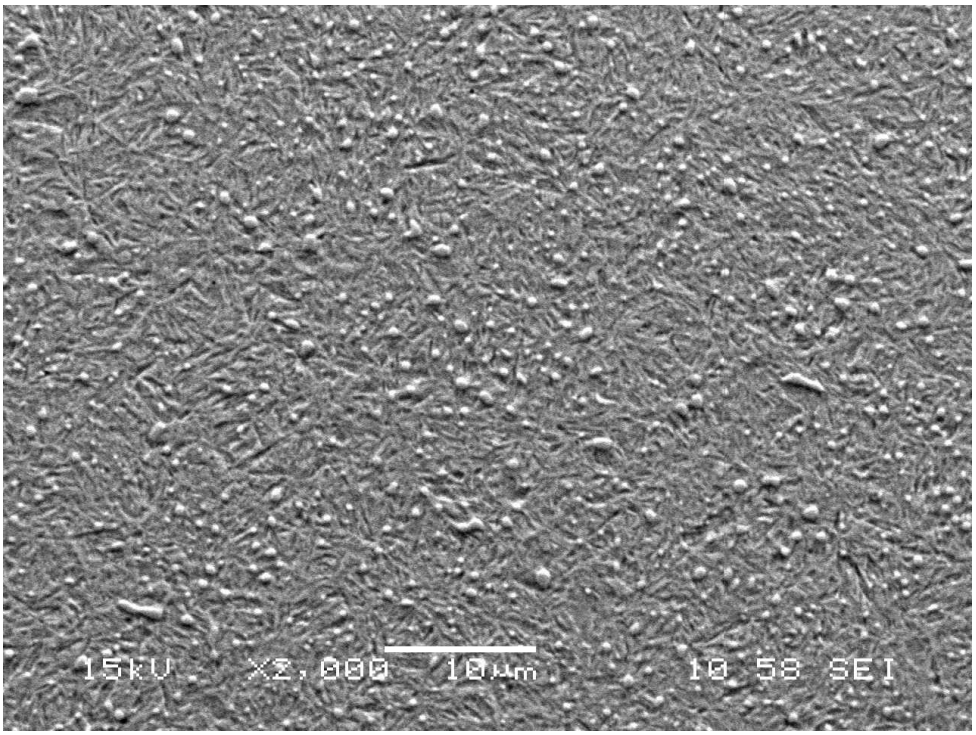

Figure 4.1.1-58 SEM image of the etched roller material, indicating tempered martensite and dispersed spheroidised fine carbide

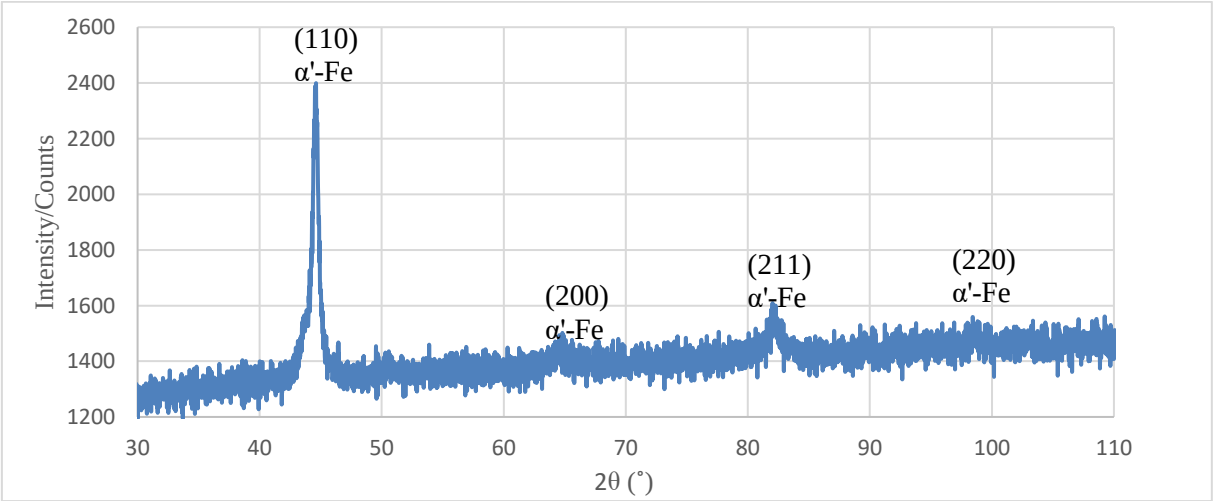

Figure 4.1.1-59 XRD pattern of the big spherical roller

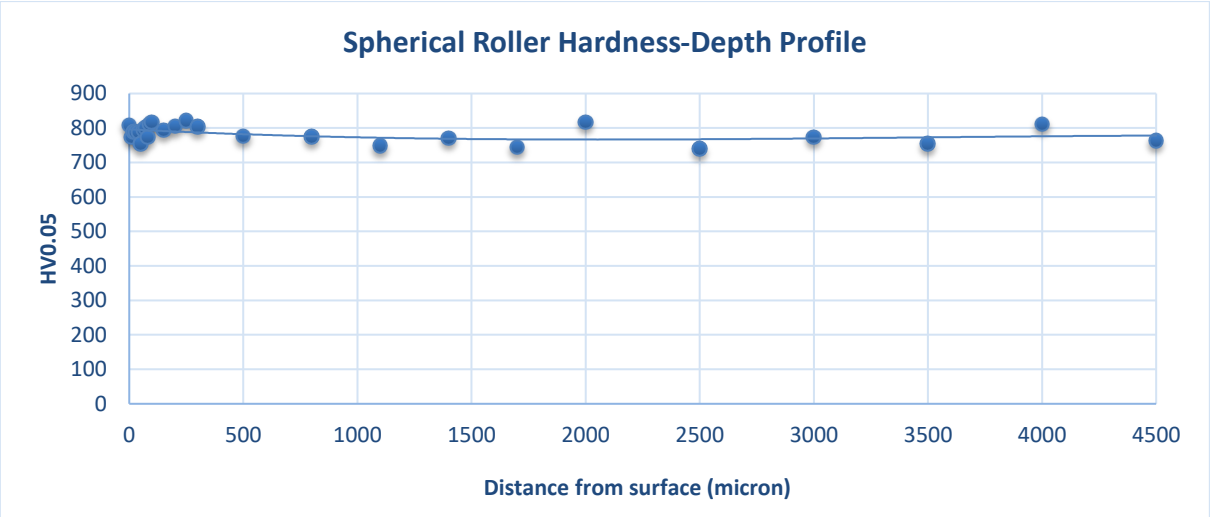

Figure 4.1.1-60 Hardness-depth profile of the spherical roller from low-speed planetary gear bearing showing the average value of 784.26±23.69 HV0.05.

In summary, the roller steel has been spheroidising annealed and through-hardened using quenching and low temperature tempering resulting in a uniform microstructure of tempered martensite with dispersed fine carbides. The main failure mode has been due to macro-pitting, one form of rolling contact fatigue. This low-speed bearing is difficult to generate sufficient lubricant film thickness even with the use of high viscosity lubricant. Hence the combination of low rotational speed and high fluctuating loads can generate high contact stress and cause initiation of surface damage, especially when accompanied by sliding movements (Michael N Kotzalas and Gary L Doll, 2010). The through-hardened roller could be changed for a case-hardened one due to their beneficial compressive residual stress resulting in retardation of crack propagation. In addition, WC dispersed DLC coating (WC/a-C:H) with low friction coefficient could be adopted to increase the bearing's resistance to rolling contact fatigue and wear.

4.1.2 High-speed and intermediate stage gear teeth and debris from low-speed stage

Gear tooth damage is one of the common factors leading to gearbox failure. Gear damage occurs in all speed-up stages of a wind turbine gearbox. Therefore, three fractured gear teeth from the high-speed stage gear and five from intermediate stage gear were retrieved from the field for root cause analysis. In addition, some debris retrieved from the low-speed stage was considered.

According to the information made available it is known that the ring wheel was manufactured from 31CrMoV9 alloy, the low speed shaft from 42CrMo4 alloy. All other gears were made of 18CrNiMo7-6 carburising steel. The chemical composition of 18CrNiMo7-6 is summarised in Table 4.1-1. 18CrNiMo7-6 generally supplied in annealed condition with a hardness around 240 HV (S&T-Stainless, 2014).

Table 4.1-1 The chemical composition of 18CrNiMo7-6 (T. Ohji et al., 2016)

Analysis composition %		C	Si	Mn	P	S	Cr	Mo	Ni
18CrNiMo7-6	min.	0.15	-	0.50	-	-	1.50	0.25	1.40
	max.	0.21	0.40	0.90	0.025	0.035	1.80	0.35	1.70

4.1.2.1 The gear teeth from the high-speed stage

Gear tooth fracture of high-speed gears is common due to the high mesh frequency and stresses sustained. Three fractured gear teeth from the gears of the high-speed stage of the gearbox were retrieved from the field as shown in Figure 4.1.2-1. It is known that they have been manufactured from 18CrNiMo7-6 carburising steel. The failure modes of all the three teeth are micro-pitting, destructive wear and final tooth fracture.

The morphology of the contact surface of the damaged gear tooth is shown in Figure 4.1.2-2, containing information related to its failure. Firstly, a large crack was found at the dedendum (root of tooth) area. The shape of the crack suggests that the fracture developed from left to

right, which possibly indicates that the tooth was under left-side positioned loading. Thus the bending stress on the left is higher than right (S Pehan et al., 2006). Secondly, large area of the tooth material on the left was excessively worn and a concave surface has formed. The material volumetric loss decreases from left to right, indicating that the contact stresses on the left were higher than right. This may also imply a left-side positioned loading. Both bending stresses and contact stresses on the left side of the gear tooth are higher than the right, meaning an angular misalignment existed in the gear pair. Thirdly, micro-pits were observed in the gear contact surface.

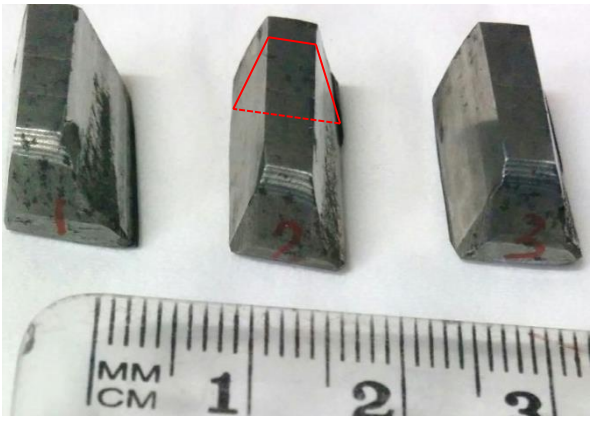

Figure 4.1.2-1 The three gear teeth from the high-speed gear

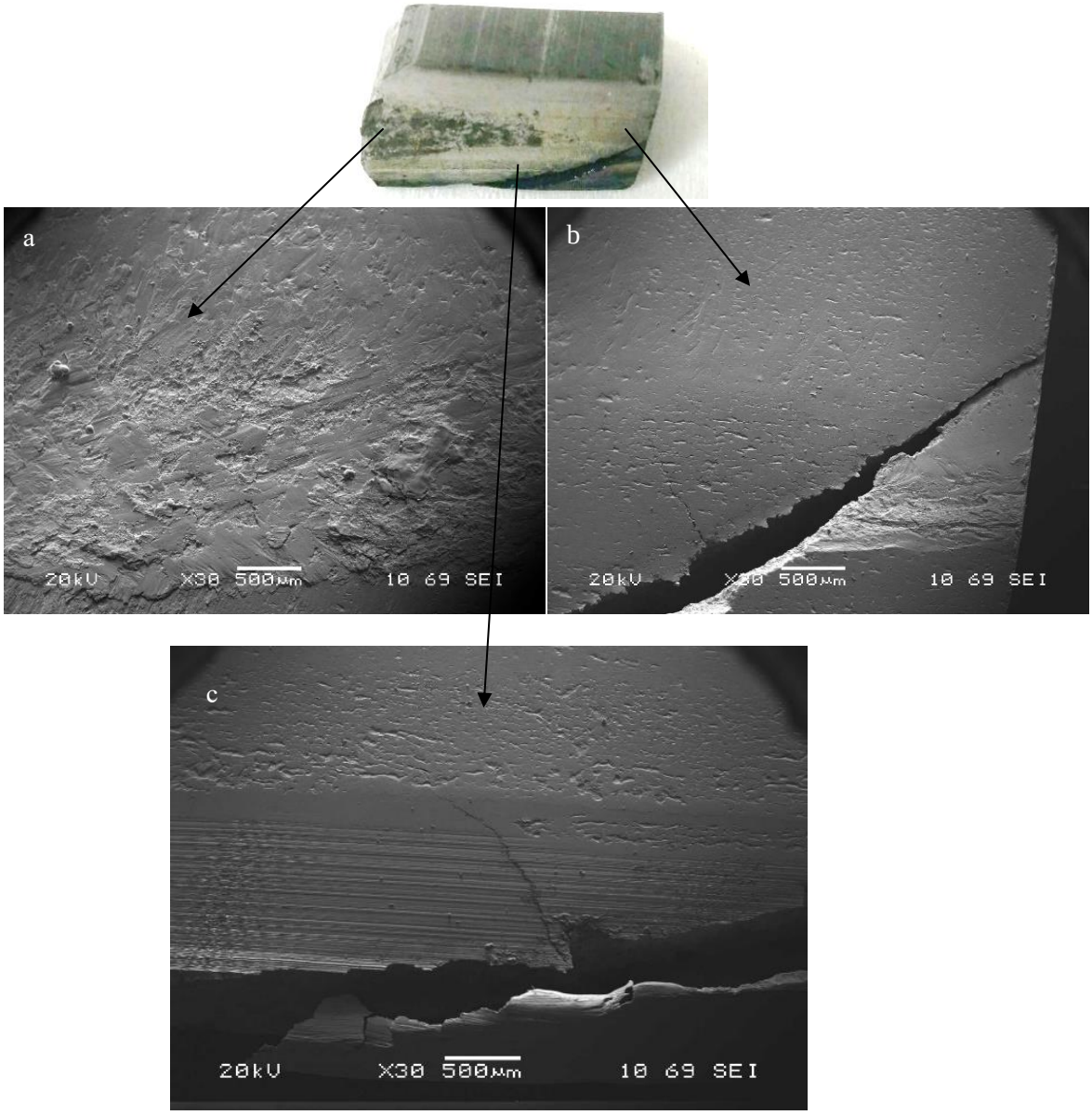

Figure 4.1.2-2 Surface morphology of the damaged contact surface of the gear tooth, showing severe scuffing, micro-pitting and cracking

In order to characterise the gear material and get more information of the gear tooth failure, the tooth was cut through the red lines as shown in Figure 4.1.2-1. From the hardness-depth profile obtained by hardness test on the tooth cross section (Figure 4.1.2-3), the superficial hardness of the gear tooth is around 750 HV0.05, then the hardness decreases with the increase of depth, until it reaches a core hardness value which is around 490 HV0.05. It is

obvious that the gear material was case-hardened and that the core hardness was also improved. The case depth reaches as deep as about 2,000 μm.

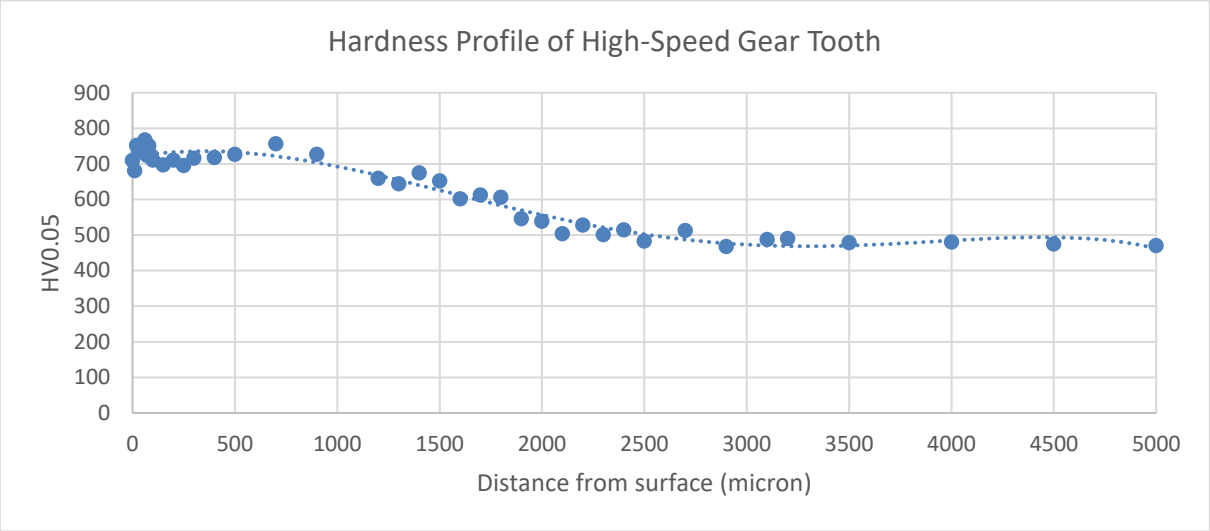

Figure 4.1.2-3 Hardness-depth profile of the gear tooth from high-speed stage showing the superficial hardness of the gear tooth is around 750 HV0.05, and the core hardness value is around 490 HV0.05.

In the XRD pattern of the high-speed tooth material shown in Figure 4.1.2-4, only the peaks of α'-Fe phase were observed. No peaks associated with undesirable residual austenite (γ-Fe) were found.

The micrograph of the microstructure of the gear teeth material after being etched with 2% nital is shown in Figure 4.1.2-5. It can be seen that the subsurface area is dominated by high-C martensite, with some inclusions also being present. In the core area, the microstructure is dominated by low-C martensite, also containing some inclusions and ferrite. No visible cementite was observed. All the characterisation results were in accordance with the most widely adopted treatment process for gearbox gears, which is carburising, then quenching and low-temperature tempering (Gerald D Lindell et al., 2002, Peng Fu et al., 2013). After carburising and quenching, the gear can obtain a hard surface and tough interior core, possessing high wear resistance on surface and good fracture toughness inside simultaneously.

Also, expansion caused by martensitic transformation at surface happening later than interior due to C content variance, could introduce a compressive residual stress field on the subsurface area which is desirable for good fatigue performance. The effect of low-temperature tempering is to release the undesirable internal thermal stress caused by quenching, and to make the residual austenite transform to martensite (H.S. Bawa, 2004, R.A. Higgins and W. Bolton, 2010).

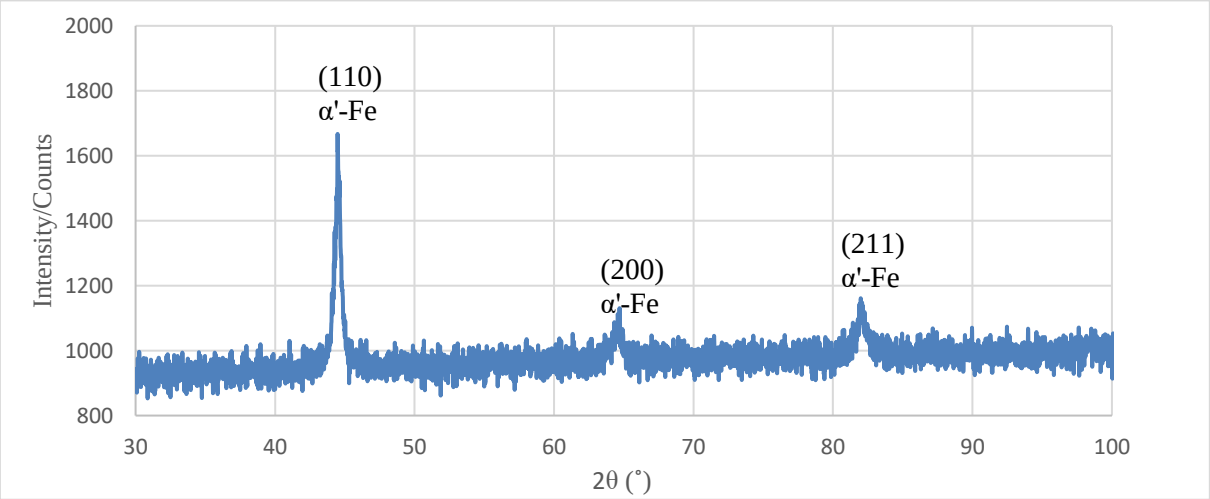

Figure 4.1.2-4 XRD pattern showing the main phase of the gear teeth from the high-speed stage

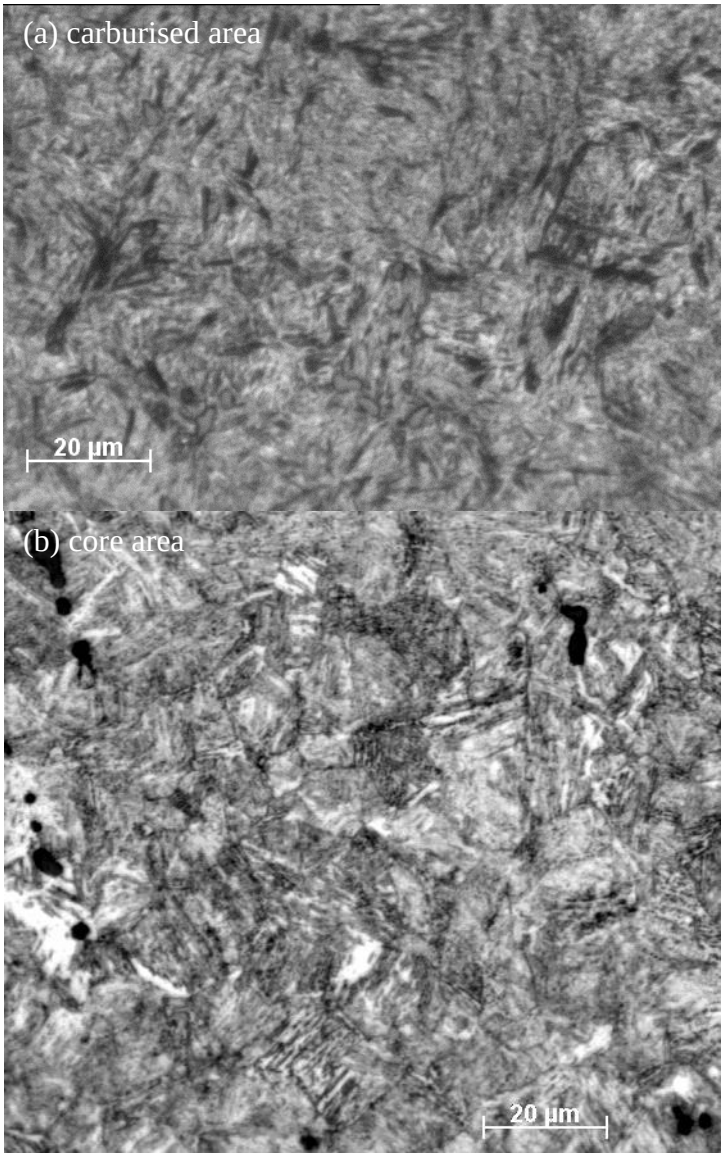

Figure 4.1.2-5 Metallography of high-speed gear teeth, (a) the sub-surface, and (b) the core (2% natal, 500×)

The initial damage mode of the high-speed gear teeth is micro-pitting. Micro-pitting is not harmful to a gear directly, since it does not affect the meshing of gear pair. However, micro-pitting could stimulate or be a precursor of more extensive surface damage such as macro-pitting and severe wear. Thus, changes in the tooth profile can reduce the durability of the gears. SEM micrographs of some micro-pitting-related cracks observed in the tooth surface are shown in Figure 4.1.2-6. The direction of all micro-cracks is identical. Their depth can be

seen to be up to 10 μm. Most micro-pitting cracks are thought to have initiated at the surface. The formation of some other micro-cracks has been related to the presence of MnS inclusions in the surface or subsurface of the sample. For instance, as shown in Figure 4.1.2-7, one coarse MnS particle was found in the micro-pitting crack. In the vicinity of the crack, another MnS particle with larger size was also observed, which may easily cause enlargement of the local crack. The number of MnS inclusions in the gear material is so high that many of them are close to the gear surface, some even exposed to the surface as seen in Figure 4.1.2-8. The high number of coarse MnS inclusions in steel can improve machinability, but they are harmful to the strength and homogeneity of the material.

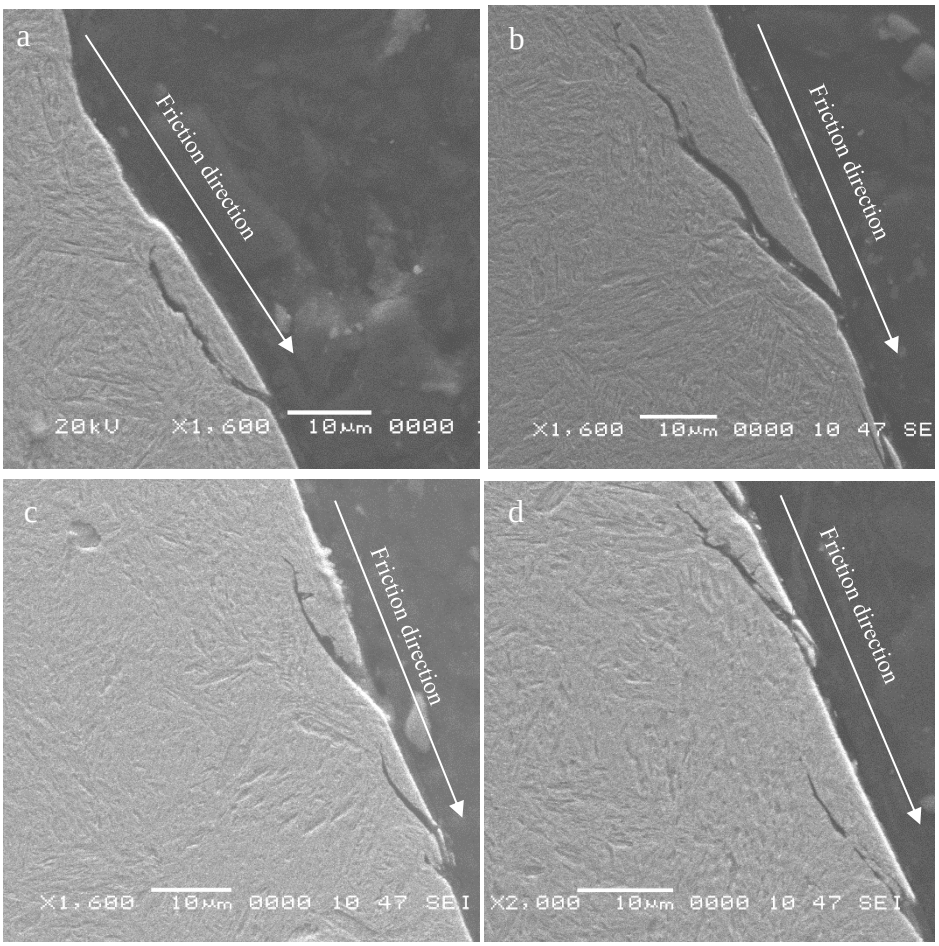

Figure 4.1.2-6 Cross section of the micro-pitting cracks in the high-speed gear tooth

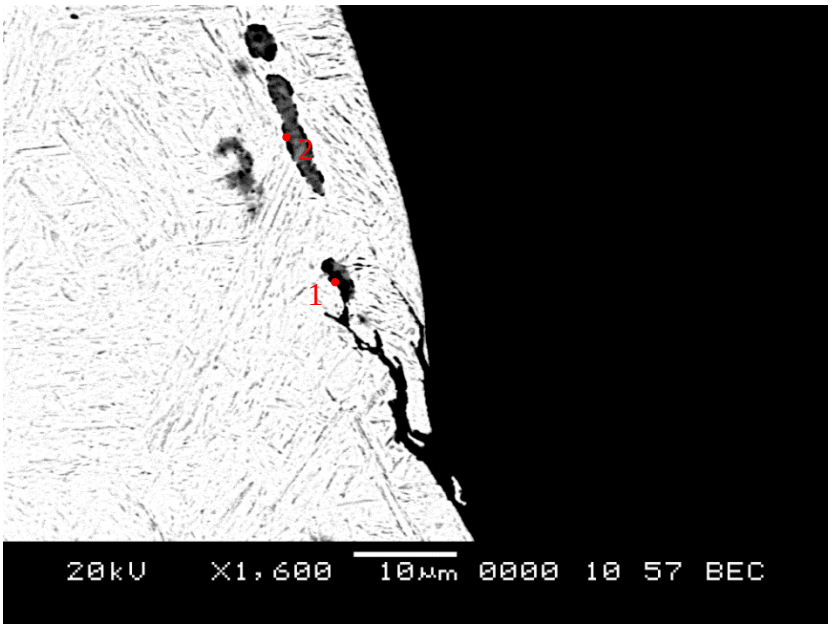

Spectrum (wt%)	C	S	Cr	Mn	Fe	Comment
1	8.91	24.33	0.61	41.97	24.17	MnS
2	4.02	31.22		53.31	11.46	MnS

Figure 4.1.2-7 One MnS particle was observed in the crack, and another in the vicinity of the crack

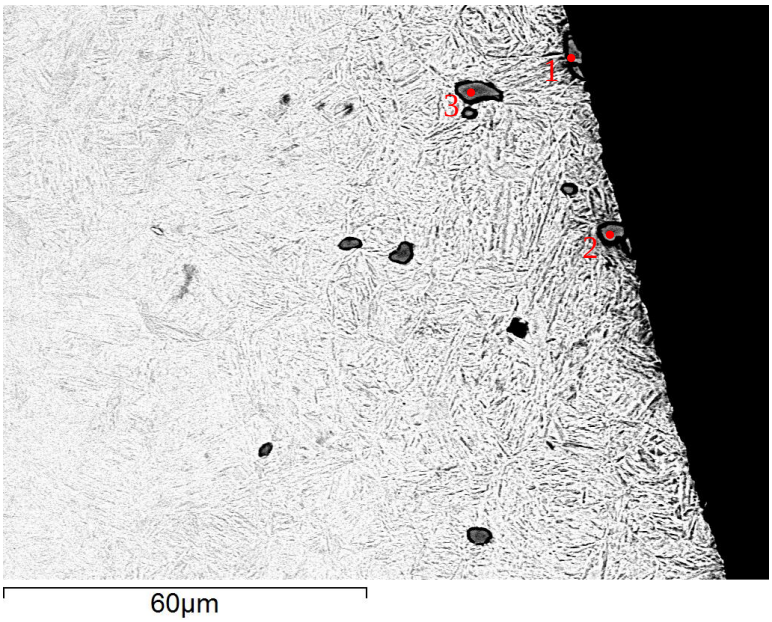

Spectrum (wt%)	C	S	Mn	Fe	Comment
1	22.90	30.97	44.22	1.91	MnS
2	16.15	32.75	46.80	4.30	MnS
3	10.64	34.98	50.48	3.90	MnS

Figure 4.1.2-8 Two MnS particles were observed in the contact surface, also many in the subsurface area

The second failure mode is partially attributed to excessive wear. The surface morphology of the concave surface due to destructive wear is shown in Figure 4.1.2-9, illustrating the wear mode is severe adhesive wear. When lubrication has failed, adhesive wear occurs in the metal-to-metal contacted meshing gear pair due to the combination of adhesion force, normal contact pressure and frictional shear stress. Adhesion results from attractive atomic forces between the real contact regions (i.e. the contacting asperities on surface) of two friction bodies, which 'weld' the contacting asperities together. Enough normal contact pressure and frictional shear stress could strengthen the local material of contacting asperities through plastic deformation, increasing the area of the asperity junction (G. Stachowiak and A.W. Batchelor, 2013). Then the movement of the gear pair would tear the 'welded' and cold worked asperity material away from the main body leading to rapid material removal from the tooth surface. The gear pair in the high-speed stage of wind turbine gearbox is prone to severe adhesive wear. This is due to the fact that the gear pair is made of same material and the operating conditions involve high rotational speed and heave loads which can result in large plastic deformation, high surface temperature and large adhesive area (Shizhu Wen and Ping Huang, 2012). Furthermore, adhesive wear selectively occurs in the area where contact pressure is high (normally around the pitch line), and also at the tip and root of the gear tooth where sliding velocities are high (Rexnord-Industries, 1978). Excessive and destructive adhesive wear that has caused changes in the tooth profile impairs the smooth meshing action of gears, increases vibration and can eventually lead to tooth fracture (Rexnord-Industries, 1978, NOVEXA, 2017). In order to prevent destructive adhesive wear and secondary tooth fracture, gear surface hardness and lubrication need to be further improved (G. Stachowiak and A.W. Batchelor, 2013). The friction force between the gears of a pair also needs to be decreased whilst the contact pressure should also be reduced.

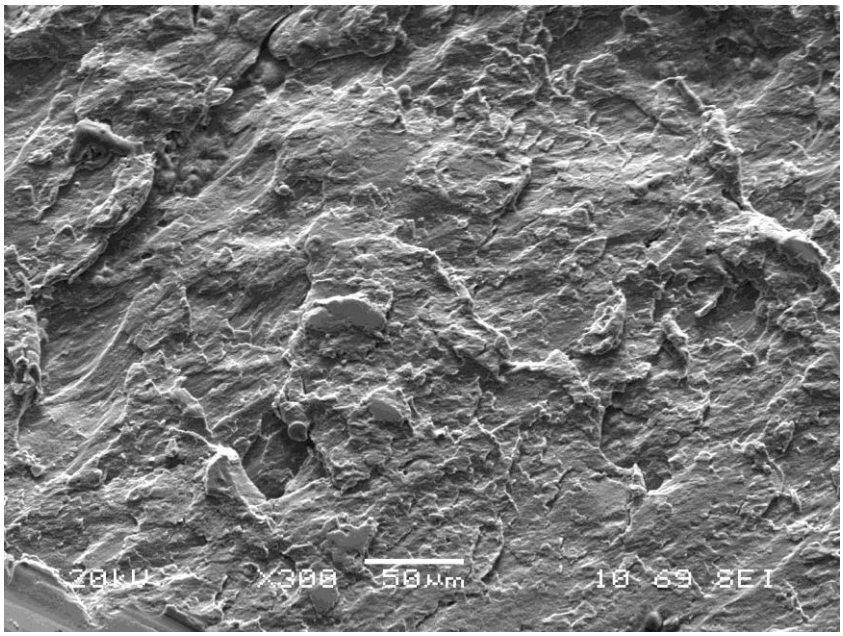

Figure 4.1.2-9 Surface morphology of the concaved surface

The third type of failure of gear teeth is tooth fracture. Gear tooth fracture is thought to be related to misalignment effects, coarse MnS inclusions, micro-pitting and excessive wear. Figure 4.1.2-10 shows the SEM micrograph of the obtained cross-section of the cracked area. Due to the severe deformation and possible loss of the material in the outer section of the cracked area, little information can be obtained. However, in the deeper section of the cracked area as shown in Figure 4.1.2-10, where crack has reached its maximum depth and material deformation is limited, valuable clues can be found. The framed area shown in Figure 4.1.2-10 was observed under higher magnification using back-scattered electron microscopy. As indicated in the back-scattered electron micrograph shown in Figure 4.1.2-11, four inclusions can be identified along the crack path, easily seen due to the colour contrast with respect to the bright surrounding matrix material. From the EDS results, it has been ascertained that these inclusions are MnS. MnS inclusions exhibit low hardness making them much softer than the matrix material. MnS inclusions may act as the crack initiation points (L. de Campos

Franceschini Canale, 2008). It is worth noticing that the crack propagation followed the path along these inclusions. It is likely that the soft MnS inclusion caused stress concentration, weakening the local strength of the material. As a result, the crack was prompted to grow along these weaker MnS inclusions. MnS inclusions were also observed in other sections of the cracked area in the gear tooth, as indicated in Figure 4.1.2-12. The propagation of cracks along the soft MnS inclusions has been successfully simulated in section 4.2.2 (as shown in Figure 4.2.2-2). Therefore, the effect of MnS inclusions on the gear teeth bending fracture need to be taken into consideration, especially when the size of MnS particles is coarse and their number present in the matrix is high (as shown in Figure 4.1.2-13).

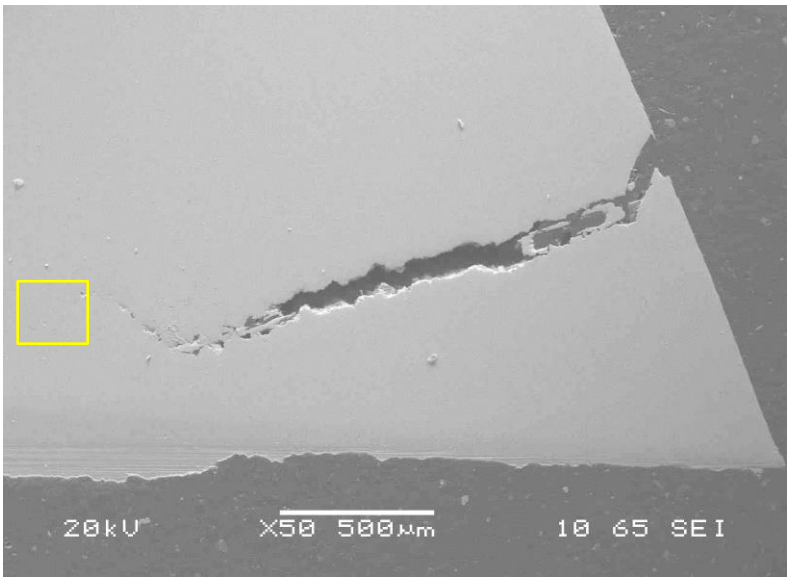

Figure 4.1.2-10 Cross section of the big crack in the high-speed gear tooth

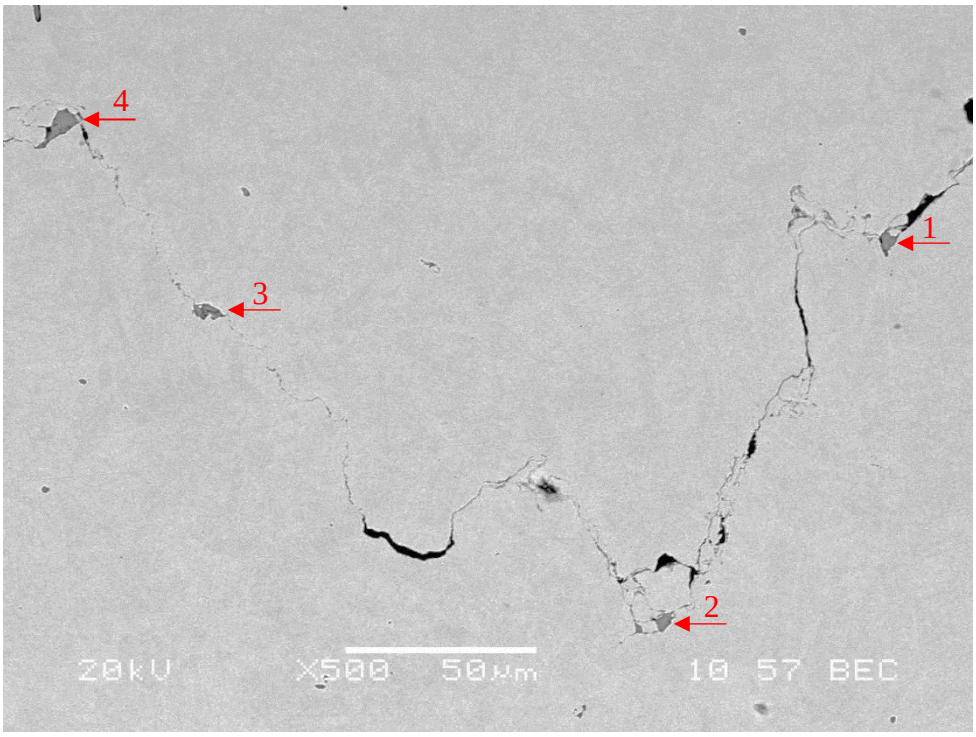

Spectrum/wt%	C	S	Cr	Mn	Fe	Comment
1	8.19	26.45	0.31	51.63	13.43	MnS
2	5.62	27.48	0.34	54.53	12.02	MnS
3	7.03	23.66	0.44	48.24	20.62	MnS
4	6.05	32.14		60.06	1.75	MnS

Figure 4.1.2-11 SEM/EDS results of inclusions in the end of the big crack, indicating the crack propagated along the soft MnS inclusions. This phenomenon has been successfully simulated in section 4.2.2 (as shown in Figure 4.2.2-2).

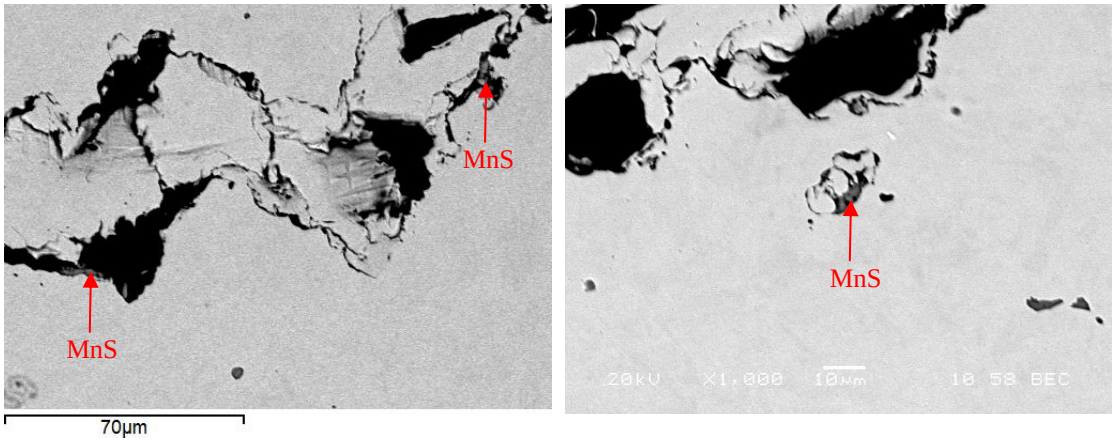

(a) (b)

Figure 4.1.2-12 MnS inclusions were also observed under SEM and proved by EDS, as arrowed, in other sections of the big crack in the gear tooth

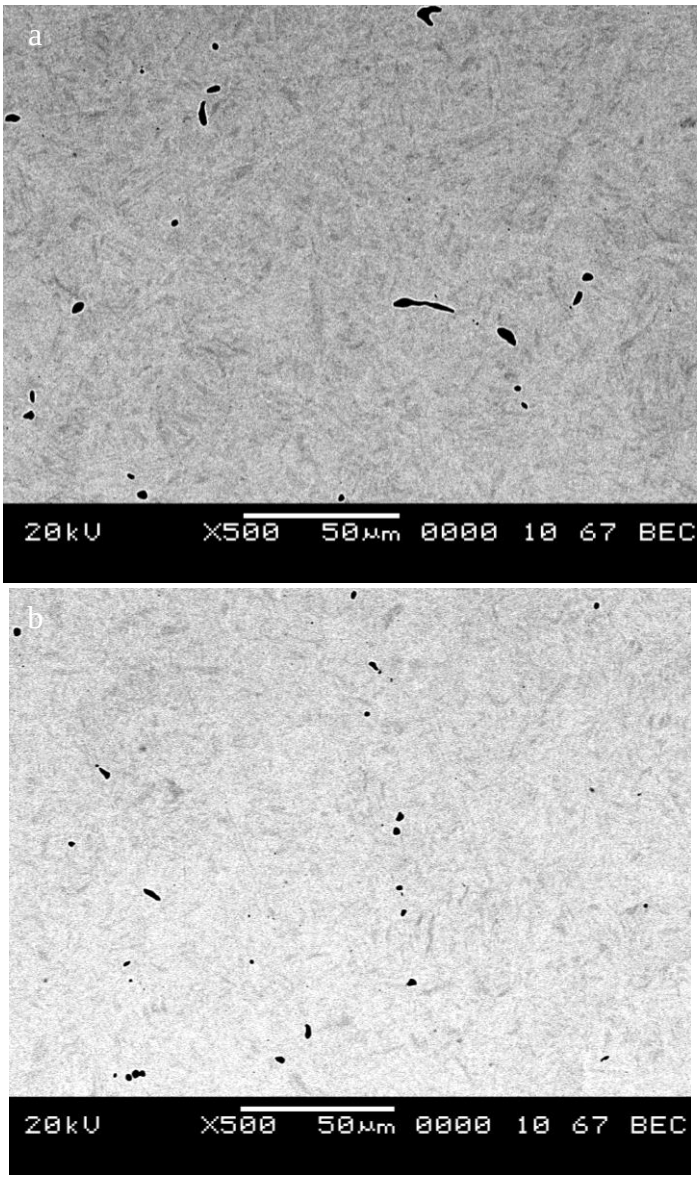

Figure 4.1.2-13 Back-scatted-electron images of the gear tooth cross-section, showing the material containing large amount of coarse MnS inclusions

In summary, the gear teeth made from 18CrNiMo7-6 steel have been case-hardened using a process of carburising, quenching and low-temperature tempering. Through this process a progressively hardened case with a ductile core has been obtained. The microstructure of the gear material is mostly tempered martensite with some ferrite present. However, significant numbers of coarse MnS inclusions are also present in the gear material. The surface hardness

of 750 HV meets the requirements of the relevant ISO standard, ISO 6336-5:2003 (ISO, 2003). However, this may be inadequate for the harsh operational conditions prevailing at the high-speed stage of wind turbine gearboxes. The three gear teeth examined have all been deemed to have failed due to micro-pitting, excessive adhesive wear and tooth-root fracture. Angular misalignment was identified from the shape of the cracked area and the trend of concave surface area. The inadequate lubrication and surface hardness, together with the misalignment, produced unevenly distributed pitting and excessive wear. Thus, the tooth profile was significantly changed, impairing the smooth meshing action of the gears. Moreover, the combination of these factors, surface damage, and together with the high number of coarse MnS inclusions, accelerated the initiation and development of cracks resulting in final tooth facture causing the gears to fail.

4.1.2.2 Intermediate stage gear teeth

As mentioned before, tooth fracture of intermediate stage gear is common in wind turbine gearboxes. The damaged five gear teeth shown in Figure 4.1.2-14 were manufactured from 18CrNiMo7-6 carburising steel. They were all retrieved from the intermediate stage gear after failure.

Discolouration and scuffed surface can be clearly seen on every tooth examined. The tips of teeth, T1-T4, were all deformed or broken as seen in Figure 4.1.2-15. The discolouration and tip deformation/breakage seem to have been caused by extremely high temperatures due to inadequate lubrication and severe friction. Figure 4.1.2-16 shows the SEM micrograph of the gear tooth contact surface. The condition of the surface is very poor, with high roughness, with scuffing scratches and cracks present, whilst part of it is plastically deformed. The

observed features suggest that lubricant starvation and high friction affected the gear during operation.

Figure 4.1.2-17 shows the fractured surface of one of the teeth. Area 1 above the red line is different from area 2 below it. The roughness of area 1 is lower than area 2, indicating the area 1 is where the crack propagated slowly area, whilst area 2 is where the crack propagated fast prior to final fracture.

Figure 4.1.2-14 Five broken gear teeth from intermediate stage

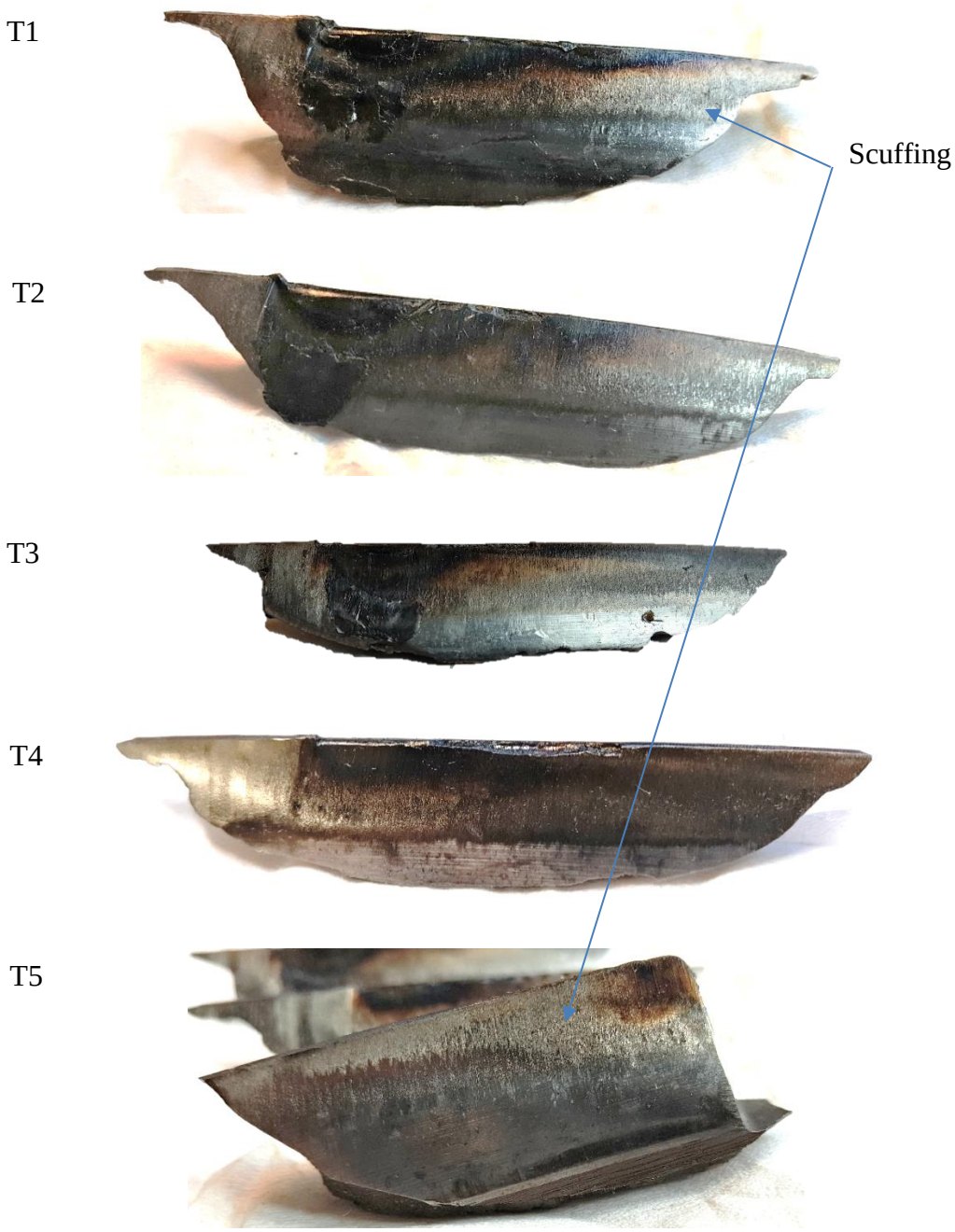

Figure 4.1.2-15 Discolouration and scuffing can be seen on all the teeth surface, and the tips of teeth T1-T4 are all deformed/broken.

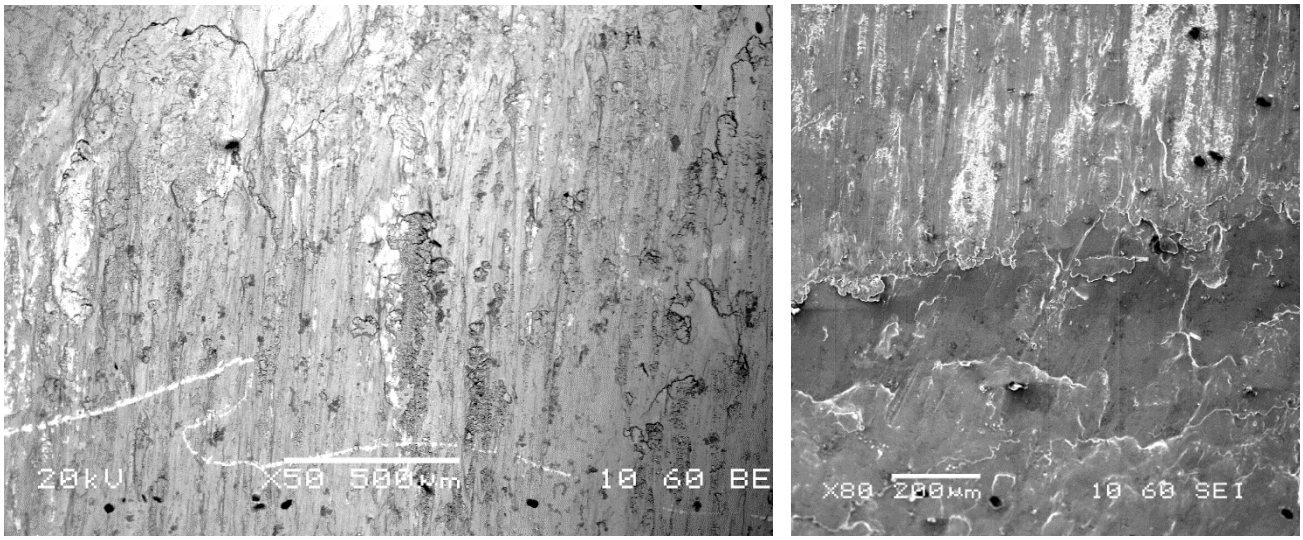

(a) (b)

Figure 4.1.2-16 The tooth surface is scuffed, cracked and plastically deformed

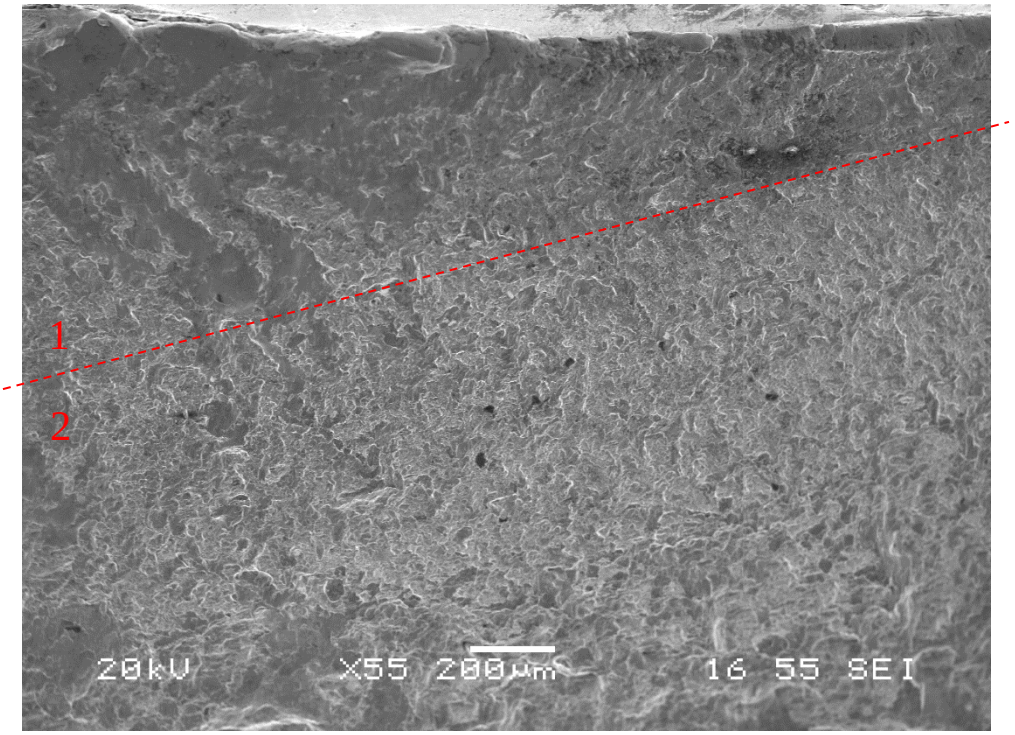

Figure 4.1.2-17 The SEM image of the fracture surface of the broken gear tooth

The cross-section of the broken tooth was examined to obtain more information. The hardness profile of the gear tooth is plotted in Figure 4.1.2-18, indicating a case hardened material. The surface hardness increased to about 720 HV0.05, whilst the core hardness was measured to be about 440 HV0.05. The thickness of the case-hardened layer is about 2,000 μm. The hardness of the gear teeth met the recommended value of the international standard ISO 6336-5:2003. In the XRD pattern of the tooth material, shown in Figure 4.1.2-19, only peaks of α'-Fe phase are observed.

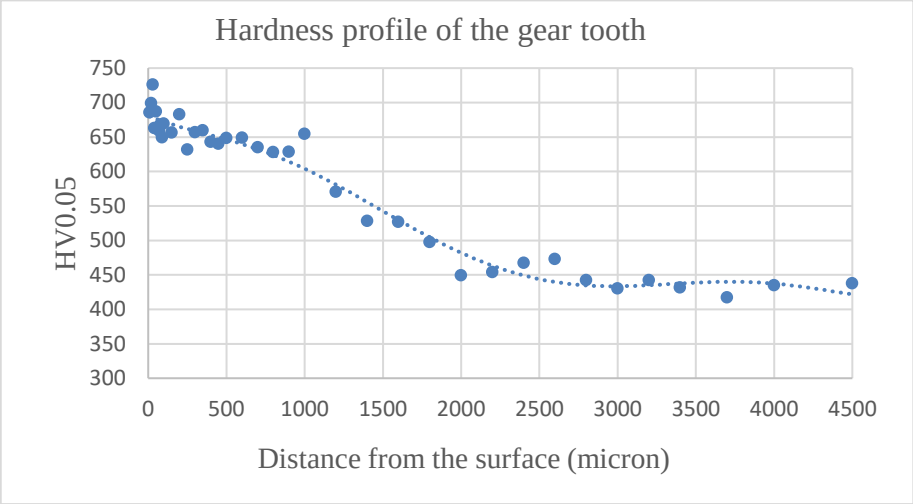

Figure 4.1.2-18 The hardness profile of the gear tooth from intermediate stage indicating a case hardened material. The surface hardness is about 720 HV0.05, whilst the core hardness was measured to be about 440 HV0.05.

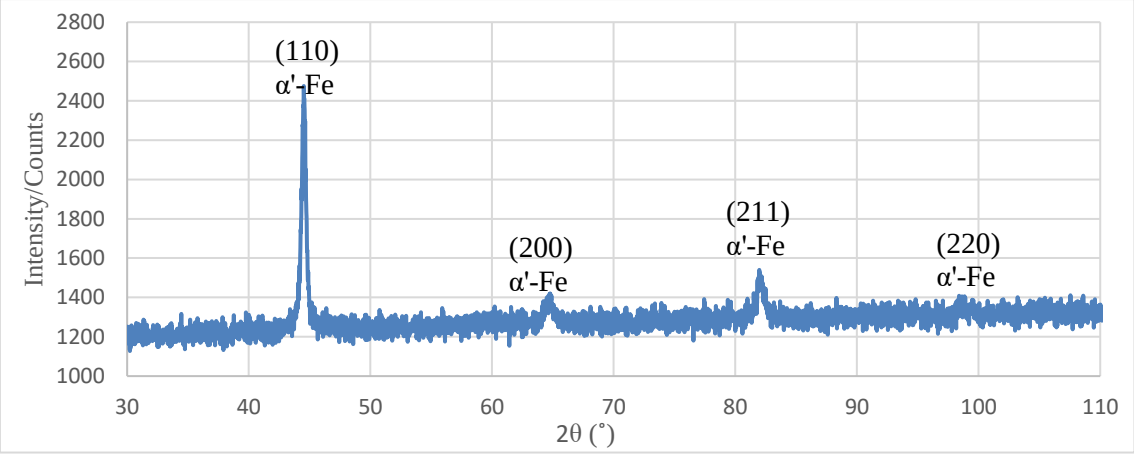

Figure 4.1.2-19 XRD pattern showing the main phase of the gear teeth from the intermediate stage

The micrographs of the microstructure gear teeth material after etching with 2% nital is shown in Figure 4.1.2-20. In the subsurface area where C has diffused, the microstructure is dominated by high C martensite, with some inclusions also present. In the core area, low C martensite is the dominant phase with a lower number of inclusions present together with some ferrite. The material characterisation results obtained revealed that the treatment process employed was based on carburising, then quenching and low-temperature tempering. Under SEM, inclusions such as MnS and Al_2O_3 surrounded by MnS were observed in the cross–section examined as shown in Figure 4.1.2-21. These inclusions can act as local stress raisers and crack nuclei. The narrow elongated MnS inclusions can act as a crack themselves (S. K. Dhua et al., 2000, T Bruce et al., 2016). It is very likely that these inclusions in gear material would prompt gear damage.

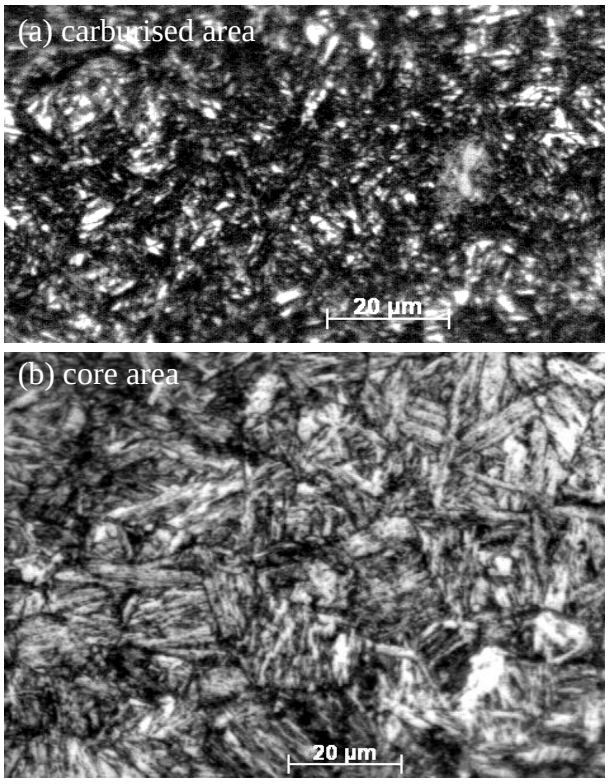

Figure 4.1.2-20 Metallography of intermediate-stage gear teeth, (a) the sub-surface, and (b) the core (2% natal, 500×)

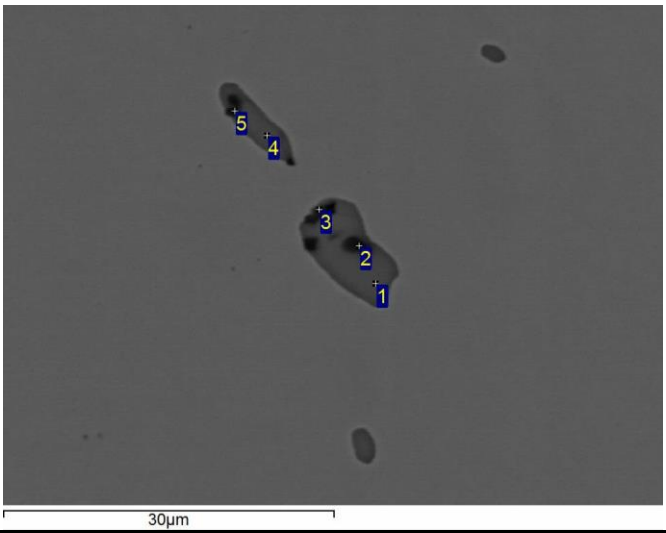

No.	C	O	Mg	Al	S	Ca	Cr	Mn	Fe	Ni	Comment
1	4.66		0.34		30.70	0.51	0.58	59.60	3.61		MnS
2	9.76	17.57		38.91	10.38		0.41	16.68	6.28		Alumina
3	4.96	9.26	0.62	23.05	7.18		1.09	10.88	42.35	0.60	Alumina
4	4.50		0.34		29.07	0.52	0.52	59.88	5.17		MnS
5	4.68	5.73	0.58	12.75	22.07	0.32	0.67	44.71	8.49		MnS/Alumina

Figure 4.1.2-21 Alumina inclusions surrounded by MnS in gear material (all results in weight%)

Based on the observations made, the main reason for the gear teeth fracture is the extremely high friction and high temperature due to inadequate lubrication. The evidence is the large discolouration and scuffing area in the gear tooth flank. The high friction and temperature led to severe plastic deformation, adhesion and adhesive wear between the meshing gear surfaces. The damaged surface profile caused non-uniform loading distribution and together with the presence of non-metallic inclusions gear tooth failure eventually was the result. The use of low friction DLC coating has great potential to prevent gear tooth fracture due to poor lubrication conditions.

4.1.2.3 Planetary gear debris

It is known that gear damage is greater in the low-speed stage due to the higher loads sustained combined with wind turbulence effects. Therefore, some debris particles from the

damaged planetary gear at the low-speed stage of the gearbox were retrieved (as shown in Figure 4.1.2-22) to study the failure causes. The retrieved debris particles have a grey metallic appearance, without any black, red or brown oxide colour present. The dimension of the retrieved debris particles varies from less than 1 mm to more than 4 cm. Those large debris particles indicate a catastrophic damage event occurred in the planetary gears.

Figure 4.1.2-22 The debris from the low-speed planetary gears

Under SEM examination, the debris particles are chunky, while they display a non-uniform shape and morphology. Six representative debris particles are shown in Figure 4.1.2-23. The surface of Particle 1 is very flat, with scratches and cracks present as seen in Figure 4.1.2-24. It is very likely that Particle 1 was broken off from the tooth surface, judging from its flat surface and features present. The surface of Particle 2 is concave, while the surface of Particle 3 is convex. Particle 4 has two relatively flat surfaces meeting, forming a ridge. The morphology of the surface of Particle 5 is granular and step-like, which is a symptom of brittle cleavage fracture. The surface of the Particle 6 is crushed and full of deep cracks. It

may be part of the case-hardened surface layer, which is very hard, brittle and easy to be cracked. Usually, these chunky debris particles are generated due to a fatigue mechanism (Amin Almasi and Rotating Machinery Consultant, 2014).

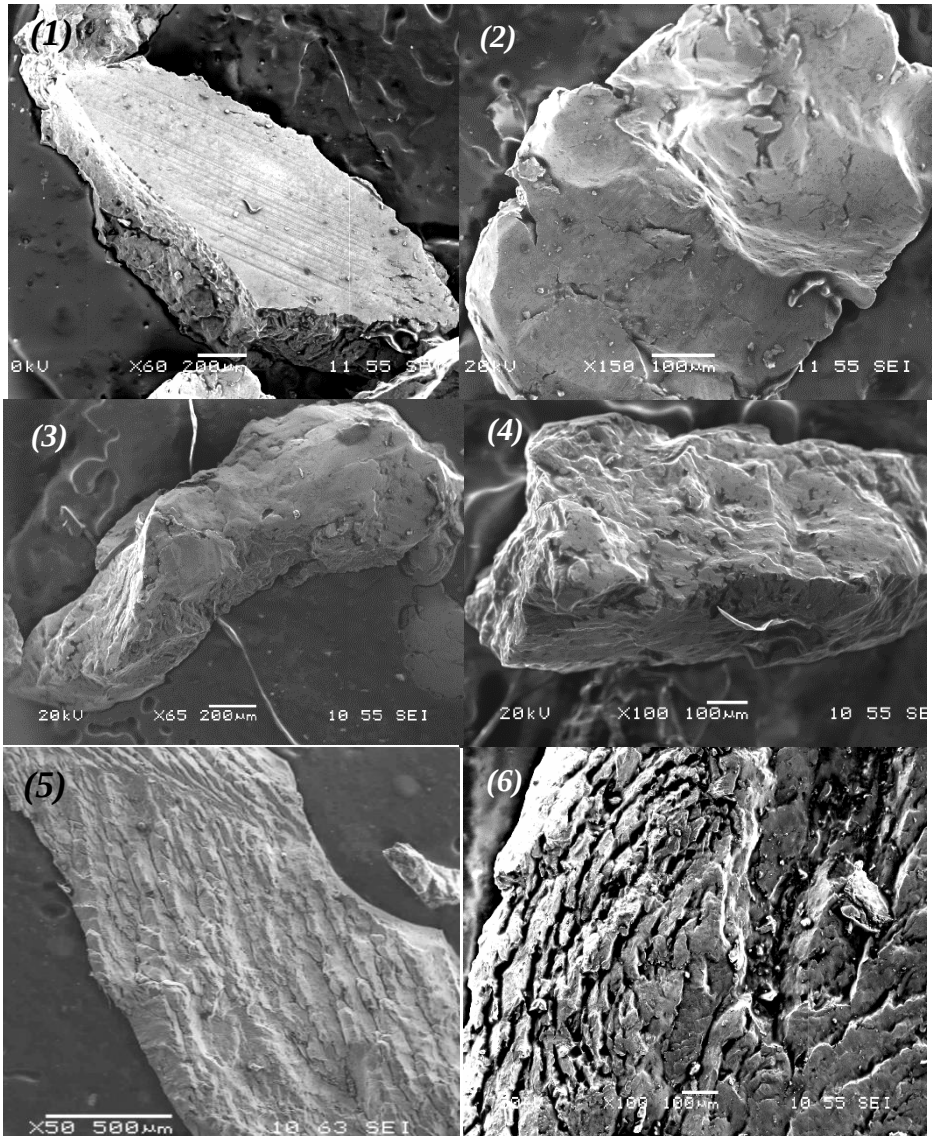

Figure 4.1.2-23 SEM images of debris in various shape and with different morphology from the planetary stage

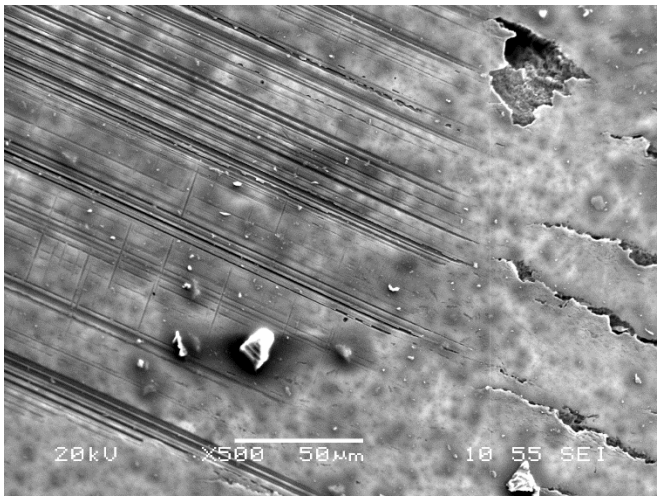

Figure 4.1.2-24 The flat surface with scratches and cracks of particle 1

Through EDS analysis, all debris were found to have similar composition, including Si content of 0.12-0.23 in wt%, Cr 1.29-1.50 in wt%, Mn 0.43-0.95 in wt%, Ni 1.27-2.63 in wt% and Mo 0.28-0.44 in wt%. The large range of detected element content is due to the uneven surface of debris particles, which caused unsteady generation of X-rays. Due to C contamination in the SEM chamber and the sloped surface of the debris particle, the EDS detected a C content which is erroneously high. However, the composition of the debris particles examined could be deemed to be in accordance to that expected based on the manufacturing material used which was 18CrNiMo7-6 alloy.

4.2 Simulation of meshing gears, crack development and rotating/sliding test using ABAQUS

Based on the observation and failure analysis results of the previous section, the main reasons for wind turbine gearbox failures have been identified to be high stresses related to misalignment, poor lubrication and the presence of non-metallic inclusions in the matrix

resulting in the reduction of the fatigue and wear resistance properties. In order to validate the failure causes of wind turbine gearbox components, FE software ABAQUS was used to study the stress field of gear pair and crack evolution which is difficult through other method. In addition, ABAQUS was used to validate the contact stresses which were estimated using Hertz contact theory for the wheel samples of Amsler rolling/sliding wear tests.

4.2.1 Contact stress on meshing gears

In order to study the effects of misalignment, input torque and friction coefficient on contact stress of wind turbine gearbox components, and verify the observed failure causes of wind turbine gearbox components, finite element analysis was conducted using ABAQUS. At first, the procedure of building the model was presented. Secondly, the effect of model element was studied. Thirdly, the model has been verified by comparing the simulated stress with Hertz contact stress. At last, the effects of misalignment, input torque and friction coefficient were studied using the model.

4.2.1.1 Building the model of meshing gears

To study and get a better understanding of the stress distribution of meshing gears inside the wind turbine gearbox, the commercial finite element analysis software ABAQUS was employed to carry out relevant simulations. First, two gears were designed in SOLIDWORKS. Subsequently, the gear and pinion were imported into the Part module of ABAQUS. Within the Property module of ABAQUS, the material properties were defined and applied to corresponding section and region of the components. Then in the Assembly module, the gear and pinion were assembled and placed in the contact position. In the Interaction module, their contact mode is set as ‘surface to surface contact’, and the friction coefficient is also defined.

Next in the Load module, the torque, rotating speed and other boundary conditions were set. In the Mesh module, the gear and pinion were divided into small elements (the Hexahedron element C3D8I was used to mesh the components). Finally, in the Job module, the job was submitted for computation. The results can subsequently be studied in the Visualization module.

A typical set of high-load gear pair parameters and material properties are listed in Table 4.2-1 and Table 4.2-2 respectively. Based on these gear pair parameters, the model of meshing gear pair was built and illustrated in Figure 4.2.1-1.

Table 4.2-1 A typical set of high-load gear pair parameters used for FEA simulation

Module	0.016 m
Teeth number of the pinion	17
Teeth number of the gear	67
Face width	0.05 m
Pressure angle	20°

Table 4.2-2 A typical set of steel properties used for FEA simulation

Density	7850 kg/m^3
Young's modulus	200 GPa
Poisson ratio	0.3

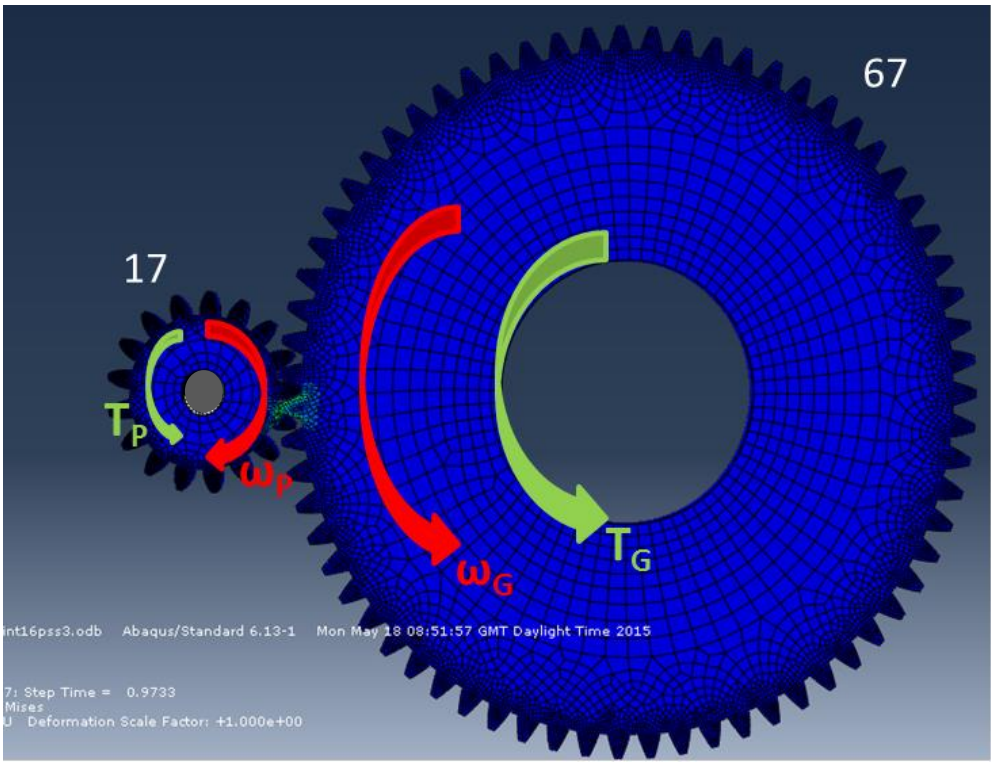

Figure 4.2.1-1 The model of meshing gear pair

With an input torque of 8 kN·m and friction coefficient of 0.16, the contact and bending stresses (Von Mises stresses) between two gear teeth in contact can be seen in the contour plots in Figure 4.2.1-2. In the contour, ABAQUS presents the Von Mises stress by default. The different stress levels are shown as a different colour. More information about the stress levels can be seen in the legend on the upper-left corner. ABAQUS can point out the exact position of the Maximum and Minimum stress value. In Figure 4.2.1-2, the highest Von Mises stress is concentrated around the contact area of the gear pair. Also, the concentration of the bending stress around the gear root can be identified from Figure 4.2.1-2. The bending stress is much lower than the contact stress in this case. At higher magnification (Figure 4.2.1-3), the max Von Mises stress can be identified in the subsurface of the contacting gear teeth. Figure 4.2.1-4 shows the contact pressure distribution on the pinion surface. The other gear wheel has been hidden to obtain a better view. From Figure 4.2.1-4, it can be seen that the

contact area is a rectangle and the maximum contact pressure is located along the longer centreline crossing the midpoint. The distribution of the contact stress and contact pressure obtained from ABAQUS is consistent with those expected from the common contact theory.

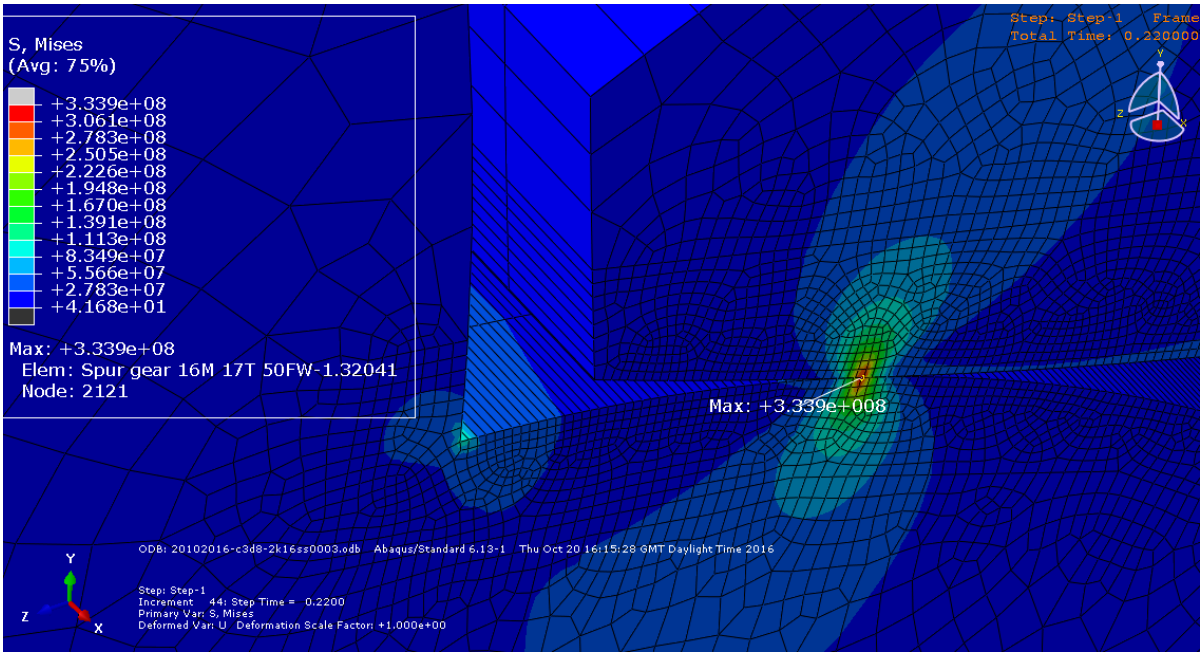

Figure 4.2.1-2 The contours of Mises stress levels in the contact gear teeth under the input toque of 2,000 N·m and with friction coefficient of 0.16.

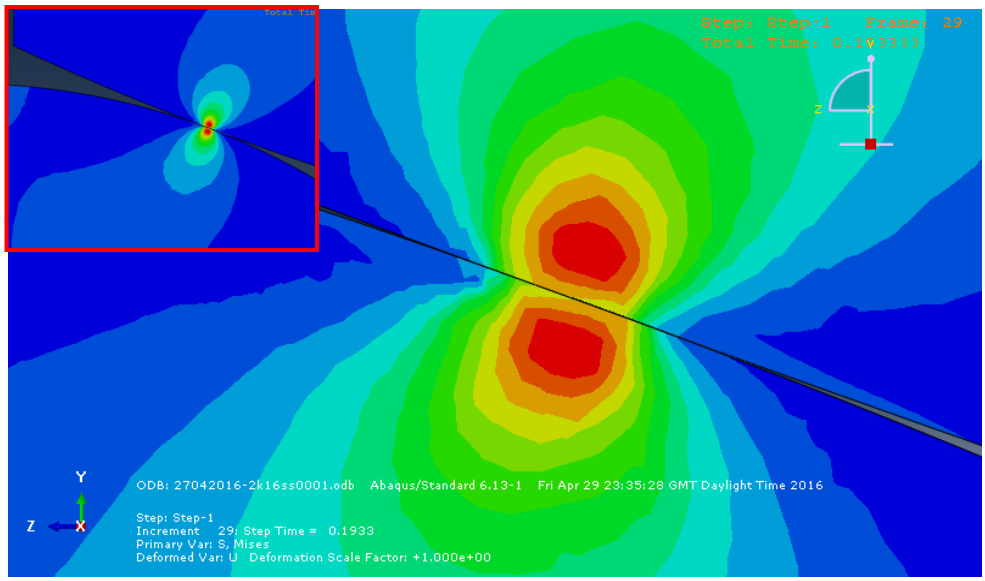

Figure 4.2.1-3 Contour of Mises stress in the gear pair contact area

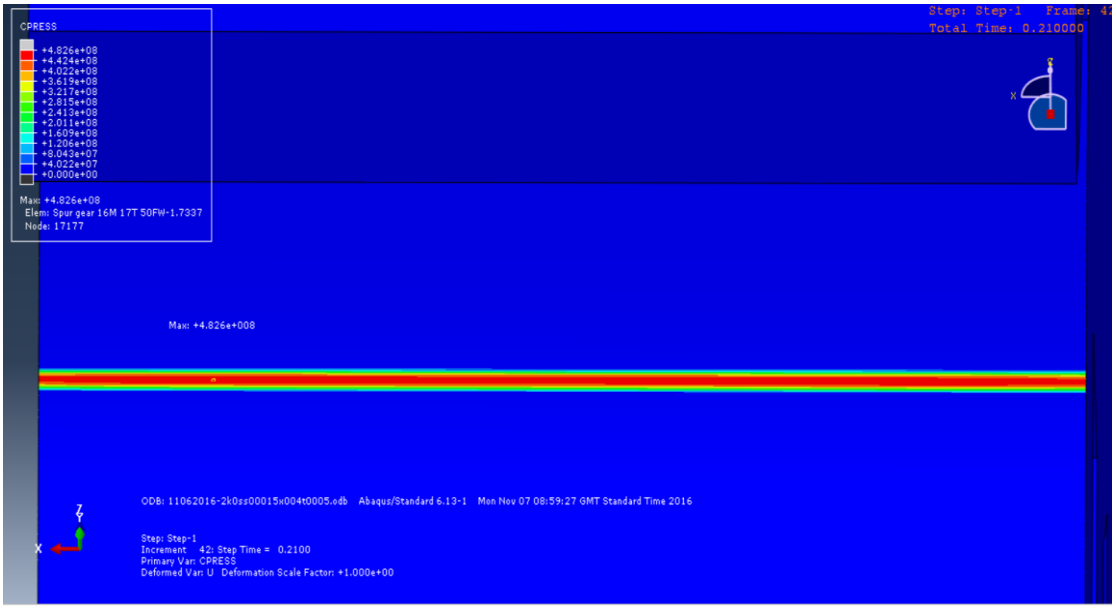

Figure 4.2.1-4 Contour of contact pressure in the gear pair

4.2.1.2 The effect of the element size

The element size fundamentally affects the computational efficiency of the finite element analysis calculations and accuracy of the stress levels obtained. In theory, smaller element sizes would lead to results of higher accuracy. However, smaller element means increased number of elements and nodes amount, hence higher computational expense (longer running time) will be needed.

In order to get relatively accurate results with acceptable running time, an optimal range of element size should be determined at the beginning of the simulation. Therefore, the stress levels of meshing gears were tested with a series of element size in descending order, namely 0.005, 0.002, 0.001, 0.0005, 0.0004, 0.0003, 0.0002 and 0.0001 (see Table 4.2-3). The maximum Von Mises stress around the pitch line of the gear pair was only 64 MPa with the large element size of 0.005. It increased dramatically to 126 MPa when the element size

decreased to 0.002. With a further reduced element size of 0.001, the maximum Von Mises stress was accordingly increased to 248 MPa. When the element size became 0.0005, 0.0004, 0.0003, 0.0002 and 0.0001 respectively, the maximum Von Mises stress was 373, 382, 372, 342 and 349 MPa respectively, which was relatively stable. Hence there was no need to further decrease the element size to lower than 0.0001. In terms of Von Mises stress, the element size to be adopted in the following simulations should be picked from the range between 0.0001 and 0.0005. With respect to the contact pressure (as shown in Table 4.2-3), the same trends as for the Von Mises stress were observed with decreasing element size used for the simulation. The contact pressure was only 52.2 MPa with the large element size of 0.005. It kept increasing to 121, 213 and 490 MPa respectively when the element size decreased to 0.002, 0.001 and 0.0005. When the element size ranged from 0.0005 to 0.0001, the contact pressure was also relatively stable, with a value of around 500 MPa being obtained. Therefore, the optimal element size is in the range between 0.0001 and 0.0005.

Table 4.2-3 The effect of seed size on calculated stress levels

Seed size of driven/driving gear, master/slave surface	Max contact Mises stress around pitch line from ABAQUS (Pa)	Max contact pressure around pitch line from ABAQUS (Pa)
0.005/0.005	6.40E+07	5.22E+07
0.002/0.002	1.26E+08	1.21E+08
0.001/0.001	2.48E+08	2.13E+08
0.0005/0.0005	3.73E+08	4.9E+08
0.0004/0.0004	3.82E+08	5.24E+08
0.0003/0.0003	3.72E+08	5.35E+08
0.0002/0.0002	3.42E+08	5.05E+08
0.0001/0.0001	3.49E+08	5.14E+08

4.2.1.3 Verification of the model

For the purpose of validating the contact pressure calculated using ABAQUS, Hertzian contact theory was used to estimate the contact pressure in the gear pair. As shown in Figure

4.2.1-5, the contact of two spur gear teeth can be analogously simplified as two cylinders that are in contact (Karlebo-Handbok, 1992, MARCUS SLOGÉN, 2013). The radii of the two analogous cylinders in contact are $\mathbf{r_{k1}}$ and $\mathbf{r_{k2}}$, and the $\mathbf{r_{ki}}$ can be expressed as

$$r_{ki} = \frac{Pitch\ radius}{sin\,20°} \qquad Equation\ 17$$

Based on the Hertzian contact theory, the maximum contact pressure is then given by

$$\sigma_H = \sqrt{\frac{N}{\pi(k_1 + k_2)L}\left(\frac{1}{r_{k1}} + \frac{1}{r_{k2}}\right)} \qquad Equation\ 18$$

in which **N** is the contact force, and

$$N = \frac{Output\ torque}{Pitch\ radius\ of\ pinion \div cos\,20°} \qquad Equation\ 19$$

L is the length of the line of contact, which is the width of the gear tooth in this case. **k1** and **k2** are the material constants, which are given by

$$k_i = \frac{1 - {v_i}^2}{E_i} \qquad Equation\ 20$$

in which **E** is the Young's modus, and **υ** is the Poisson ratio (Mart Mägi and Kjell Melkersson, 2009, MARCUS SLOGÉN, 2013). Using the gear pair parameters and the material properties shown in Table 4.2-1&2, together with the output torque of 2 kN·m, the calculated Hertzian contact pressure σ_H in the contacted gear teeth is found to be 557 MPa. Figure 4.2.1-6 compares the simulated contact pressure using ABAQUS with the estimated Hertzian contact pressure, which obviously indicates that the simulated contact pressure with the element size of 0.0003 (535 MPa) is closest to the Hertzian contact pressure. Their difference is only about 3.95%, which is acceptable.

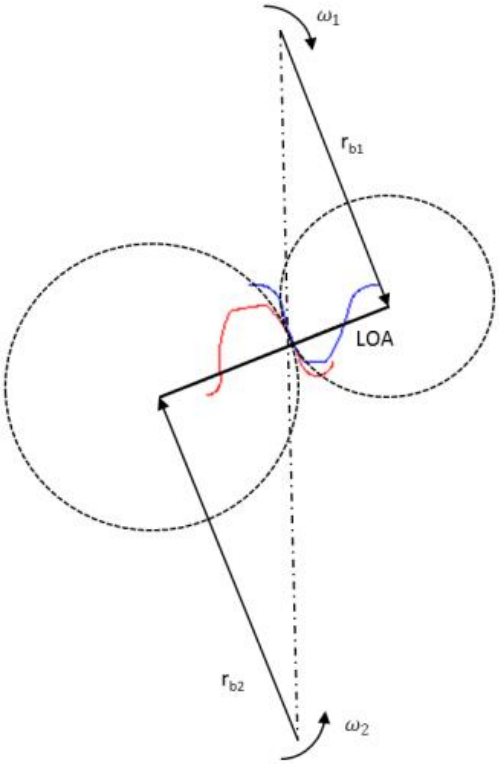

Figure 4.2.1-5 Simplified definition of Hertzian contact of a gear pair based on a definition obtained from Karlebo-Handbok (1992).

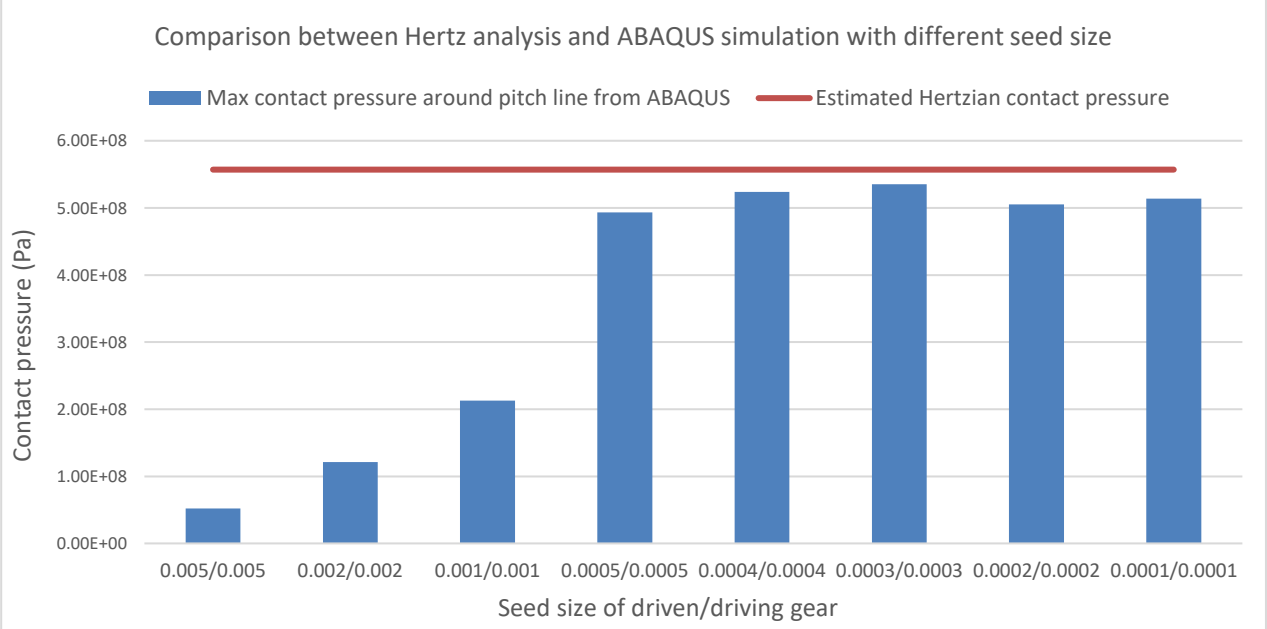

Figure 4.2.1-6 Comparison between Hertzian contact pressure and the contact pressure of different seed size in ABAQUS

In addition, the American Gear Manufacturers Association (AGMA) adopt another equation to estimate the contact pressure of spur gears, which is

$$\sigma_c = Z_E \sqrt{W^t K_o K_v K_s \frac{K_H}{d_{w1} b} \frac{Z_R}{Z_I}} \qquad \text{Equation 21}$$

$\mathbf{Z_E}$ is an elastic coefficient, $\mathbf{W^t}$ is the tangential transmitted load, in (N), $\mathbf{K_o}$ is the overload factor, $\mathbf{K_v}$ is the dynamic factor, $\mathbf{K_s}$ is the size factor, $\mathbf{K_H}$ is the load distribution factor, $\mathbf{d_{w1}}$ is the pitch diameter of the pinion, in (mm), **b** is the face width of the narrower member of gear pair, in (mm), $\mathbf{Z_R}$ is the surface condition factor, $\mathbf{Z_I}$ is the geometry factor for pitting resistance. All these terms have been explained in detail by Joseph Edward Shigley (2011), including the equations to calculate them and the value table for some of the terms. The calculated contact pressure σ_c based on the AGMA equation is about 599.5 MPa, which is higher than the value obtained through the Hertzian contact equation (557 MPa). The difference between the ABAQUS contact pressure (535 MPa) and the AGMA contact pressure is 10.7%, which is higher than that the calculated ABAQUS and Hertzian contact pressures (3.95%), but still within acceptable range.

Therefore, this model can be thought to be sufficiently reliable for further analysis.

4.2.1.4 The effect of input torque, friction coefficient and misalignment degree on the contact stress levels

The contact stress levels of operating wind turbine gearbox components will be influenced primarily by the load conditions (i.e. input torque), the lubrication quality (e.g. coefficient of friction) and degree of misalignment. Extreme high input torque, poor lubrication quality and misalignment are expected to significantly increase the contact stress of wind gearbox

components. Hence, they are suspected to be the responsible factors for most of the gearbox failures recorded. To verify this, finite element analysis was conducted using ABAQUS.

4.2.1.4.1 Input torque

According to the wind speed, the torque level in a wind turbine gearbox will keep changing between zero and the rated torque which is in the range of several kN·m at the high speed stage to more than one thousand kN·m at the low speed stage. In addition, gearboxes will experience occasionally much larger torques of short duration due to some transient load events like gusts or emergency safety shutdowns to avoid failure. The impact of higher loads upon the contact stress and contact pressure as shown in Figure 4.2.1-7, was simulated using ABAQUS under different torque conditions at 8 kN·m, 24 kN·m, 40 kN·m, 60 kN·m and 80 kN·m respectively. Both the contact stress and contact pressure were increased significantly as input torque increased. With respect to contact stress, the maximum Von Mises stress value was calculated to be 372 MPa, 606 MPa, 779 MPa, 975 MPa and 1.22 GPa for torque value of 8 kN·m, 24 kN·m, 40 kN·m, 60 kN·m and 80 kN·m respectively. As for the contact pressure, the value also increased significantly, calculated at 535 MPa, 862 MPa, 1.11 GPa, 1.36 GPa and 1.57 GPa for a torque of 8 kN·m, 24 kN·m, 40 kN·m, 60 kN·m and 80 kN·m respectively. In addition, the contact pressure under the same torque set was calculated using the Hertzian equation. The obtained Hertzian contact pressure was compared with the results obtained from ABAQUS in Figure 4.2.1-8. The contact pressure of Hertzian analysis is slightly higher than those obtained with the ABAQUS simulations for each input torque value. However, they are comparable to each other and show the same increasing trend in both cases.

Occasionally much higher torque can be introduced due to some transient loading events, e.g. sudden wind gusts, grid disconnection and emergency braking. Although these high loads are relatively infrequent and of short duration, their large magnitude means that extremely high

stress levels could be sustained by the gears and bearing rollers, accelerating failures due to micro-pitting and smearing.

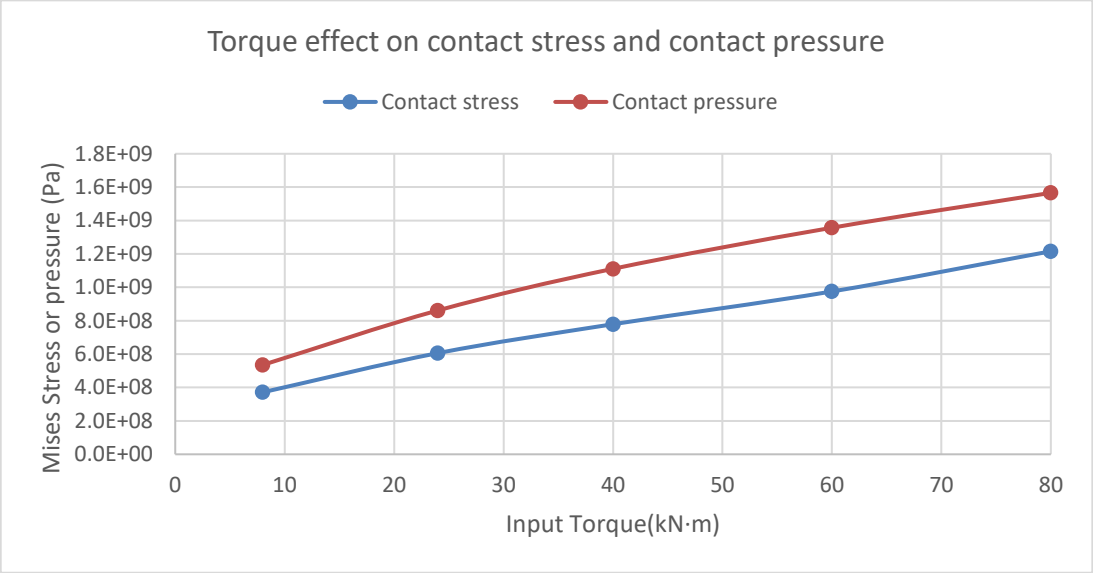

Figure 4.2.1-7 The effect of input torque on contact stress and contact pressure under different torque from 8 kN·m to 80 kN·m

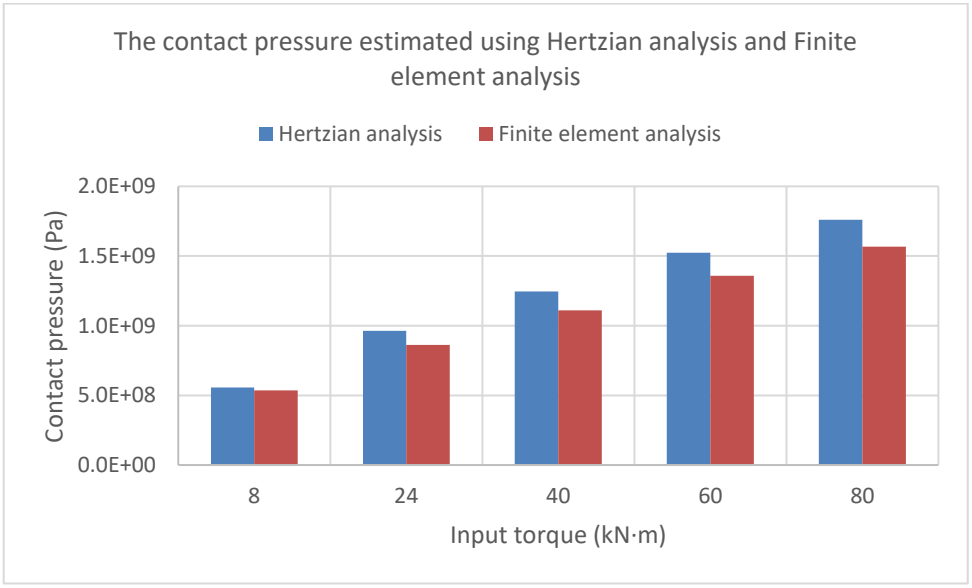

Figure 4.2.1-8 Comparison of the contact pressure estimated by Hertz analysis and Abaqus simulation under different torque of 8 kN·m, 24 kN·m, 40 kN·m, 60 kN·m and 80 kN·m respectively

4.2.1.4.2 Friction coefficient

For good lubricated gears and bearings, their friction coefficient for steel to steel contact is about 0.16. For components where lubricant is inadequate, the friction coefficient is about 0.4-0.8 (The Engineering ToolBox, 2017, Roy Beardmore, 2013).

The effect of friction coefficient on contact stress and contact pressure of the contact gear teeth has been evaluated using finite element analysis, as shown in Figure 4.2.1-9. From the simulations carried out, it is possible to see that the higher friction coefficient results in much higher contact Von Mises stresses, especially when the friction coefficient increases from 0.3 to 0.5. The contact stress increases from 309.3 MPa to only 338.6 MPa when the friction coefficient raised from 0 to 0.3. But when the friction coefficient continued to increase to 0.5, the contact stress became as large as 442.8 MPa. Hence, the effect is not linear. As for the contact pressure in Figure 4.2.1-9, the effect of friction can be neglected as expected, because friction only introduces tangential force and shear stress so there is no significant effect on the normal contact pressure. However, this does not accommodate frictional heating effects which can affect the mechanical properties of the material. When the friction coefficient increased from 0 to 0.5, the contact pressure decreased slightly from 490.2 MPa to 477.4 MPa, or by 2.6 %.

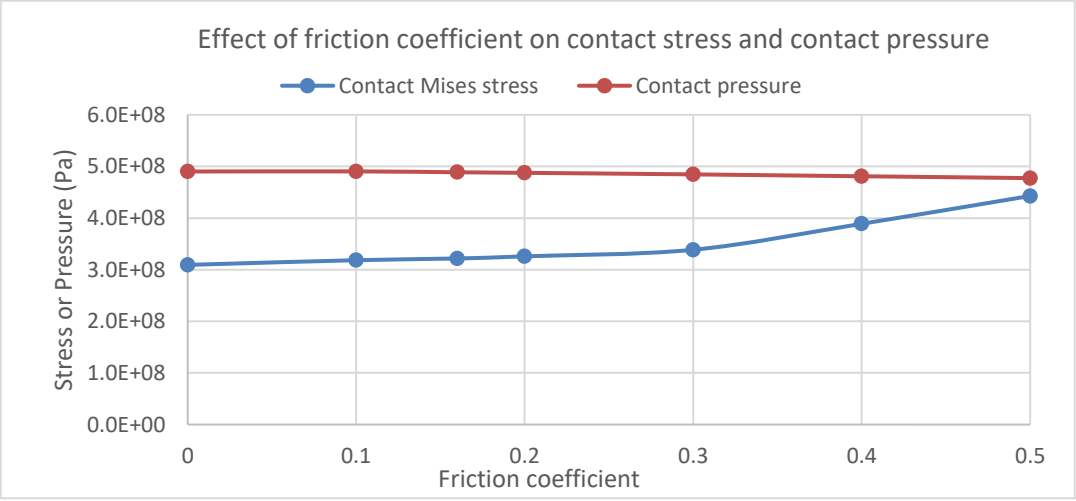

Figure 4.2.1-9 The effect of friction coefficient on contact stress and contact pressure

Figure 4.2.1-10 and Figure 4.2.1-11 illustrate the contour of the contact stress when the friction coefficient was 0 and 0.5 respectively. Comparing Figure 4.2.1-10 with Figure 4.2.1-11, it can be seen that higher friction made the maximum Von Mises stress moving tangentially and separating them from each other. More importantly, higher friction would move the position of maximum Von Mises stress vertically and towards the teeth surface. It is known that fatigue cracks tend to initiate in highly stressed regions around de-bonded or cracked inclusions, normally at or near component surface (WC Leslie, 1983, Joseph Maciejewski, 2015). Therefore, a higher friction coefficient would cause maximum shear stress to rise towards the surface. Therefore, crack initiation sites further close to surface can be activated, facilitating subsequent crack propagation to the surface. Moreover, the tension stress caused by high frictional force will accelerate the rapid growth of cracks. As shown in Figure 2.2.4-1, the frictional force exerted on the contact surface has great impact on the contact-fatigue lifetime of the material. Even the introduction of slight friction between the contact parts will significantly reduce the contact fatigue resistance of the components. The reason is that the friction coefficient of pure rolling is only about 1~2%，while the friction coefficient can be as high as 10% if sliding friction occurs (Shizhu Wen and Ping Huang, 2012)

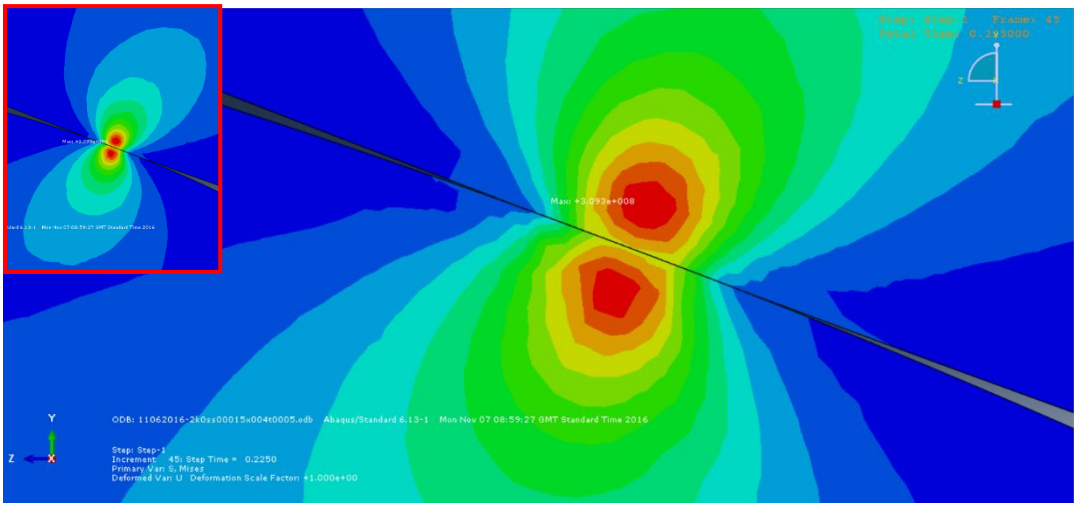

Figure 4.2.1-10 When friction coefficient 0, the maximum Mises stress is located at subsurface

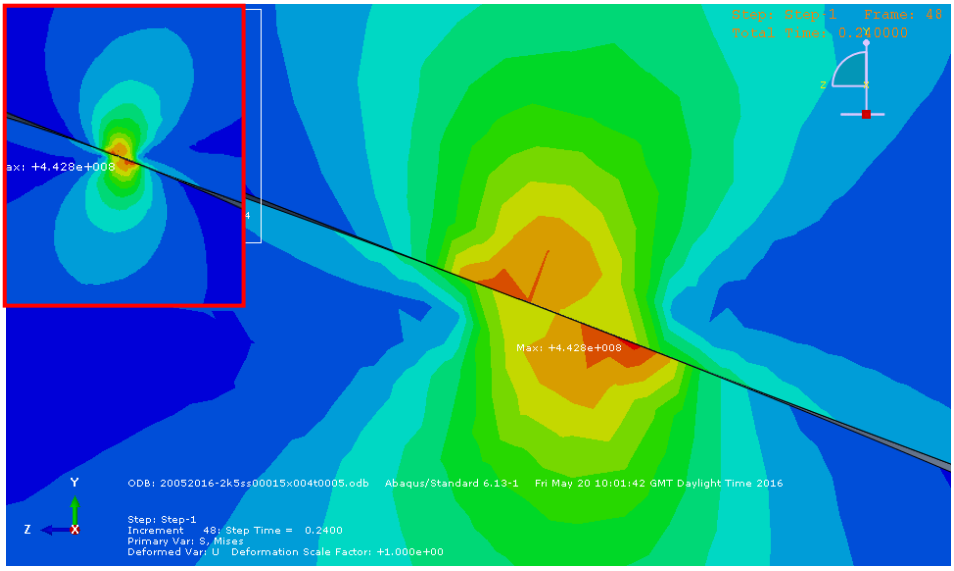

Figure 4.2.1-11 When friction coefficient increased to 0.5, the location of the maximum Mises stress moved to surface

4.2.1.4.3 Misalignment degree

The angular misalignment results in a non-uniform load distribution and smaller contact area on gear and bearing surface. This will result in increased local contact stresses at the overloaded side, accelerating component failure. To assess the impact of angular misalignment on the stress levels, angular misalignment of up to 1° was introduced into the

gear pair and compared with the stress level of a gear pair in perfect alignment. For instance, Figure 4.2.1-12 shows the gear pair with an angular misalignment of 1°.

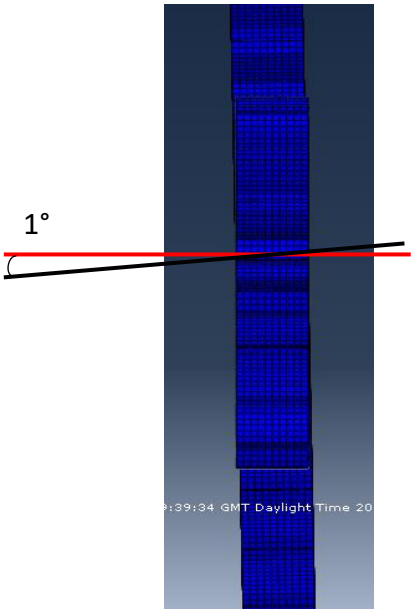

Figure 4.2.1-12 Angular misalignment of 1° was introduced to the gear pair

The corresponding contact stress of gear pair with different alignment degree is shown in Figure 4.2.1-13. It clearly shows that angular misalignment has a great effect on the contact stress. The contact stress is 372 MPa between two gears meshing in perfect alignment. Even a small amount of misalignment, such as 0.20° can increase contact stress to as high as 930 MPa, which is about 2.5 times the contact stress obtained without any misalignment. At 0.5° and 0.8° degree of angular misalignment, the contact stress is 1.57 GPa and 2.40 GPa respectively. When the angular misalignment is 1°, the contact stress achieving 3.10 GPa can be almost 8.3 times higher than the contact stress at perfect alignment. Such a dramatic increase in the contact stress level could lead to severe plastic deformation causing initiation and subsequent rapid growth of damage, such as micro-pitting and cracking.

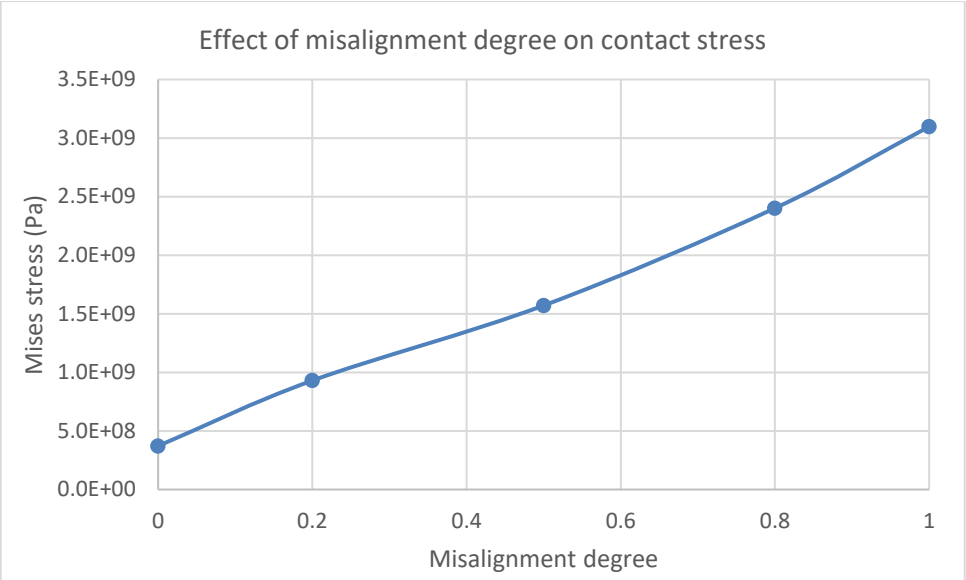

Figure 4.2.1-13 The effect of misalignment degree on contact stress levels

Based on the FEA simulations, it can be seen that when the input torque increased from 8 kN·m to 80 kN·m, the contact stress increased from 372 MPa to 1.22 GPa, by 227.96 %. When the friction coefficient increased from 0 to 0.5, the contact stress increased from 309.3 MPa to 442.8 MPa, by 43.16%. In addition, higher friction coefficient values shift the maximum stress to positions closer to the surface. Moreover, when the angular misalignment is 1°, the contact stress can reach 3.10 GPa which is almost 8.3 times higher than the contact stress during perfect alignment. It can be concluded that higher input torque, friction coefficient and level of misalignment can lead to significantly higher contact stress levels on wind turbine gearbox components, prompting the initiation and subsequent rapid development of defects which can then cause premature failure of the wind turbine gearbox.

4.2.2 Crack initiation and propagation in materials with soft inclusion

To verify the observations made on the micrographs of Figure 4.1.2-11 in section 4.1.2.1 and evaluate the effect of soft inclusions on fracture of gear teeth, the crack initiation and propagation behaviour of one gear tooth containing two soft sulfide inclusions under bending force was simulated using ABAQUS.

As shown in Figure 4.2.2-1, the shape of the inclusion cross-section is quadrilateral imitating the real MnS inclusion observed in the micrographs. The dimensions of the inclusion are about 66 μm×40 μm×277 μm. The gear tooth belongs to a gear with module 16 mm, face width 277 μm and pressure angle 20°. The tooth bottom is fixed and the load of 1.18×10^{9} N is applied at the tip of the tooth.

The matrix and inclusion material properties adopted in the simulation are shown in Table 4.2-4 (Daniel C Harris et al., 2008, E Dehner and F Weber, 2007).

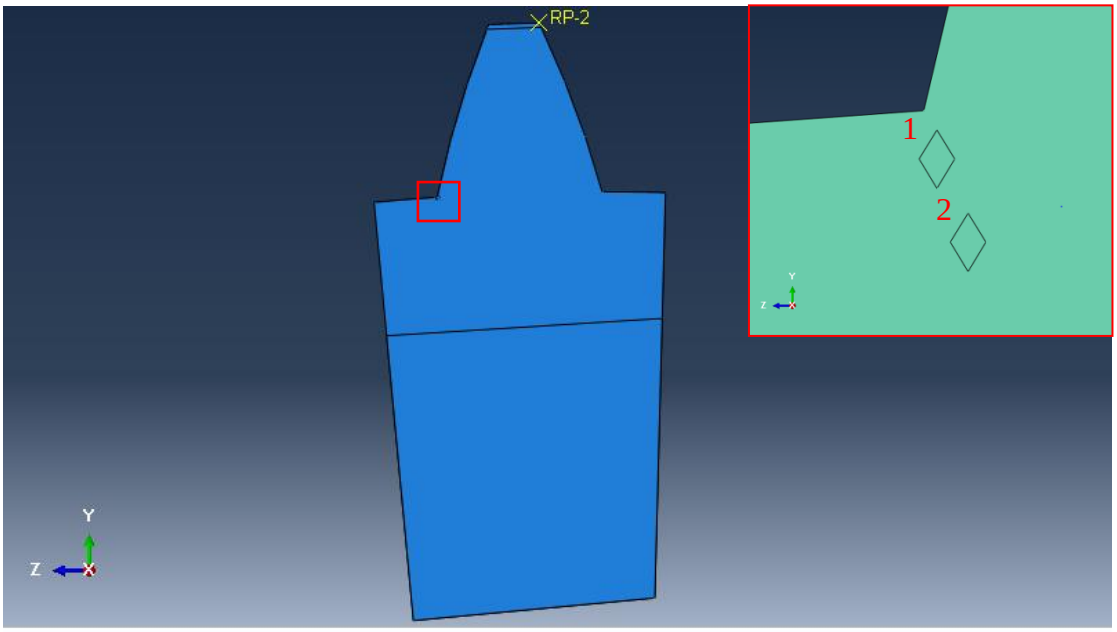

Figure 4.2.2-1 One gear tooth with two soft sulfide inclusions

Table 4.2-4 The matrix and inclusion material properties adopted in FEA simulation (Daniel C Harris et al., 2008, E Dehner and F Weber, 2007)

Name	Steel (E. DEHNER & F. WEBER 2007)	Soft Sulfide (Daniel C Harris et al., 2008)
Density	7820 kg/m^3	4000 kg/m^3
Young's Modulus	200 GPa	74.5 GPa
Poisson's Ratio	0.3	0.28
Max Principal Stress (Tensile Strength)	1 GPa	50 MPa
Fracture Toughness	78 MPa·m$^{1/2}$	1.0 MPa·m$^{1/2}$
Fracture Energy	30420 J/m^2	13.4 J/m^2

The key to simulating crack growth in ABAQUS is to apply the method XFEM (i.e. eXtended Finite Element Method). It is extremely difficult to handle significant discontinuities (i.e. displacement jumps), e.g. cracks and holes in structures, using conventional finite element analysis methods. Because the crack tip is very tiny and its propagation route is unpredictable, it is not practical to simulate a crack using the traditional finite element analysis approach. If the conventional approach is employed the mesh near the tiny crack tip needs to be very fine, because a few nodes have to be placed on and around the crack tip. In addition, the adjustment or regeneration of the mesh (i.e. re-meshing) will be required as the crack propagation path is unpredictable. Therefore, simulating crack with high accuracy using conventional finite element analysis is computationally expensive and difficult to achieve. XFEM is especially fit for handling discontinuities by restricting them to mesh edges. Thus, there is no need to mesh and re-mesh the discontinuity surfaces. It allows the crack to be simulated independently of the mesh, and the propagation of a crack can be simulated along the solution determined path without the need of re-meshing. In comparison with conventional FEM, XFEM requires much lower computational expense and can reach higher accuracy easily. But it is worth noticing that several limitations exist in XFEM of ABAQUS. For instance, forming branching cracks through XFEM are not permitted, because no more than one crack can intersect each element.

Additionally, the maximum angle a crack can turn is 90° in each time increment of ABAQUS analysis (Dassault-Systèmes, 2015).

To define a crack using XFEM in ABAQUS, firstly, in the Property module, the Material Editor is activated and then for each material the Mechanical → Damage for Traction Separation Laws → Maxps Damage. Then the Max Principal Stress is input as listed in Table 4.2-4. After that, Damage Evolution is activated where the Fracture Energy is input as summarised in Table 4.2-4. The fracture energy, $\mathbf{G_{IC}}$, was calculated by dividing the square of the fracture toughness, $\mathbf{K_{IC}^2}$, by the Young's modulus, **E**, which can be expressed as $G_{IC}=K_{IC}^2/E$ (Lyonel Reinhardt and JA Cordes, 2010, CM Weaver et al., 2011). Next, in the Interaction module, under the Special tab, the following function is performed, Crack → Create → XFEM, and then 'Allow crack growth' is toggled and the crack domain is selected.

The screenshots of the simulation results are shown in Figure 4.2.2-2. At first, the stress is concentrated around the edge of inclusion 1 which is close to the tooth surface. Meanwhile, the first crack (or void) initiated in inclusion 1 and from the edge with the highest local stress. Then the second crack also occurred in inclusion 2. The first crack became longer and crossed the first inclusion. After that, the first crack grew towards the tooth surface, eventually reaching it at a later stage. Beyond that, the first crack developed towards the deeper area of the tooth. Subsequently, it is interesting to see that the growing direction of the first crack changed, propagating towards the second inclusion. At last, the first crack coalesces with the second crack in inclusion 2, forming a larger open crack running from the tooth surface to the deeper area intersecting the two inclusions.

This model presented the crack initiation caused by the inclusion fracture and subsequent propagation sufficiently verifying the observations reported earlier in the thesis in section 4.1.2.1. The experimental observations together with the results from the simulation carried

out revealed that the soft MnS inclusions play an important role in the initiation and propagation of wind turbine gearbox damage.

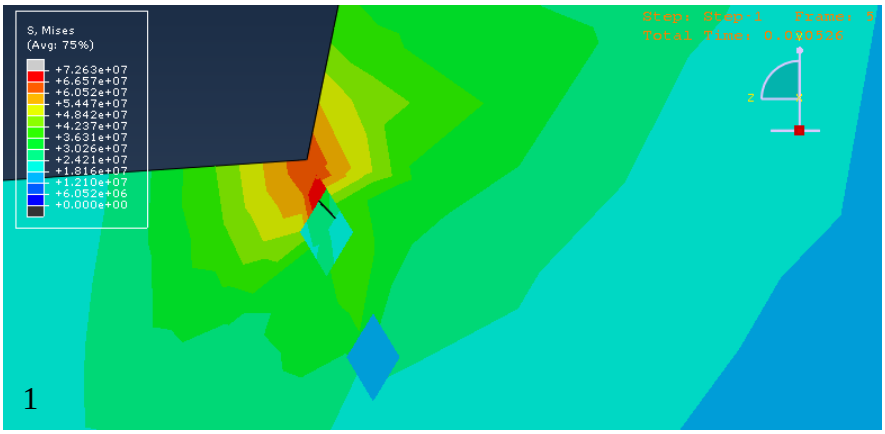
S, Mises
(Avg: 75%)
+7.263e+07
+6.657e+07
+6.052e+07
+5.447e+07
+4.842e+07
+4.237e+07
+3.631e+07
+3.026e+07
+2.421e+07
+1.816e+07
+1.210e+07
+6.052e+06
+0.000e+00
1

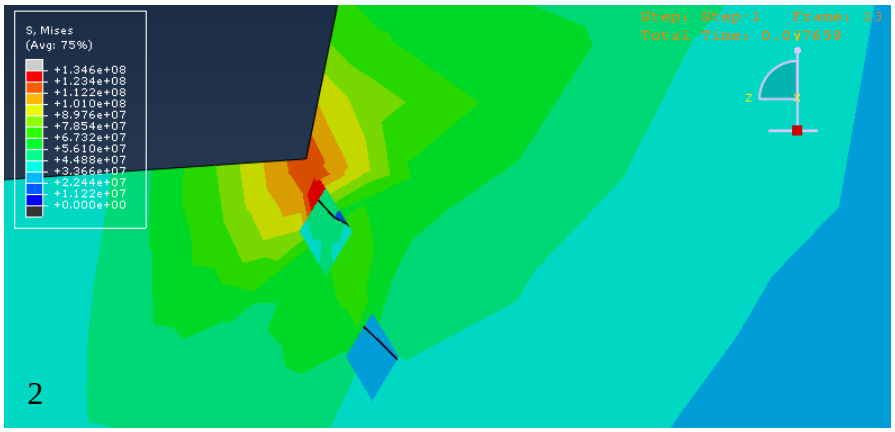
S, Mises
(Avg: 75%)
+1.346e+08
+1.234e+08
+1.122e+08
+1.010e+08
+8.976e+07
+7.854e+07
+6.732e+07
+5.610e+07
+4.488e+07
+3.366e+07
+2.244e+07
+1.122e+07
+0.000e+00
2

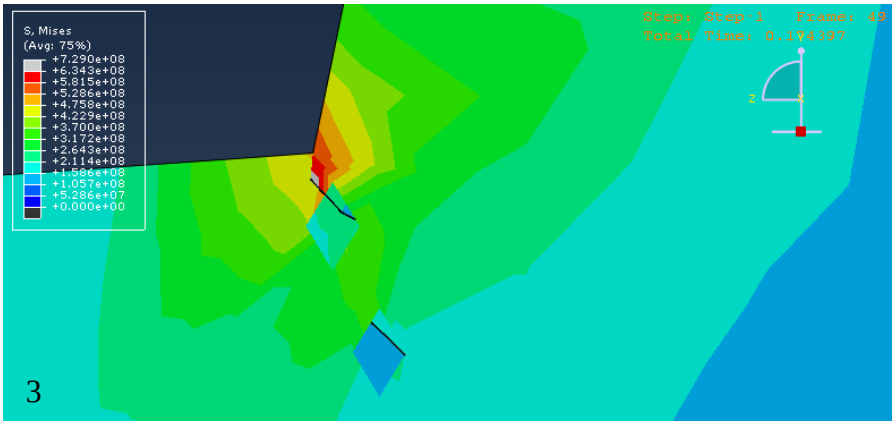
S, Mises
(Avg: 75%)
+7.290e+08
+6.343e+08
+5.815e+08
+5.286e+08
+4.758e+08
+4.229e+08
+3.700e+08
+3.172e+08
+2.643e+08
+2.114e+08
+1.586e+08
+1.057e+08
+5.286e+07
+0.000e+00
3

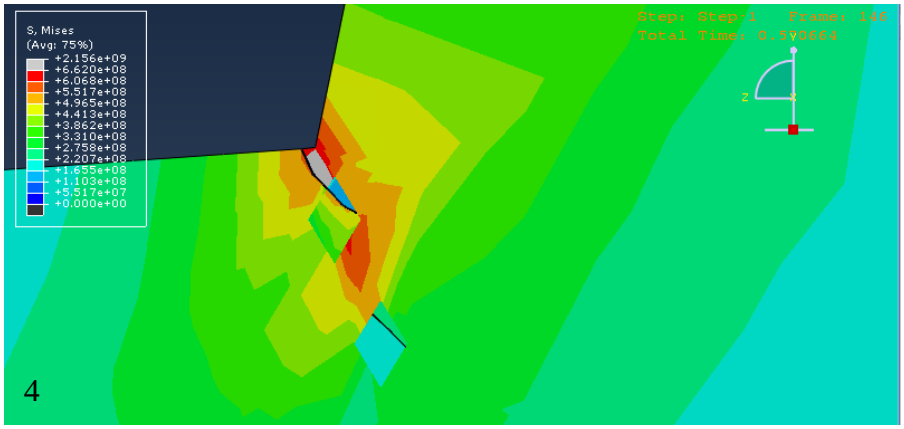
S, Mises
(Avg: 75%)
+2.156e+09
+6.620e+08
+6.068e+08
+5.517e+08
+4.965e+08
+4.413e+08
+3.862e+08
+3.310e+08
+2.758e+08
+2.207e+08
+1.655e+08
+1.103e+08
+5.517e+07
+0.000e+00
4

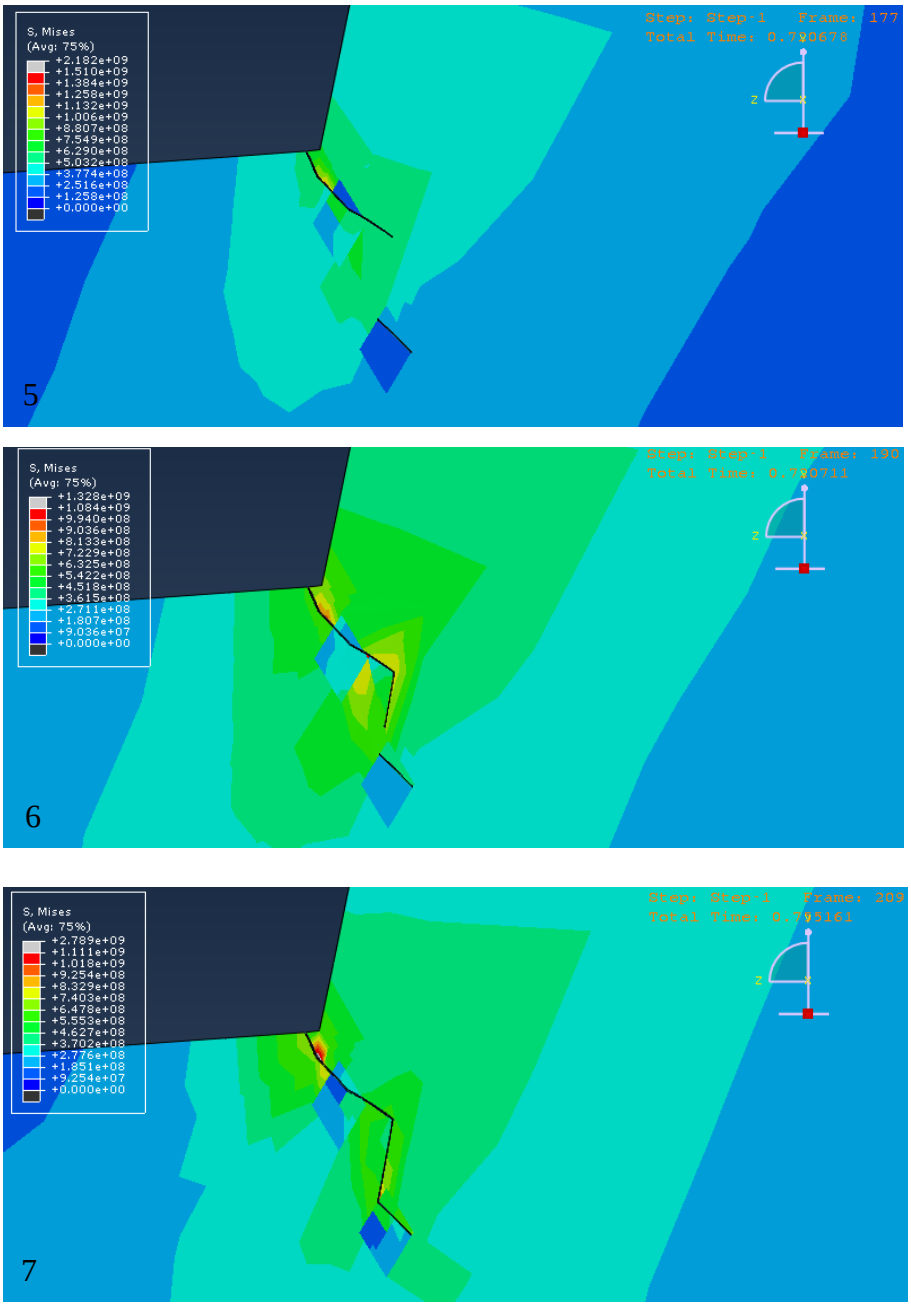

Figure 4.2.2-2 XFEM results successfully simulated crack developing within and along two inclusion particles, which verified the observations made on the micrographs of Figure 4.1.2-11 in section 4.1.2.1.

Non-metallic inclusions may act as stress raisers because their mechanical and thermal properties are different from the surrounding matrix material, having a similar effect to voids being present (Roland Kiessling and Nils Lange, 1968, Joseph Maciejewski, 2015). On one hand, hard inclusions, like alumina, are commonly regarded as the origin of cracks, since they

can cause local stress concentration when the surrounding material deformed (Roland Kiessling and Nils Lange, 1968, Joseph Maciejewski, 2015). On the other hand, soft inclusions, like MnS, are thought harmless in some cases because they may avoid stress concentration effect by elongating easily with the matrix material. However, some studies (L. de Campos Franceschini Canale, 2008, Joseph Maciejewski, 2015, PA Thornton, 1971, ZZ Yuan et al., 2006) pointed out that the ductile MnS inclusions would initiate fractures in the absence of hard inclusions, and cracks were observed to preferentially propagate through soft sulfide inclusions, which is consistent with the metallographic observation and XFEM simulation here. In addition to promoting the initiation and propagation of damage, elongated MnS inclusions would also cause anisotropy in the mechanical properties of the component (L. de Campos Franceschini Canale, 2008, Joseph Maciejewski, 2015). When the loading direction is the same to the longitudinal direction of MnS inclusions, the tested stress to cause fracture of the steel sample is greater than that when the load is in the short transverse direction of the MnS inclusion. The tested transverse strength of the material with elongated MnS inclusions present were approximately 25% lower than the strength in the longitudinal direction (WC Leslie, 1983, Joseph Maciejewski, 2015). Hence, the potential for component failure would be significant if the material is anisotropic and the loading directions have not been considered (WC Leslie, 1983, Joseph Maciejewski, 2015).

Based on above results and discussion, the existence of coarse MnS inclusions in the gear teeth need to be considered. MnS inclusions have been identified as possible microstructural features that may act as crack initiation points, weakening the mechanical strength of the steel alloy that the gearbox component has been manufactured of.

4.2.3 Simulation of rotating/sliding test

The contact stress between the Tungsten Carbide (WC) wheel and steel wheel samples used for the Amsler rolling/sliding wear test was estimated using the Hertzian contact theory first. To validate the Hertz contact stress, finite element analysis has been carried out ignoring frictional effects.

The configuration of the contacting wheel samples used in the Amsler wear tests and the dimensions of the wheels are shown in Figure 4.2.3-1. The WC wheel was placed on top, and the steel wheel samples at the bottom. A static load was applied on the top WC wheel, so the top wheel pressed against the bottom wheel with the full applied load. Considering their geometry, the contact area between the wheel pair is expected to be an ellipse under the static load ignoring frictional effects.

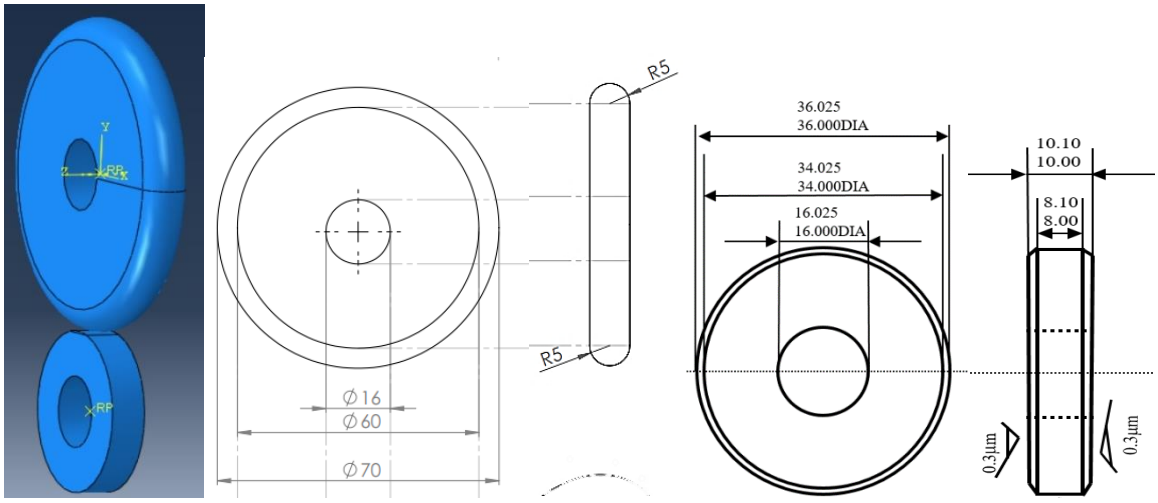

(a) (b) (c)

Figure 4.2.3-1 (a) The configuration of the wheel samples for Amsler wear test, (b) the dimensions of the top WC wheel, and (c) the dimensions of the bottom steel wheel

1) Estimating contact pressure using Hertzian analysis

The Hertzian analysis adopted for components with complex geometry and ellipse contact is given by (R S Dwyer-Joyce, 1997). The reduced radii along the x and y axes were defined as,

$$\frac{1}{R_x} = \frac{1}{R_{1x}} + \frac{1}{R_{2x}} \qquad Equation\ 22$$

$$\frac{1}{R_y} = \frac{1}{R_{1y}} + \frac{1}{R_{2y}} \qquad Equation\ 23$$

$$\frac{1}{R} = \frac{1}{R_x} + \frac{1}{R_y} \qquad Equation\ 24$$

According to the Hertzian contact theory the semi-shorter and semi-major axes length of the contact ellipse are given as,

$$a = \sqrt[3]{\frac{3k^2IPR}{\pi E^*}} \qquad Equation\ 25$$

$$b = \sqrt[3]{\frac{3IPR}{\pi k E^*}} \qquad Equation\ 26$$

where E* is the reduced Young's modulus, k is the ellipticity parameter (k=a/b) and I is an elliptic integral of the second kind. These terms are given by

$$E^* = \left(\frac{1-v_1^2}{E_1} + \frac{1-v_2^2}{E_2}\right)^{-1} \qquad Equation\ 27$$

$$k = 1.0339\left(\frac{R_y}{R_x}\right)^{0.6360} \qquad Equation\ 28$$

$$I = 1.0003 + \frac{0.5968R_x}{R_y} \qquad Equation\ 29$$

It is known that R_{1x}=0.005 m, R_{2x}=∞, R_{1y}=0.035 m, R_{2y}=0.018m (as shown in Figure 4.2.3-1), and the Young's modulus and Poisson ratio of tungsten carbide and steel are listed in Table 4.2-5. Based on the previous equations, it is straightforward to obtain R_x=0.005 m, R_y=0.01189 m, R=0.00352 m, E*=162.78 GPa, k=1.79339 and I=1.25133.

The maximum contact pressure is expressed as

$$p_m = \frac{3P}{2\pi ab} \qquad Equation\ 30$$

When the load **P** is known, the corresponding max pressure $\mathbf{p_m}$ can be determined using this equation. For instance, under the load of 200 N, the max pressure is 2.63 GPa. When the load increased to 2000 N, the max stress reached 5.67 GPa. The calculated contact stress between the two wheels under different load in the range from 200 N to 2000 N is summarised in Table 4.2-6.

Table 4.2-5 Young's modulus and Poisson ratio of WC (E_1, v_1) and steel (E_2, v_2) for contact stress estimation using ABAQUS

E_1	6E+11 Pa
v_1	0.21
E_2	2E+11 Pa
v_2	0.3

Table 4.2-6 The load applied on the WC/steel wheels (from 200 N to 2000 N) and their corresponding estimated Hertzian stress

Load(N)	Stress(GPa)
200	2.63
300	3.01
400	3.31
500	3.57
600	3.79
700	3.99
800	4.17
900	4.34
1000	4.5
1100	4.64
1200	4.78
1300	4.91
1400	5.03
1500	5.15
1600	5.26
1700	5.37
1800	5.47
1900	5.57
2000	5.67

2) Simulating the contact pressure between the wheel pair using Finite Element Analysis

In the Part module of ABAQUS, two wheels with the dimensions shown in Figure 4.2.3-1(b)&(c) were built. In the Property module, the material properties were defined and applied to the WC wheel and steel wheel respectively. Then in the Assembly module, the wheel pair were assembled to the contact position as shown in Figure 4.2.3-1(a). In the Interaction module, their contact mode is set as 'surface to surface contact', and the friction coefficient was set to 0. After that, the load and the degree of freedom of the wheels were set in the Load module. In the Mesh module, the Hexahedron element C3D8I was used to mesh the parts. Finally, the job was submitted for computation in the Job module and the results can be studied in the Visualization module.

Figure 4.2.3-2 shows the contour of the contact pressure on the surface of the bottom cylinder wheel under the load of 2,000 N. The obtained contact area is an ellipse as expected, and the maximum contact pressure is located in the centre of the contact area. Table 4.2-7 lists the simulated maximum contact pressure increasing from 2.193 GPa under 200 N to 5.348 GPa under 2000 N.

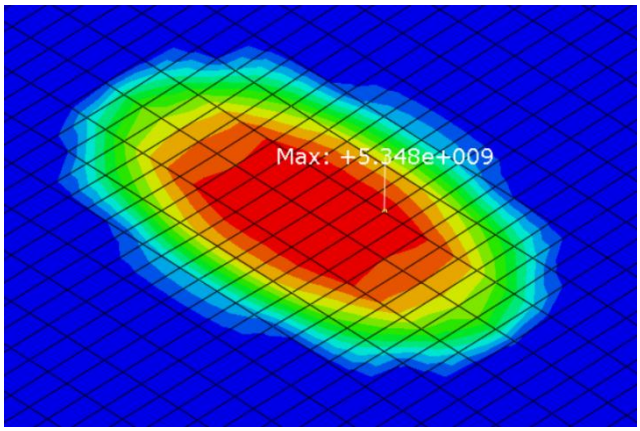

Figure 4.2.3-2 The contact pressure on the steel wheel surface under the load of 2,000 N (The WC wheel is set invisible to provide direct view of the surface contact pressure)

Table 4.2-7 The load applied on the WC/steel wheels (from 200 N to 2000 N) and the corresponding contact stress calculated using Abaqus

Load(N)	Stress(GPa)
200	2.193
300	2.714
400	3.127
500	3.361
600	3.549
700	3.723
800	3.883
900	4.022
1000	4.149
1100	4.271
1200	4.392
1300	4.508
1400	4.637
1500	4.81
1600	4.962
1700	5.073
1800	5.17
1900	5.26
2000	5.348

Figure 4.2.3-3 compares the contact pressure value obtained through Hertz analysis and ABAQUS simulation. It can be seen that the value of contact pressure obtained from both methods is increased under higher load, but the pressure value anticipated using Hertzian analysis is always higher than those from ABAQUS simulation under the load between 200 N and 2000 N. The contact pressure difference between ABAQUS and Hertzian analysis is shown in Figure 4.2.3-3. The difference between the pressure values obtained from the two methods is as high as 16.6 % under the lowest load 200 N. However, beyond that, the difference is in the range from 5 % to 10 % under loads between 300 N and 2000 N.

This simulation indicates that the contact pressure simulated using ABAQUS is very close to that estimated using the Hertzian contact theory.

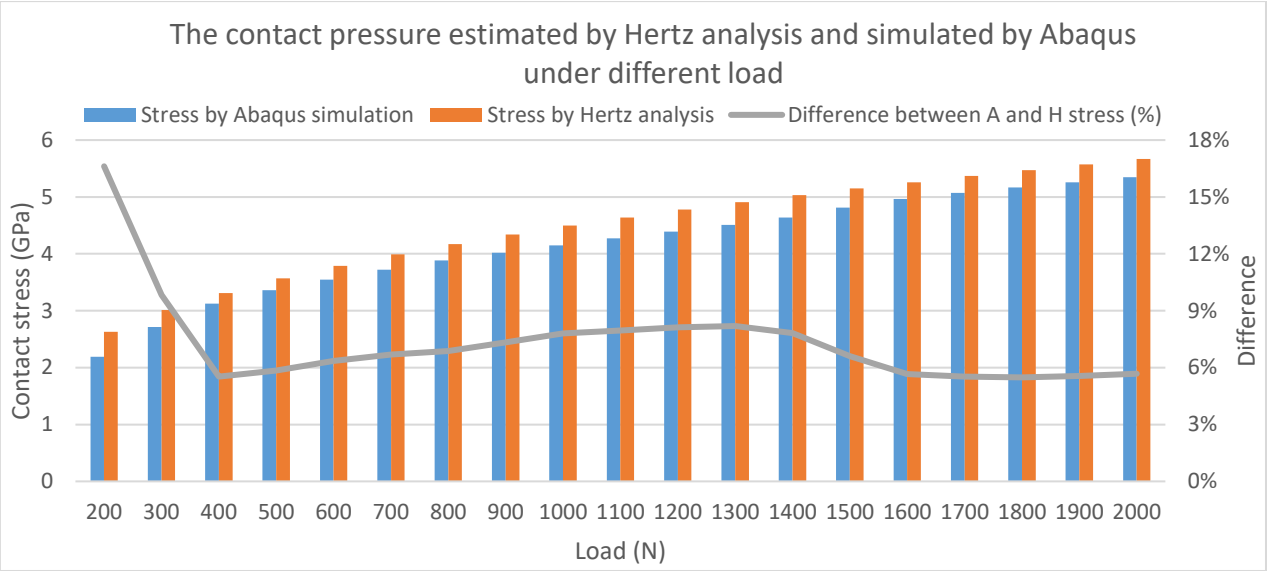

Figure 4.2.3-3 Comparison of the contact pressure estimated by Hertz analysis and Abaqus simulation under different load from 200 N to 2000 N

4.3 Surface engineering of wind gearbox materials

In order to prevent the life-limiting problems of wind turbine gearbox components, novel surface engineering systems with excellent properties, such as low friction coefficient, high hardness and high load-bearing capacity, have been designed relevantly to mitigate the effects of identified failure causes, such as high friction due to poor lubrication condition, and local contact stress concentration due to high load and misalignment.

EN36 and EN40BT steels were used as substrate for surface treatment in this project. The as-received EN36 and EN40BT were characterised firstly. Then, EN36 samples were carburised and EN40BT were nitrided successfully. Nitrided samples possess similar or higher hardness at much lower treating temperature than carburised sample. Duplex surface systems were designed as DLC coating deposited on surface hardened EN36 and EN40BT steel. For the purpose of comparison, single surface systems, i.e. DLC coating deposited on as-received steel samples, were also produced. The properties and performance of duplex surface systems

were evaluated and compared with single coating systems and carburised samples to demonstrate the advantages of duplex surface systems.

4.3.1 As-received EN36 and EN40BT materials

EN36 and EN40BT steels were used as substrate for surface treatment in this project. Before surface treatment, the as-received EN36 and EN40BT were characterised.

EN36 was supplied in the as-rolled condition, no heat treatment has been carried out on this material. The hardness of as-received EN36 is 356.87±9.99 HV0.05. The microstructure of as-received EN36 is shown in the optical micrograph Figure 4.3.1-1, from which ferrite and pearlite can be identified. The elongation of grains along the hot rolling direction is observed, which is common in the hot rolled steels (FA Khalid et al., 1999). Some coarse stripped inclusions were also observed in the micrograph, and these inclusions were also along the rolling direction. It is very likely that the inclusions found in EN36 were MnS, a common inclusion in traditional steels, and it is known that the soft MnS inclusions will be elongated in the direction of rolling during steel manufacture (CE Sims and FB Dahle, 1938, T Bruce et al., 2016). This surmise was proved using EDS analysis (as shown in Figure 4.3.1-2), high content of Mn and S was detected. MnS inclusions may act as the stress raiser and nuclei of cracks (L. de Campos Franceschini Canale, 2008). Moreover, the long, thin and narrow MnS inclusions may themselves act as or easily become real cracks (S. K. Dhua et al., 2000, T Bruce et al., 2016). Only peaks of α-Fe can be seen in the XRD spectrum of as-received EN36 (as shown in Figure 4.3.1-3).

It is known that surface roughness R_a plays an important role in friction, adhesion and lubrication degree (e.g. the ratio Λ of lubricant thickness to surface roughness). Moreover, the surface roughness Ra normally changes after surface treatment. Hence, the R_a of the sample

surface was measured. Surface roughness R_a of as-ground EN36 was 29.37 ± 1.86 nm (1200 grit sandpaper). After polishing, its Ra reduced to 18.72 ± 2.15 nm.

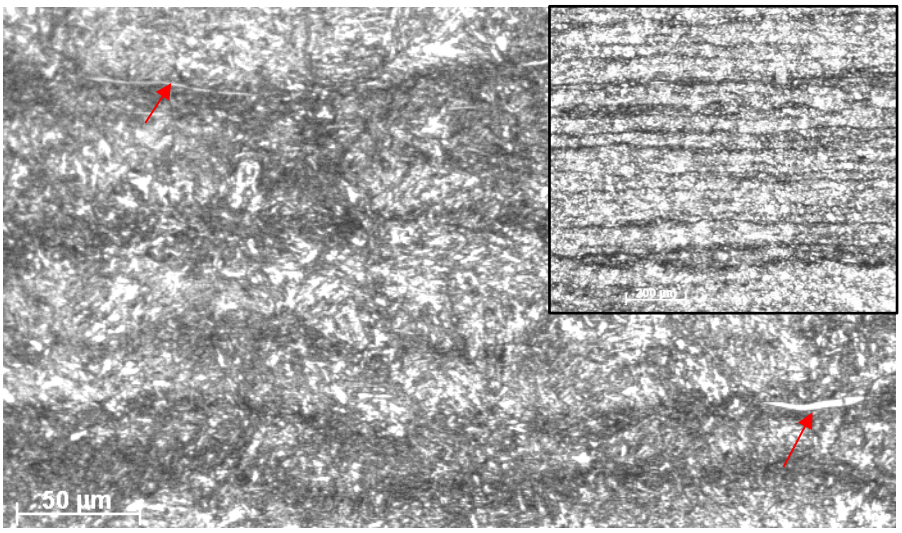

Figure 4.3.1-1 Optical micrograph of EN36 (2% Nital, top right 50×, background 200×), indicating ferrite and pearlite structure and some inclusions as arrowed.

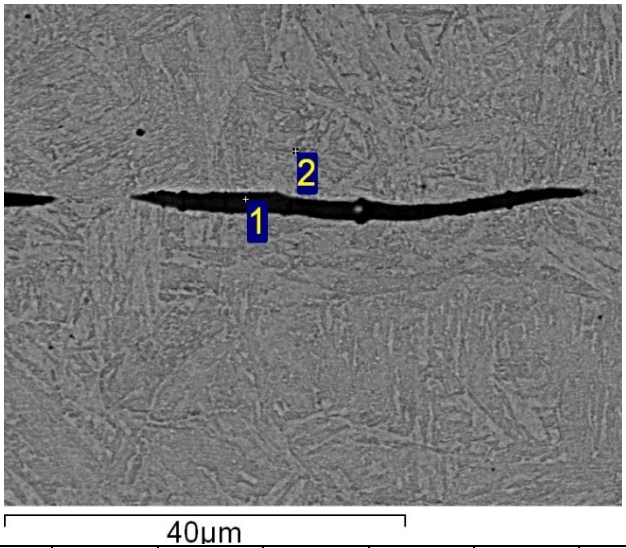

Spectrum/w%	C	Si	S	Cr	Mn	Fe	Ni	Comment
1	1.60	0.30	14.67	1.52	23.77	57.33	0.82	MnS
2	1.31	0.41		1.86	0.93	94.07	1.41	Steel matrix

Figure 4.3.1-2 SEM image and EDS results of EN36 and MnS inclusion

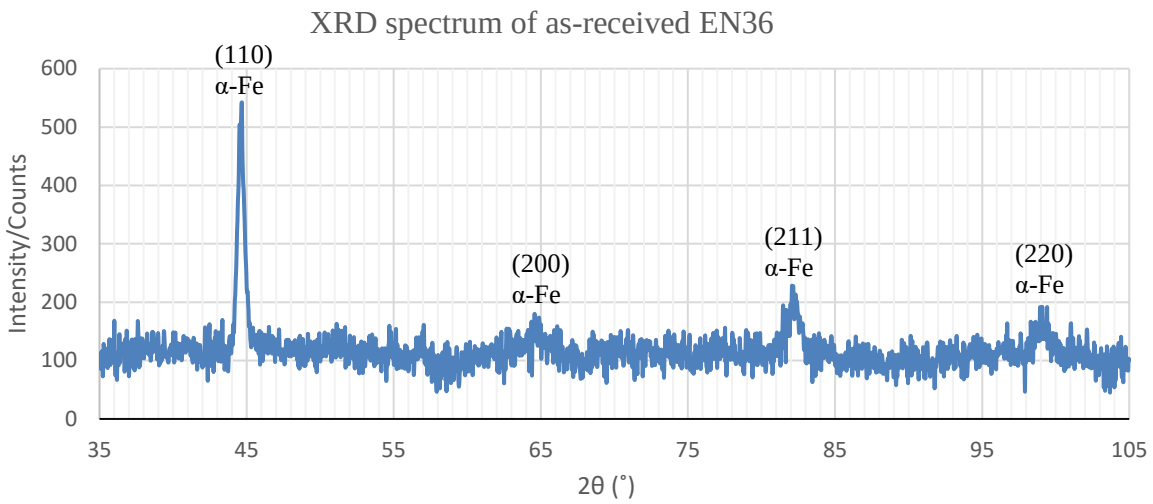

Figure 4.3.1-3 XRD pattern of as-received EN36

EN40BT was received in the hardened and high-temperature tempered condition (between 570 and 700 °C). Its hardness is 321.47 ± 8.76 HV0.05 on average. As shown in Figure 4.3.1-4, the microstructure of as-received EN40BT is dominated by high-temperature tempered martensite (also called as tempered sorbite in old-fashioned books). High-temperature tempering is normally conducted to obtain enough toughness and ductility, at the price of decreased hardness and some strength. Some script type inclusions were also observed, and they were still MnS, as confirmed through SEM and EDX (as shown in Figure 4.3.1-5). The peaks in the XRD pattern of as-received EN40BT (as shown in Figure 4.3.1-6) represent alpha prime iron. The surface roughness R_a of as-ground EN40BT was 27.22 ± 2.52 nm. On polished surface, the Ra decreased to 16.83 ± 1.63 nm.

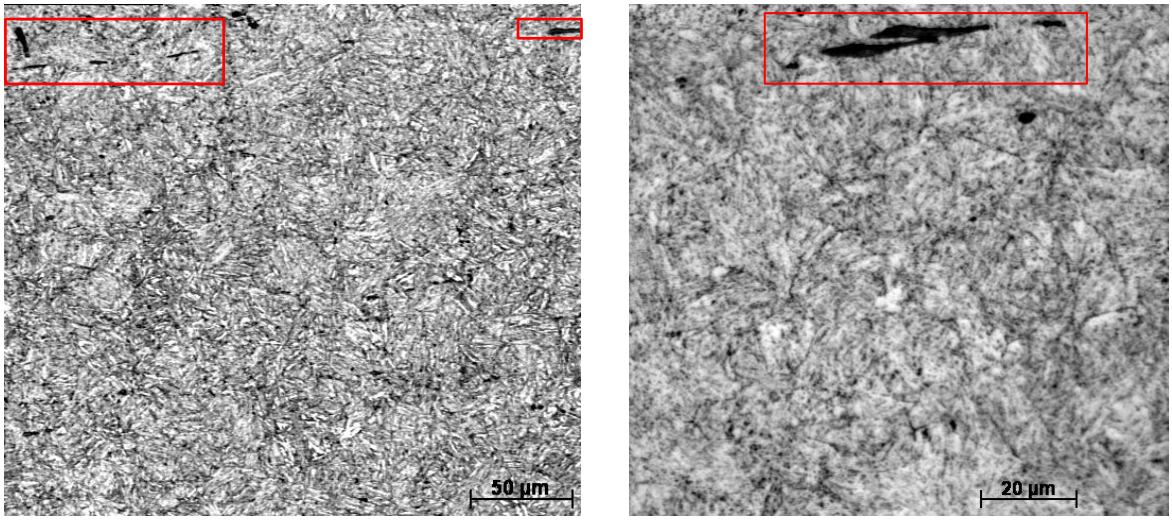

(a) (b)

Figure 4.3.1-4 Optical micrographs of EN40BT (2% Nital as etchant, left 200×, right 500×), illustrating high-temperature tempered martensite (also called as tempered sorbite) and stripped inclusions (as framed)

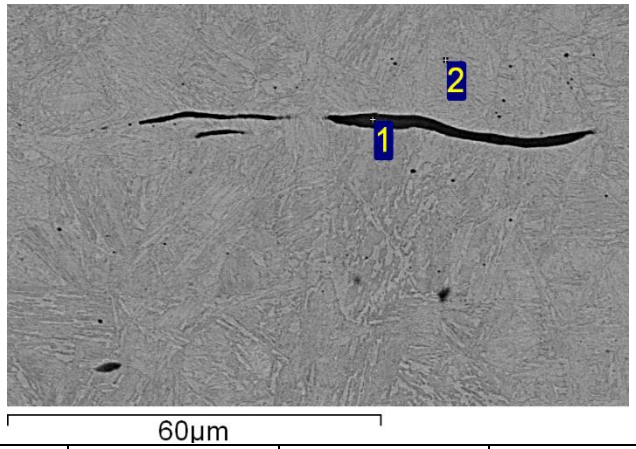

Spectrum	C	S	Cr	Mn	Fe
1	1.81	11.53	3.38	17.50	65.78
2	1.21	0.36	3.91	0.59	93.93

Figure 4.3.1-5 SEM image and EDX result (wt%) of as-received EN40BT and MnS inclusions

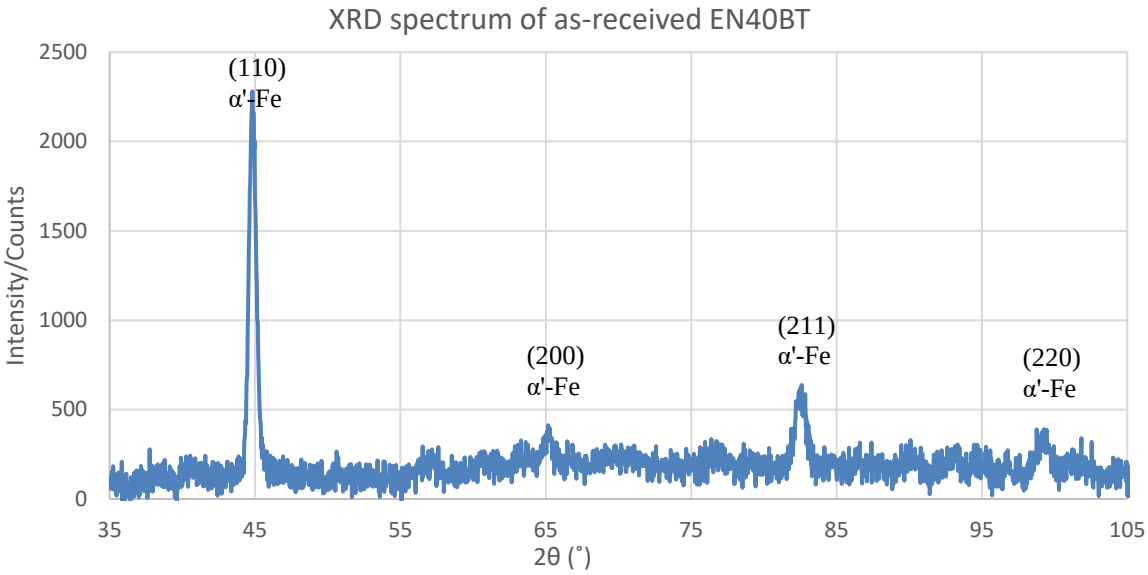

Figure 4.3.1-6 XRD spectrum of as-received EN40BT

4.3.2 Carburised EN36

Atmosphere carburising treatment of EN36 was performed at a temperature of 920 – 930 °C, followed by hot oil quenching in a sealed quench furnace. Then the carburised EN36 samples were characterised and evaluated. The results revealed that the properties of carburised EN36 samples were desirable and consistent with the recommended values in international standards for carburised gears (ISO, 2003). Since carburised steels have been widely used to produce gears and bearings, its rolling-sliding wear performance was evaluated.

4.3.2.1 Characterisation of carburised EN36

The carburised EN36 samples were characterised to evaluate whether their microstructure and mechanical properties are desirable and meet the international standards.

As can be seen from Figure 4.3.2-1, the untreated wheel sample made of EN36 with as-polished surface finish was mirror-like and shiny, while the carburised wheel lost the original metallic lustre and became in the colour of dull grey.

Under SEM, only some scratches were observed in the untreated EN36 wheel surface (Figure 4.3.2-2(a)). After carburising, the surface finish became rougher, and the surface was covered with condensed papillae (Figure 4.3.2-2(b)).

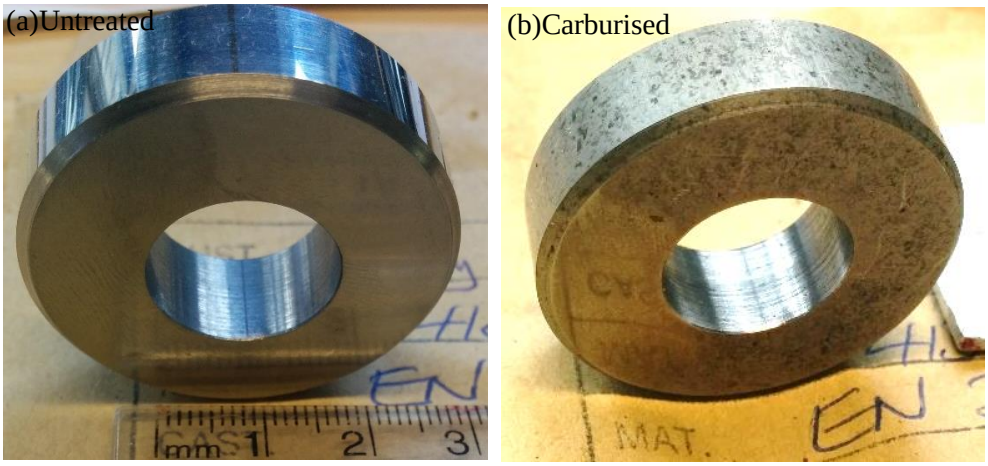

Figure 4.3.2-1 Digital camera images of untreated (left) and carburised (right) EN36 wheels

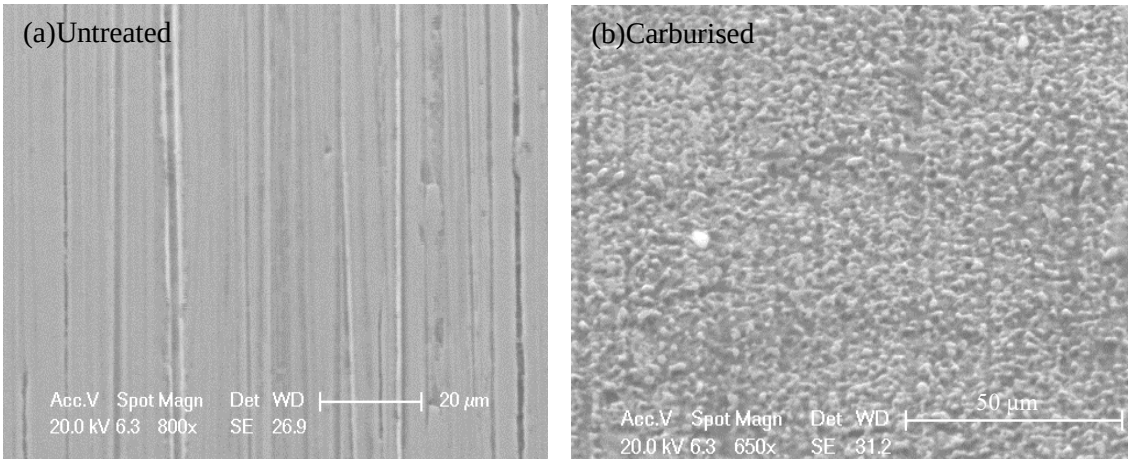

Figure 4.3.2-2 SEM images of untreated (left) and carburised (right) EN36 wheel surface

The surface roughness Ra of carburised sample increased dramatically to 0.1789 ± 0.0090 µm after carburising from around 0.0187 µm for the as-polished samples. The friction coefficient of carburised EN36 is 0.46±0.03. After repolishing, the Ra decreased to 0.0205 ± 0.0013 µm.

Comparing the XRD pattern of untreated with carburised EN36 (Figure 4.3.2-3), all α-Fe peaks shifted to the left and became broader after carburising. This alteration can be explained as α-Fe was expended by carbon in the diffusion zone. The XRD pattern of carburised EN36 did not show any peaks of undesirable residual austenite (γ-Fe).

The hardness-depth profile of carburised EN36 (Figure 4.3.2-4) revealed that the superficial hardness is around 850 HV0.05, then it drops slowly with the depth until reaches the hardened core material which was around 600 HV0.05, thus the case depth was about 2 mm.

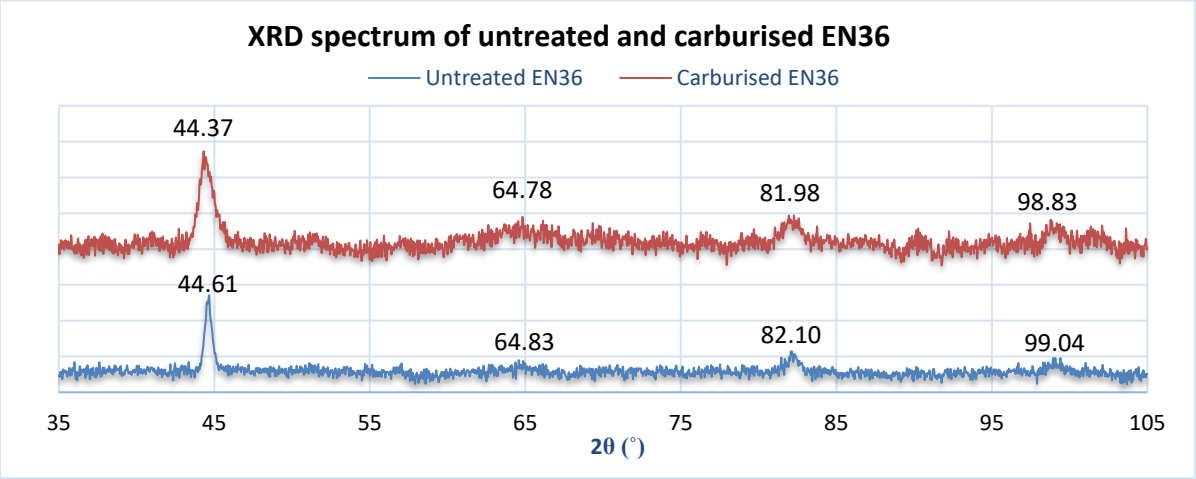

Figure 4.3.2-3 XRD pattern of untreated and carburised EN36

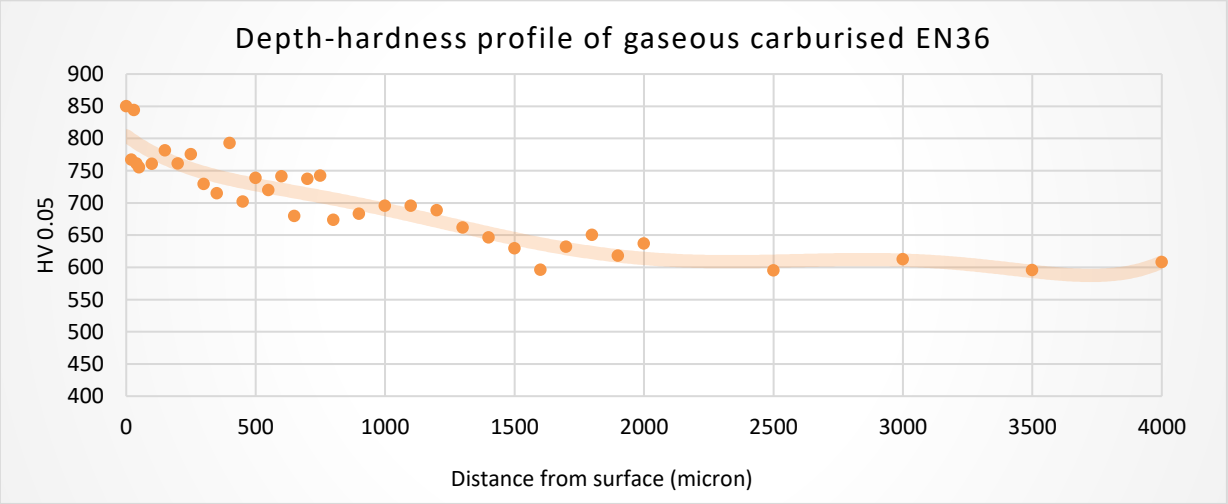

Figure 4.3.2-4 Depth-hardness profile of carburised EN36 (up to 4,000 μm from surface) indicating that the superficial hardness is around 850 HV0.05, the core hardness is around 600 HV0.05,

In the optical micrograph of carburised EN36, the dominant microstructure was fine high-carbon martensite in the surface and subsurface area (Figure 4.3.2-5(a)). In the core area, the microstructure is low-carbon martensite (Figure 4.3.2-5(b)). Undesirable continuous carbide precipitation was not found.

Based on the characterisation, it can be concluded that the properties of carburised EN36 samples were desirable and consistent with the recommended values in international standards for carburised gears (ISO, 2003).

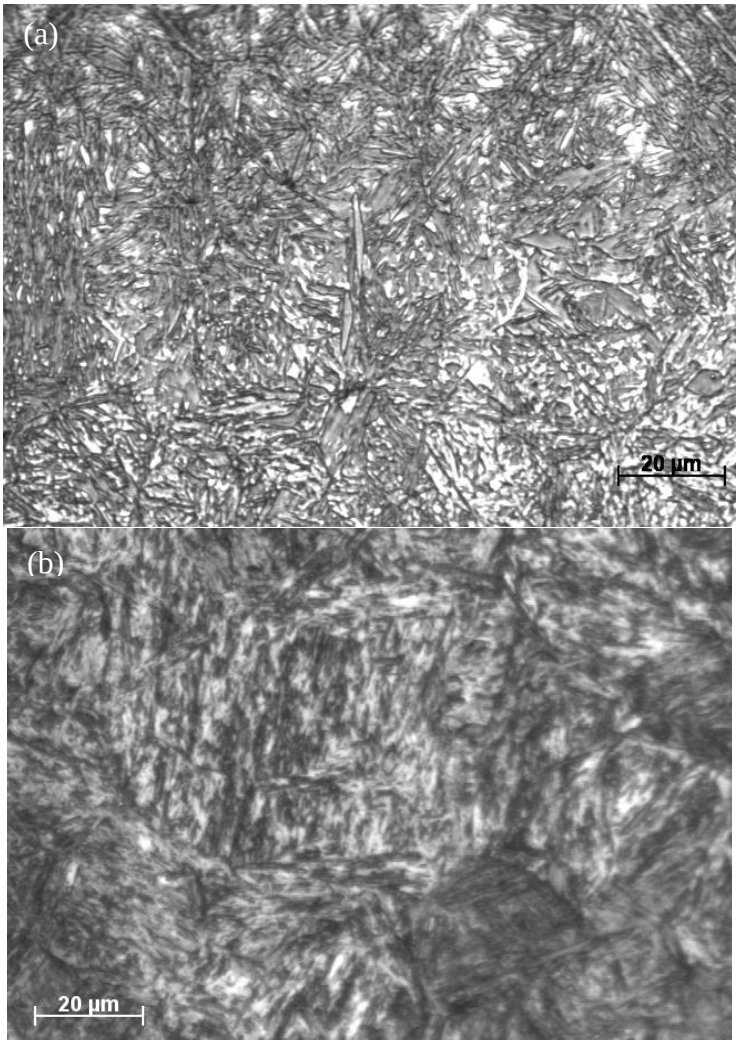

Figure 4.3.2-5 Optical micrograph of cross section of carburised EN36, (a) surface and subsurface area, and (b) core area

4.3.2.2 Rolling-sliding wear performance of carburised EN36

The rolling-sliding wear tests were conducted in oil and dry conditions, to simulate carburised gears or bearings working in wind turbine gearbox with good lubrication and inadequate lubrication respectively. The angular speed of bottom wheel was 10% faster than the top wheel, and both the wheels had the same diameter, thus the slip ratio is about 10.5 %.

4.3.2.2.1 With lubrication

With good lubrication (engine oil), the wear of carburised En36 wheels was neglectable, even under the load of 200 kg, i.e. 1,010 MPa, for as long as 284 hours. The weight of two wheels only slightly changed from 63.4342 g to 63.4317 g for the top wheel, and from 63.3387 g to 63.3350 g for the bottom wheel (Figure 4.3.2-6). The average wear rate for the top and bottom wheels were only about 0.009 mg/hour and 0.013 mg/hour respectively. Most of the weight loss happened at the beginning of the test, then the weight of both the wheels was quite stable. It proves, with good lubrication, the severe adhesive wear can be avoided in the carburised material.

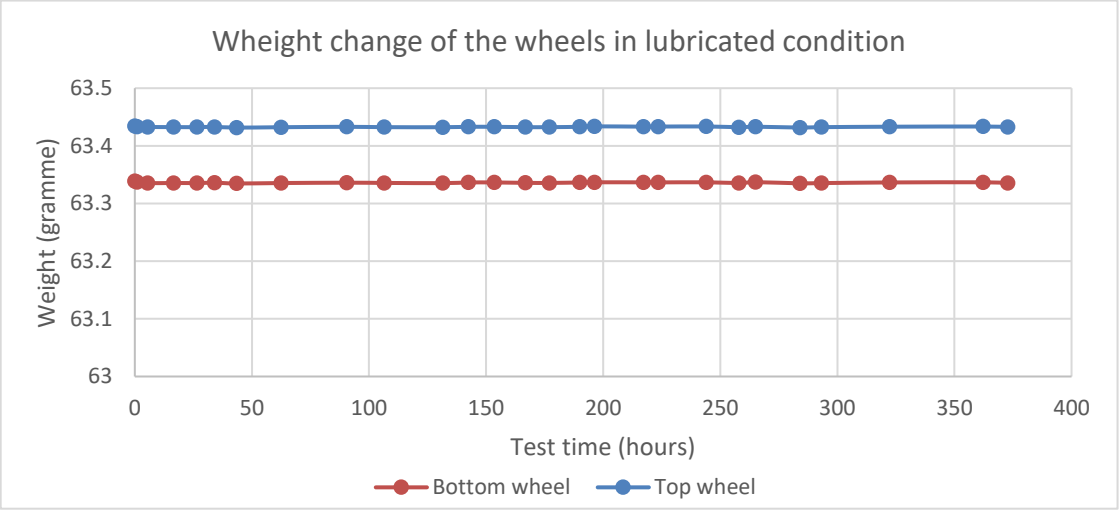

Figure 4.3.2-6 Weight of the rolling-sliding samples were stable in lubricated condition

Observed by naked eyes, the sample surface did change, but obvious damage, such as cracks or macro-pits, were not found on the sample surface (Figure 4.3.2-7). Under SEM, it is found that all the papillae on the as-carburised surface have been polished to some level (as shown in Figure 4.3.2-8). It explains the slight weight reduction of wheels.

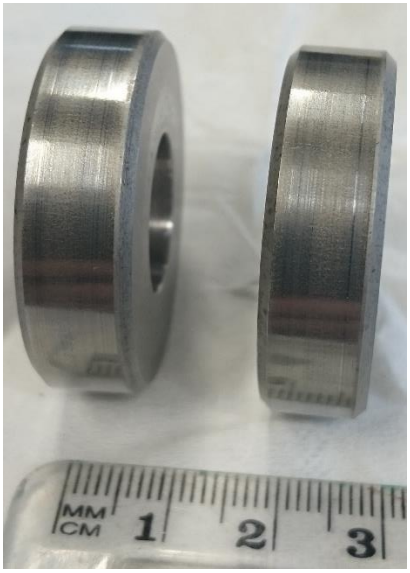

Figure 4.3.2-7 Photo of the wheel samples after 280 hours of the lubricated test, the left wheel is top wheel, the right is the bottom wheel

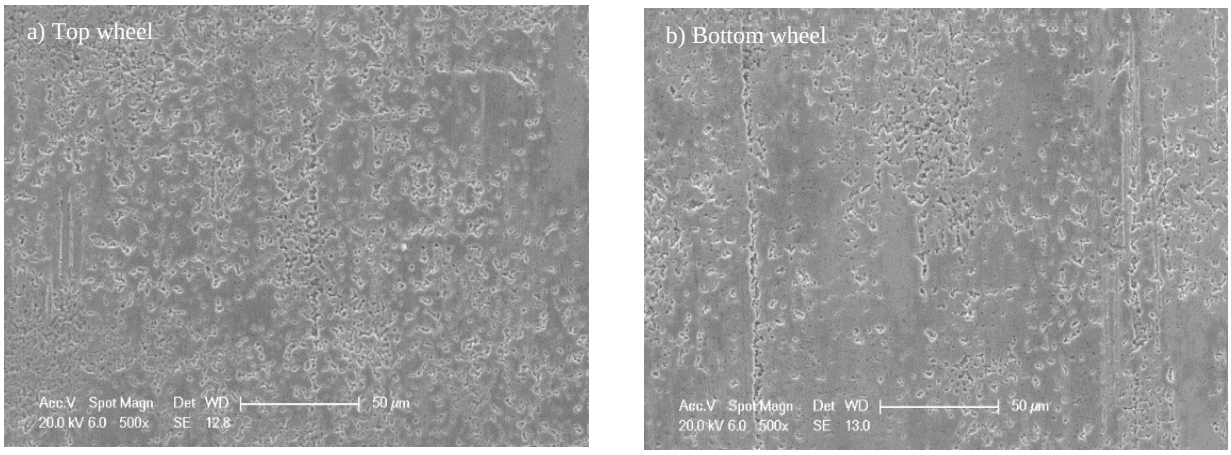

Figure 4.3.2-8 SEM images of the samples' surface after 250 hours of the lubricated test

4.3.2.2.2 Without lubrication

Once the lubricant is removed, the rolling-sliding wear of carburised EN36 is severe.

Two carburised wheel samples ran against each other in rolling-sliding wear tester under the load of 200 kg (equals 1,010 MPa Hertz contact stress) for about 122 hours without lubricant, the line graph Figure 4.3.2-9 shows the weight loss of each wheel, the top wheel lost more weight than bottom one. The average wear rate was 40.8 mg/hour and 29.5 mg/hour for the top and bottom wheels respectively.

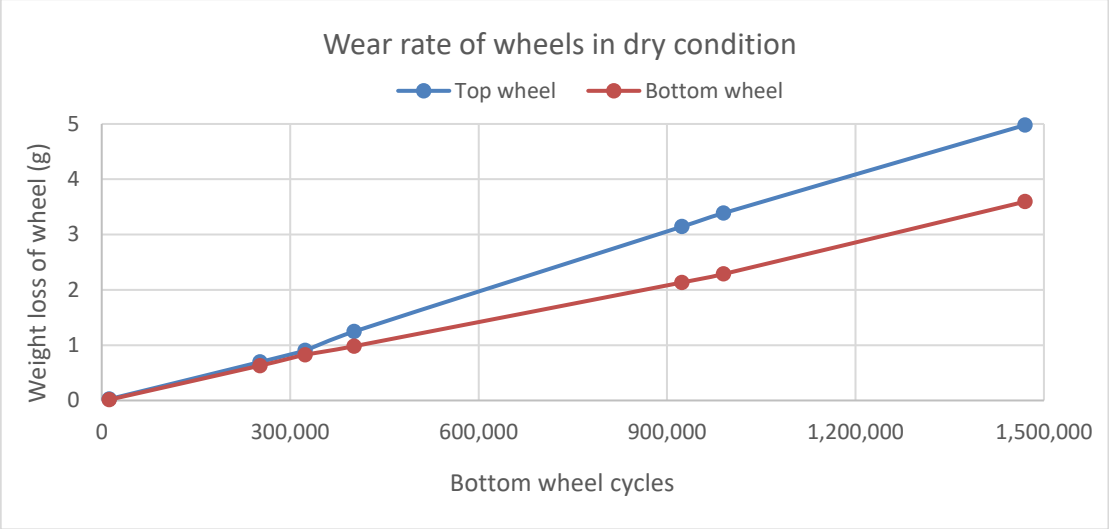

Figure 4.3.2-9 Weight loss of the top and bottom wheels through the unlubricated rolling-sliding wear test

Surface morphology and EDS analysis of both worn wheels are shown in Figure 4.3.2-10. Grooves can be clearly identified on top wheel. While, on bottom wheel surface, a lot of strips can be found. This implies the material of top wheel was torn away and transferred to the bottom wheel, so the top wheel lost more weight than the bottom wheel. The material transfer between the wheel pair also indicates the wear mechanism is adhesive wear. The EDS results illustrate the wheel surface was oxidised.

Figure 4.3.2-11(a) shows that the wear debris is in 2-dimensional flake/platelet shape mostly and their size is various. The 2D platelet debris normally indicates metal-to-metal contact (Amin Almasi and Rotating Machinery Consultant, 2014). The EDS result of these flake

debris (Figure 4.3.2-11(b)) also shows that the contact surface was oxidised. Therefore, the unlubricated rolling-sliding wear mechanism of carburised EN36 can be a combination of oxidation wear and adhesive wear.

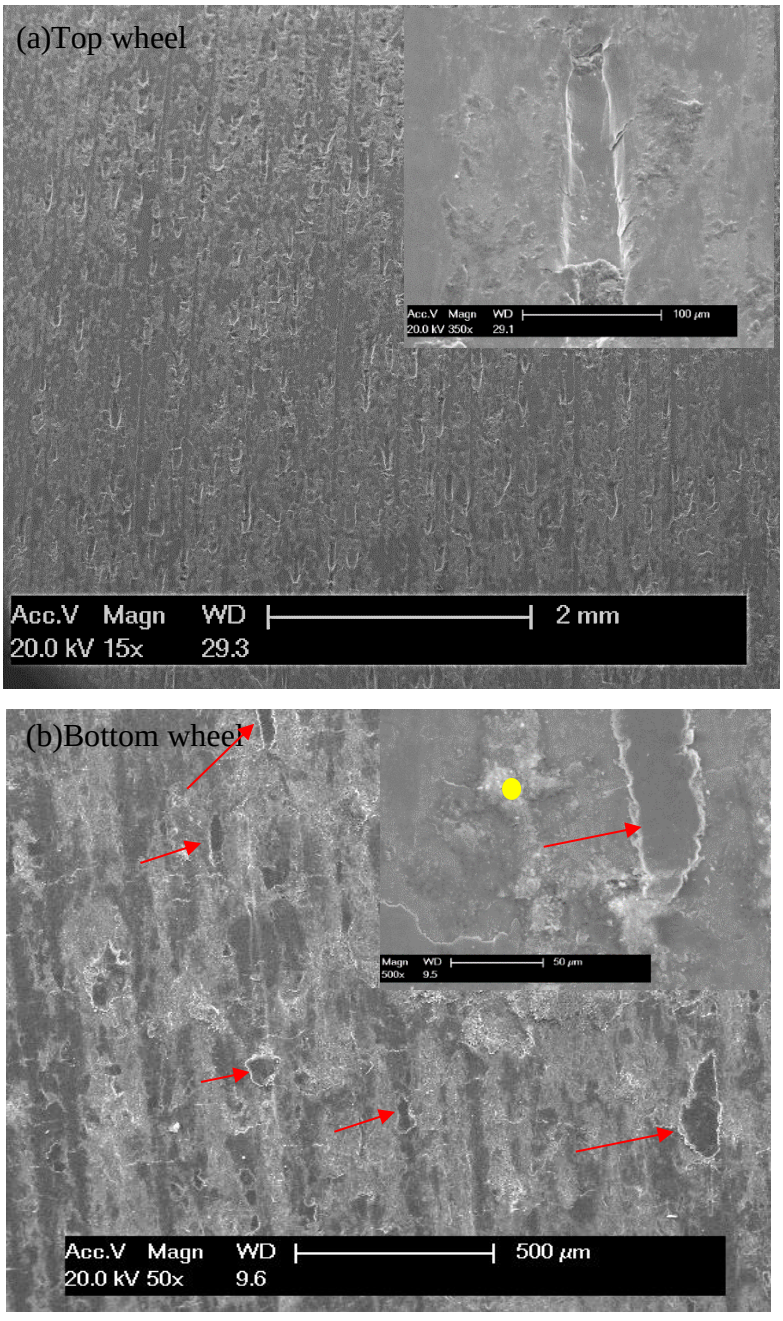

Elements	C	O	Si	Cr	Fe	Ni	Total
Weight%	5.77	11.10	0.32	0.32	81.33	1.17	100

Figure 4.3.2-10 Surface morphology of carburised EN36 wheels after unlubricated rolling-sliding wear test indicating a severe adhesive wear, (a) the top wheel and (b) the bottom wheel (The red arrows show the strips) and EDS results. The EDS analysis indicates the contact surface was oxidised (the yellow dot shows where the EDS spectrum came from).

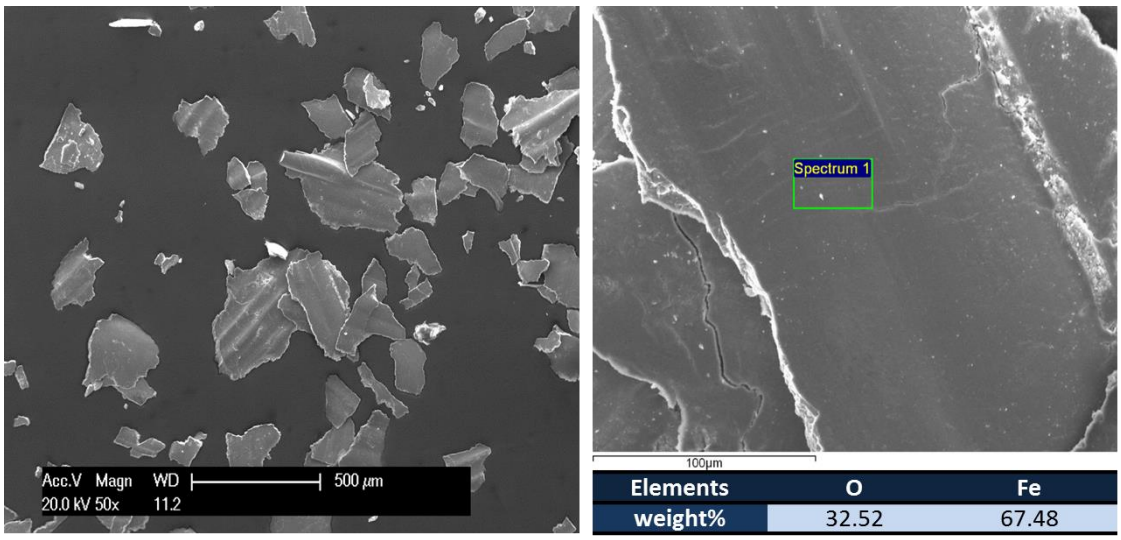

(a) (b)

Figure 4.3.2-11 (a) SEM image and (b) the EDS results of flake wear debris collected from unlubricated rolling-sliding wear test

The effect of different load (between 500 N and 800 N) on wear rate (weight loss) of carburised EN36 in dry condition with slip ratio 0.105 was studied (Figure 4.3.2-12). In general, the wear rate linearly increased with the load applied, and the top wheel lost more weight than the bottom one under the same load. Under the load of 500 N (505.03 MPa), the wear rate of the top wheel was 22.0 mg/hour, bottom wheel 12.0 mg/hour. Under the load of 600 N (553.23 MPa), top wheel lost weight 22.3 mg per hour, bottom 13.6 mg per hour. When the load increased to 700 N (597.56 MPa), the wear rate for the top and bottom wheel was 24.1 mg/hour and 15.4 mg/hour respectively. At the load of 800 N (638.82 MPa), the wear rate was 24.5 mg/hour for the top wheel and 17.1 mg/hour for the bottom. Combing with the wear rate under the load of 2000 N (1010 MPa), the linear trend of wear rate between the contact stress 500 MPa and 1000 MPa is shown in Figure 4.3.2-13. It clearly shows that without lubrication, the wear rate of carburised EN36 is very high and the wear rate increases with load.

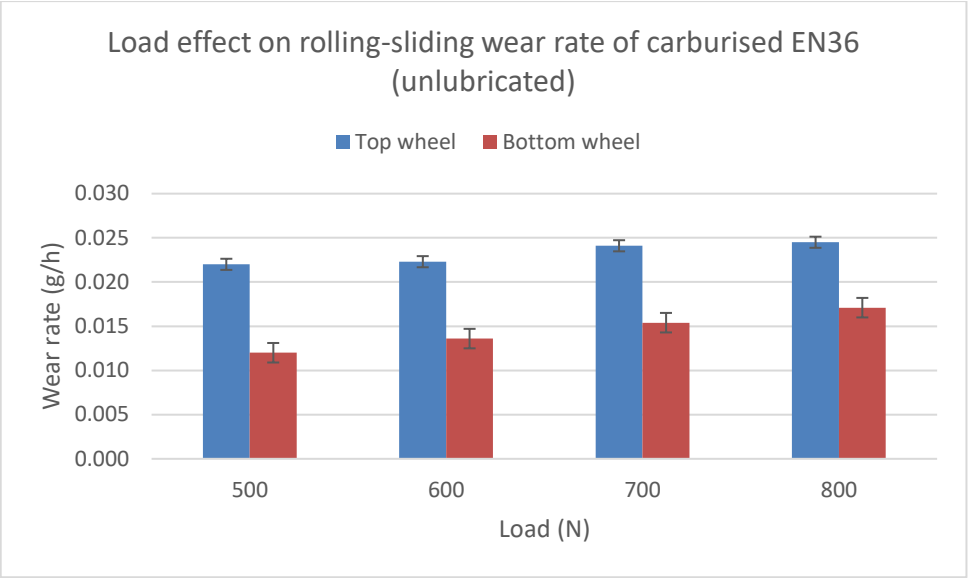

Figure 4.3.2-12 Load effect on rolling-sliding wear rate of carburised EN36 in dry condition (top wheel speed 180 rpm, bottom wheel 200 rpm, slip ratio 0.105)

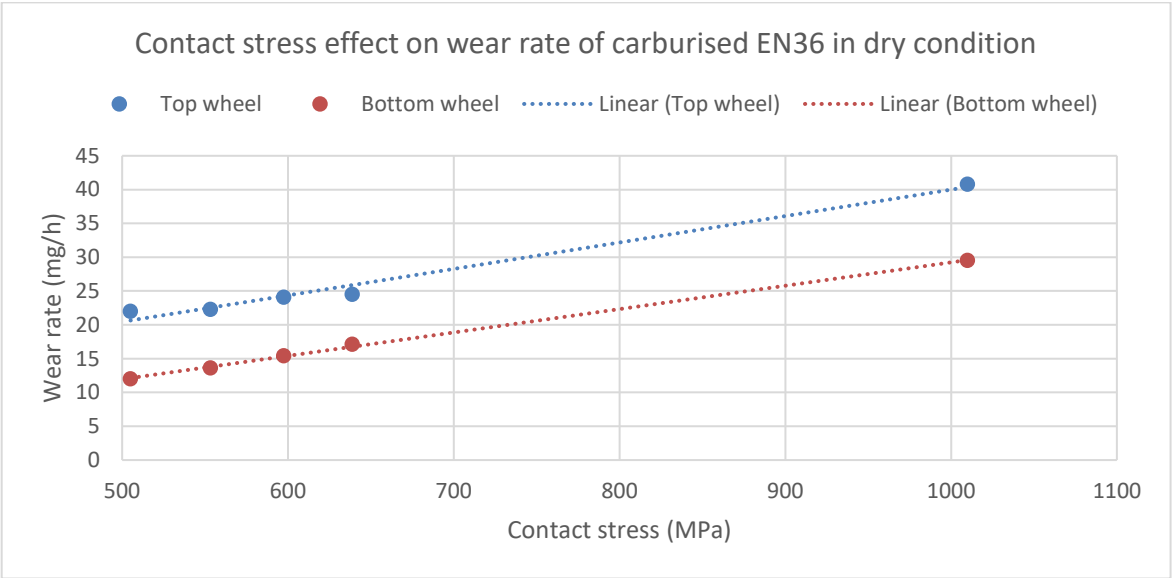

Figure 4.3.2-13 Contact stress effect on wear rate of carburised EN36 in dry condition

In summary, the properties of carburised EN36 samples were desirable and consistent with the recommended values stated in international standards for carburised gears (ISO, 2003). In dry condition (without lubrication) under the load of 1.010 GPa, the average rolling/sliding wear rate of carburised EN36 was extremely high as 40.8 mg/hour and 29.5 mg/hour for the

top and bottom wheels respectively. The major wear mode was attributed to severe adhesive wear. During good lubrication (engine oil), the wear of the carburised EN36 wheels became negligible. The average wear rate for the top and bottom wheels were only about 0.009 mg/hour and 0.013 mg/hour respectively. It shows that with good lubrication, severe adhesive wear can be avoided in the carburised material.

4.3.3 Nitrided EN40BT

Compare with carburising, nitriding can be conducted at a much lower temperature, thus reducing distortion of components, which make nitriding an alternative case-hardening method to carburising. In this study, the surface of EN40BT has been effectively hardened by direct-current plasma nitriding (DCPN) and active-screen plasma nitriding (ASPN) methods. The nitrided EN40BT samples with different treating time and temperature were characterised and compared.

4.3.3.1 Direct-current plasma nitriding (DCPN)

Comparing with traditional gas nitriding and liquid nitriding methods, plasma nitriding is more environmentally friendly. The EN40BT samples nitrided using DCPN method have been characterised to study the effect of DCPN process on the EN40BT steel.

Figure 4.3.3-1 shows surface morphology of sample DCPN530-20, which is very rough. The rough surface morphology is believed to be the result of combination of plasma sputtering effect and nitride precipitation effect on the sample surface (H. Aghajani and S. Behrangi, 2016).

The cross-sectional microstructure of DCPN530-20 is shown in (Figure 4.3.3-2). A very dense and hard compound layer (white layer) is found on the surface. Below the compound

layer, the nitrogen diffusion zone can be clearly identified, where the area close to the top surface is much darker than the core. The darker colour of diffusion zone is from the precipitation of nitrides, which formed after the nitrogen content exceeded its solid solubility.

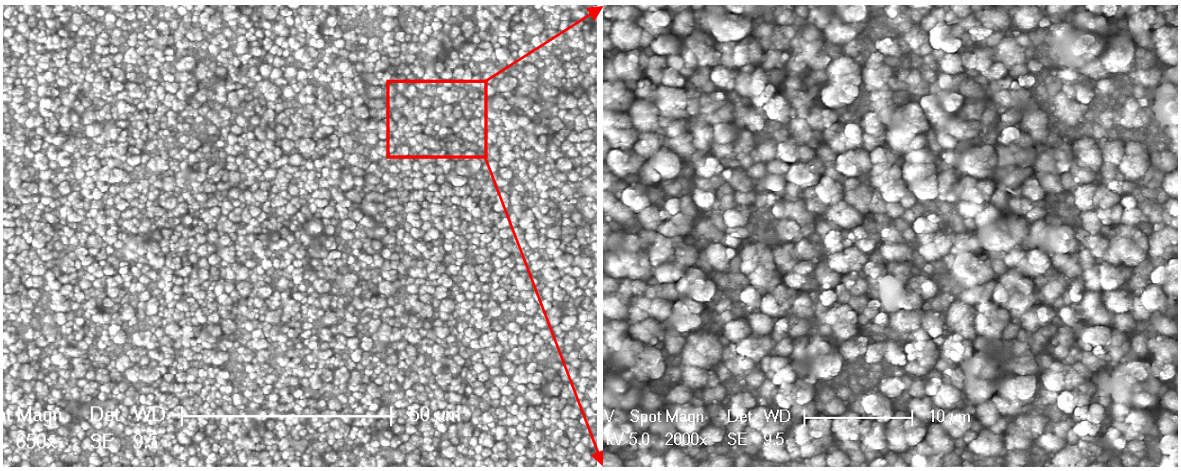

Figure 4.3.3-1 Surface morphology of direct-current plasma nitrided EN40BT sample DCPN530-20

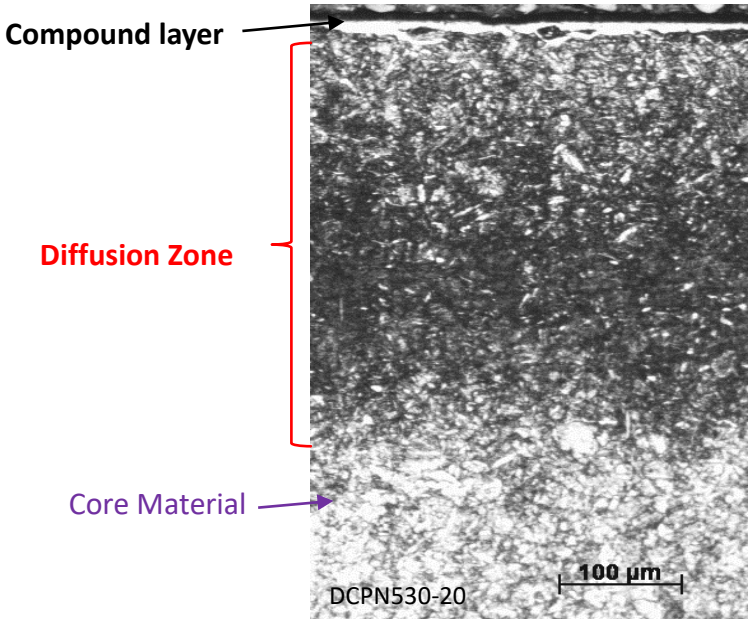

Figure 4.3.3-2 Optical image of the cross section of direct-current plasma nitrided EN40BT sample DCPN530-20

Figure 4.3.3-3 shows the XRD pattern for as-received EN40BT and DCPN530-20. Compared with as-received EN40BT, the peak of α'-Fe can still be identified in DCPN530-20, but its

intensity has greatly reduced. Strong peaks of γ'-Fe_4N are identified in DCPN530-20, indicating the major phase of the hardened surface.

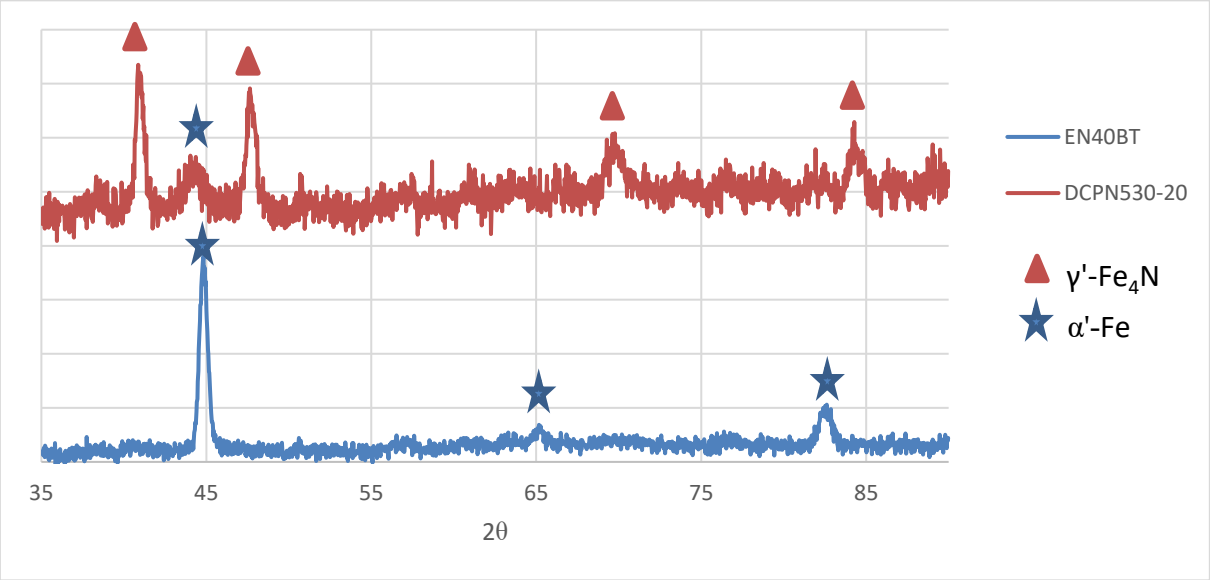

Figure 4.3.3-3 XRD spectra of as-received EN40BT and direct-current plasma nitrided EN40BT (DCPN530-20)

To study the temperature and time effect of direct-current plasma nitriding (DCPN), samples DCPN550-20, DCPN570-20, DCPN530-40 and DCPN530-60 were produced and characterised.

After direct-current plasma nitriding, the samples' surface roughness Ra increased dramatically from that of as-polished EN40BT (Figure 4.3.3-4), which can be explained by the combination of sputtering effect of plasma and growth of nitride precipitates on the sample surface. For example, Ra of DCPN530-20 is as high as 0.3479 μm, while that of as-polished EN40BT is only 0.0168 μm, i.e. the Ra of DCPN530-20 is about 20 times higher than that of as-polished sample. In addition, it is found from Figure 4.3.3-4 that longer treating time and higher treating temperature increases the Ra further, especially the treating temperature. Take the sample DCPN570-20 with Ra of 0.7143 μm for instance, its Ra is more

than twice of that for DCPN530-20. The very high Ra value of DCPN570-20 is thought related to the extremely strong sputtering effect at high temperature.

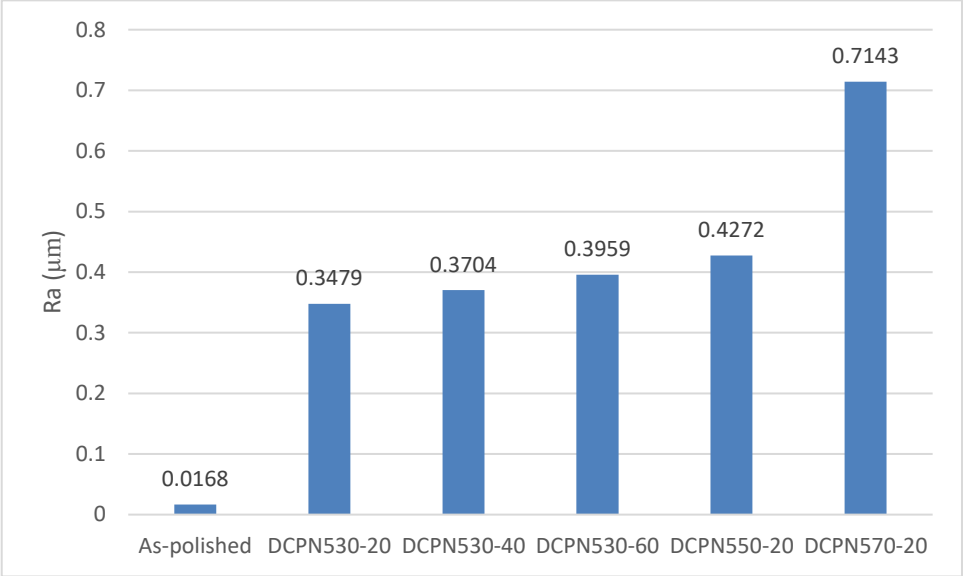

Figure 4.3.3-4 Surface roughness of as-polished EN40BT and DCPN samples with different treating conditions

Figure 4.3.3-5 shows the cross-sectional microstructures of DCPN550-20, DCPN570-20, DCPN530-40 and DCPN530-60. The darker diffusion zone is formed in all samples. However, the white compound layer is only formed on DCPN550-20, DCPN530-40 and DCPN530-60. No compound layer is found on the DCPN570-20, which can be explained as that the remove rate by the extremely strong sputtering effect is higher than the growth rate of compound layer.

The cross-sectional depth-hardness profiles of DCPN samples treated at 530, 550 and 570 ˚C for 20 hours, which measured under 0.05kg, are shown in Figure 4.3.3-6. Within the diffusion zone in all the samples, the hardness value drops gradually with the depth to its core hardness. The effective thickness of hardened case is defined as the distance from the surface to a point at which the hardness is 400 HV0.05. The effect thickness and maximum hardness of the nitrogen diffusion layers determined from the depth-hardness profiles are summarised in a table below the line graph. It can be seen that both the depth and hardness decreased when the

treatment temperature increases. The maximum hardness of DCPN530-20 and DCPN550-20 is close to each other, which are 963 and 920 HV0.05 respectively. The maximum hardness of DCPN570-20 is relatively low as 720 HV0.05. The reduction in surface hardness at higher nitriding temperatures is thought to be due to coarser alloy nitride precipitation at higher temperatures (Shahjahan Mridha and Ahsan Ali Khan, 2008). The effective harden case thickness of DCPN530-20, DCPN550-20 and DCPN570-20 is 360, 345 and 320 μm respectively. The decrease in case depth with increased temperature is thought to be due to the extremely strong sputtering effect removing more material away from the surface than the diffusion rate at a higher temperature. In terms of the effective depth and hardness, 530 and 550 °C is much better than the higher temperature 570 °C for direct current plasma nitriding of EN40BT.

It is noticed that the core hardness of DCPN samples is similar to the as-received EN40BT, which indicates that the DCPN treatment did not cause any unwarranted softening or strength reduction of the substrate material. This proves that the tempering temperature for the as-received EN40BT material is higher than 570 °C such that no over-tempering occurred during the plasma nitriding in this study. The XRD results of DCPN530-20,550-20 and 570-20 are shown in Figure 4.3.3-7. The phase composition of the 3 samples treated by DCPN at different temperature is identical, which is mainly γ'-Fe_4N and some α'-Fe. It is noticed that though no compound layer in the DCPN570-20, the detected peaks are possibly from the γ'-Fe_4N precipitates in the diffusion zone.

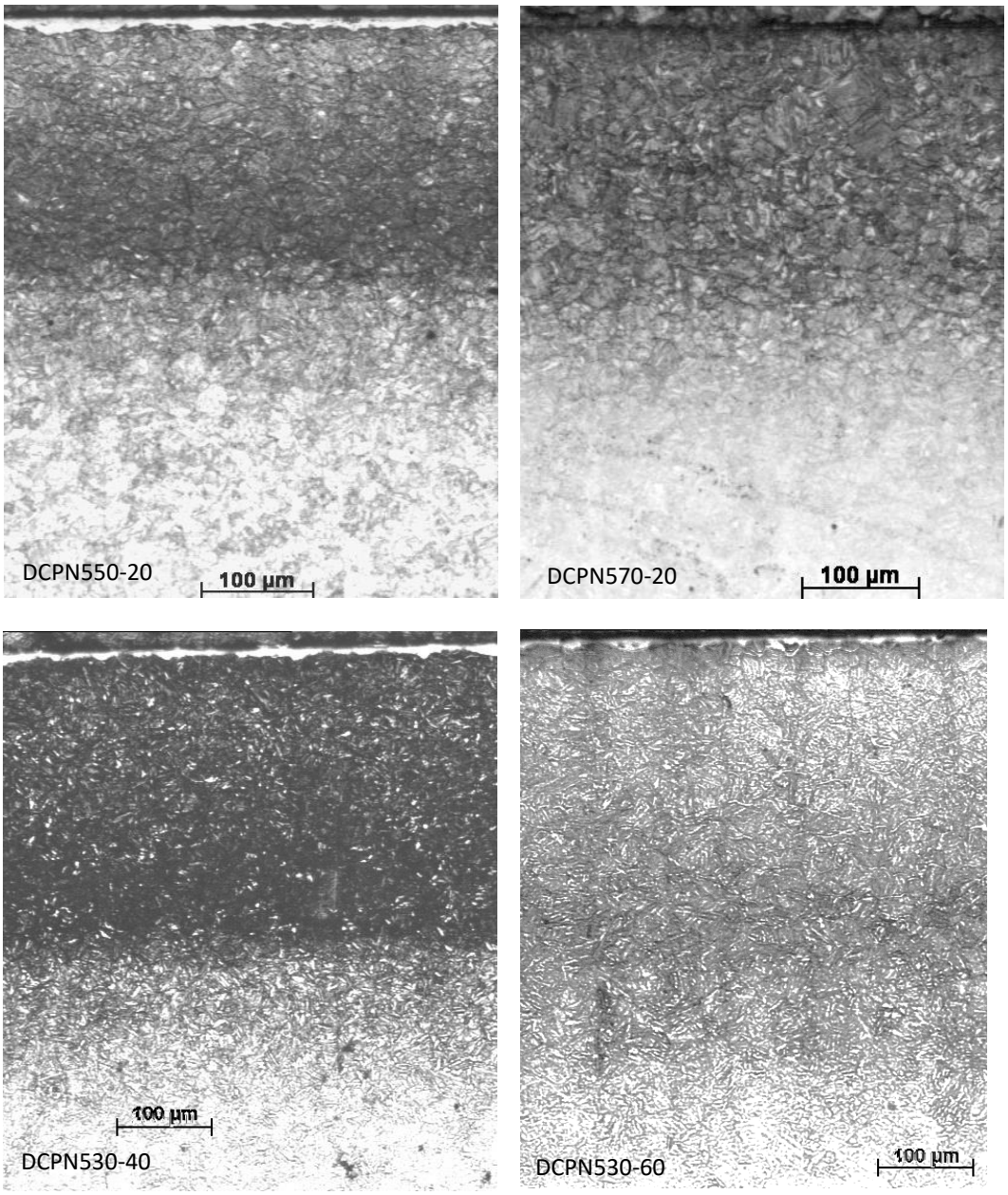

Figure 4.3.3-5 Optical images of cross section of direct-current plasma nitrided EN40BT sample DCPN550-20, DCPN570-20, DCPN530-40 and DCPN530-60

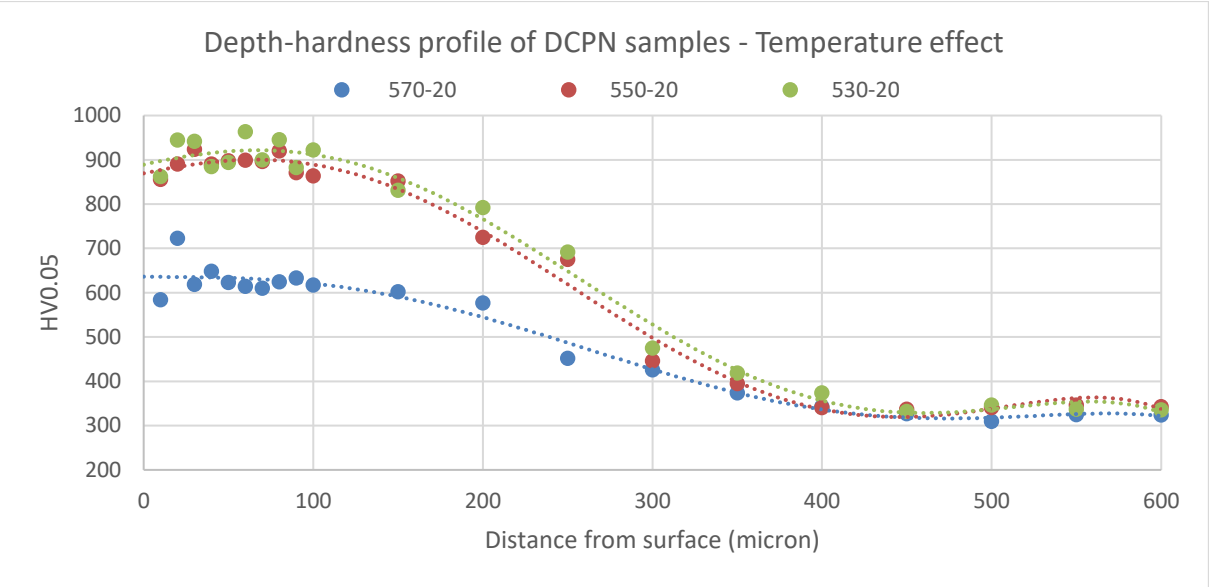

Sample code	Maximum hardness (HV0.05)	Effective nitride case depth (micron)
DCPN530-20	963	360
DCPN550-20	920	345
DCPN570-20	720	320

Figure 4.3.3-6 Hardness and thickness of DCPN samples treated at 530, 550 and 570 ˚C for 20 hours

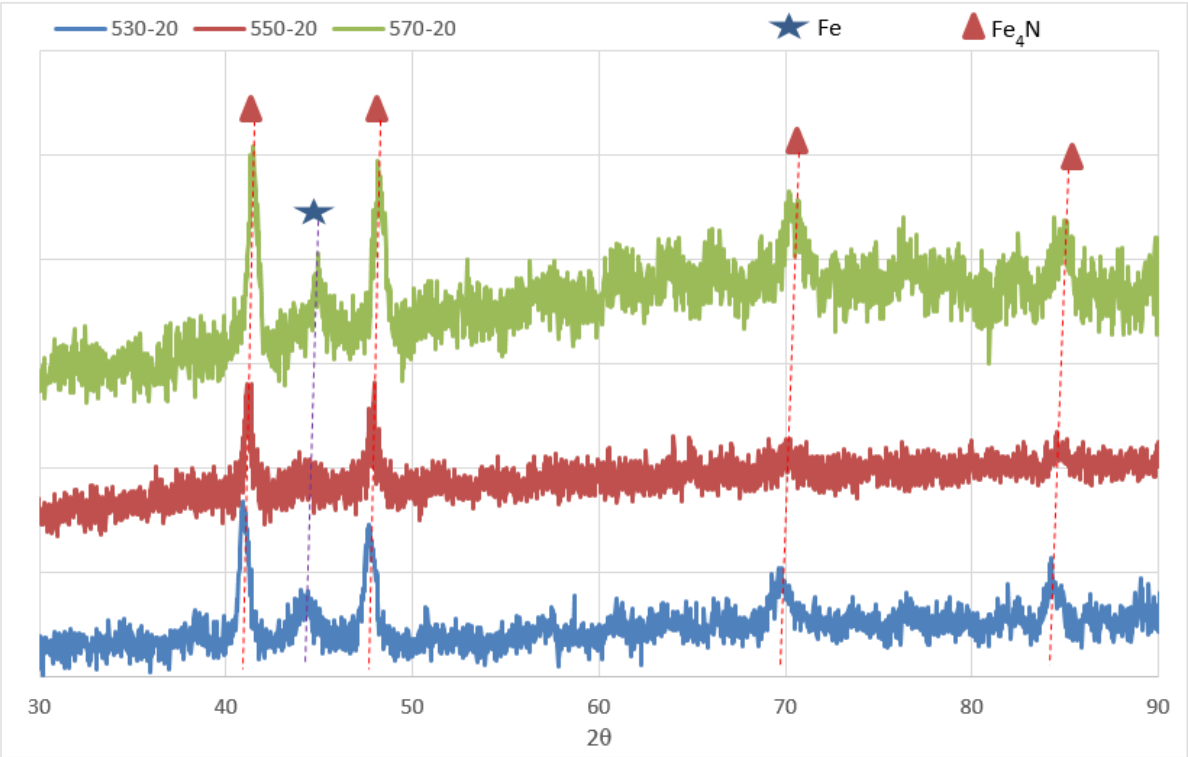

Figure 4.3.3-7 XRD patterns of DCPN samples treated at 530, 550 and 570 ˚C for 20 hours

The effect of treatment duration on hardness and thickness of the hardened layer is evaluated by treating EN40BT samples at 530 °C for 20, 40 and 60 hours. The cross-sectional depth-hardness profiles of DCPN samples with different treatment duration are shown in Figure 4.3.3-8. It clearly illustrates the case depth increases with treatment duration, while lower maximum hardness was obtained with longer treating time. The effective nitride case depth is 360, 440 and 500 μm for samples with treatment time of 20, 40 and 60 hours respectively. The maximum hardness of DCPN530-20 is relatively high as 963 HV0.05. The peak hardness of DCPN530-40 and DCPN 530-60 is similar, which is 860 and 839 HV0.05 respectively. Longer treating time leading to thicker hardened case is in agree with Fick's second law of diffusion. Increasing treating duration resulting in lower hardness, it could be explained that the size of nitride precipitate increases with time. The XRD results of DCPN530-20,530-40 and 530-60 are shown in Figure 4.3.3-9. The phase composition of the 3 samples is identical, which are mainly γ'-Fe_4N and α'-Fe.

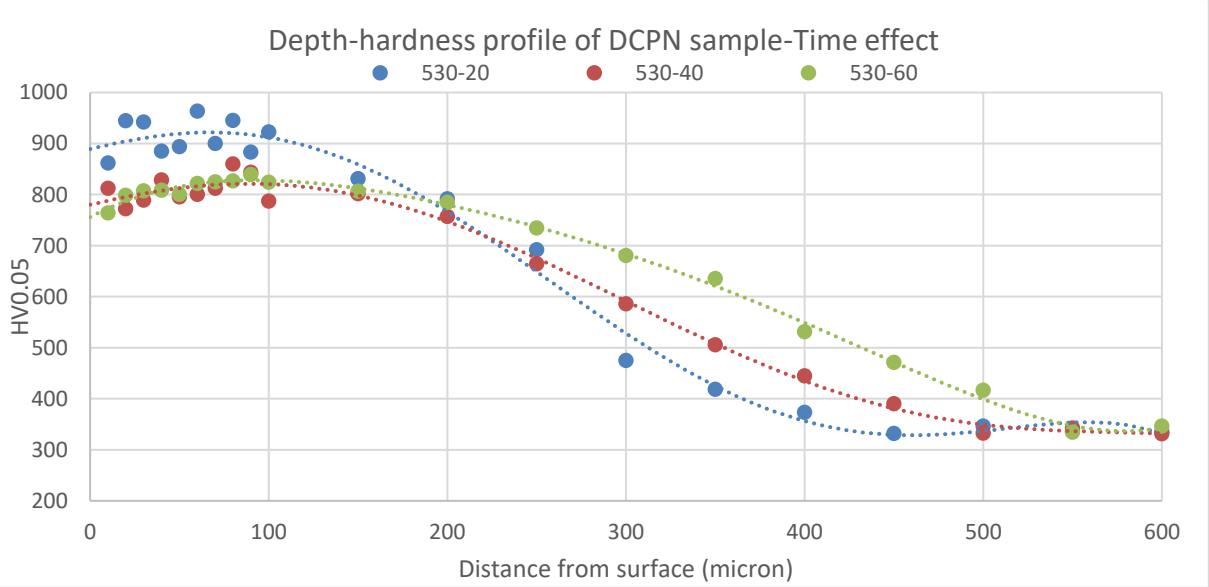

Sample code	Maximum hardness (HV0.05)	Effective nitride case depth (micron)
DCPN530-20	963	360
DCPN530-40	860	440
DCPN530-60	839	500

Figure 4.3.3-8 Hardness and thickness of DCPN samples treated at 530 ˚C for 20, 40 and 60 hours

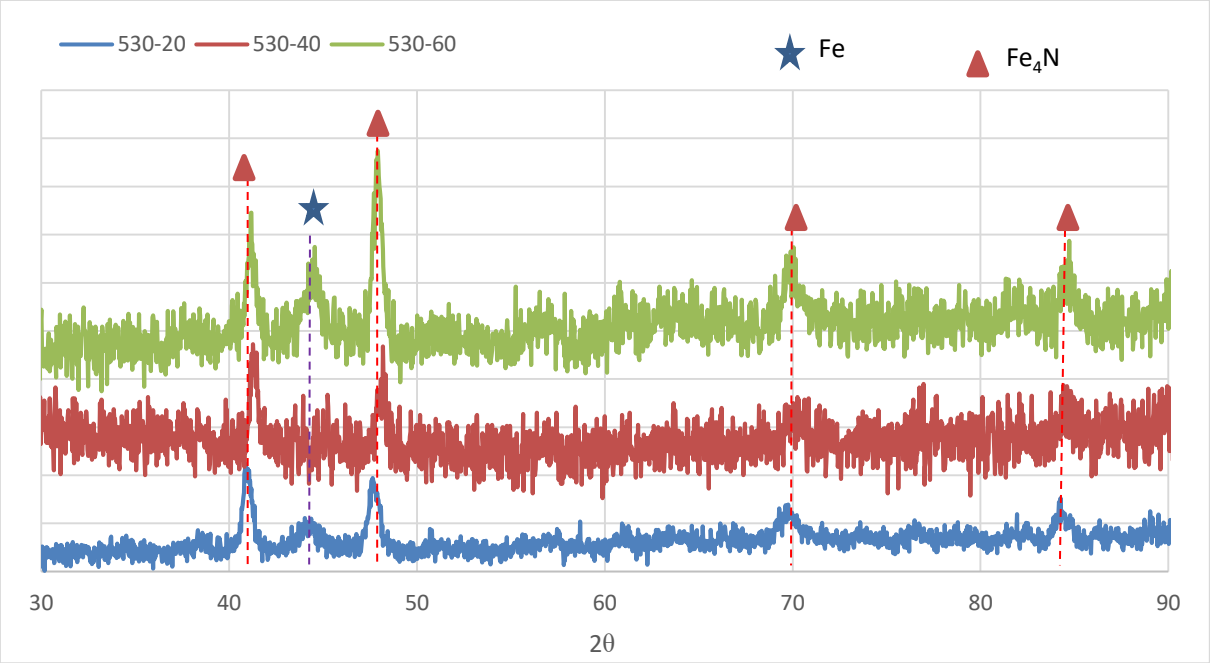

Figure 4.3.3-9 XRD patterns of DCPN samples treated at 530 ˚C for 20, 40 and 60 hours

4.3.3.2 Active screen plasma nitriding (ASPN)

The EN40BT steel was also nitrided using ASPN method. The ASPN samples have been characterised to study the effect of ASPN process on the EN40BT steel.

Figure 4.3.3-10 shows surface morphology of active screen plasma nitrided sample ASPN530-20, on which the surface is coved with fine faceted particles. These particles were very likely generated by the sputtered material from the active screen, which were then deposited on the sample surface during the active screen plasma nitriding process (P. Hubbard et al., 2010b).

The cross-sectional microstructure of ASPN530-20 is shown in Figure 4.3.3-11. A very thin compound layer (white layer) is found on the surface. Below the compound layer, the dark nitrogen diffusion zone can be clearly identified.

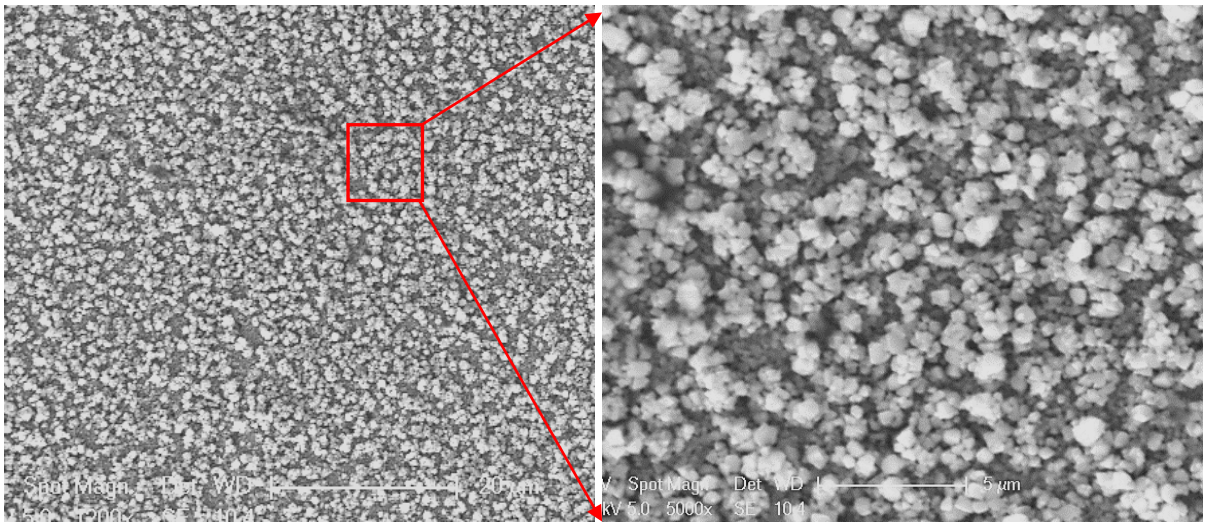

Figure 4.3.3-10 Surface morphology of active-screen plasma nitrided EN40BT sample ASPN530-20

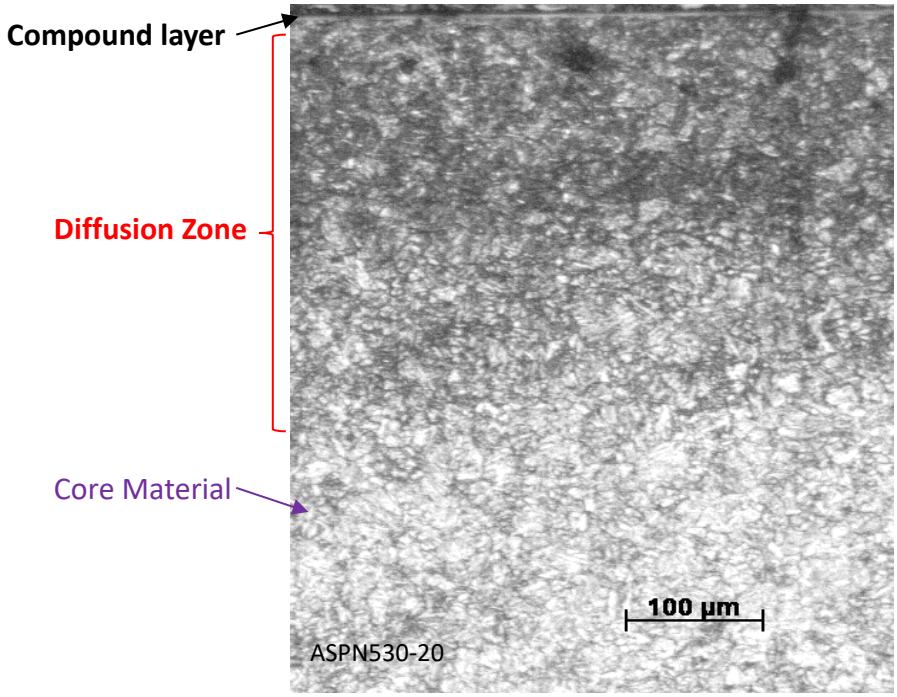

Figure 4.3.3-11 Optical image of the cross section of active-screen plasma nitrided EN40BT sample ASPN530-20

To study the temperature and time effect of active-screen plasma nitriding (ASPN), samples ASPN550-20, ASPN570-20, ASPN530-40 and ASPN530-60 were produced and characterised.

After active-screen plasma nitriding, the samples' surface roughness Ra became much higher than that of as-polished EN40BT (Figure 4.3.3-12). However, the growth rate caused by ASPN is much smaller than DCPN. For example, Ra of ASPN530-20 is about 0.0643 μm, which is only about 4 times higher than that of as-polished sample. The increase of Ra by ASPN is likely caused by the particles which is sputtered from the active-screen and dropped on the sample surface. It is also found from Figure 4.3.3-12 that longer treatment time and higher treatment temperature increases the Ra further.

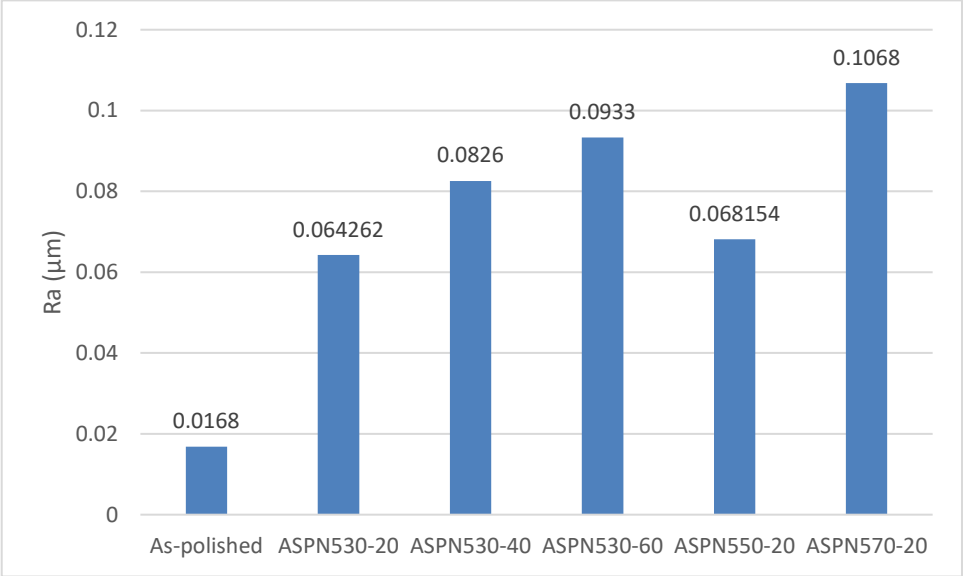

Figure 4.3.3-12 Comparison of surface roughness of as-polished EN40BT and ASPN samples with different treating conditions

Figure 4.3.3-13 shows the cross-sectional microstructures of ASPN550-20, ASPN570-20, ASPN530-40 and ASPN530-60. The compound layer and dark diffusion zone are found in all samples.

The cross-sectional depth-hardness profiles of ASPN samples treated at 530, 550 and 570 ˚C for 20 hours are shown in Figure 4.3.3-14. At the surface, the hardness decreases when the treatment temperature increases, but the hardness values of the three samples are relatively close to each other. The maximum hardness of ASPN530-20, ASPN550-20 and ASPN570-20

is 874, 816 and 784 HV0.05 respectively. Within the diffusion zone of samples ASPN550-20 and ASPN570-20, the hardness value drops gradually with the depth to its core hardness, while in ASPN530-20, the hardness drops extremely fast. Different from the temperature effect on DCPN samples, the case depth of ASPN samples increases with treatment temperature, which is in accordance with Fick's second law of diffusion. The effective harden case thickness of ASPN530-20 is only 280 μm. While the hardened case of ASPN550-20 and ASPN570-20 is 410 and 420 μm thick respectively, which are close to each other and are both much thicker than that of ASPN530-20. Considering the optimum combination of effective depth and surface hardness, 550 and 570 °C are much better than the lower temperature 530 °C for active-screen plasma nitriding of EN40BT.

The XRD results of ASPN530-20,550-20 and 570-20 are shown in Figure 4.3.3-15. The main phase composition of the 3 samples treated at different temperature are identical, which are γ'-Fe_4N and α'-Fe.

The effect of ASPN treatment duration on hardness and thickness of hardened layer is also evaluated. The cross-sectional depth-hardness profiles of ASPN samples with different treatment duration 20, 40 and 60 hours are shown in Figure 4.3.3-16. It clearly illustrates the case depth increases with treating duration. The effective nitride case depth is 280, 310 and 330 μm for samples with treating time of 20, 40 and 60 hours respectively. As to the maximum hardness value, it decreases from 874 HV0.05 to 836 HV0.05 when the treating time increases from 20 hours to 40 hours. When the treating time increases to 60 hours, the maximum hardness slightly decreases to 833 HV 0.05. The XRD results of ASPN530-20,530-40 and 530-60 are shown in Figure 4.3.3-17. The main phase composition of the 3 samples are identical, which are γ'-Fe_4N and α'-Fe.

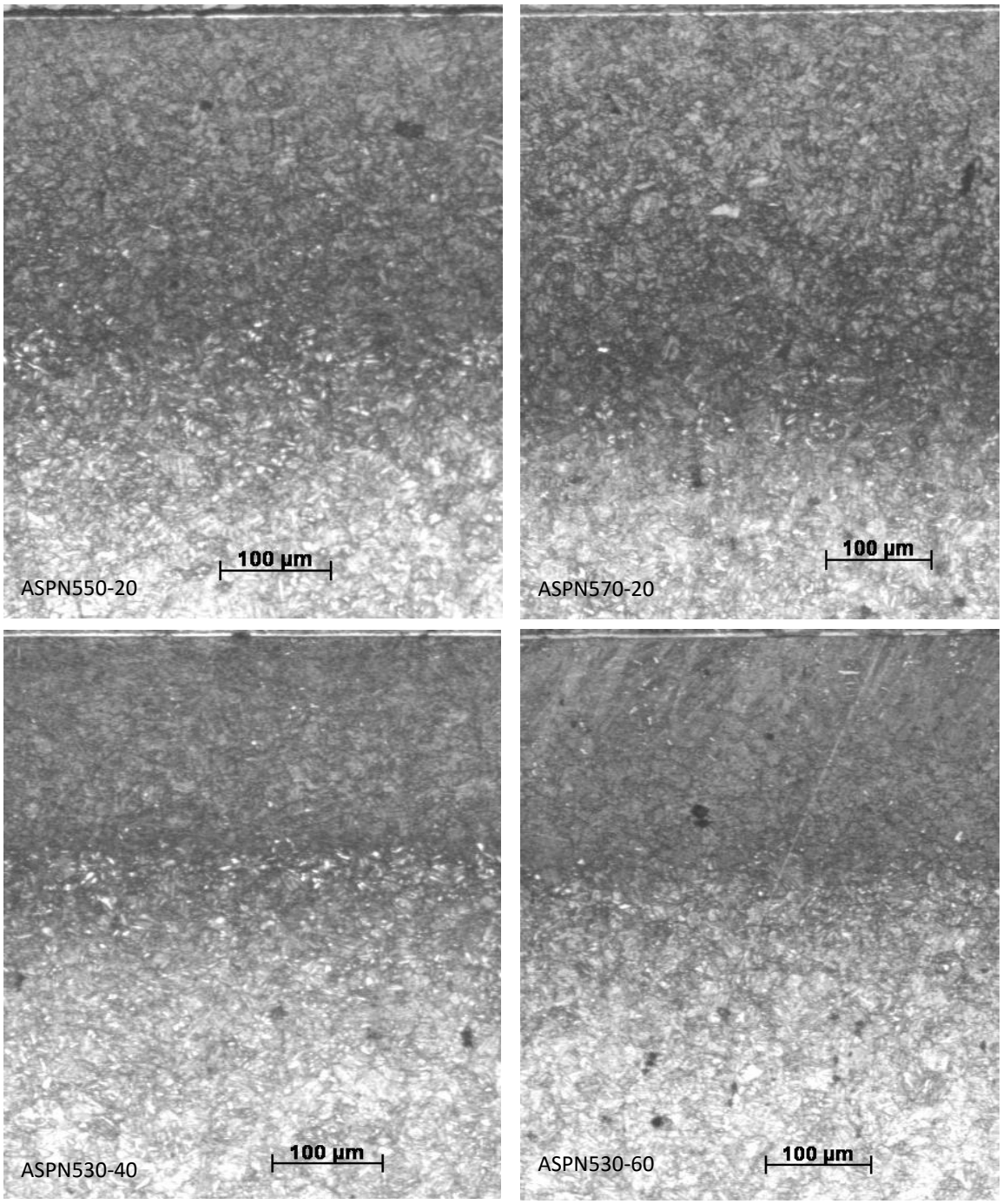

Figure 4.3.3-13 Optical images of cross section of active-screen plasma nitrided EN40BT sample ASPN550-20, ASPN570-20, ASPN530-40 and ASPN530-60

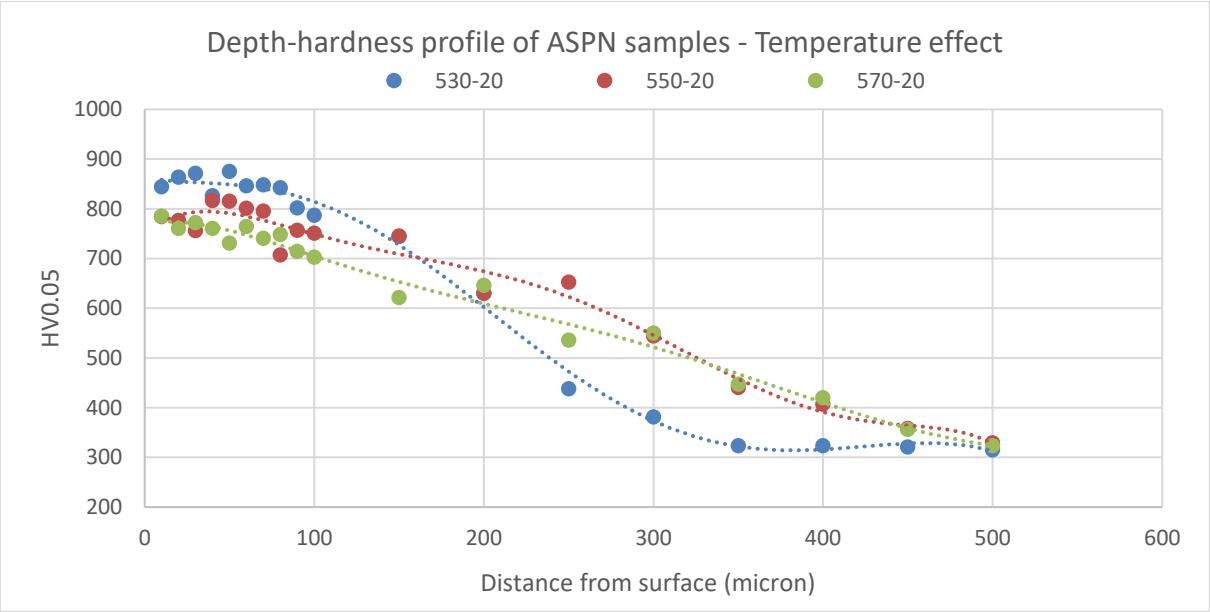

Sample code	Maximum hardness (HV0.05)	Effective nitride case depth (micron)
ASPN530-20	874	280
ASPN550-20	816	410
ASPN570-20	784	420

Figure 4.3.3-14 Hardness and thickness of ASPN samples treated at 530, 550 and 570 ˚C for 20 hours

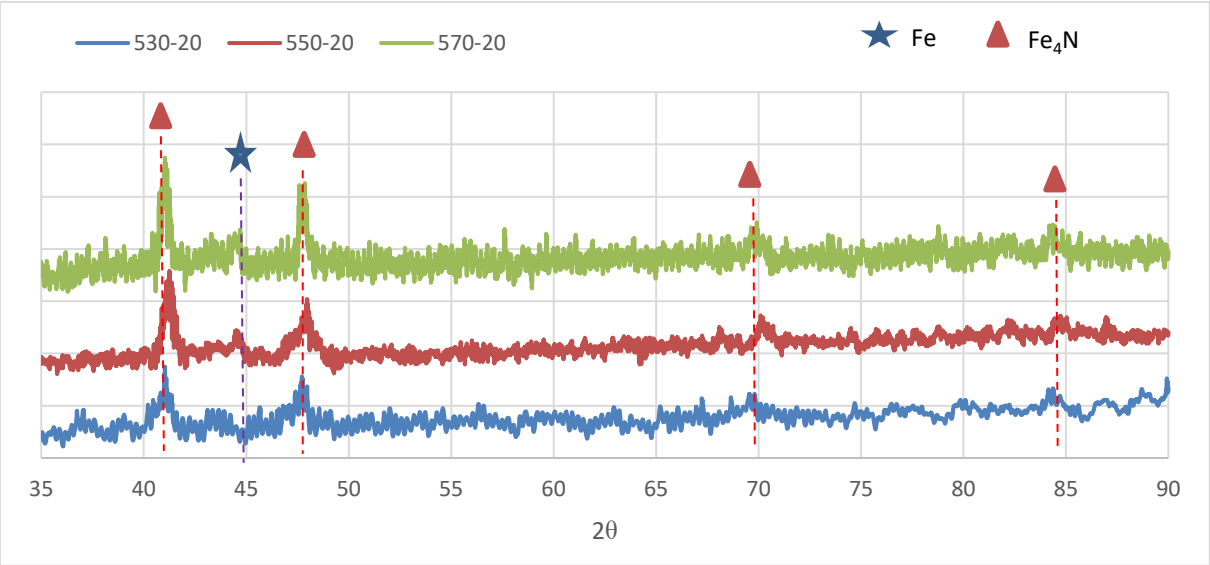

Figure 4.3.3-15 XRD patterns of ASPN samples treated at different temperature for 20 hours

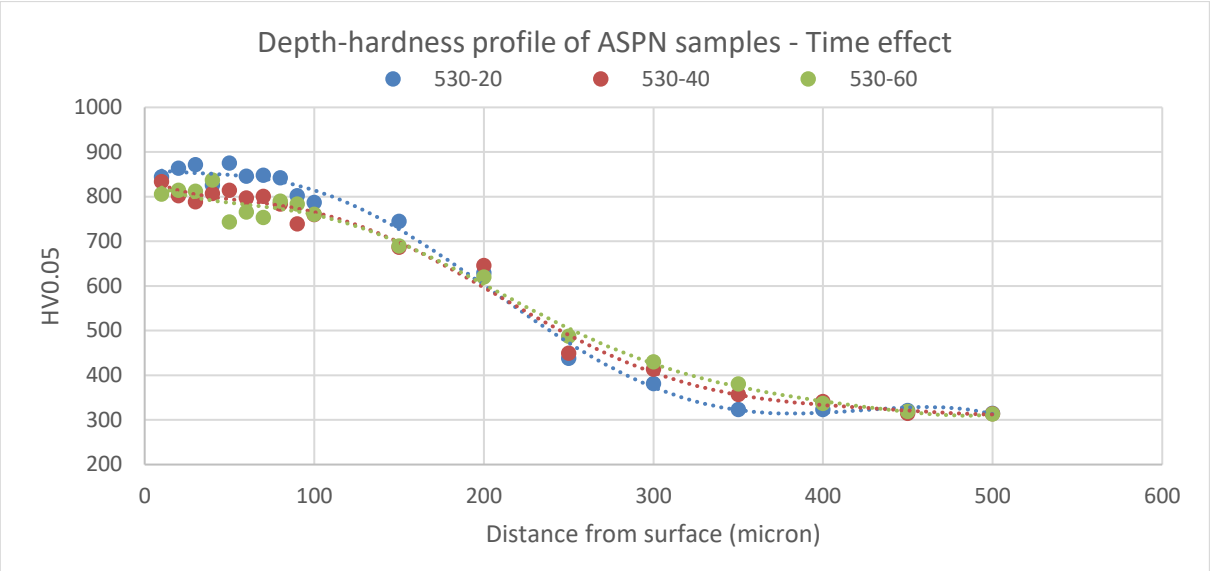

Sample code	Maximum hardness (HV0.05)	Effective nitride case depth (micron)
ASPN530-20	874	280
ASPN530-40	836	310
ASPN530-60	833	330

Figure 4.3.3-16 Hardness and thickness of ASPN samples treated at 530 ˚C for 20, 40 and 60 hours

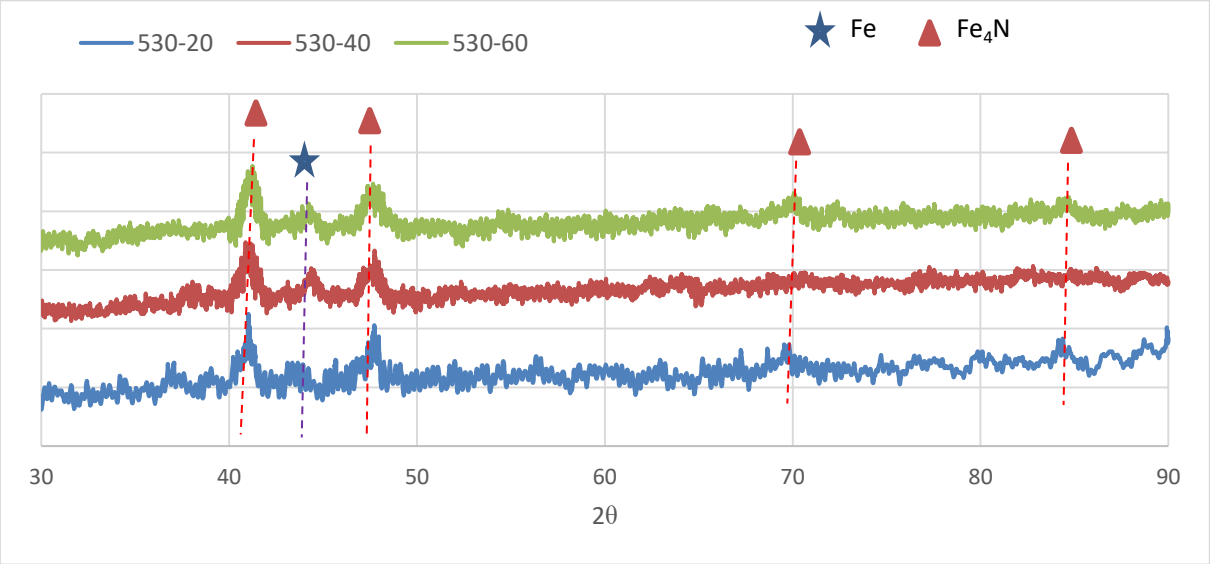

Figure 4.3.3-17 XRD patterns of ASPN samples treated at 530 ˚C with different treating duration

4.3.3.3 Summary and discussion

Based on the depth-hardness profile of DCPN and ASPN samples, contemplating the combination of effective depth and maximum surface hardness, and considering the treatment efficiency, treating temperature 550 ˚C and treating duration 20 hours are selected as the optimum parameters for further DCPN, ASPN and duplex treatment. After repolishing, the surface roughness Ra of DCPN550-20 and ASPN550-20 both reduced to 0.0175±0.0040 μm, which is close to the Ra of as-polished untreated samples.

Based on the results in section 4.3.3, it can be concluded that both DCPN and ASPN methods can effectively increase the surface hardness of EN40BT steel. After plasma nitriding, the surface hardness of EN40BT increased from 321 HV0.05 to about 920 HV0.05 (DCPN550-20) and 816 HV0.05 (ASPN550-20). Once the N is diffused into the material surface, the composition and microstructure of the surface material are changed. It is known that the microstructure and hardness of material have great effects on its strength and resistance to plastic deformation. The nature of plastic deformation is the motion of dislocations. The general yield strength can be expressed by $\sigma_0=\sigma_s+\sigma_i$. σ_s is the stress under which dislocations can form slip bands, σ_i is the friction stress which hinders the motion of dislocations (George Ellwood Dieter, 1976). The hardening mechanism of plasma nitriding is a combination of the solid-solution and precipitation strengthening effect.

The N atom forms interstitial solid solutions in diffusion zone, because the N atom is much smaller than the solvent Fe atom. The solute N atoms resistant the motion of dislocations leading to higher strength in two ways. Firstly, the interstitial atoms N will significantly increase the frictional resistance to dislocation motion. Secondly, the interstitial N will contribute to the static locking of dislocations (George Ellwood Dieter, 1976). Therefore, plasma nitriding can improve the hardness of materials via solid-solution effect.

In addition, γ'-Fe_4N precipitates were formed in plasma nitride samples. The precipitates effectively hinder the motion of dislocations and thus harden the nitrided layer in two ways depending on the size of the precipitate particles (George Ellwood Dieter, 1976). On one hand, if the particles are small and weak, the dislocation will cut and shear the particles. On the other hand, if the particles are large and strong, dislocations have to bend and leave segments around the precipitates to bypass the particles. Therefore, plasma nitriding can improve the material hardness through precipitation hardening effect in the nitrogen diffusion zone.

4.3.4 WC/a-C:H coating

The low friction DLC coating chose for this project is the WC/a-C:H coating. The reason for adopting this coating is its extremely low friction coefficient which can mitigate the effect of insufficient lubrication. The WC/a-C:H coating were deposited by Oerlikon Balzers Coating UK Ltd, and its trade name is BALINIT® C. It is mainly used to reduce adhesive wear, surface fatigue and tribo-oxidation (Oerlikon-Balzers, 2017), which are common failure modes of wind turbine gearbox components. The DLC coating sample was characterised to study the morphology, microstructure and properties.

The as-coated surface morphology of WC/a-C:H coating is shown in Figure 4.3.4-1(a) (magnification of 5,000 times), which illustrates the coating surfaces are uniform and nearly flawless. Under a higher magnification of 25,000 times, Figure 4.3.4-1(b) shows the coating is with a cauliflower-like structure.

Under SEM, the coating was found to have a double-layer structure. Figure 4.3.4-2 shows the cross-sectional BALINIT® C coating layer structure which consists of a top WC/a-C:H layer of about 2.97 μm thick and an interface layer of 0.61 μm thick.

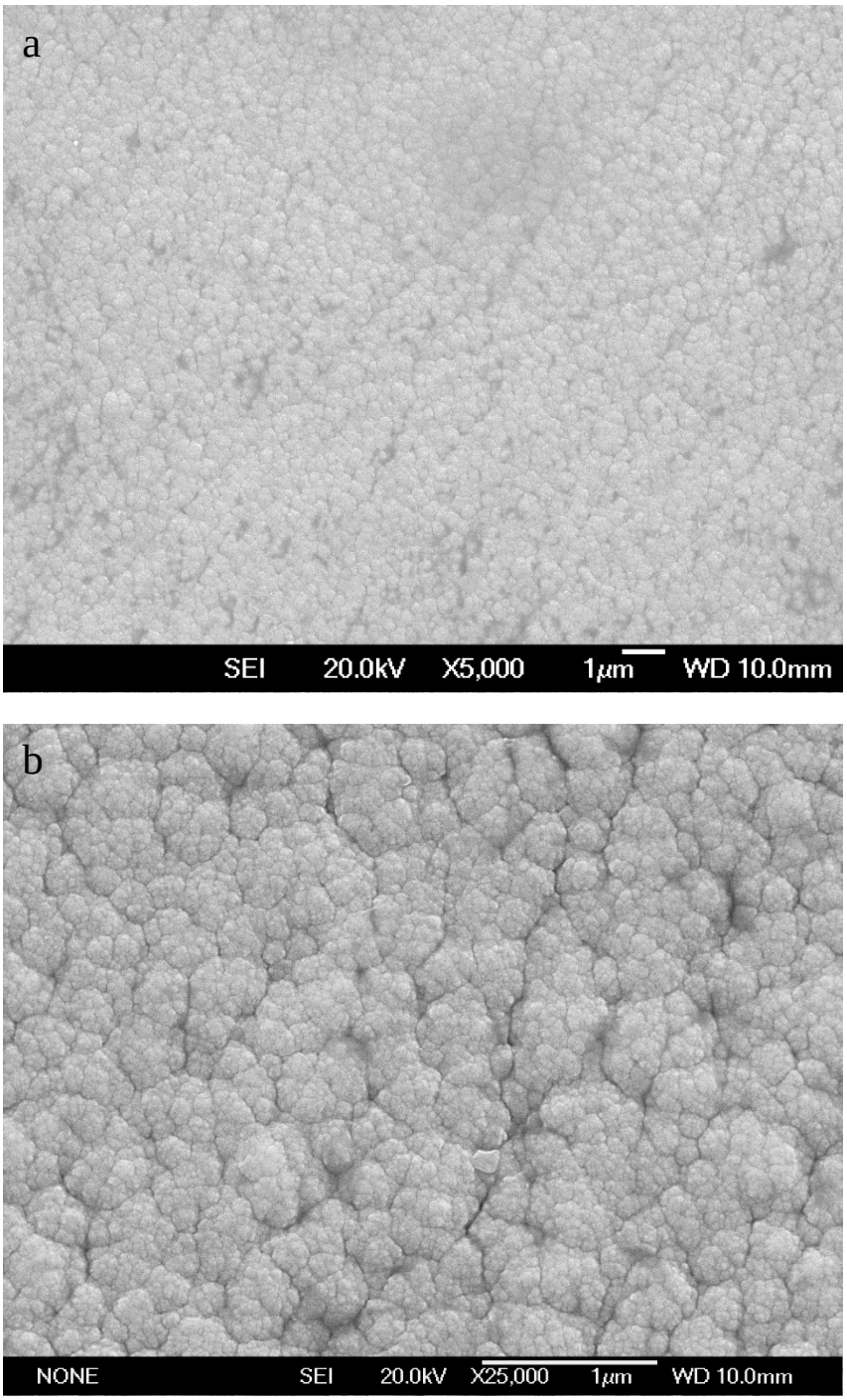

Figure 4.3.4-1 SEM image of BALINIT® C coating surface, (a) under low magnification, and (b) under high magnification

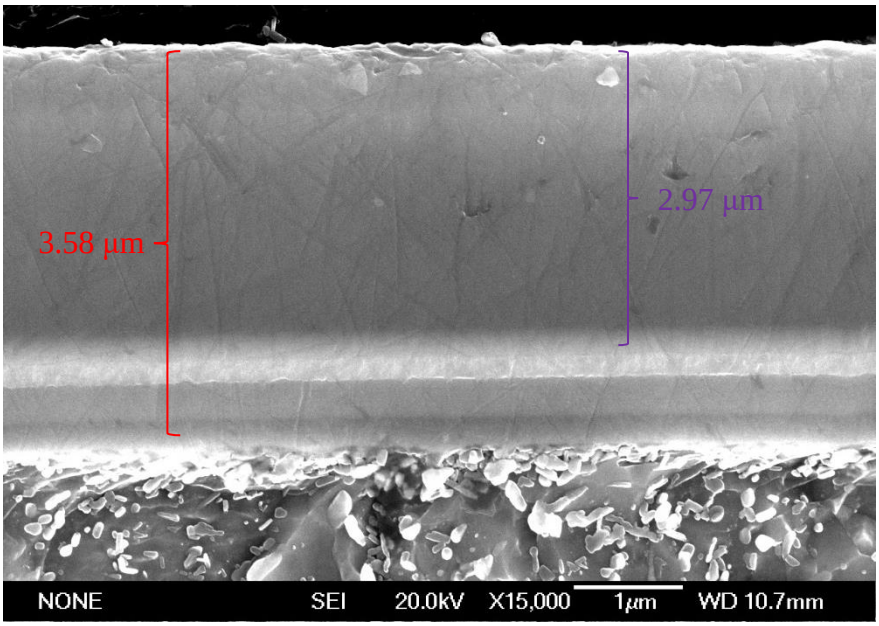

Figure 4.3.4-2 SEM image of the WC/a-C:H coating layer structure

Figure 4.3.4-3 shows the EDX line scan across the coating layers. The green, red, purple and blue lines stand for Cr, Fe, C and W respectively. It can be seen that the top layer is rich in carbon and tungsten. The carbon content decreases with increasing the depth, while the tungsten content increases with the depth until reaching the interface layer. In the first 0.3 µm of the coating layer, the carbon content is higher than tungsten, below that point, tungsten content is higher than carbon. The interface layer is dominated by chrome with a trace of tungsten and carbon.

Figure 4.3.4-4 shows the Raman spectrum of the WC/a-C:H coating. The positions of the G (graphite sp^2) peak and D (disordered sp^3) peak are located at 1573 and 1399 cm^{-1} respectively.

The ratio of the intensity of D peak and G peak I_D/I_G is 0.78, indicating the content proportion of sp^2 and sp^3 clusters in the DLC coating.

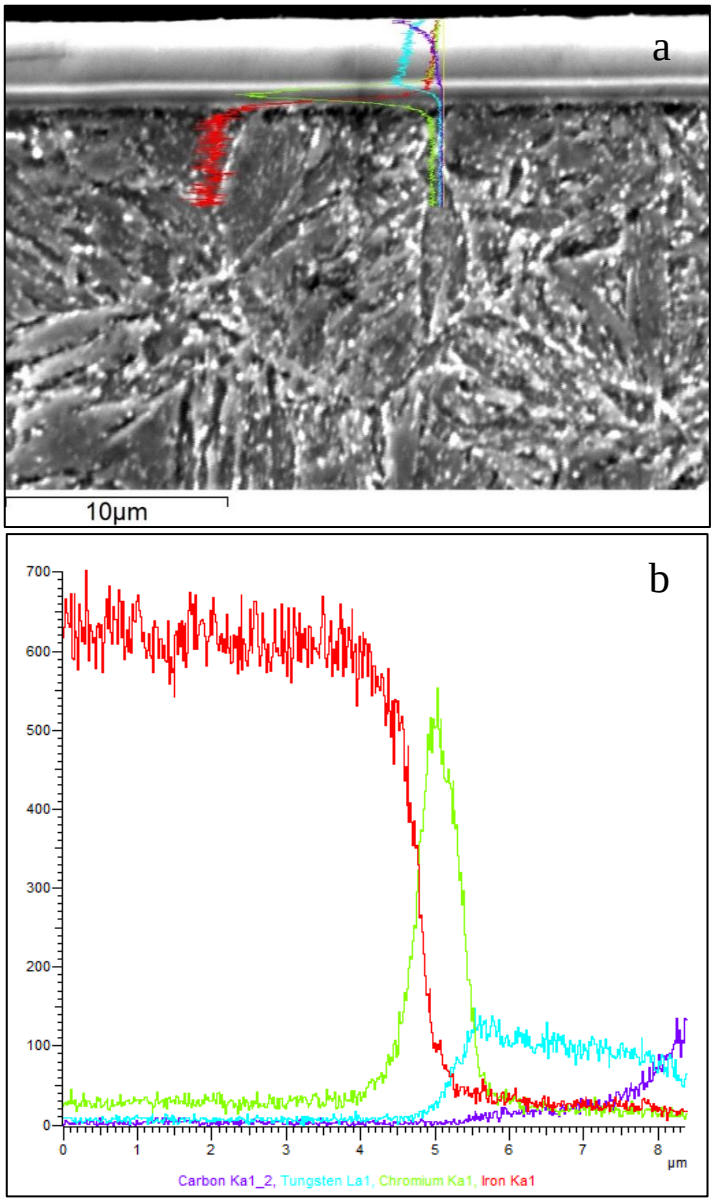

Figure 4.3.4-3 (a) EDX line-scan position, and (b) EDX line-scan results of the WC/a-C:H coating layer structure

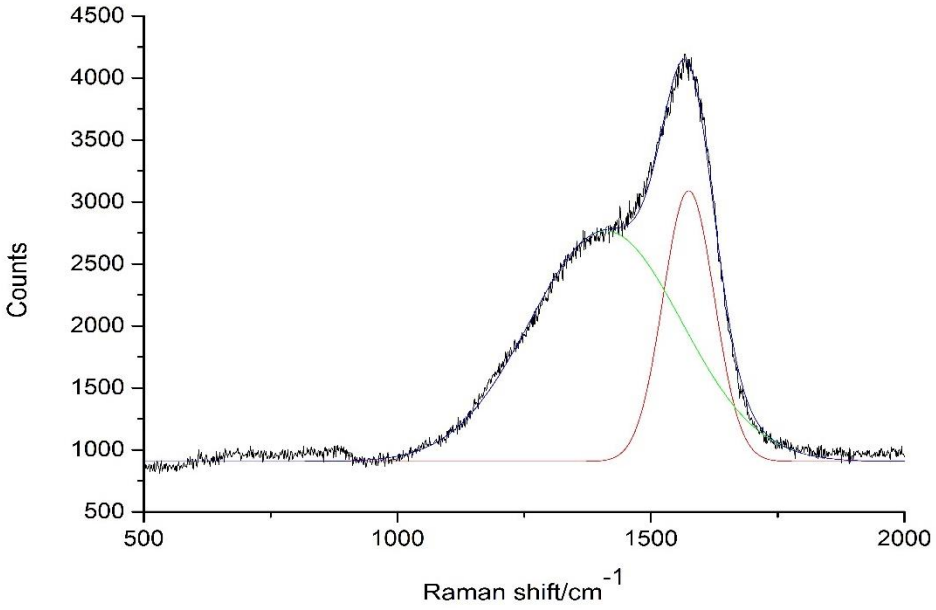

Figure 4.3.4-4 Raman spectrum of the WC/a-C:H coating

The valid nanoindentation data of WC/a-C:H coating (as shown in Figure 4.3.4-5) were analysed and the calculated results indicated that the nano-hardness (H) and the reduced modulus (Er) of the WC/a-C:H coating are 11.43±0.70 GPa and 129.80±3.92 GPa, respectively.

The XRD pattern of WC/a-C:H coating (as shown in Figure 4.3.4-6) only shows a typical 'amorphous halo', i.e. a very broad diffraction peak, indicating a non-crystalline structure of this coating. It does not show any sharp peaks from long range order of crystalline (e.g. WC or steel substrate).

The surface roughness R_a of the WC/a-C:H coating is 17.312 ± 3.303 nm. The friction coefficient of WC/a-C:H coating is 0.16±0.01.

The low friction coefficient of WC/a-C:H coating is due to its microstructure and the unique friction reaction. The nature of WC/a-C:H is a metastable, amorphous and hydrogenated carbon-based coating, containing sp^2 and sp^3 bonds. When they are rolling or/and sliding with a counterpart, a friction-induced local annealing will be produced at the real contact area due

to the movement of the two bodies. The local annealing will then destabilise the sp^3 bonds and release the hydrogen, forming a lubricious graphite-like transfer film (Y Liu et al., 1996b). The low-friction graphite-like transfer film will act as a third body between the carbon-based coating and the counterpart (S. K. Field et al., 2004), thus the WC/a-C:H coatings exhibit a low coefficient of friction (Y Liu et al., 1996a, A Erdemir et al., 1995).

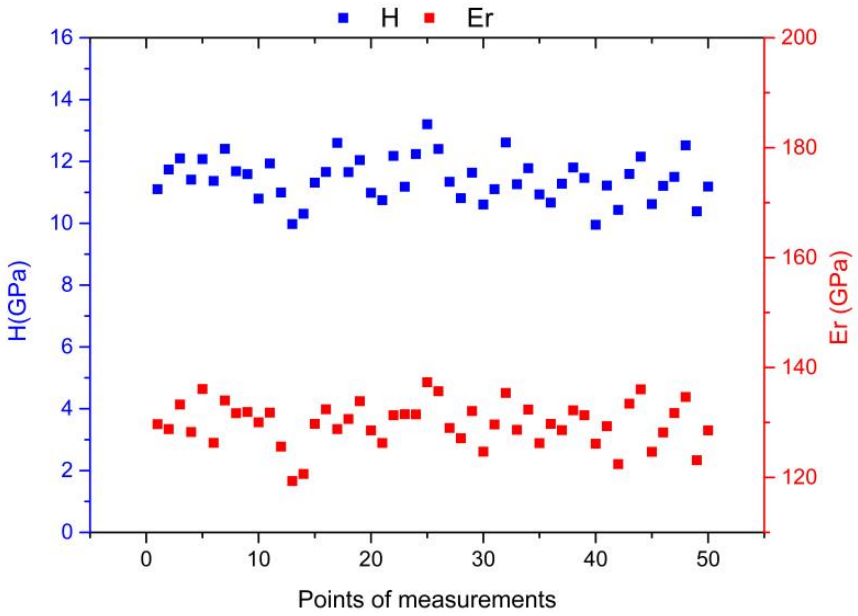

Figure 4.3.4-5 Nanoindentation data of WC/a-C:H coating surface

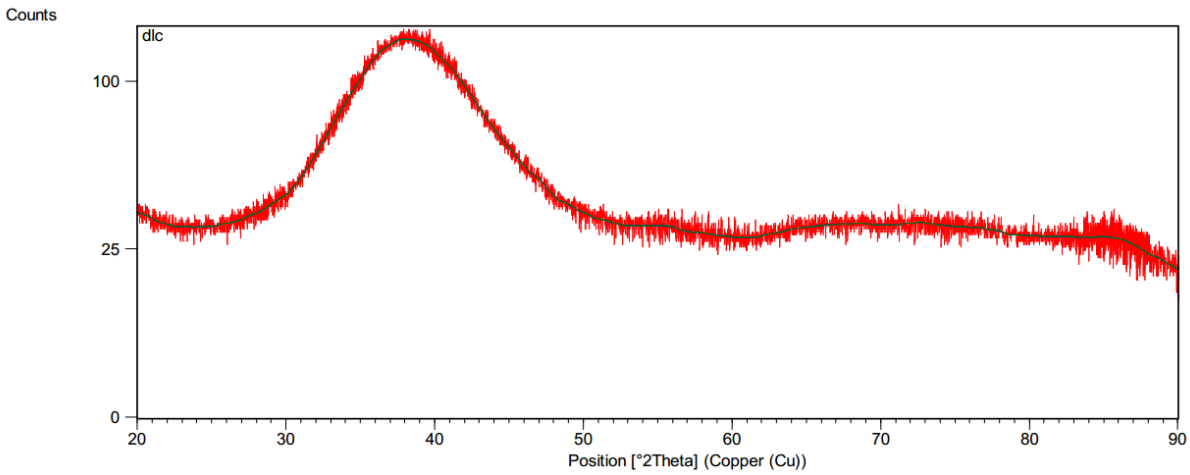

Figure 4.3.4-6 XRD pattern of WC/a-C:H coating

4.3.5 Single and duplex WC/a-C:H coating surface systems

In order to prevent the life-limiting problems of wind turbine gearbox components, duplex surface systems with excellent properties, such as low friction coefficient, high hardness and high load-bearing capacity, have been designed relevantly to mitigate the effects of identified failure causes, which are high load, misalignment (i.e. local contact stress concentration) and poor lubrication condition (e.g. high friction).

Duplex surface systems were designed as DLC coating deposited on surface hardened EN36 and EN40BT steel. For the purpose of comparison, single surface systems, i.e. DLC coating deposited on as-received steel samples, were also produced.

Two single surface systems were produced as WC/a-C:H coating deposited on untreated EN36 (DUA) and untreated EN40BT (DUB), and 3 duplex surface systems were fabricated, namely coating on carburised EN36 (DC), coating on direct-current plasma nitrided EN40BT (DDN) and coating on active-screen plasma nitrided EN40BT (DAN).

4.3.5.1 Load bearing capacity

Load bearing capacity (LBC) is a critical property of surface systems. Coating layer in the surface system with a low LBC is easy to be damaged under high concentrated stresses. Indentation hardness of substrate significantly affects the LBC of coating systems.

To evaluate and compare the LBC of single DUA/DUB and duplex DC/DDN/DAN surface systems, micro-indents were made on samples with progressive loads ranging from 25 to 1,000 g. The highest load without causing any cracks within or around the indents on a sample is used as the LBC of the surface system.

The indentation hardness values of these single and duplex surface systems obtained at different loads are shown in Figure 4.3.5-1. The hardness value decreased in all samples with

increasing the applied load, especially in the single system samples. However, the duplex surface systems DC/DDN/DAN designed from this project exhibited a higher hardness than the single DLC coating systems DUA/DUB especially when the applied load is relatively high. This indicates that the duplex systems designed have superior load bearing capacity compared to the single coating samples.

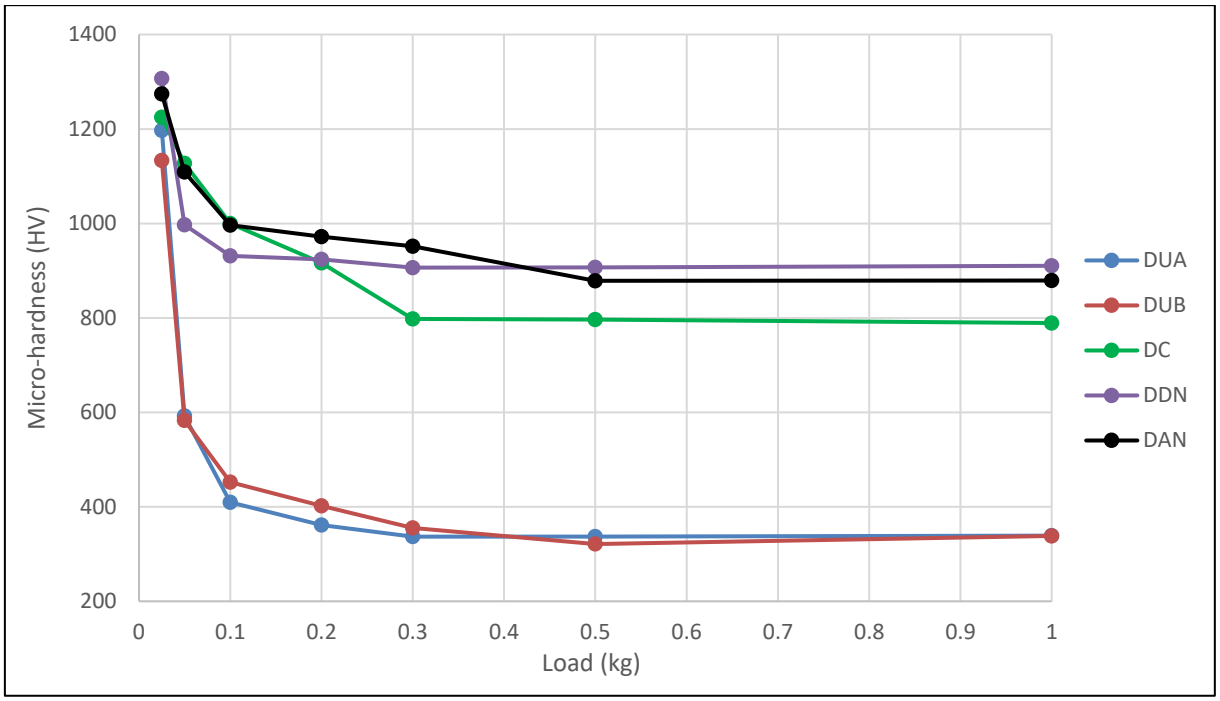

Figure 4.3.5-1 Indentation hardness of single systems DUA and DUB, and duplex systems DC, DDN and DAN

At the load of 25 g, the indentation hardness of the single system DUA and DUB turned out to be 1197 and 1133 HV respectively; the measured hardness reduced to only about 337 and 321 HV when the load of 500 g was applied (as shown in Figure 4.3.5-1). The rate of hardness reduction is 71.8 % and 71.7 % for DUA and DUB. On the other hand, the indentation hardness of the duplex systems DC, DDN and DAN is 1225, 1307 and 1274 HV at the load of 25 g. When the load increased to 500 g, the hardness decreased but is still as high as 797, 907 and 879 HV respectively, which is much higher than that of the single system samples. The

rate of hardness reduction for DC, DDN and DAN is only 34.9 %, 30.6 % and 31.0 % respectively. The rapid drop in hardness from low load to high load could be explained by (I) the increased penetration depth of the indenter and the stress field at higher load, and (II) the effect of the hardness or strength of the substrate on the performance of the surface system. It is known that the indentation hardness of a material reflects its resistance to plastic deformation. The indentation hardness or plastic deformation resistance of a coating system depends on both the surface and subsurface. This is because the stress field formed in most engineering applications will well beyond the coating and extend into the substrate. Hence, the measured microhardness of a coating system is not only the intrinsic hardness of the surface coating but is the combination of the surface coating and the supporting substrate, and the effect of the substrate increases with higher applied load (Jun Zhou, 2014). It is known that the steel substrate is softer than the DLC coating layer, especially in the single surface system. Higher applied load leads to more contribution from the soft substrate, thus the indentation hardness is lower at higher load until the contribution from thin coating layer is negligible at extremely high load. The less hardness reduction in duplex surface systems than in single systems is due to the stronger support from the hardened subsurface by carburising and nitriding than as-received steel substrate. When the substrate under a coating is strong enough, less plastic deformation will occur in the substrate. Therefore, pre-hardening of a substrate could be used to improve the LBC of coating systems.

The cracks formed during micro-indentation within and around the indents were examined by SEM. The micrographs of cracks in single system sample DUB and duplex system sample DDN are given in Figure 4.3.5-2. It can be seen that severe cracking formed in the single DLC coated surfaces even under a low load of 200 g, both within and around the indents. Without the adequate mechanical support from the substrate, DLC coating collapsed under

loading mainly due to so-called ‘thin-ice’ or ‘egg shell’ effect (Bell et al., 1998). Under a high load, the thin and hard coating layer failed due to insufficient mechanical support from the soft substrate. In contrast with the single coating system, no cracks could be found in the duplex system under loads up to 300 g. Well defined cracks were formed only at the load of 500 and 1,000 g. Clearly, the duplex surface system designed from this project have superior load bearing capacity to the single DLC surface system, which can be mainly attributed to the hard and strong carburised and nitrided case. Therefore, it can be concluded that the pre-hardened substrate can contribute greatly to the LBC of engineered surface systems, which is in accordance with other researchers’ reports (P. Kaestner et al., 2001, ZX Zhang et al., 2006, T. Michler et al., 1998, J. C. Avelar-Batista et al., 2006).

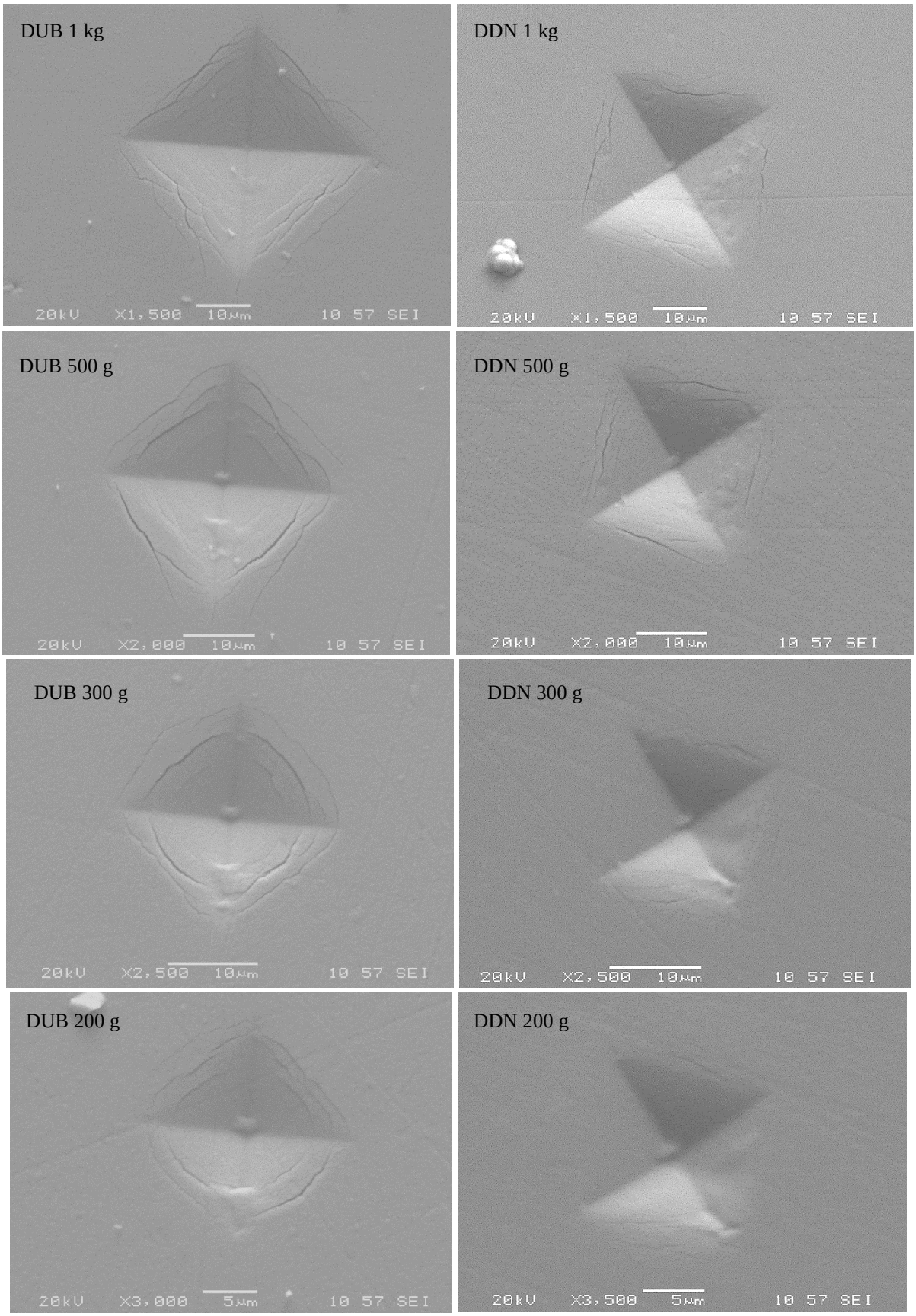

Figure 4.3.5-2 SEM micrographs showing intents in single system and duplex system under different loads

4.3.5.2 Scratch test

The scratch resistance and adhesive strength of coating samples was evaluated through scratch testing. Figure 4.3.5-3 shows scratches formed on one WC/a-C:H coated single surface system (i.e. coating on untreated EN36 (DUA)) and three duplex surface systems, namely coating on carburised EN36 (DC), coating on direct-current plasma nitrided EN40BT (DDN) and coating on active-screen plasma nitrided EN40BT (DAN).

Coating cracking or delamination is evidenced by the bright area within or around the scratch scar where the steel substrate was exposed. It can be clearly seen that the degree of coating cracking and delamination of single DLC coating system is much severer than that of duplex DLC coating systems, as the bright area in Figure 4.3.5-3 (a) is much larger than that in Figure 4.3.5-3 (b), (c) and (d). In the duplex surface systems, starting of severe cracking/chipping was effectively delayed to higher load as compared with the single surface system sample. In addition, no complete delamination occurred in duplex surface system samples even at high load as evidenced by the discontinuous white coloured areas towards the end of the scratch scar. These demonstrate better bonding strength and scratch resistance of the duplex surface systems compared to the single coating system.

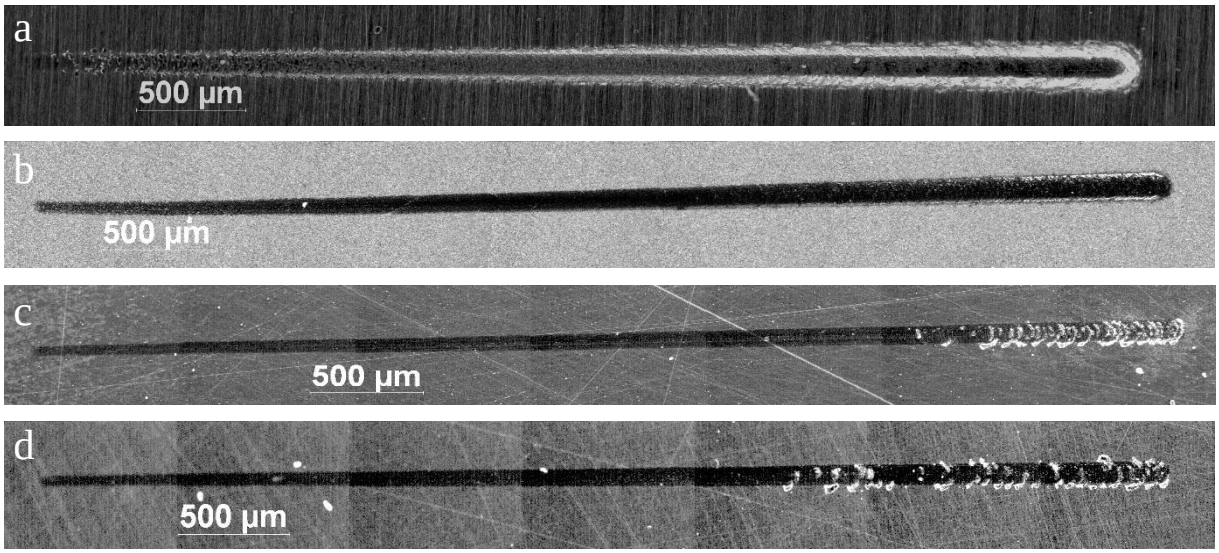

Figure 4.3.5-3 Optical microscope image of the scratch scar in WC/a-C:H coating deposited on (a) untreated EN36, (b) carburised EN36, (c) direct-current plasma nitrided EN40BT and (d) active-screen plasma nitrided EN40BT

The digital data of the friction force and its first derivative recorded from the scratch tests can be utilised to evaluate the adhesive and cohesive strength of the coating systems (Jun Zhou, 2014). Data were plotted (Figure 4.3.5-4, Figure 4.3.5-5, Figure 4.3.5-6 and Figure 4.3.5-7) and analysed by utilising two critical loads, namely L_{C1} and L_{C2}. L_{C1} is the lower critical load where the first derivative of the friction curve changes from relatively smooth to a sharp fluctuation, indicating the first crack in coating layer occurred (cohesive strength). L_{C2} is the upper critical load where the friction force increases dramatically and its first derivative fluctuates dramatically. This is an indication of contact between the diamond tip and steel substrate, i.e. coating delamination (adhesive strength) (Jun Zhou, 2014), since the WC/a-C:H coating has a much lower friction coefficient than EN36 and EN40BT steels. The critical load L_{C1} and L_{C2} of single WC/a-C:H coated sample can be determined to 35 N and 45 N respectively (Figure 4.3.5-4). In duplex surface systems (Figure 4.3.5-5, Figure 4.3.5-6 and Figure 4.3.5-7), the L_{C1} is both 46 N for coating on carburised EN36 and direct-current plasma nitrided EN40BT, and it is 43 N for coating on active-screen plasma nitrided EN40BT,

where the large fluctuation occurred in the first derivative of friction force. Since the friction force in all the three duplex surface systems increased steadily during the whole test, the L_{C2} for all of them should be at least 60 N which is the maximum load used. The digital scratch results also clearly show the bonding strength of duplex surface systems is higher than the single surface system to some level.

Except for better bonding strength of duplex systems than the single system, the scratch results also exhibit that the duplex systems composing with nitrided substrate possess similar bonding strength to the duplex system containing carburised substrate.

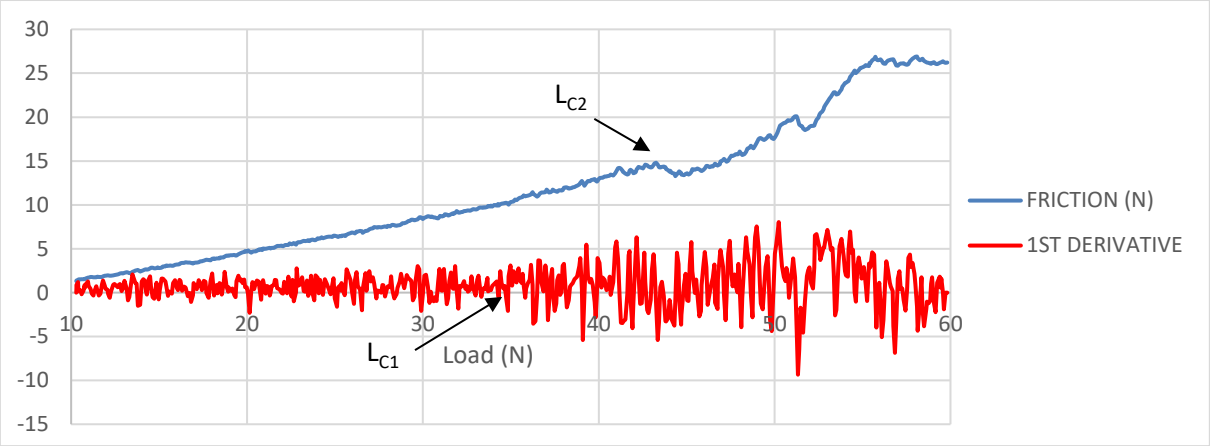

Figure 4.3.5-4 Friction force and its first derivative of the single surface system, i.e. WC/a-C:H coating on untreated EN36

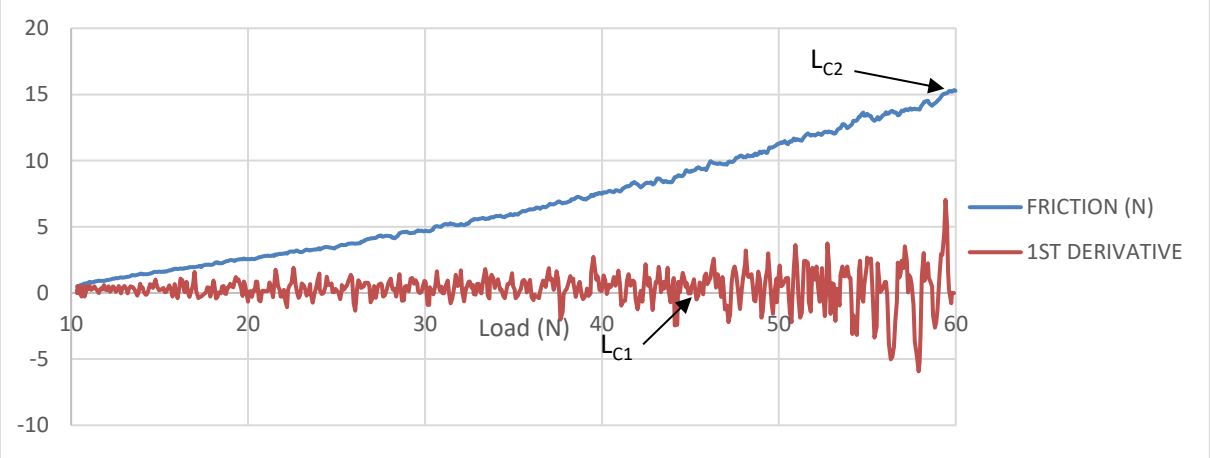

Figure 4.3.5-5 Friction force and its first derivative of the duplex surface system, i.e. WC/a-C:H coating on carburised EN36

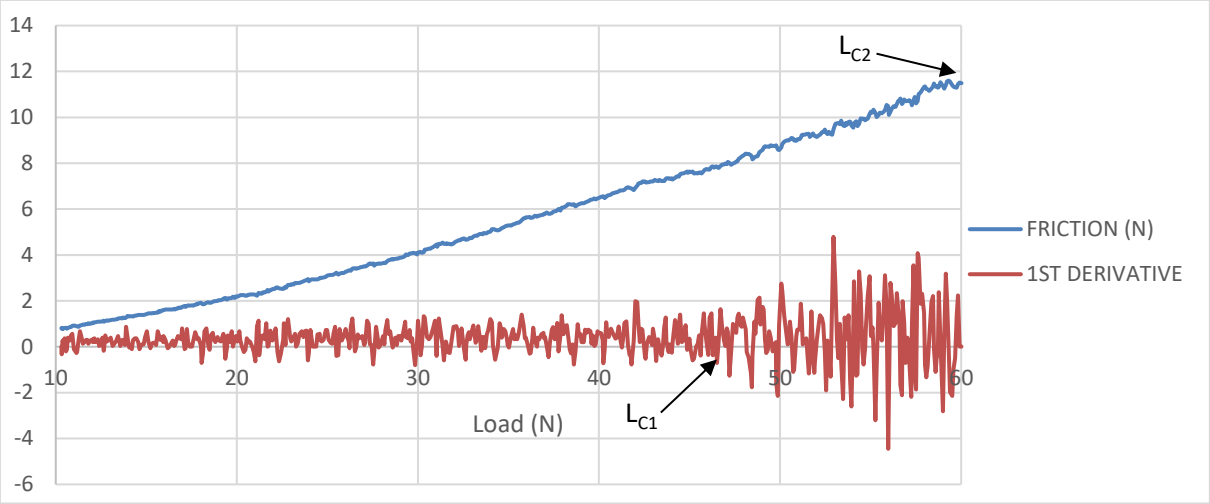

Figure 4.3.5-6 Friction force and its first derivative of duplex surface system, i.e. WC/a-C:H coating on direct-current plasma nitrided EN40BT

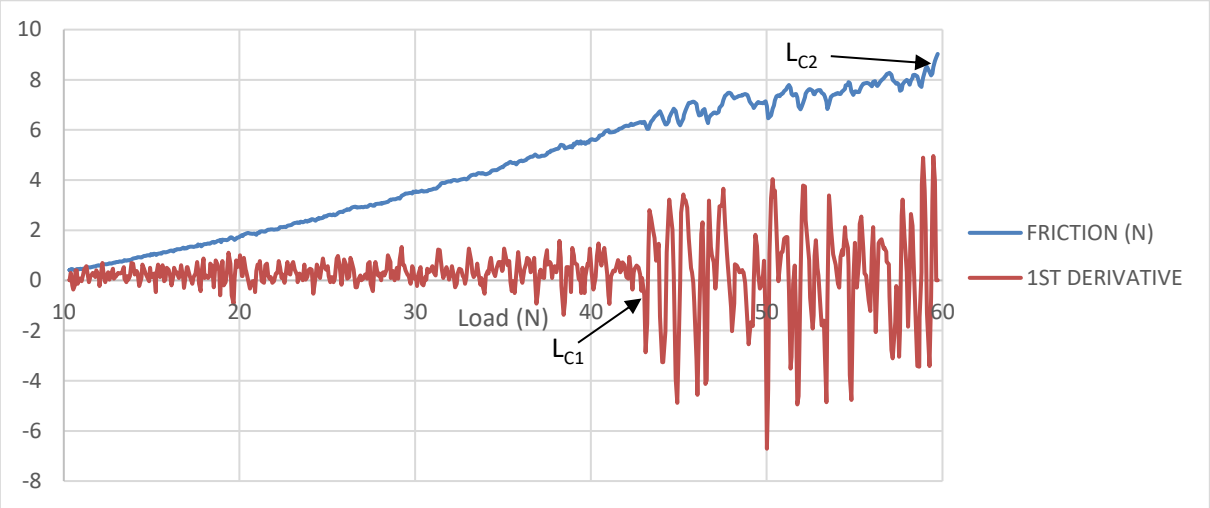

Figure 4.3.5-7 Friction force and its first derivative of duplex surface system, i.e. WC/a-C:H coating on active-screen plasma nitrided EN40BT

4.3.5.3 Rolling-sliding wear behaviour

To evaluate the wear performance of designed duplex surface systems, rolling-sliding wear tests were conducted in dry and lubricated conditions. For comparison purposes, the wear tests were also conducted on single system samples.

4.3.5.3.1 Lubricated condition

Rolling-sliding wear behaviour of lubricated single surface system samples DUA and DUB, and duplex surface system samples, namely DC, DDN and DAN were tested in oil under the load 500, 600, 700 and 800 N respectively for 5 hours. All duplex surface system samples survived from the 5-hours lubricated wear tests under different load, no visible coating damage was observed with the naked eye or SEM. Single coating samples DUA and DUB did not show any damage after the tests under 500 and 600 N, but visible large coating cracking and delamination formed during the test under 700 N.

The surface of coating cracked and delaminated samples DUA and DUB was examined using SEM. Figure 4.3.5-8 illustrates a representative back-scattered-electron image of large delamination area. The dark grey area is the raw coating surface, and the white area is the exposed surface after coating removal, which is approved through EDS analysis (Figure 4.3.5-9).

The weight loss of all the DLC coated samples after the wear tests were neglectable including the delaminated samples since the density of carbon-based coating is very small.

The results of lubricated rolling-sliding wear tests illustrate duplex surface systems have a longer duration at high load than single coating system. This can be explained by the higher bonding strength of the coating systems on a pre-hardened substrate, which is shown in the scratch tests.

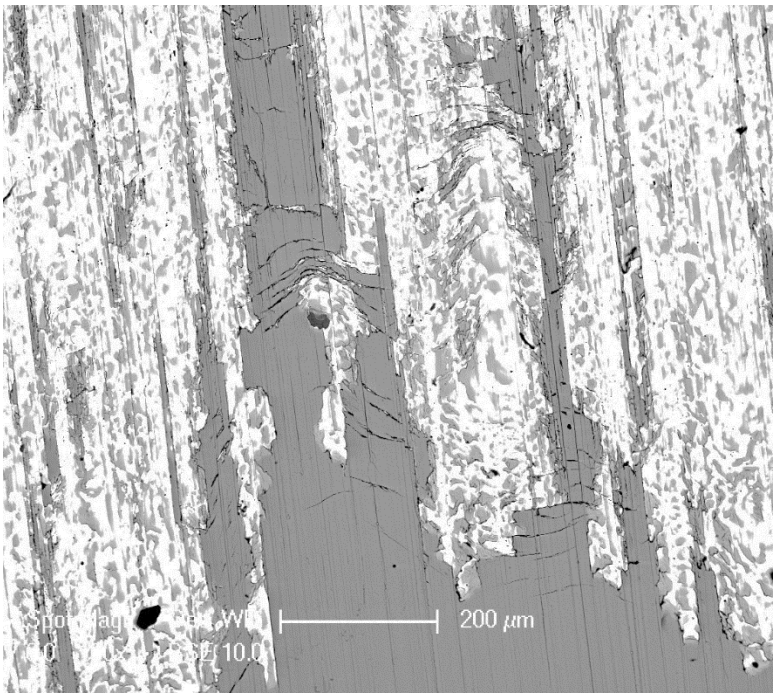

Figure 4.3.5-8 SEM (back-scattered-electron) image (×100) of coating delaminated surface of single surface system sample DUA after lubricated wear test under 700N (i.e. 597.56 MPa Hertz contact stress)

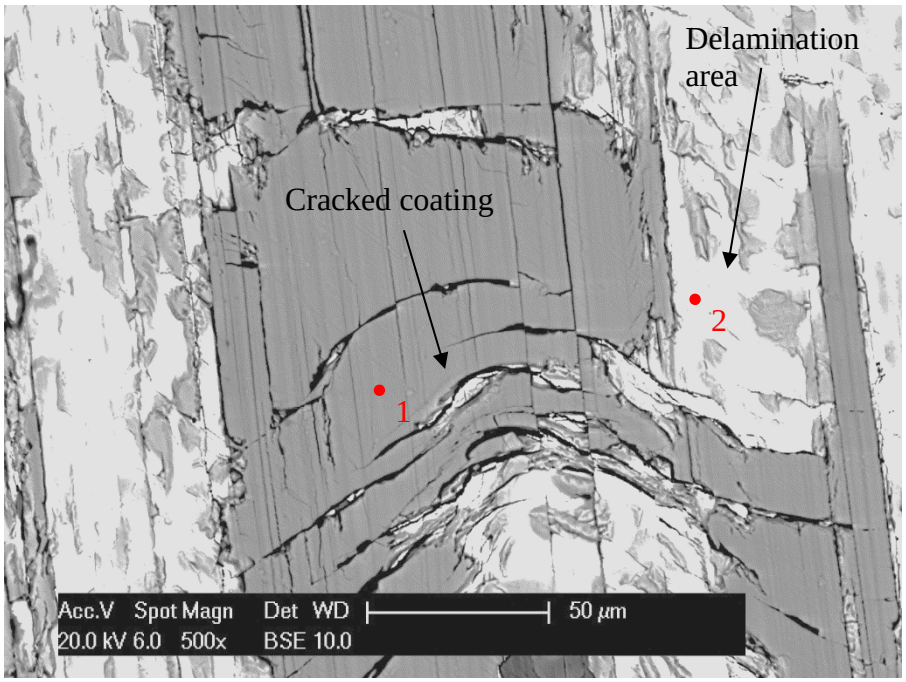

Spectrum	C	Cr	Fe	Ni	W	Comment
1	40.92	1.09	1.91	4.02	52.06	DLC coating surface
2	23.13	5.92	3.11	3.74	64.11	Exposed area due to delamination

Figure 4.3.5-9 EDS analysis of coating delaminated surface

4.3.5.3.2 Dry condition

Rolling-sliding wear performance of unlubricated single surface system samples DUA and DUB, and duplex surface system samples DC, DDN and DAN were tested in dry condition under the load 500, 600, 700 and 800 N respectively for 5 hours. All duplex surface system samples survived from the 5-hours dry wear tests under different load. Single surface system samples DUA and DUB both survived the test under 500 and 600 N, while coating damage was observed under 700 N only after about 30 minutes of the test.

The surface of coating damaged samples DUA and DUB was examined using SEM. The representative back-scattered-electron image of coating damaged area is shown in Figure 4.3.5-10. Under higher magnification and based on the EDS analysis (Figure 4.3.5-11), it is observed that some part of the DLC coating was cracked, some coating layer was removed leaving a crater, and some coating fragment embedded into the raw coating surface. The coating fragment embedding and the coating cracking are because of the applied high load and the low load bearing capacity of the single surface system. The craters were formed due to the inadequate bonding strength of the single coating system. It is noticed that oxygen was detected in unlubricated samples, meaning the coating surface was oxidised to some level during the dry wear test.

After the dry rolling-sliding wear tests, the weight loss of all the DLC coated samples was neglectable, since the density of carbon-based coating is very small, and the reduced coating volume was very tiny, even for the damaged coating samples.

The unlubricated rolling-sliding wear tests illustrate that WC/a-C:H duplex surface systems could significantly reduce the severe adhesive wear of carburised material in dry condition. The unlubricated tests also indicate duplex systems have a longer duration than single surface

systems. In addition, the duplex systems with nitrided substrate have the excellent wear resistance similar to that containing carburised substrate.

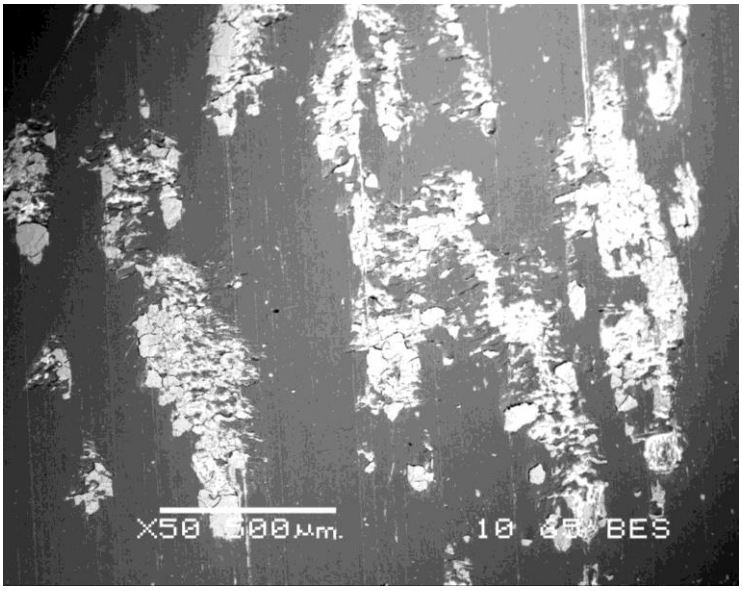

Figure 4.3.5-10 SEM (back-scattered-electron) image of coating damaged surface of single surface system sample DUB after 30 minutes of wear test under 700N (i.e. 597.56 MPa Hertz contact stress) without lubricant

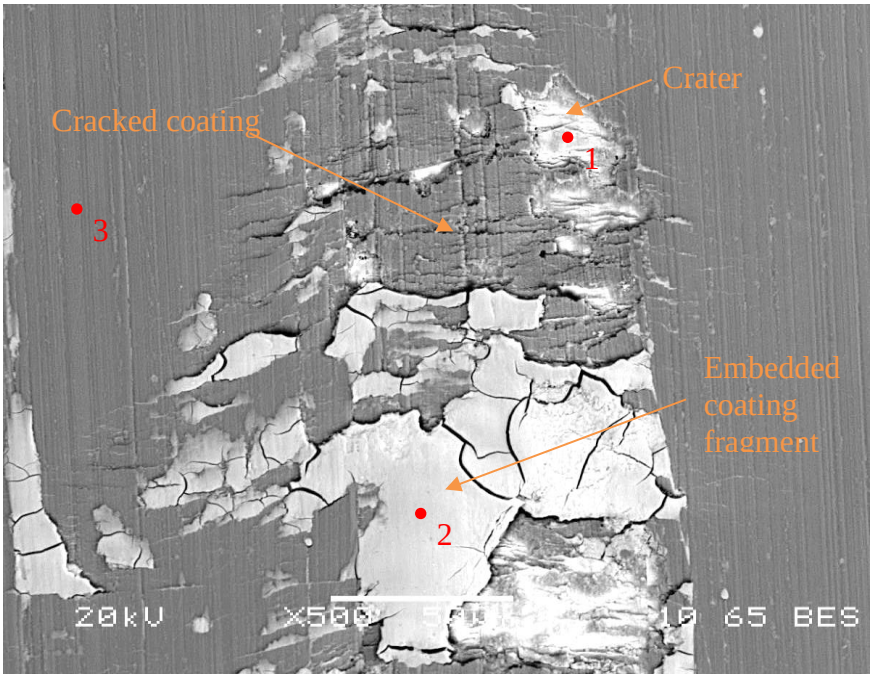

Spectrum	C	O	Cr	Fe	W	Comment
1	21.53	2.98	5.01	3.61	66.87	Crater bottom due to coating breaking off
2	3.94	10.41	1.20	2.45	82.01	Embedded coating fragment
3	31.64	1.45	0.85	2.94	63.12	DLC coating surface

Figure 4.3.5-11 EDS analysis of coating damaged surface

In both oiled and dry conditions, the duplex system samples have a longer duration than the single system under high load in the rolling-sliding wear tests. Due to the ‘thin ice’ effect, cracks and spallation can be easily formed in the hard but brittle coating layer of single coating systems. Plastic deformation will occur easily in the soft substrate under high load, while the hard coating layer cannot follow the deformation of the substrate, then stress generates in the boundary between coating and substrate, thus cracks will occur to release the strain energy after a critical value is reached. In addition, the hard coating fragments can act as indenter and cause local stress concentration, thus further prompt coating cracking in single surface systems. In contrast, when the substrate is pre-hardened, the extent of plastic deformation of substrate is reduced. Then correspondingly, the required extent of hard but brittle coating stretching to follow the substrate deformation is decreased. Hence the stress generated in the coating system is reduced. Therefore, the duplex system can withstand a high load without or with less cracking or spallation because the coating layer receives strong support from the pre-hardened substrate (Bojan Podgornik and Joze Vižintin, 2001).

Another potential benefit of the pre-hardened substrate of duplex surface system is the improved resistance to surface fatigue. Under repeated loading and unloading cycles for a long period, large pits may form in coating systems as a result of surface fatigue. Substrate hardening can reduce the deformation in the substrate and the coating layer. Thus, the formation and propagation of surface and subsurface cracks are then expected to be impeded, reducing the generation of pits on the coating layer (Jun Zhou, 2014). As J. C. A. Batista et al. (2003) reported, duplex treated samples had fewer failure than single surface systems in a cyclic loading condition.

4.3.6 Summary

After the plasma nitriding process, the surface hardness of EN40BT increased from 321 HV0.05 to about 920 HV0.05 (DCPN550-20) and 816 HV0.05 (ASPN550-20). The carburising treatment increased the surface hardness of EN36 from 356 HV0.05 to about 850 HV0.05. It can be seen that the nitrided samples possess similar or higher hardness at much lower treating temperature than the carburised samples.

The duplex surface systems were designed as Diamond Like Carbon (DLC) coating deposited on carburised EN36 and nitrided EN40BT steel. Because of the top DLC coating layer, the friction coefficient and surface hardness of duplex surface system is much better than the traditional carburised surface. The friction coefficient of duplex surface system is only 0.16, while the friction coefficient of carburised surface is much higher as 0.46. The surface hardness of duplex surface is 11.43 GPa (about 1,145 HV), while the hardness of carburised surface is lower as 850 HV0.05. In addition, comparing with the single coating system, the duplex surface systems exhibited superior properties and performance due to the hardened substrate, i.e. higher load bearing capacity and better resistance to scratch and rolling-sliding wear. The load bearing capacity of duplex surface systems is higher than 300 g, while that of single coating system is less than 200 g. In the scratch test, duplex surface system samples started cracking/chipping at a higher load of 43 N as compared with 35 N of the single surface system sample. In the rolling-sliding wear tests, duplex surface system samples survived from 500 N to 800 N, while coating damage was observed under 700 N in the single coating system samples.

The superior properties of duplex surface systems (e.g. the low friction coefficient, high surface hardness and high load bearing capacity) could increase the resistance to the high contact stresses due to high input torque, poor lubrication quality and unavoidable

misalignment and prevent the life-limiting problems of wind turbine gearbox components. In addition, the duplex surface system containing carburised substrate is similar to those with direct-current plasma nitrided substrate and active-screen plasma nitrided substrate indicating that plasma nitriding method could replace carburising in the duplex surface system.

CHAPTER 5: ROLLING-SLIDING WEAR TESTER COMBINED WITH CONDITION MONITORING SYSTEMS

Detection of early-stage defects can prevent catastrophic failures. Therefore, the relationship between AE/vibration signals and defect development has been studied by combining AE/vibration test systems with the rolling-sliding wear tester for the accurate monitoring degradation of gearbox components.

Four wheels made of as-received EN36 and EN40BT steel grades, carburised EN36 and nitrided EN40BT were tested against WC wheel using a rolling-sliding wear tester. The experimental setup is shown in Figure 3.4-2 and Figure 3.4-3. The acoustic emission and vibration signals generated during the tests were recorded and analysed. After each test, the wheel samples were examined carefully. Micro-pits, cracks and craters were observed. The development of material damage was found to be closely and sensitively interrelated with the AE signals. The vibration spectrum only significantly changed after severe and visible damage formed on the surface of the tested wheel samples.

5.1 Pencil-lead break and noise signals

Pencil-lead break test or Hsu-Nielsen source test was conducted before rolling-sliding wear tests to check the condition of the AE sensor and the transmission path between the area of interest and the sensor. A typical AE waveform generated using a pencil-lead break is shown in Figure 5.1-1. It is a burst signal with PAC-energy of 1739 μV·s and amplitude of 91 dB.

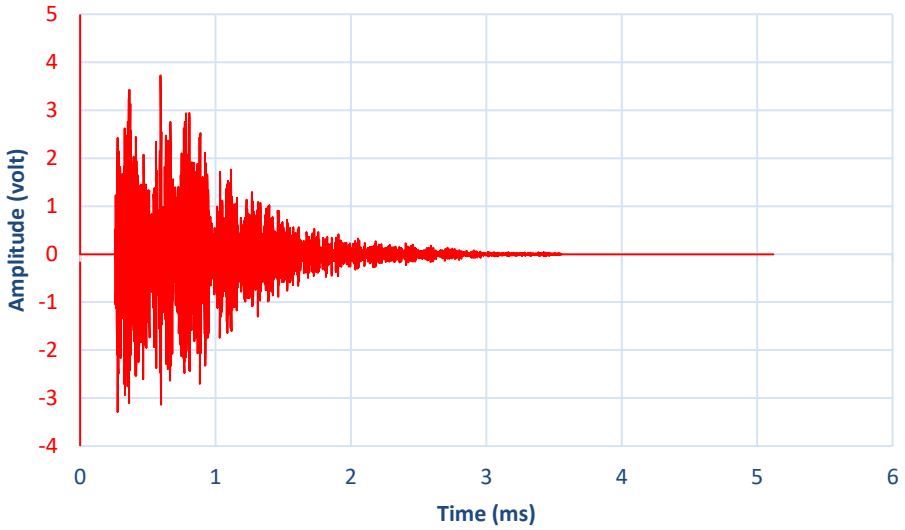

Figure 5.1-1 Typical waveform of a burst AE signal from pencil lead break

A trial was conducted to identify possible noise sources and then use proper methods to eliminate any noise signals affecting the collection of AE data to the greatest possible extent. After the trial, two main noise sources were identified. One is the frictional noise arising from the rubbing between the wheels rolling surfaces. The other noise source was due to oil splash. Both noise sources generated a large number of unwanted AE signals.

The waveform of the noise-related AE signal due to friction is continuous as shown in Figure 5.1-2. The number of AE hits and their amplitude generated from friction keep increasing at the beginning of the test. Meanwhile low-amplitude AE signals are also still generated, forming a step-like pattern. After the maximum amplitude reaches a certain value (normally around 47 dB), the friction-induced AE signals reach a relatively stable rate of generation for the rest of the test as seen in Figure 5.1-3. Figure 5.1-4 shows the PAC-energy of the friction-induced AE hits. Since the amplitude of friction-induced noise is lower than most defect-related AE signals, it can be easily eliminated by setting the threshold at 50 dB.

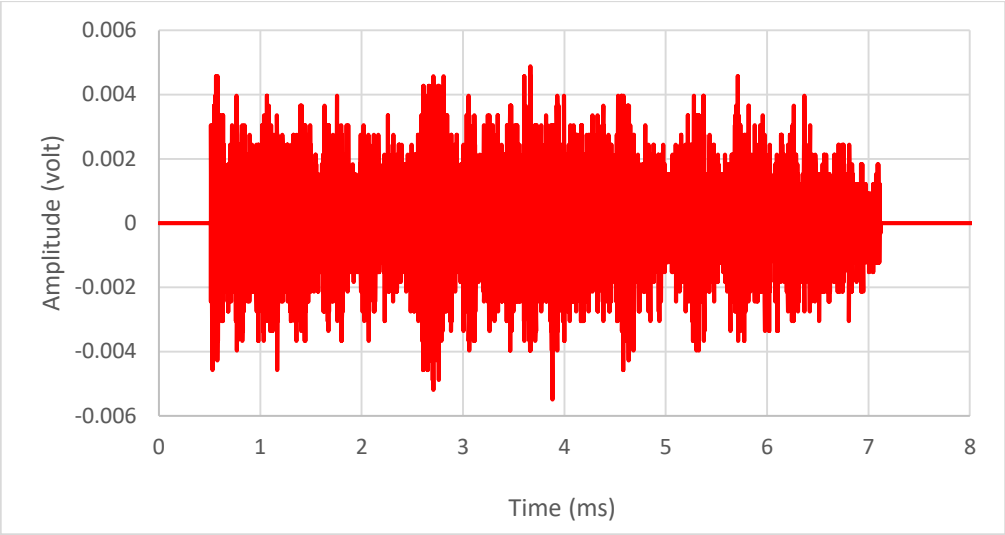

Figure 5.1-2 Typical waveform of a continuous AE signal from friction between wheels

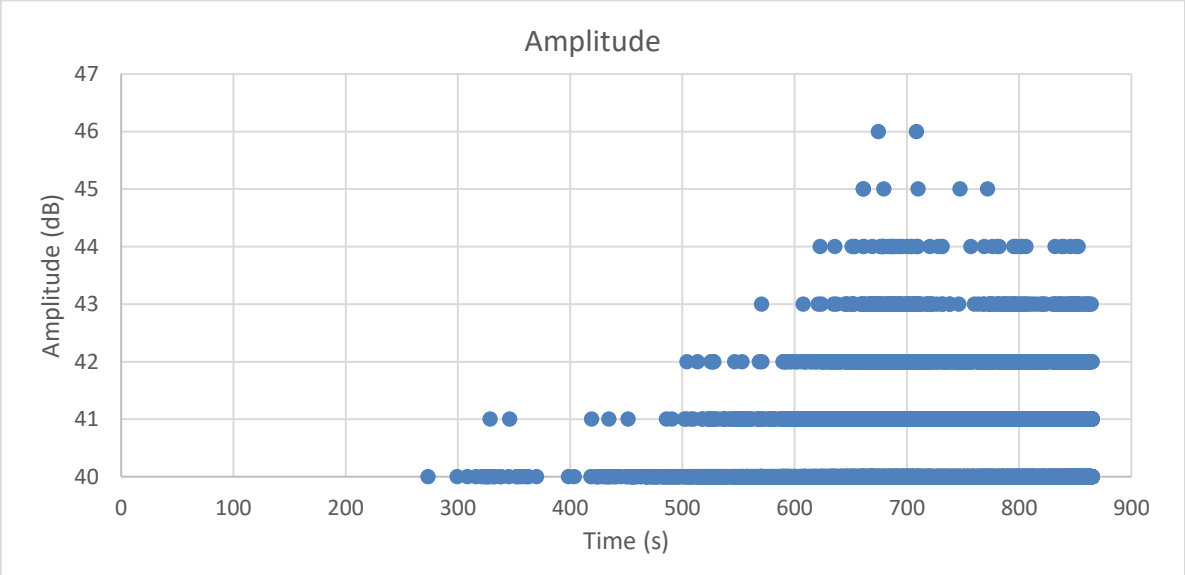

Figure 5.1-3 Typical hit amplitude distribution due to friction (threshold 40 dB)

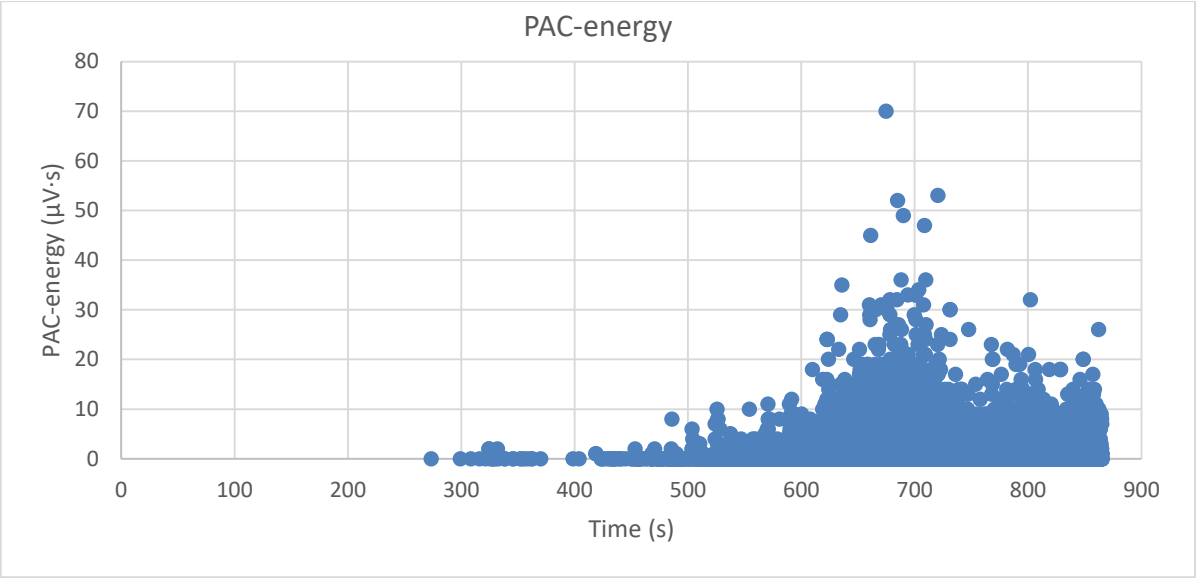

Figure 5.1-4 The PAC-energy of AE hits due to friction (threshold 40 dB)

The waveform of noise AE signals generated due to oil splash has a form of a burst as shown in Figure 5.1-5. A large number of this type of noise signals occurs suddenly, covering a wide amplitude range up to 95 dB as seen in Figure 5.1-6. The PAC-energy of most these AE hits is lower than 40 µV·s (as shown in Figure 5.1-7). There are two major reasons for oil splash in the oil tank. Firstly, the rubbing of wheels generates heat, thus increases the oil temperature and significantly reducing oil viscosity. Oil with low viscosity is prone to generate splash. In addition, used oil has been identified to be more prone to generate splashes than new oil. Secondly, the wheel contacts will become unsteady after the sample wheel surface condition changes to some certain extent. Then the oil flow also becomes very unsteady after it flows through the contact position of the wheels, causing oil splashes to occur. Since the amplitude of this type of noise signals can be as high as 95 dB, it can mask some damage-related AE signals. By simply using higher threshold value almost all useful AE signals will be filtered out also. Therefore, a foam sheet was placed over the oil surface and inner tank wall, to

prevent splash related noise. The application of the foam sheet successfully eliminated splash-induced noise signals.

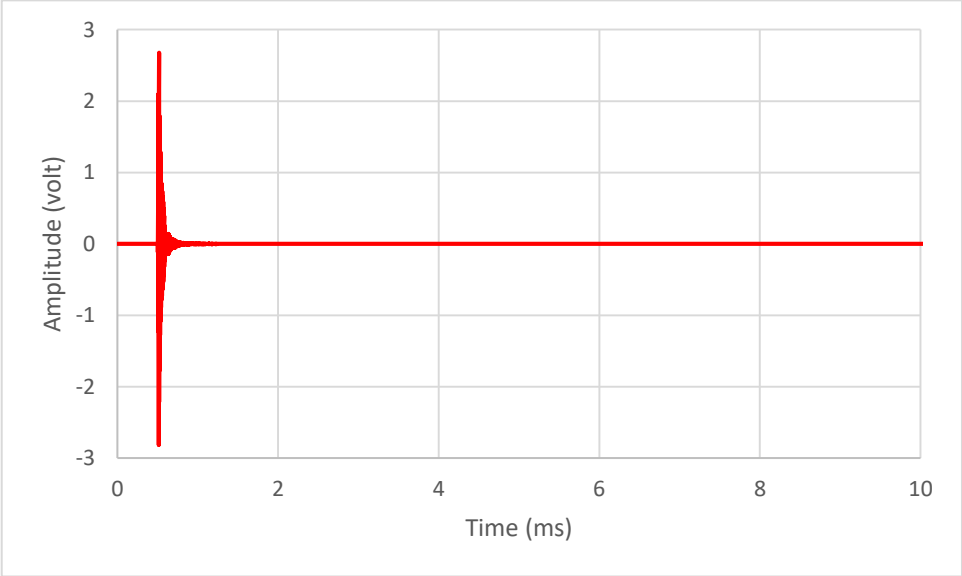

Figure 5.1-5 Typical waveform of a burst AE signal due to oil splash

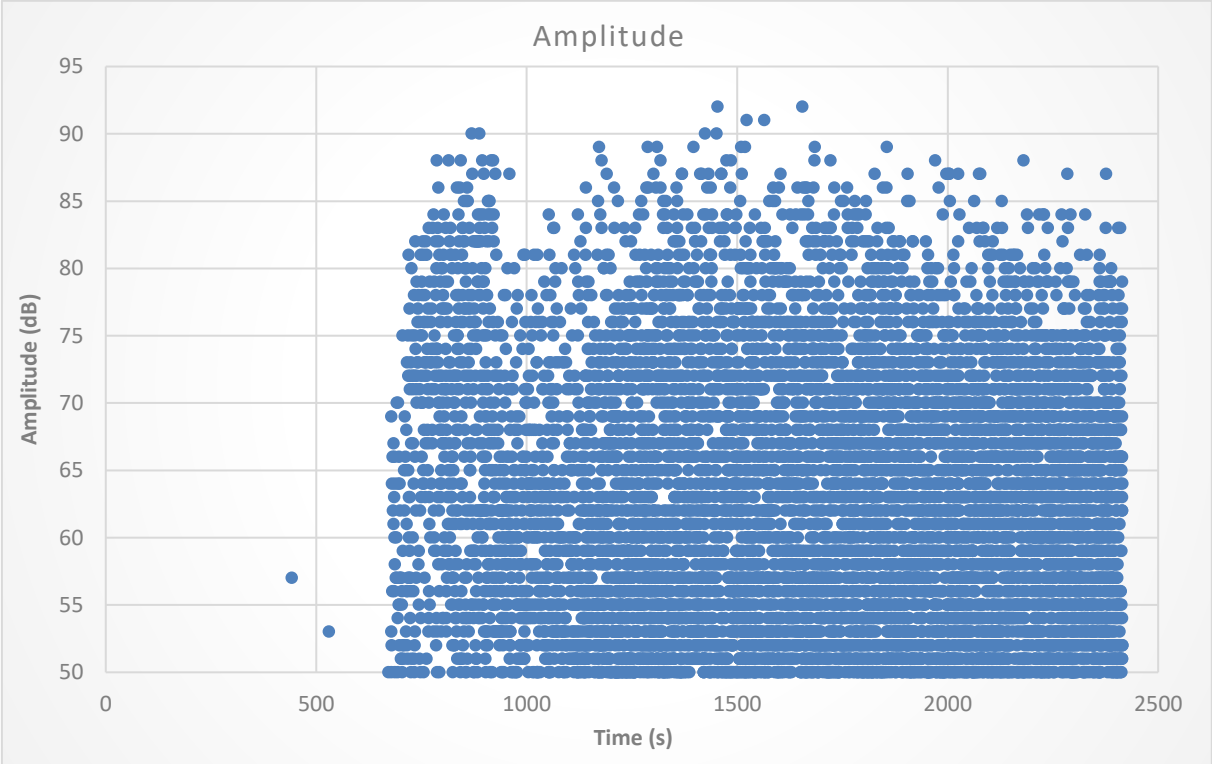

Figure 5.1-6 Typical hit amplitude distribution due to oil splash

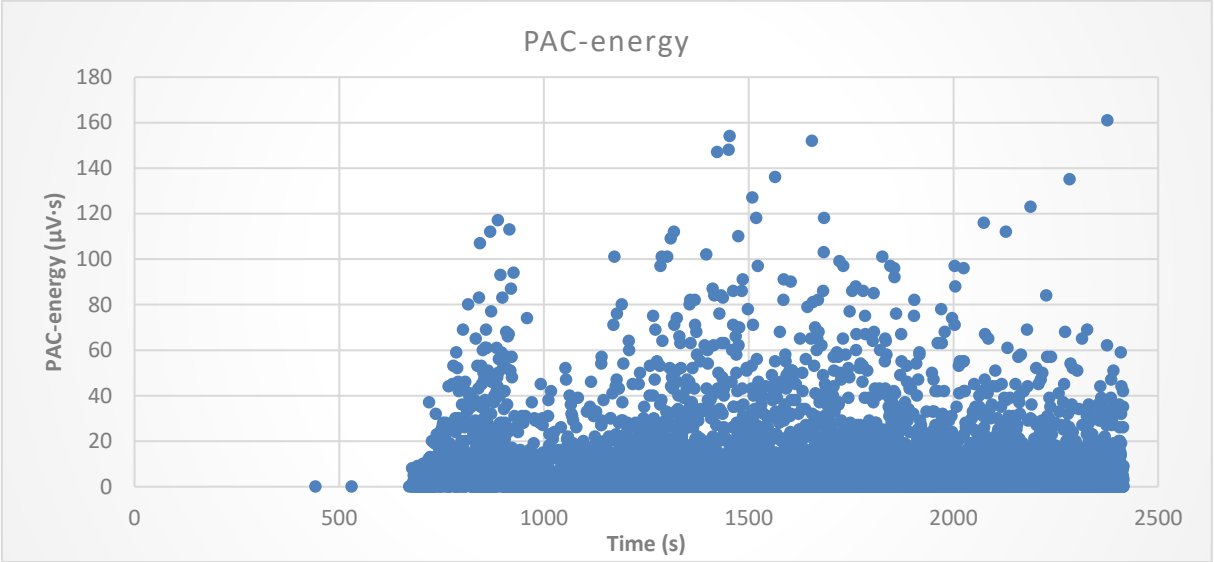

Figure 5.1-7 The PAC-energy of AE hits due to oil splash

5.2 Test 1: As-received EN36 wheel against WC wheel

The photograph and SEM micrograph of the untreated EN36 wheel surface before test is shown in Figure 5.2-1. The as-ground surface is shiny, mirror-like with some scratches present. Before testing, the weight of the untreated EN36 wheel was 63.0270 g. The photograph, SEM micrograph and EDS results of the as-received WC wheel are shown in Figure 5.2-2. The surface is shiny and looks very smooth in the photograph, but under SEM, the WC wheel surface is actually porous and scratches in one direction can be found. The results of the EDS analysis carried out on the WC wheel surface indicate that it is Co based. The elements composition present are C 8.57 in wt%, Co 5.20 in wt% and W 86.23 in wt%.

This test lasted about 24 hours. At the end of the test, 5 cracks with lengths exceeding 1,500 μm and a crater of significant size with dimensions exceeding 1 mm × 1 mm formed in the as-received EN36 wheel surface, ignoring other smaller defects. This particular test was divided into 5 periods when signals notably changed or sample damage was observed.

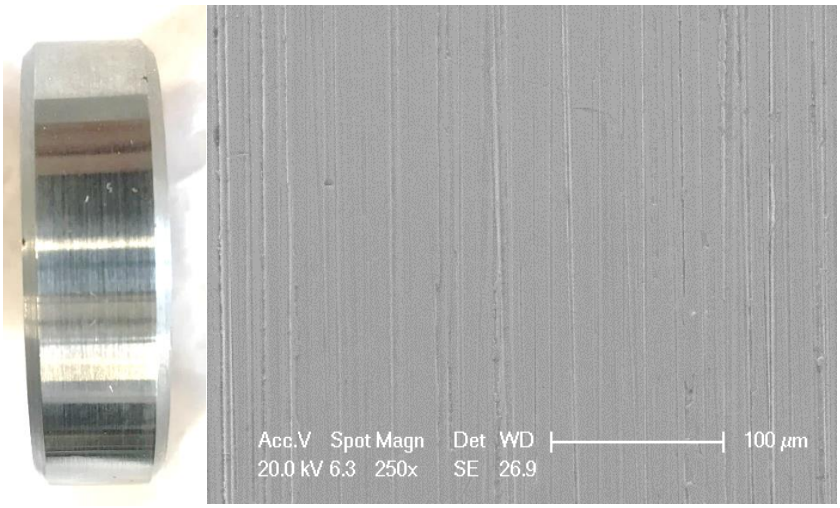

(a) (b)

Figure 5.2-1 The photo and SEM image of the untreated EN36 wheel surface before Test 1

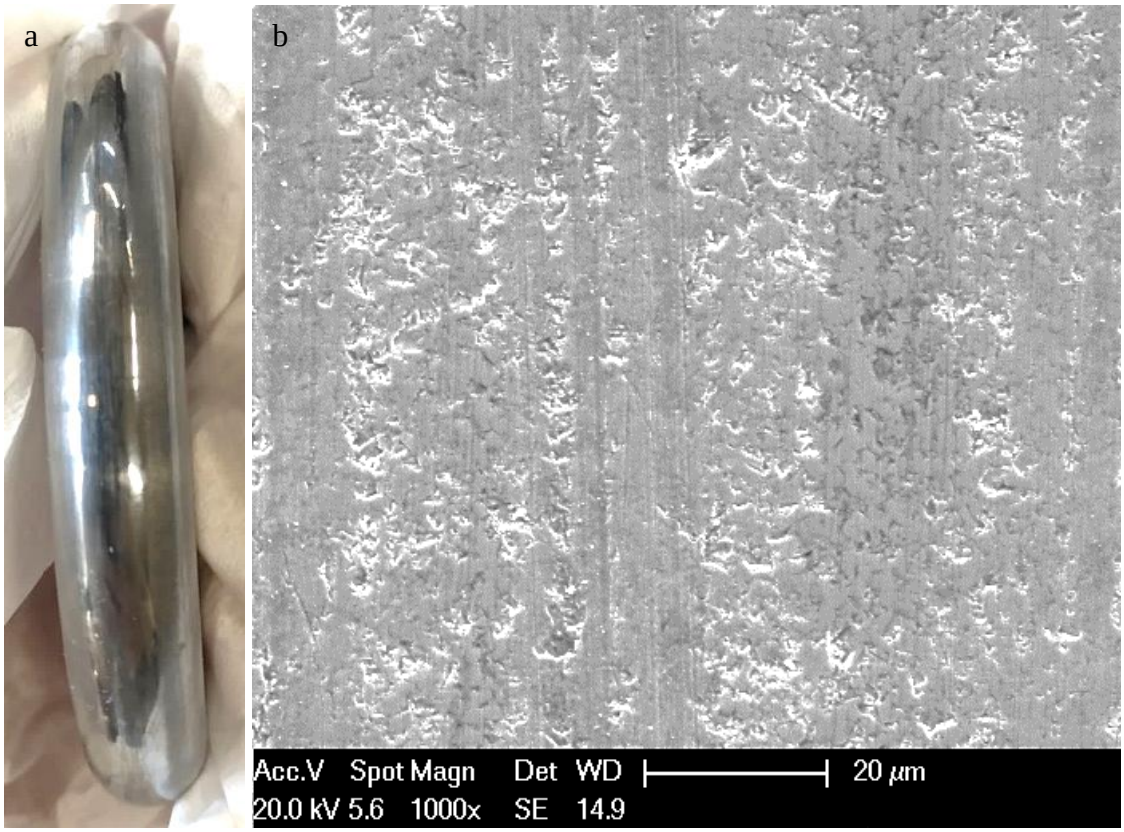

Elements	C	Co	W
Weight%	8.57	5.20	86.23

Figure 5.2-2 The photo and SEM image of the WC/Co wheel surface before Test 1, and the EDS results of the wheel surface

(1) First period (0-3,000 sec)

At the beginning of the test, the spectrum of the vibration signal generated by the Amsler wear tester is shown in Figure 5.2-3. The 50 Hz peak is the fundamental frequency from the 50 Hz motor which the Amsler wear tester is equipped with. The 100 and 150 Hz peaks are the 2^{nd} and 3^{rd} harmonics of the 50 Hz fundamental frequency. The threshold value for AE detection was set as 50 dB.

No AE hit above the threshold set was detected during the 1^{st} period. At the end of this period, a concaved surface was observed in the untreated EN36 wheel (as shown in Figure 5.2-4), and the weight loss was negligible, indicating the concave surface was because the result of significant plastic deformation. Since acoustic emission signals are related to the release of elastic strain energy, the generated signals during plastic deformation would be too weak to be detectable. The FFT spectrum of the vibration signal provided in Figure 5.2-5, did not show any significant changes from the beginning to the end of 1^{st} period either.

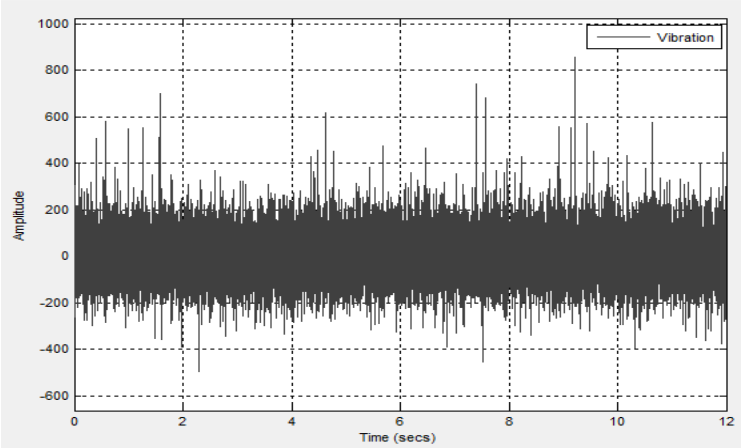

(a)

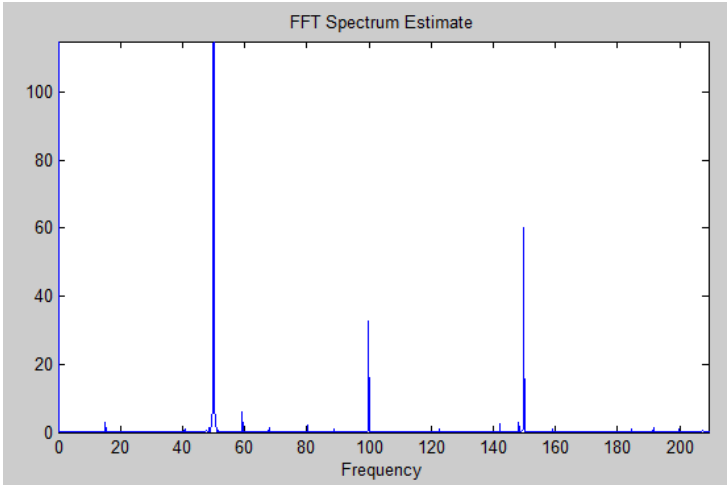

(b)

Figure 5.2-3 (a) Raw vibration signal, and (b) spectrum of vibration signal, generated at the beginning of Test 1

Figure 5.2-4 Photo of the untreated EN36 wheel after the 1st period of Test 1

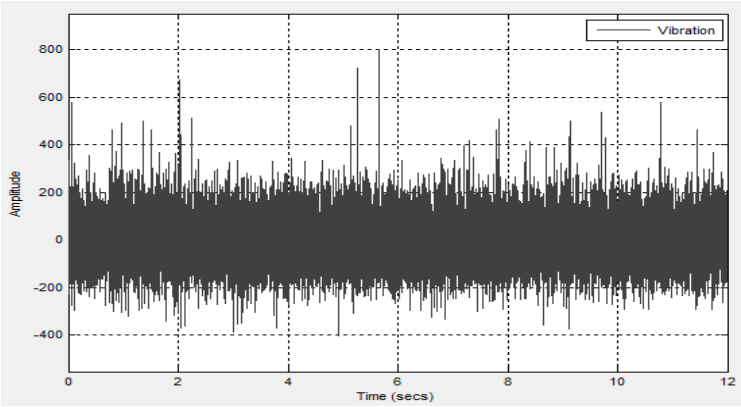

(a)

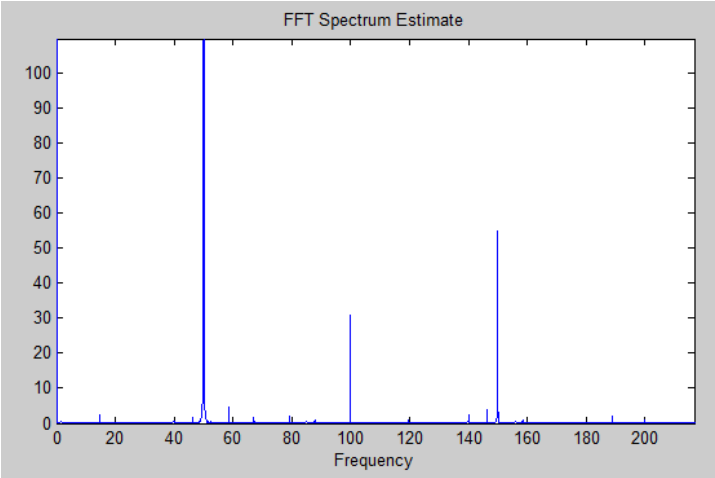

(b)

Figure 5.2-5 (a) Raw vibration signal, and (b) spectrum of vibration signal, generated after the 1st period of Test 1

(2) Second period (3,000-6,000 sec)

Only 3 AE hits were detected during this period as shown in Figure 5.2-6. The maximum amplitude recorded was 55 dB, and the maximum PAC-energy was 14 μV·s as shown in Figure 5.2-7. Every valid AE hit is deemed to have been generated from the initiation or propagation of cracks under the cyclic loading-unloading conditions of the Amsler test.

Under SEM, only micro-cracks were observed in the untreated EN36 surface after the second period as shown in Figure 5.2-8. This suggests that most of these micro-cracks were too small to generate AE signals with sufficient energy/amplitude higher than background noise and

threshold value in order to be recorded. Hence during this period, few valid AE signals were detected. In the FFT spectrum of vibration signal collected at the end of the 2nd period, no significant change was found either as seen in Figure 5.2-9.

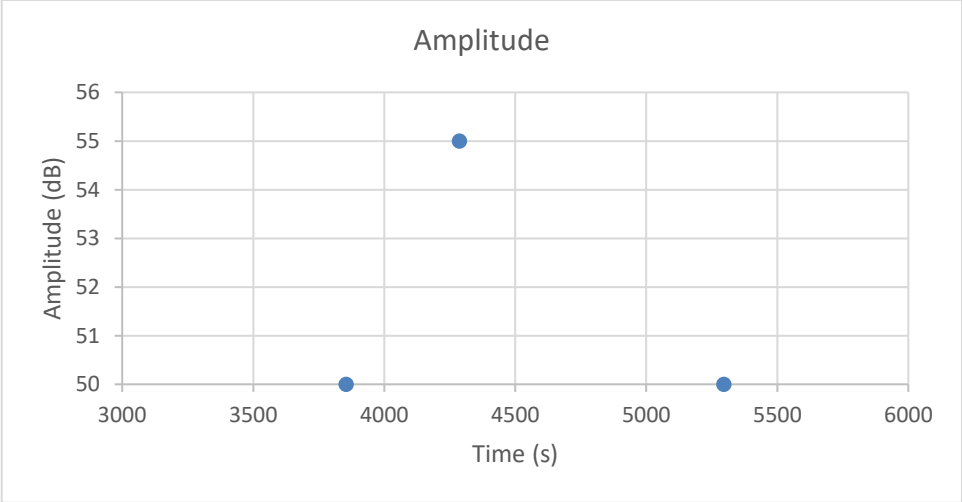

Figure 5.2-6 AE hits detected during the 2nd period of Test 1

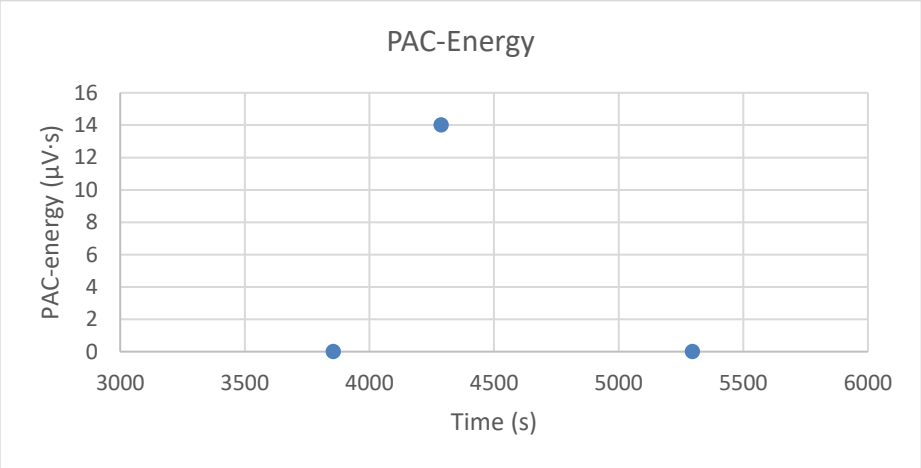

Figure 5.2-7 PAC-energy of the AE hits detected during the 2nd period of Test 1

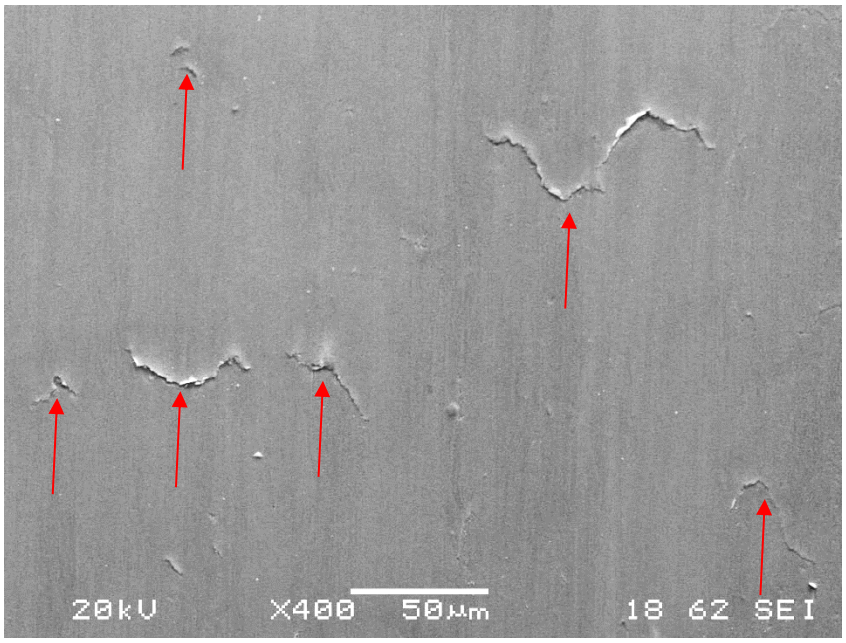

Figure 5.2-8 SEM image of the wear track surface after the 2nd period of Test 1, micro-cracks can be observed as arrowed

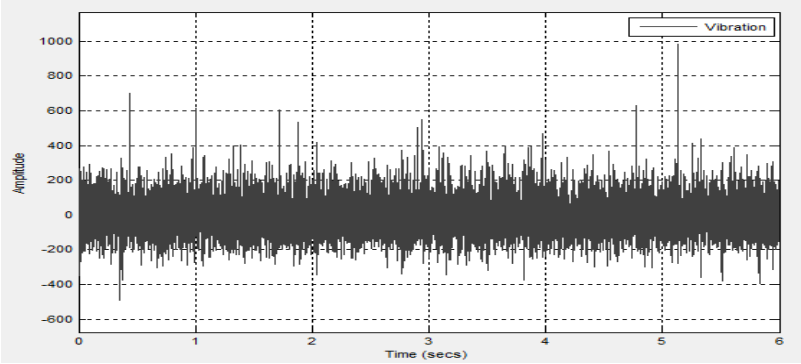

(a)

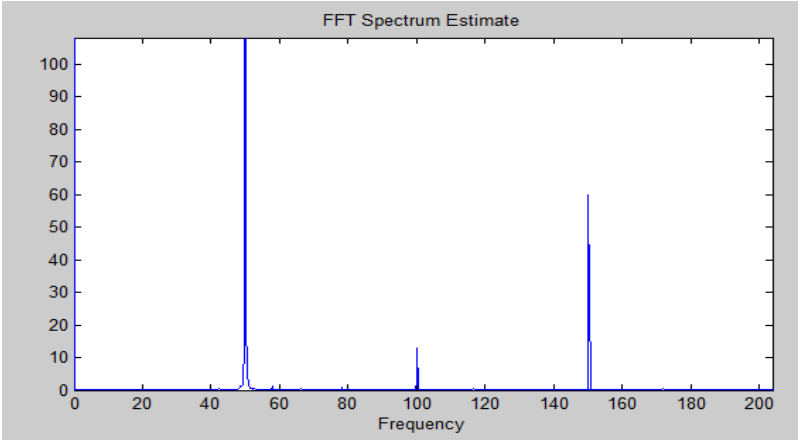

(b)

Figure 5.2-9 (a) Raw vibration signal, and (b) spectrum of vibration signal, generated after the 2nd period of Test 1

(3) Third period (6,000-20,400 sec)

Micro-cracks continued growing and became enlarged in the untreated EN36 surface during this period with 18 damage-related discrete AE signals being detected as seen in Figure 5.2-10. These signals hint irregular propagation of cracks. The maximum AE signal amplitude recorded is 73 dB. The PAC-energy of these AE hits is shown in Figure 5.2-11, in which the maximum PAC-energy is 530 μV·s. The trend of the cumulative PAC-energy in this period is shown in Figure 5.2-12.

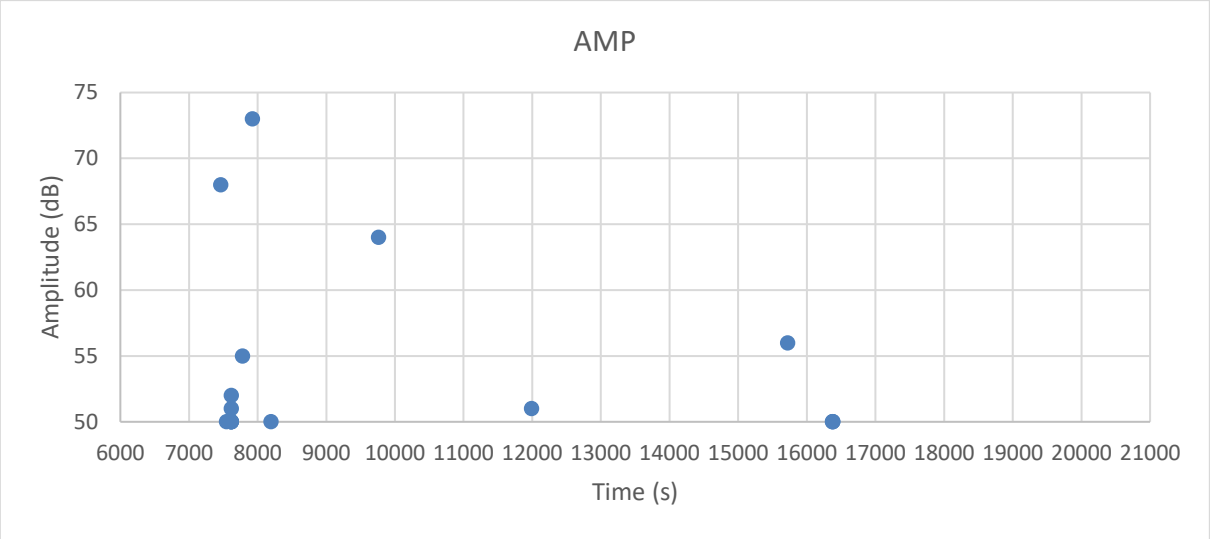

Figure 5.2-10 AE hits detected during the 3rd period of Test 1

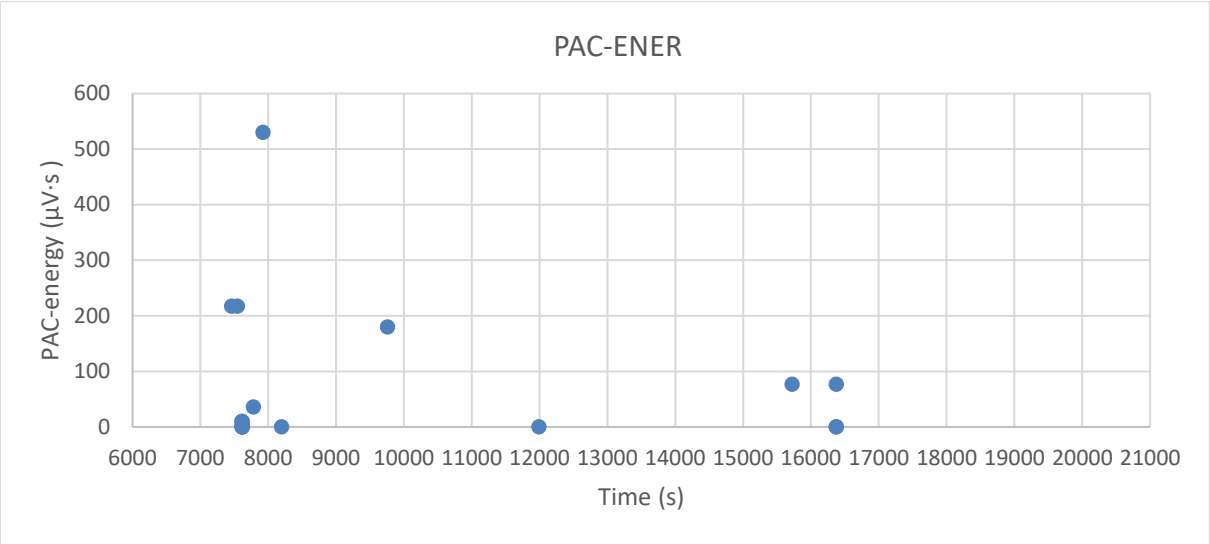

Figure 5.2-11 PAC-energy of the AE hits detected during the 3rd period of Test 1

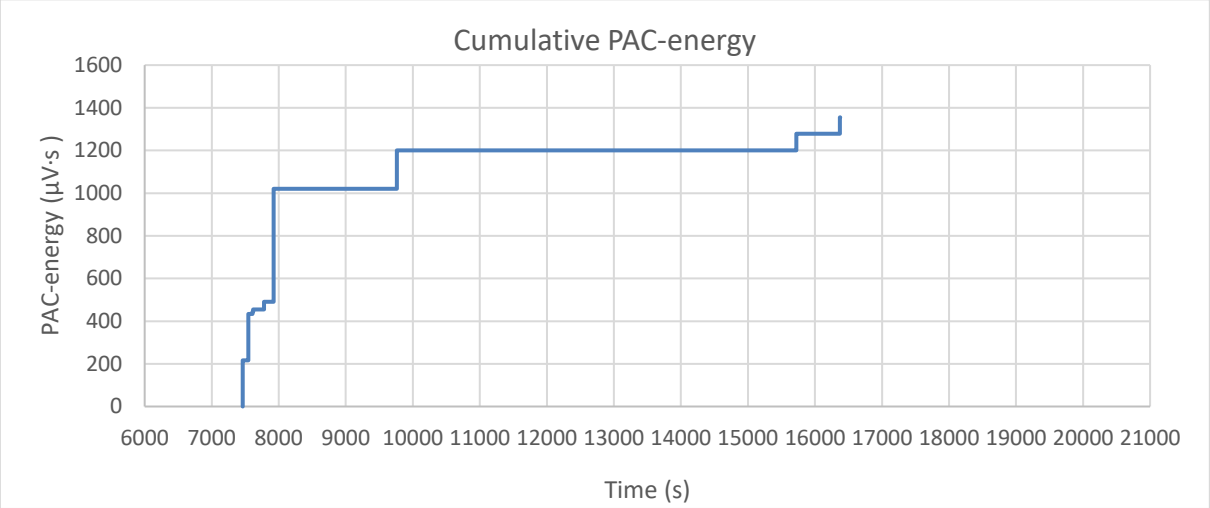

Figure 5.2-12 Cumulative PAC-energy of the AE hits detected during the 3rd period of Test 1

At the end of this period, the wheel sample was examined using SEM. Some micro-pits with a diameter of around 50 μm (as shown in Figure 5.2-13) were observed in the steel wheel sample examined. No damage was observed in the WC wheel (as shown in Figure 5.2-14). The formation of these micro-pits may be the source of the detected discrete AE signals. But the formation of these micro-pits did not change the vibration pattern of the wear tester as

shown in Figure 5.2-15. This is due to the fact that the defects were still too small to cause the generation of vibrations of sufficient energy and amplitude in order to be detectable.

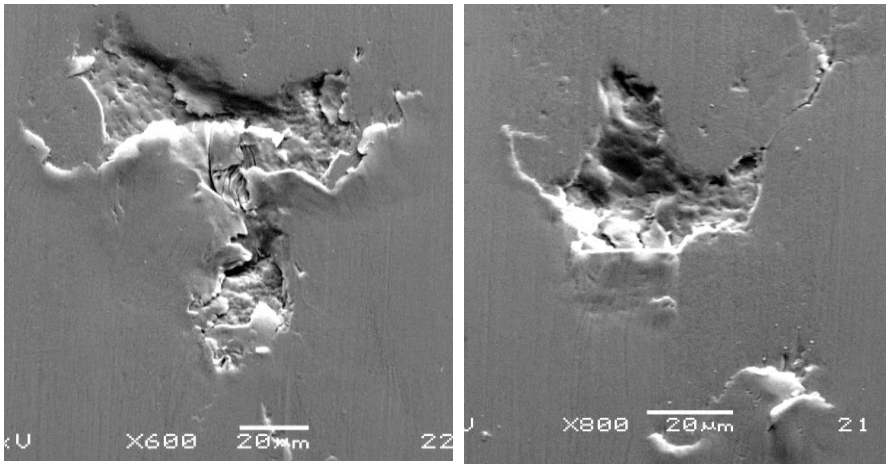

(a) (b)

Figure 5.2-13 SEM image of the wear track surface of untreated EN36 wheel after the 3rd period of Test 1, micro-pits can be observed

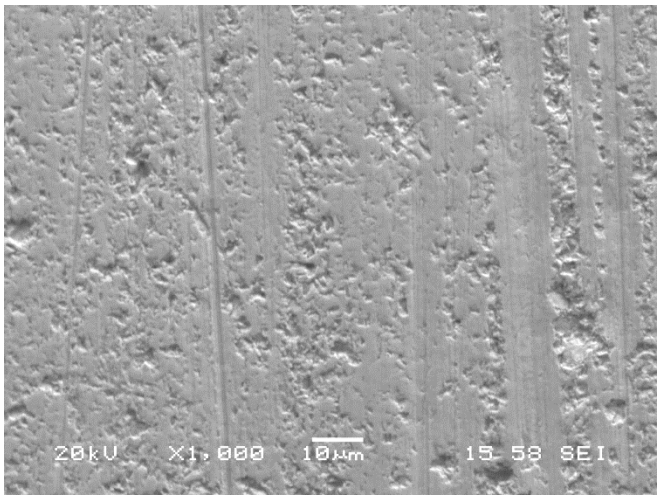

Figure 5.2-14 SEM image of the contact surface of WC wheel after the 3rd period of Test 1, no obvious damage formed

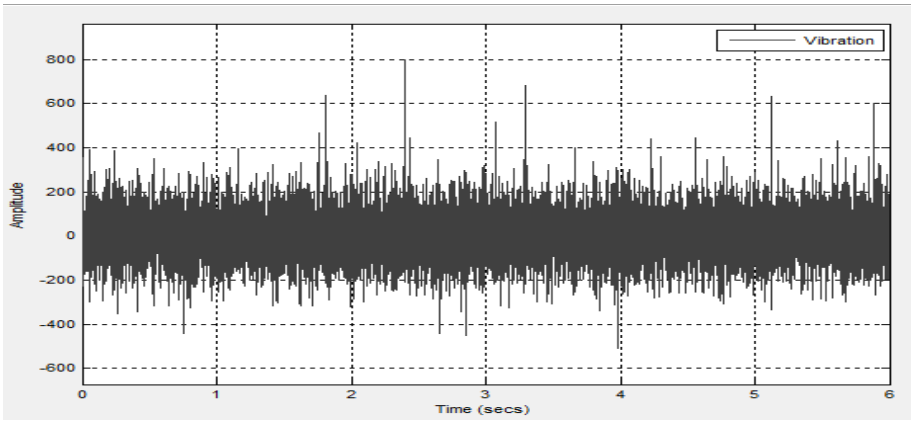

(a)

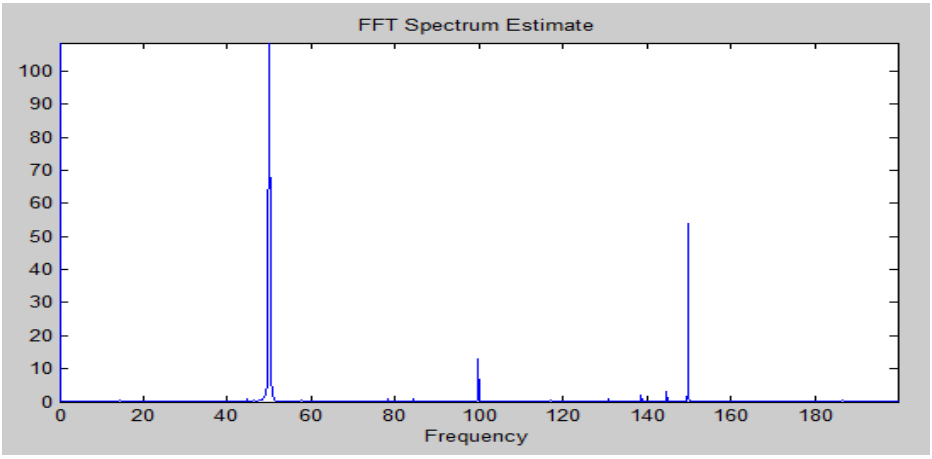

(b)

Figure 5.2-15 (a) Raw vibration signal, and (b) spectrum of vibration signal, generated after the 3rd period of Test 1

(4) Fourth period (20,400-52,200 sec)

A total of 353 defect-borne AE hits were detected. Apart from discrete AE hits, two AE clusters were collected between 24,400 and 26,400 seconds in the test. The amplitude and PAC-energy of the detected AE signals are shown in Figure 5.2-16 and Figure 5.2-17 respectively. The maximum amplitude was found to be 66 dB and the maximum PAC-energy was identified to be 101 μV·s. The cumulative PAC-energy was 1400 μV·s. The trend of cumulative PAC-energy during this period is shown in Figure 5.2-18.

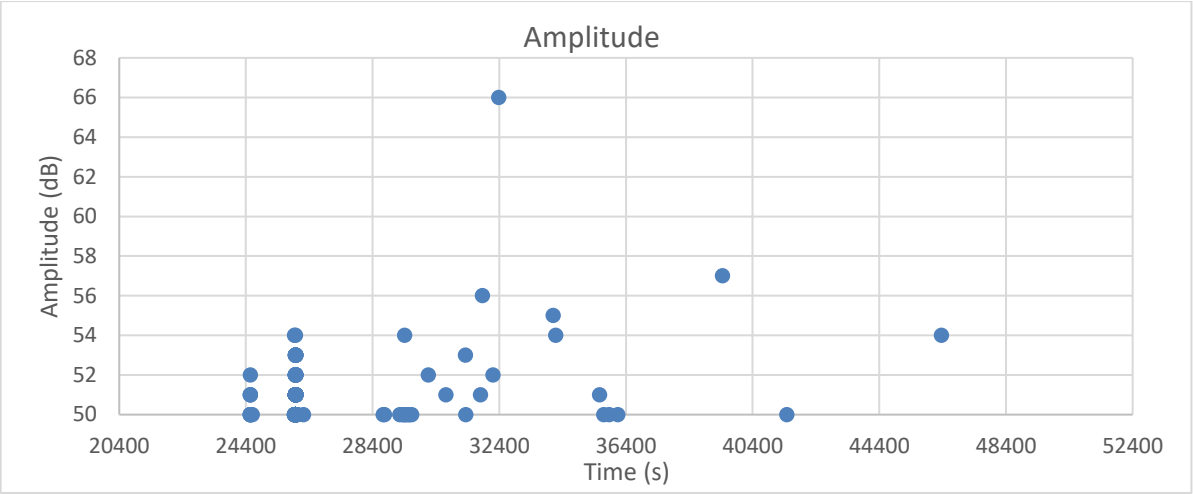

Figure 5.2-16 AE hits detected during the 4th period of Test 1

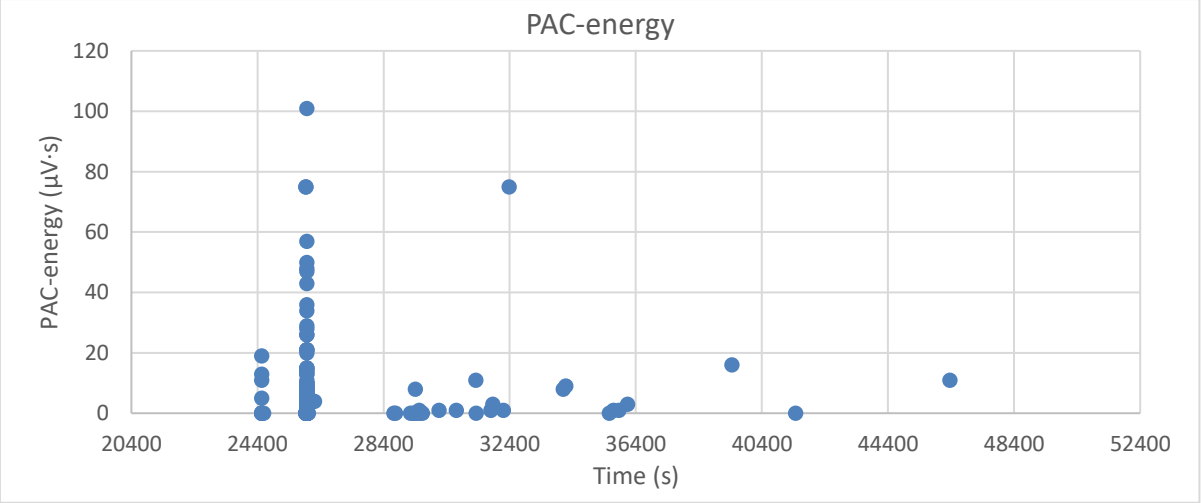

Figure 5.2-17 The PAC-energy of the AE hits detected in the 4th period of Test 1

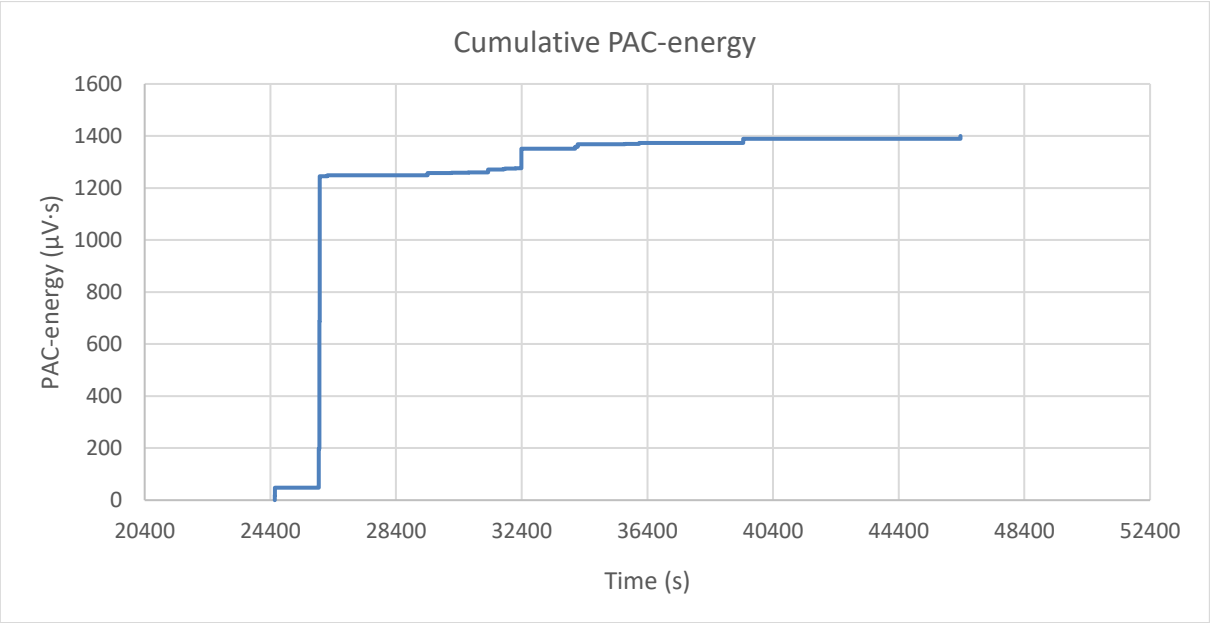

Figure 5.2-18 The cumulative PAC-energy of the AE hits detected in the 4th period of Test 1

In agreement with the AE signals, 5 visible axial cracks were found with the naked eye in the wheel made of untreated EN36 (as shown in Figure 5.2-19). Using SEM, these cracks were measured to be approximately 1,500 μm long. Some craters with dimensions up to 500 μm × 500μm were also observed (as shown in Figure 5.2-20). The formation of these large cracks and craters generated AE signals. No significant change in the vibration spectrum occurred during this period, except for two new peaks with amplitude lower than 10 μV (as shown in Figure 5.2-21). The WC wheel remained undamaged.

Figure 5.2-19 Photos of visible cracks formed during the 4th period of Test 1

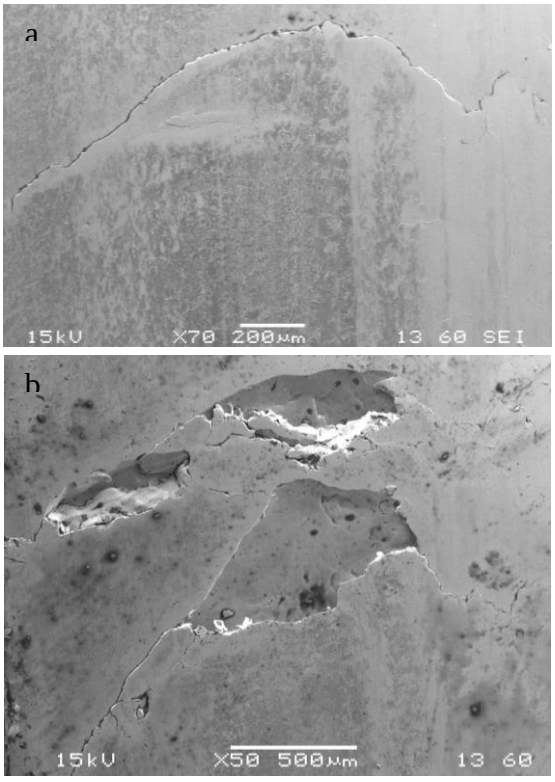

Figure 5.2-20 SEM images of big cracks and craters formed during the 4th period of Test 1, (a) crack longer than 1,500 µm, and (b) long crack and crater larger than 500 µm × 500 µm

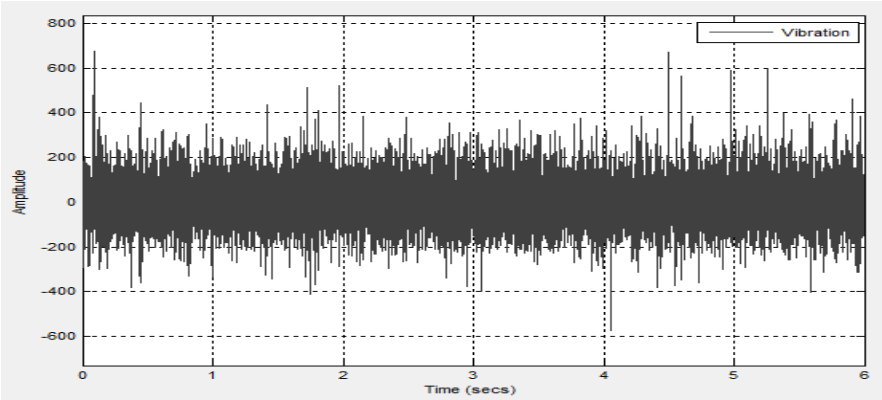

(a)

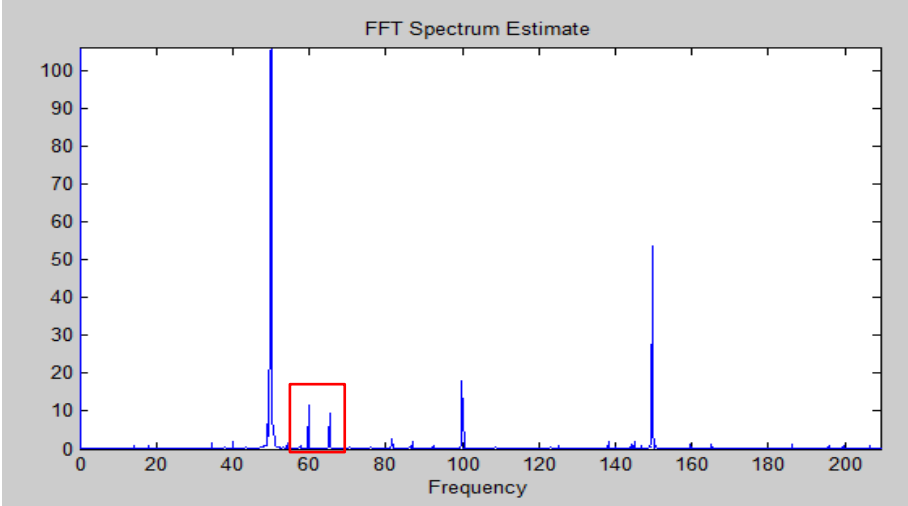

(b)

Figure 5.2-21 (a) Raw vibration signal collected after the 4th period of Test 1, and (b) the vibration spectrum, in which two new peaks occurred as framed

(5) Fifth period (52,200-86,400 sec)

A total of 15 valid discrete AE signals were recorded irregularly before 79,000 seconds of the test, indicating some slow propagation of cracks. Beyond this point, a dense cluster of 49 AE signals were collected (as shown in Figure 5.2-22). Then the vibration of the wear tester also increased significantly. The dense AE signal cluster implied a rapid propagation of cracks, probably leading to severe surface damage and profile change of the sample, resulting in significant vibration.

The PAC-energy of the detected AE is shown in Figure 5.2-23. The maximum amplitude was 70 dB and the maximum PAC-energy was 54 μV·s. The cumulative PAC-energy was 826 μV·s and increased dramatically at the end of this period (as shown in Figure 5.2-24).

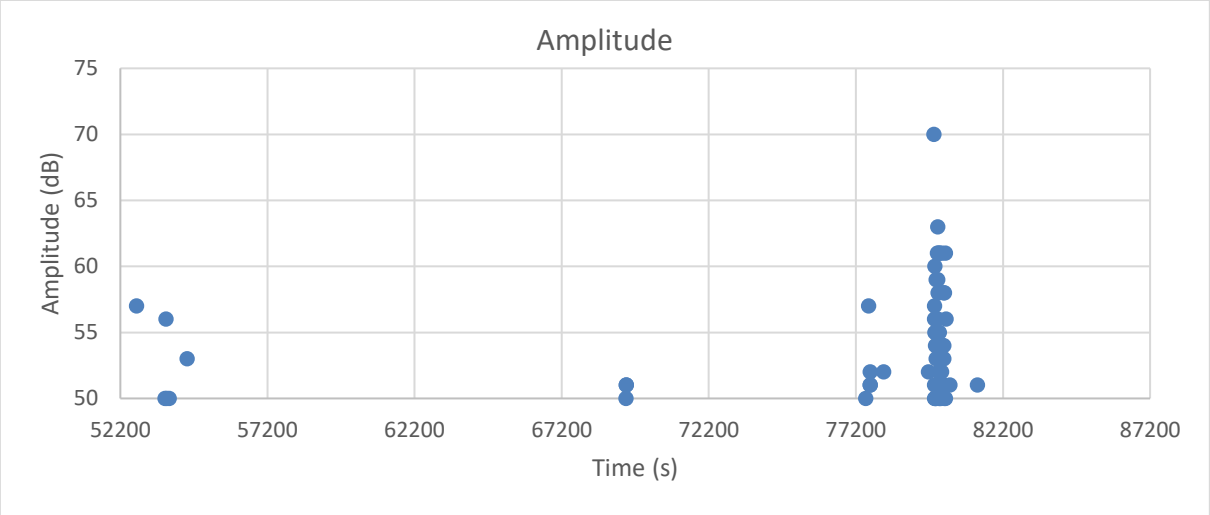

Figure 5.2-22 Amplitude of the AE hits detected in the 5th period of Test 1

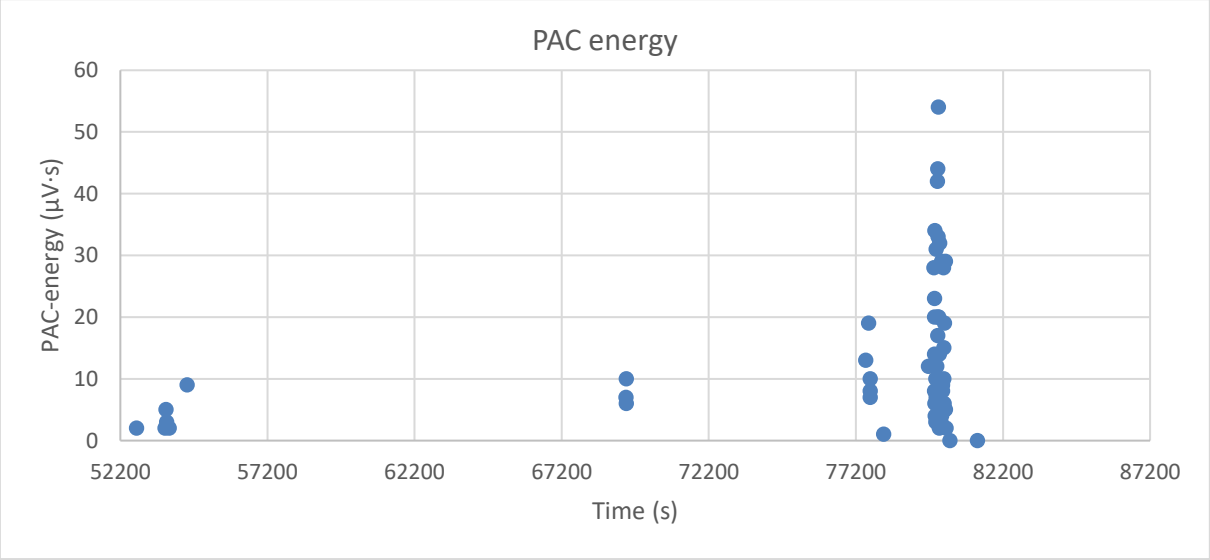

Figure 5.2-23 PAC-energy of the AE hits detected in the 5th period of Test 1

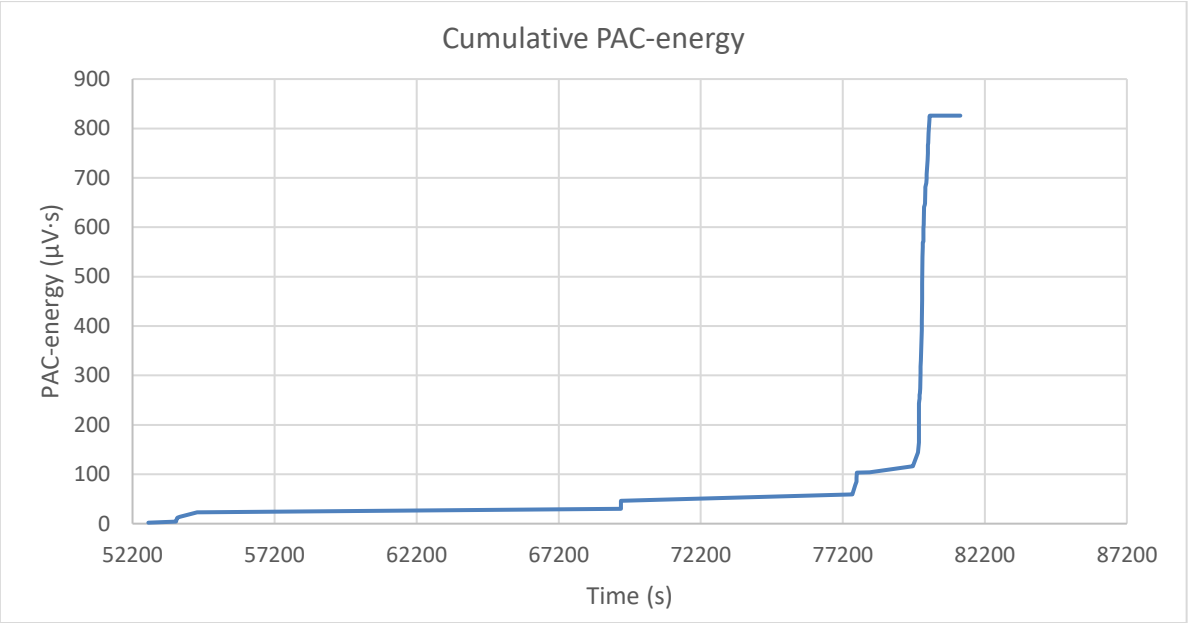

Figure 5.2-24 The cumulative PAC-energy of the AE hits detected in the 5th period of Test 1

Surface defects including one big crater larger than 1 mm^2 and other visible cracks were observed in the EN36 wheel at the end of this period (as shown in Figure 5.2-25). The AE cluster and increased vibration of wear tester was very possibly arising from the presence of the big crater. There was no damage in the WC wheel (as shown in Figure 5.2-26).

At the end, side bands of 5-6 Hz clearly occurred around the fundamental 50 Hz and its 3rd harmonic 150 Hz peaks in the vibration spectrum (as shown in Figure 5.2-27). This sample was deemed to have failed at this point.

The measured weight of the EN36 wheel had dropped to 62.8440 g after the completion of the test, so the total weight loss was 0.1830 g and the average wear rate was 7.6 mg/hour, which are quite small. The damaged wheel was subsequently cut along its radial plane to conduct failure analysis.

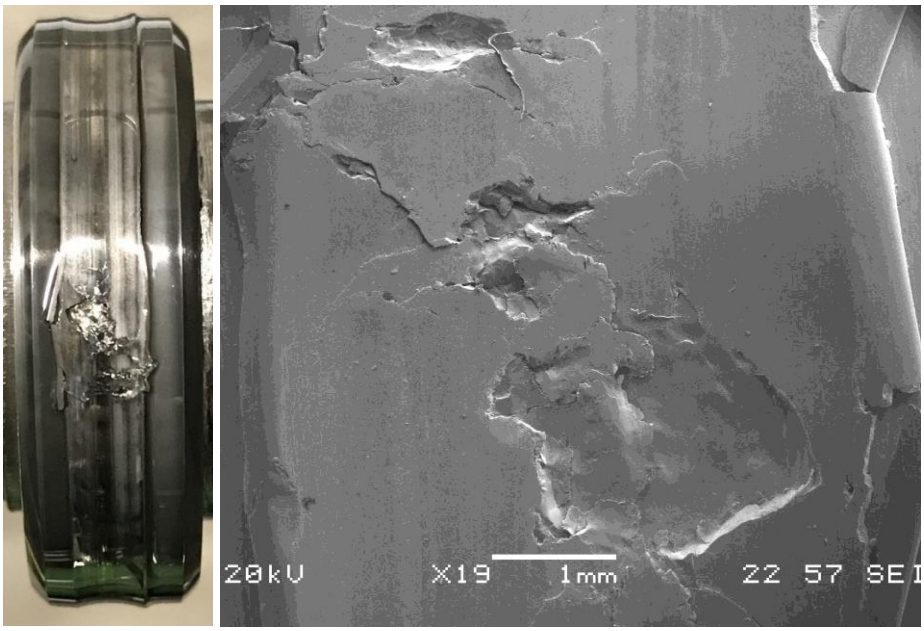

(a) (b)

Figure 5.2-25 One big crater and several small craters formed in the untreated EN36 wheel surface after the last period of Test 1, (a) the photo, and (b) the SEM image

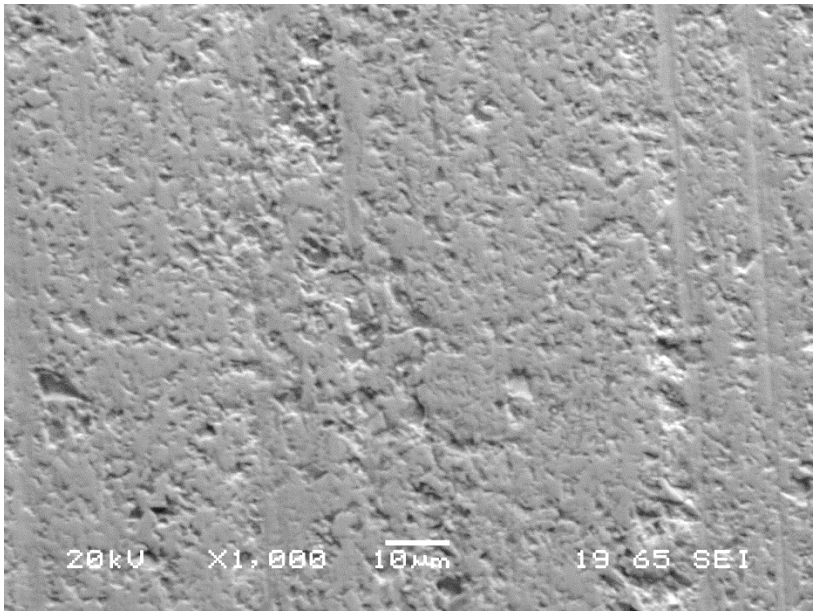

Figure 5.2-26 The contact surface of WC wheel without severe damage at the end of Test 1

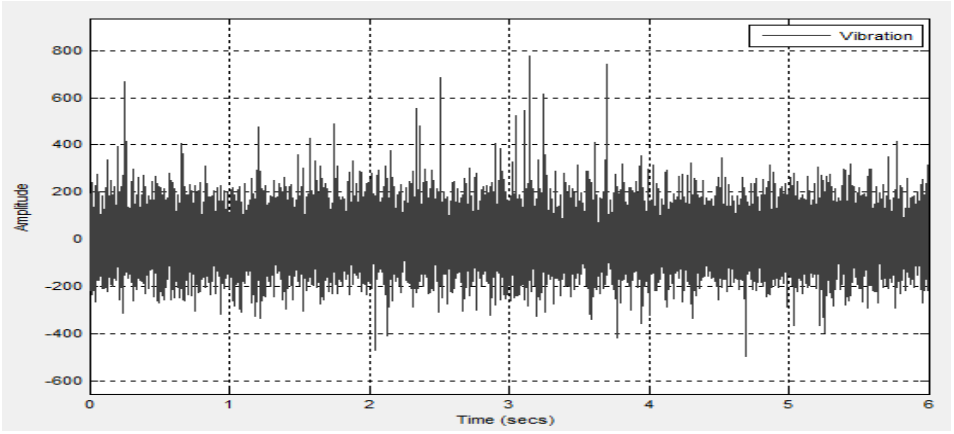

(a)

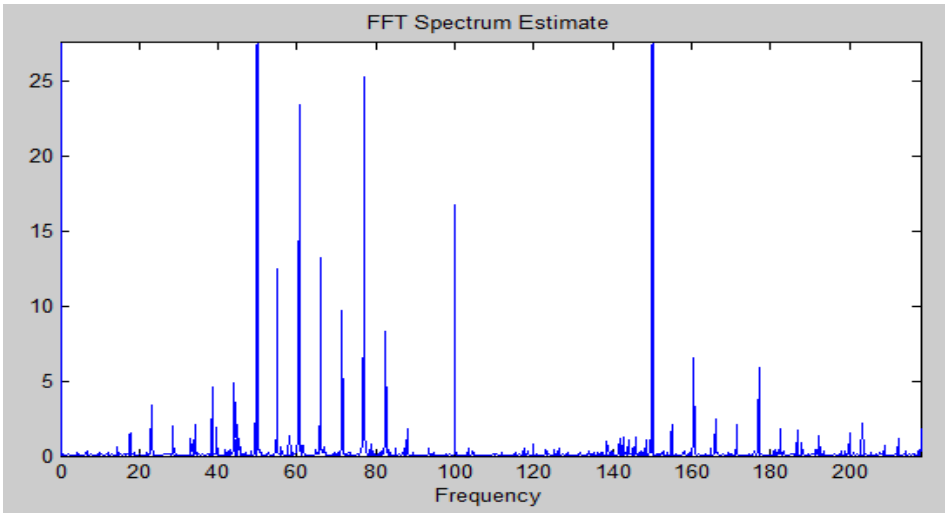

(b)

Figure 5.2-27 (a) Raw vibration signal collected after the 5th period of Test 1, and (b) the vibration spectrum, in which 5 or 6 Hz sidebands occurred around the 50 Hz fundamental frequency peak and its 3rd harmonic 150 Hz peak

Using optical microscopy, the microstructure of the top 200 μm of the tested EN36 wheel were found to differ from the core area (as shown in Figure 5.2-28). The modified microstructure of the top area shows a texture from left to right, which illustrates a directional plastic deformation (strain hardening) caused by the compressive rolling-sliding contact. The friction induces shear stress and when it exceeds the shear yield strength, the plastic deformation would occur, particularly in high load and high slippage conditions (DI Fletcher et al., 2008).

The cross-section micrographs of the cracks in the untreated EN36 are shown in Figure 5.2-29 and Figure 5.2-30. Some of them have reached the wheel sample's surface whilst others propagated towards the core. These rolling contact fatigue cracks formed after thousands of loading-unloading cycles and they propagated along the texture direction to the surface. The initiation of these RCF cracks is due to the strain/ductility exhaustion of wheel material at or near the surface after repeating load cycles (DI Fletcher et al., 2008).

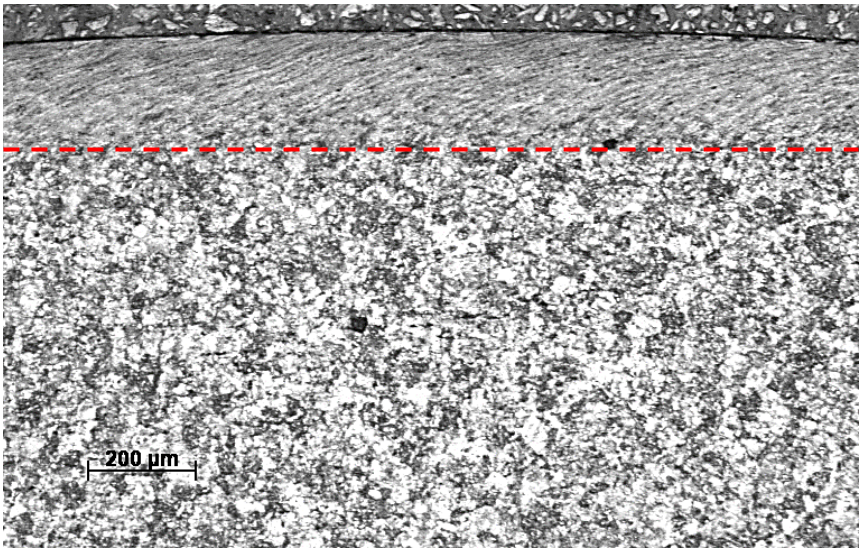

Figure 5.2-28 The top 200 µm zone of untreated EN36 was severely plastic deformed after rolling-sliding Test 1

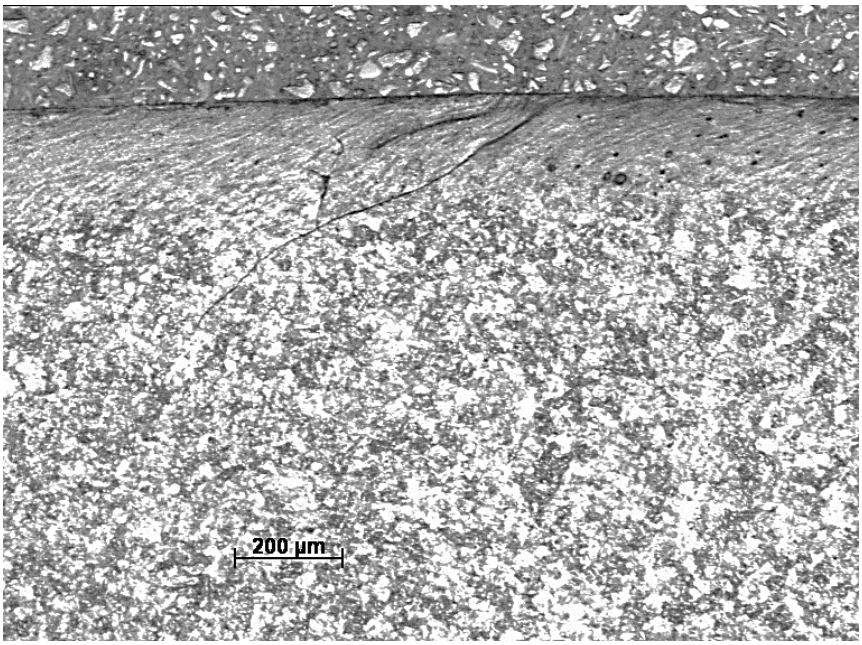

Figure 5.2-29 Cross section of cracks in the sample surface formed during Test 1

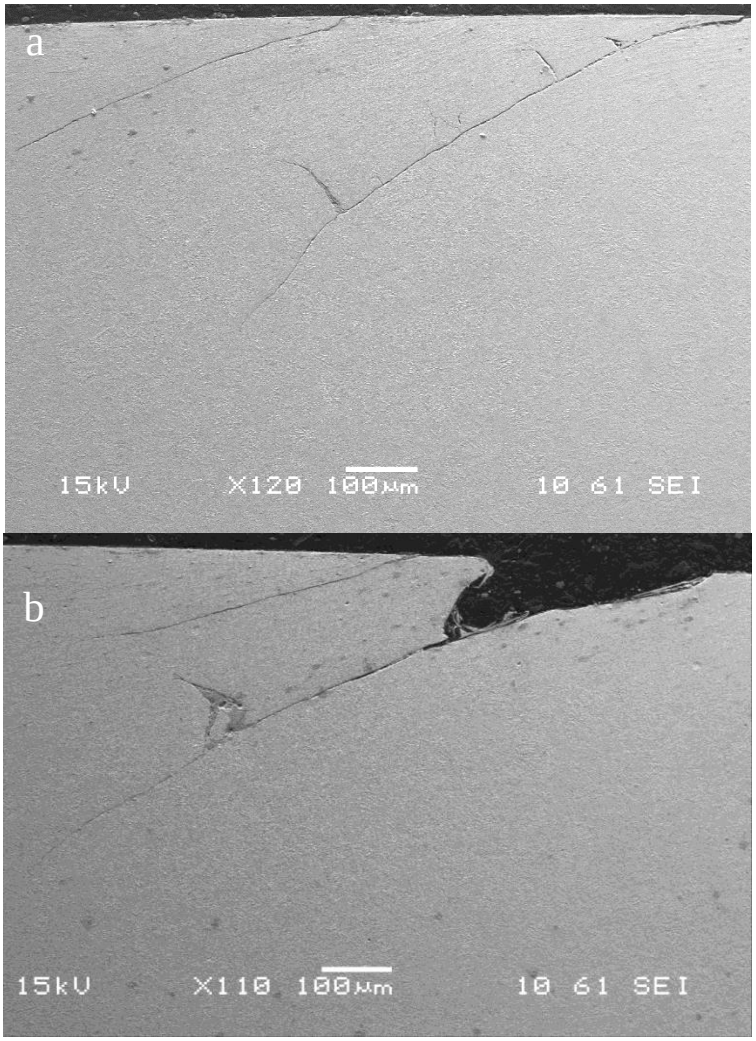

Figure 5.2-30 SEM images of long crack and crater formed during Test 1, (a) crack with long branches, and (b) cracks and a crater due to crack branch breaking off

In addition to those major surface defects, subsurface initiating cracks were also observed (as shown in Figure 5.2-31). The formation and propagation of some of these subsurface cracks may generate detectable AE as well, which means AE signals could indicate the development of subsurface cracks before visible surface cracks have formed. Particularly, if the subsurface cracks develop rapidly then an AE signal cluster may be generated.

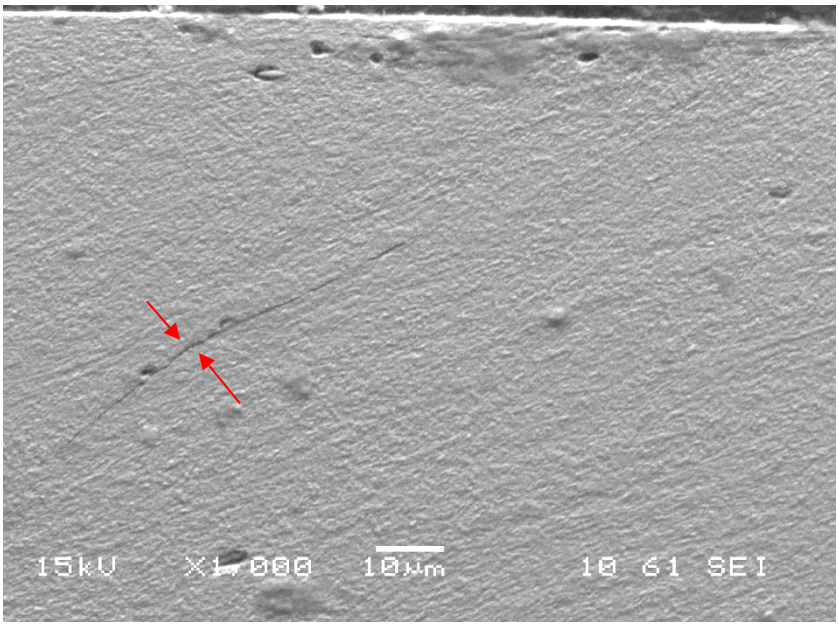

Figure 5.2-31 SEM image of subsurface initiated crack in the plastic deformation zone formed during Test 1

5.3 Test 2: As-received EN40BT wheel against WC wheel

Before testing, the weight of the machined wheel made of as-received EN40BT was measured to equal 63.1965g. The surface morphology is similar to that of as-machined EN36 wheel. The whole test of this wheel pair lasted about 22.5 hours, and it was divided into 4 periods when signals notably changed or sample damage was observed. At the end of the test, three visible major cracks up to 4,000 μm long with craters up to about 0.5mm ×1.75mm in size formed in the tested steel wheel sample. Moreover, a subsurface crack more than 1,600 μm long was observed.

(1) First period (0-6,000 sec)

A concaved surface due to plastic deformation formed on the as-received EN40BT wheel (as shown in Figure 5.3-1) soon after the load was applied. No AE was detected during that moment.

After that, a cluster of abnormal AE hits was detected, only at around 1,000 second (or about 16 minutes) in the test. The maximum AE signal amplitude recorded was 67 dB (as shown in Figure 5.3-2). The maximum PAC-energy of the AE signals recorded was measured at 88 μV·s (as shown in Figure 5.3-3). The total cumulative PAC-energy recorded reached 269 μV·s (as shown in Figure 5.3-4). The rotational speed of the wheel is 360 rpm, which means after only about 6,000 loading-unloading cycles, a crack rapidly propagated and major damage may have formed.

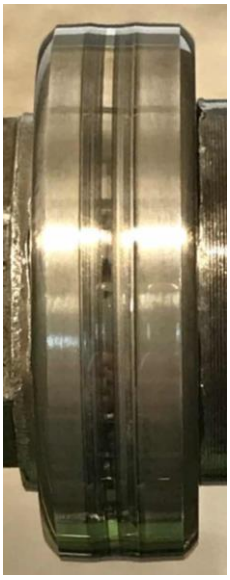

Figure 5.3-1 A concave surface formed in the untreated EN40BT wheel due to plastic deformation during the 1st period of Test 2

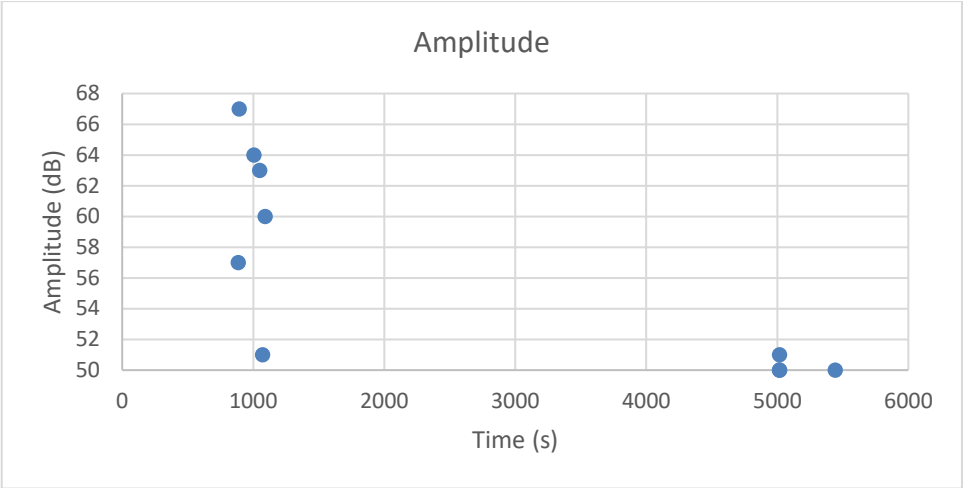

Figure 5.3-2 AE hits detected from untreated EN40BT wheel in the 1st period of Test 2

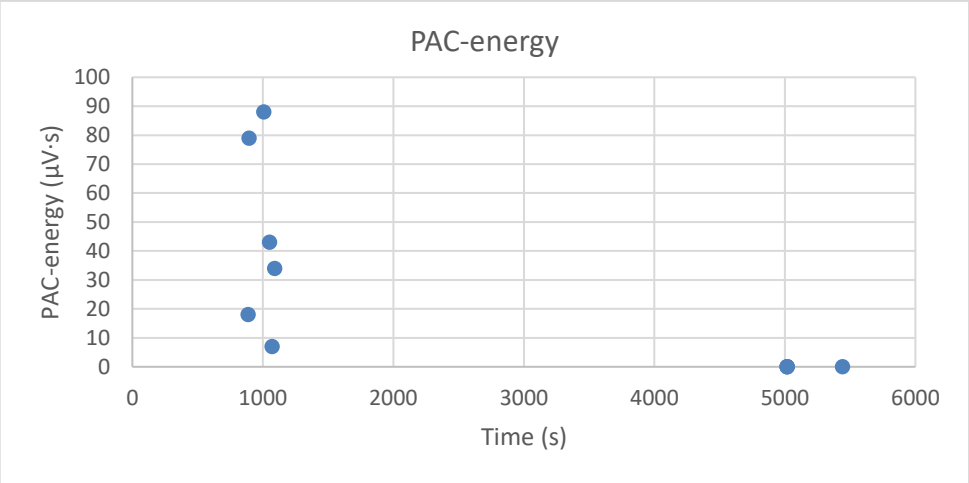

Figure 5.3-3 The PAC-energy of the AE hits detected from untreated EN40BT wheel in the 1st period of Test 2

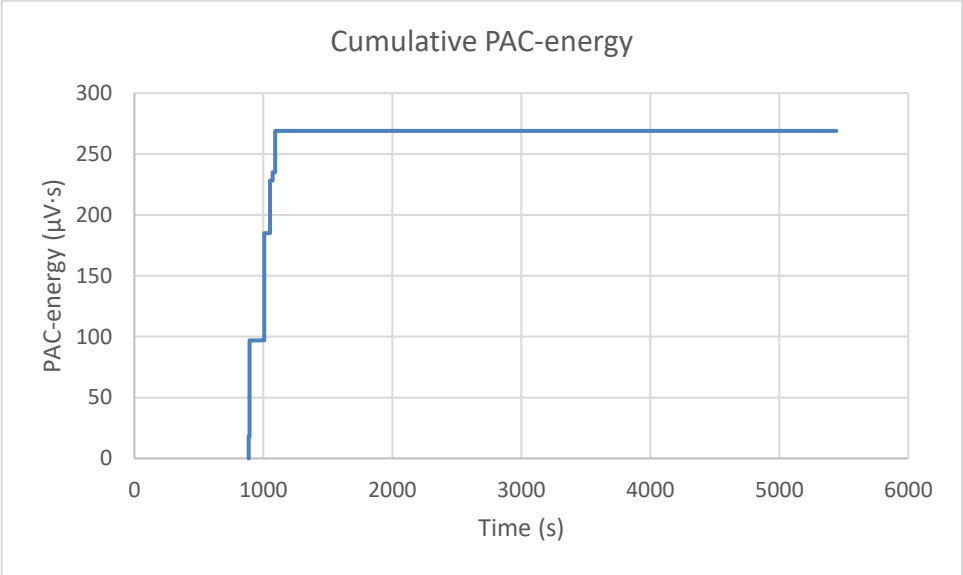

Figure 5.3-4 The cumulative PAC-energy of the AE hits detected from untreated EN40BT wheel in the 1st period of Test 2

The test was interrupted at the end of this period, and a significant crack, longer than 1,000 μm was observed along the edge of the contact area in EN40BT wheel (as shown in Figure 5.3-5). The WC wheel was still damage-free (as shown in Figure 5.3-6). It is very likely that the cluster of AE was from this crack. The direction of this early-formed crack is different from the axial rolling contact fatigue crack, and it has a different formation mechanism. The wear track cross-section of the tested wheel is shown in Figure 5.3-7. The plastic flow pushed the material from the centre to the sides of the contact area, causing the edge of the wear scar to protrude over the original wheel surface. Hence, the edge is easy to concentrate stress and eventually fracture. The crack formed very early, which could be due to some local defects or weak points introduced from the wheel machining or grinding process.

In the other contact surface, no severe damage was observed apart from micro-cracks around 50 μm long (as shown in Figure 5.3-8). These minor defects and the long edge crack did not change the wheel profile. Thus, the vibration spectrum was identical to the initial one,

comprising the peaks at the 50 Hz fundamental frequency and its 2nd and 3rd harmonics, i.e. 100 and 150 Hz (as shown in Figure 5.3-9).

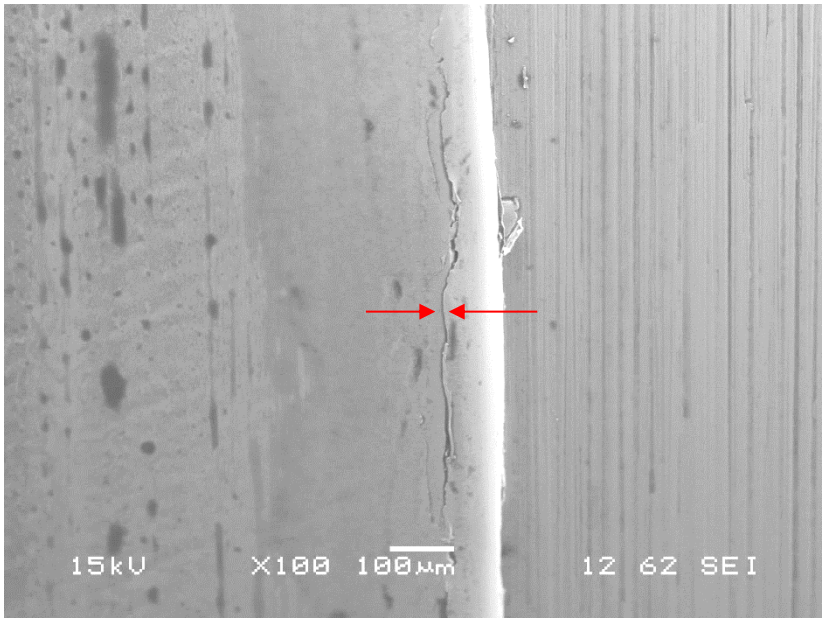

Figure 5.3-5 SEM image of a big crack longer than 1,000 µm at the edge of contact surface of untreated EN40BT wheel after the 1st period of Test 2

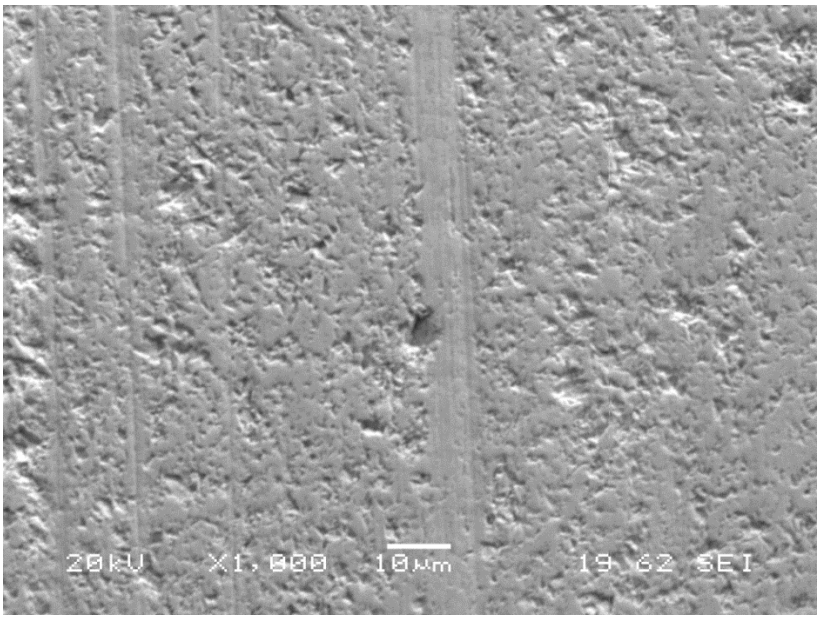

Figure 5.3-6 SEM image of damage-free surface of WC wheel after the 1st period of Test 2

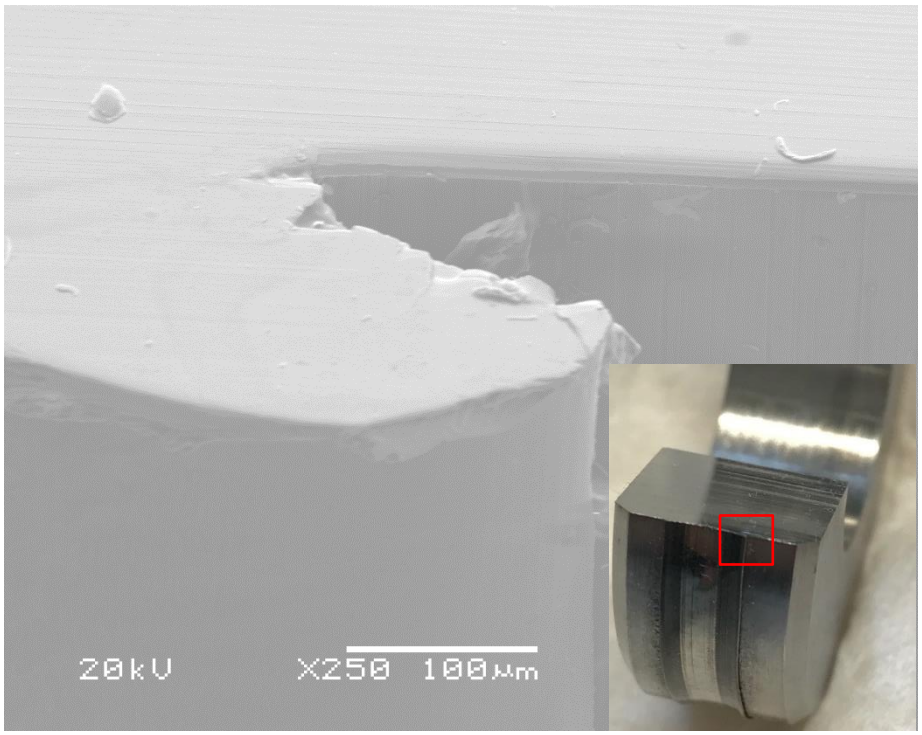

Figure 5.3-7 Images of cross section of wear track formed during Test 2, material was pushed to the edge of wear track and extruded over the original wheel surface

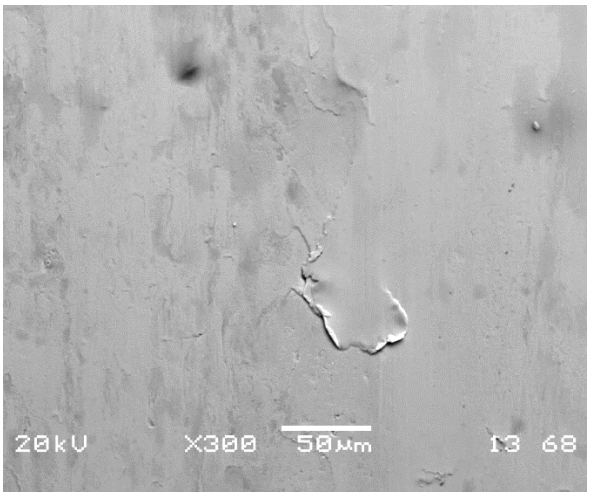

Figure 5.3-8 SEM image of micro-crack in the main contact area of untreated EN40BT wheel after the 1st period of Test 2

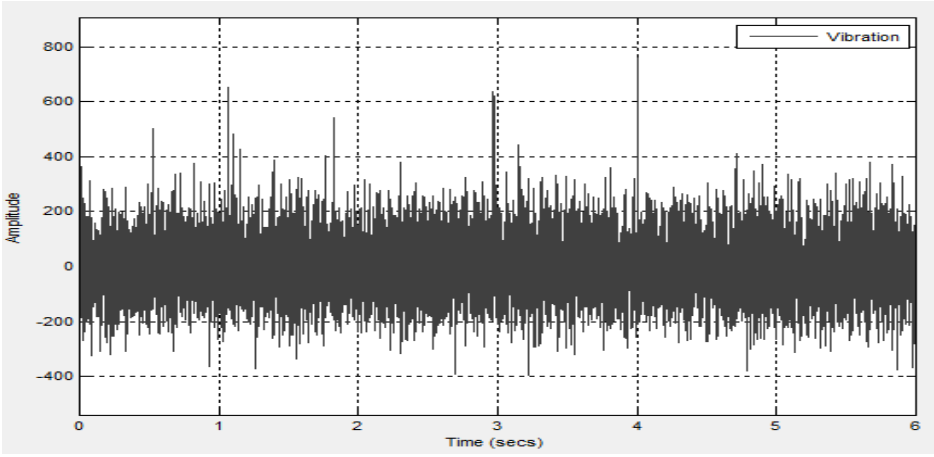

(a)

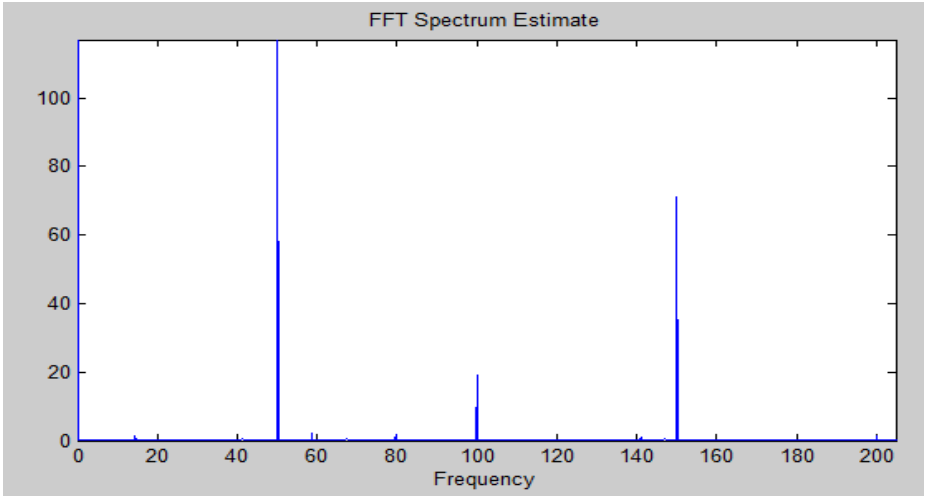

(b)

Figure 5.3-9 (a) Raw vibration signal, and (b) FFT spectrum, after the 1st period of Test 2

(2) Second period (6,000-27,600 sec)

Two clusters of AE signals were detected (as shown in Figure 5.3-10), the first cluster occurred around 16,700 seconds of the test with a peak amplitude of 57 dB. The second cluster occurred at about 27,500 seconds with a peak amplitude of 58 dB. The PAC energy of the detected AE activity during this period is shown in Figure 5.3-11. The peak PAC-energy of the first cluster was 317 μV·s, whilst for the second one it was 462 μV·s. The cumulative PAC-energy (as shown in Figure 5.3-12) of this period is 3,720 μV·s, it increased sharply when the two AE clusters occurred. The other AE signals only slightly changed the trend of

the cumulative PAC-energy. These AE cluster events may indicate severe damage of the wheel.

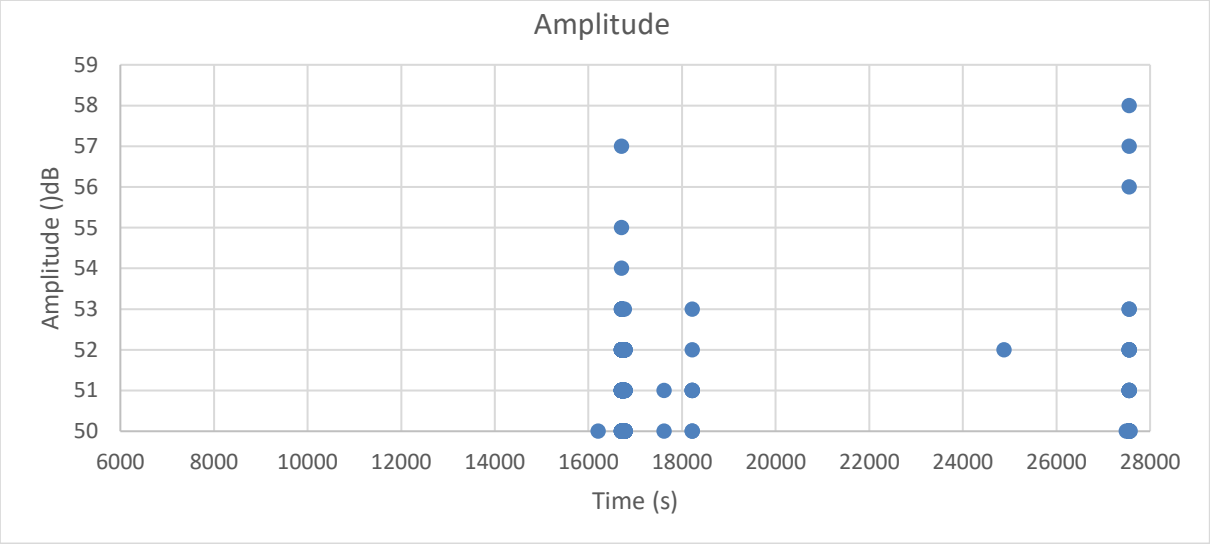

Figure 5.3-10 The AE hits detected from untreated EN40BT wheel in the 2nd period of Test 2

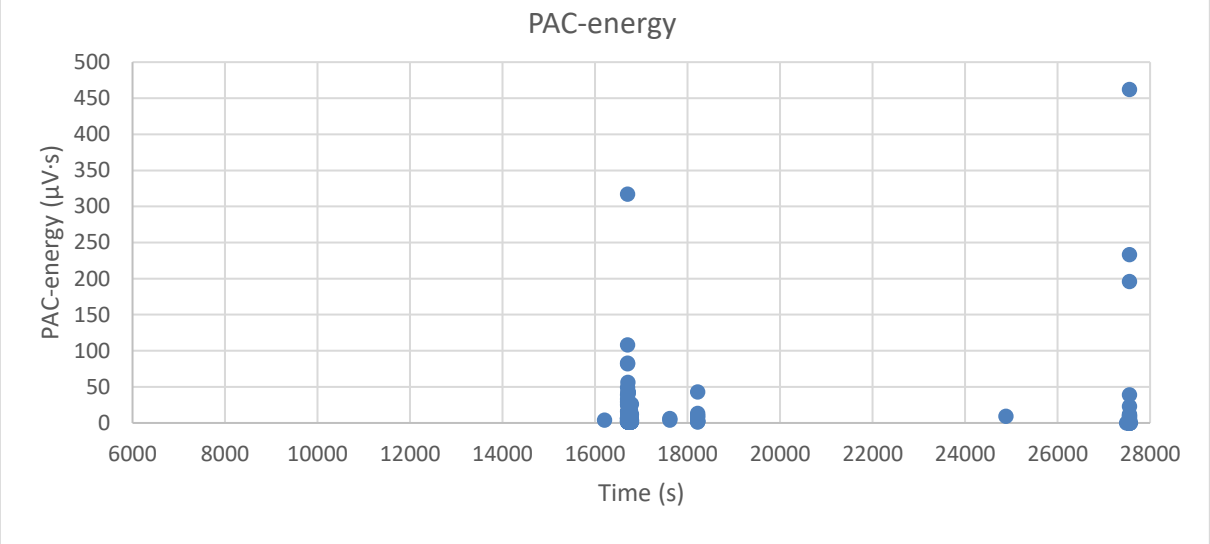

Figure 5.3-11 The PAC-energy of the AE hits detected from untreated EN40BT wheel in the 2nd period of Test 2

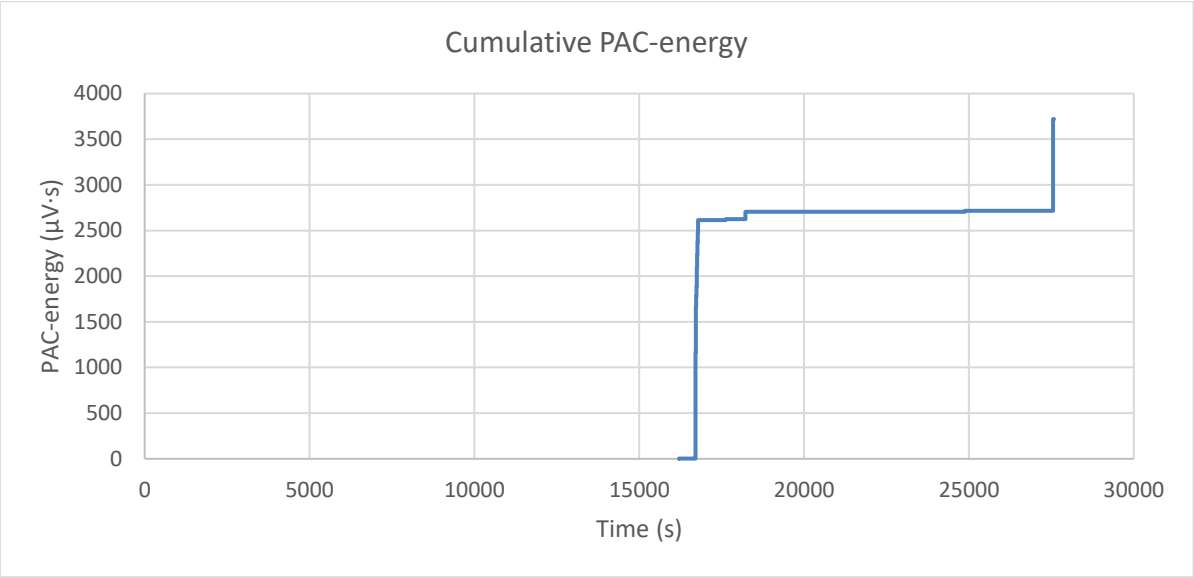

Figure 5.3-12 The cumulative PAC-energy of the AE hits detected from untreated EN40BT wheel in the 2nd period of Test 2

In the steel wheel surface, only minor surface damage was observed, with defects being micro-cracks/pits. Except that, no severe surface damage was identified either in the steel or WC wheel surfaces. Hence, the detected AE clusters may be related to rapid continuous propagation of subsurface initiating cracks. This was proven by the sample examination after the completion of the test by sectioning the failed samples and examining it using SEM. The vibration spectrum did not show any change as no severe surface damage was present.

(3) Third period (27,600-60,000 sec)

The amplitude and PAC-energy of the detected AE are shown in Figure 5.3-13 and Figure 5.3-14 respectively. These AE signals were in the form of clusters and some discrete signals. The maximum amplitude was 60 dB and the maximum PAC-energy was 240 μV·s. The cumulative PAC-energy was 677 μV·s and the trend of cumulative PAC-energy during this period is shown in Figure 5.3-15. These AE cluster signals hints continuous rapid propagation of cracks during this period. The discrete signals may be related to the sudden initiation or discontinuous development of defects.

In agreement with the AE signals, 5 visible cracks were found in the steel wheel after naked eye examination. Under SEM examination, these cracks were measured to be approximately 2,500 μm long (as shown in Figure 5.3-16). The formation of these large cracks generated strong AE signals, but no significant change in the wheel profile, thus no change in the vibration spectrum arose during this period (as shown in Figure 5.3-17).

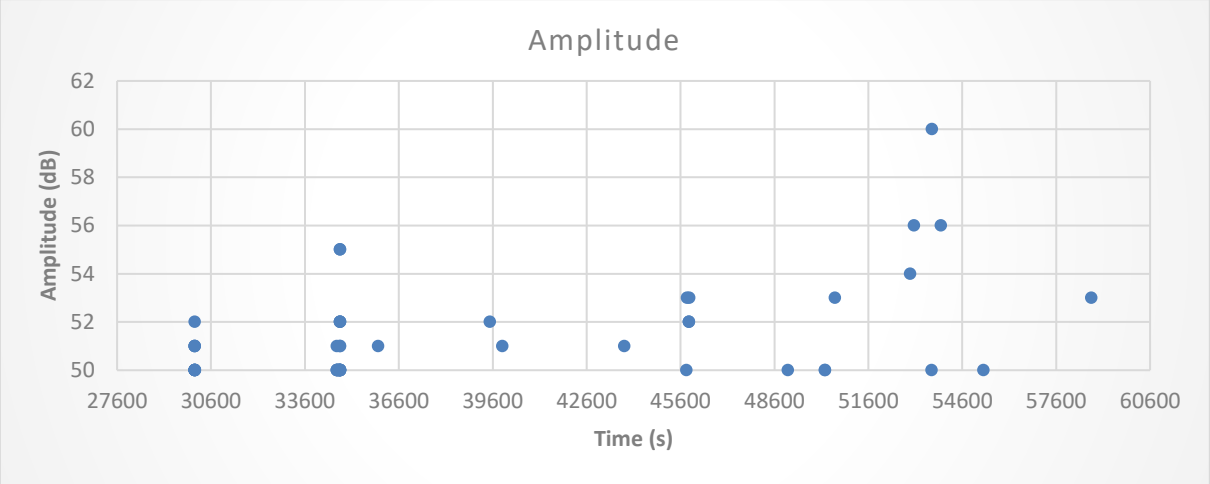

Figure 5.3-13 The AE hits detected from untreated EN40BT wheel in the 3rd period of Test 2

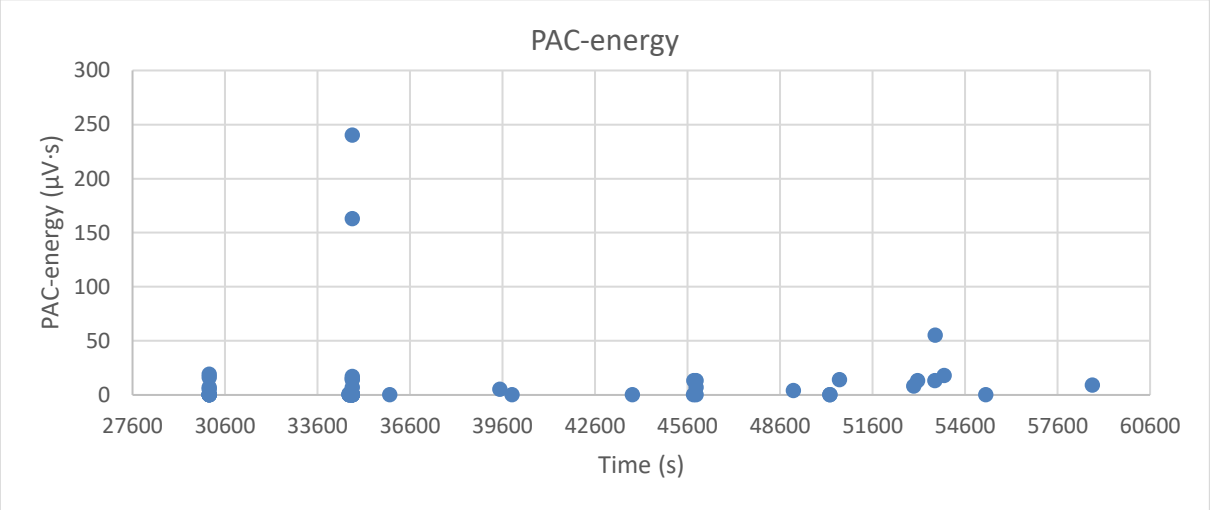

Figure 5.3-14 The PAC-energy of the AE hits detected from untreated EN40BT wheel in the 3rd period of Test 2

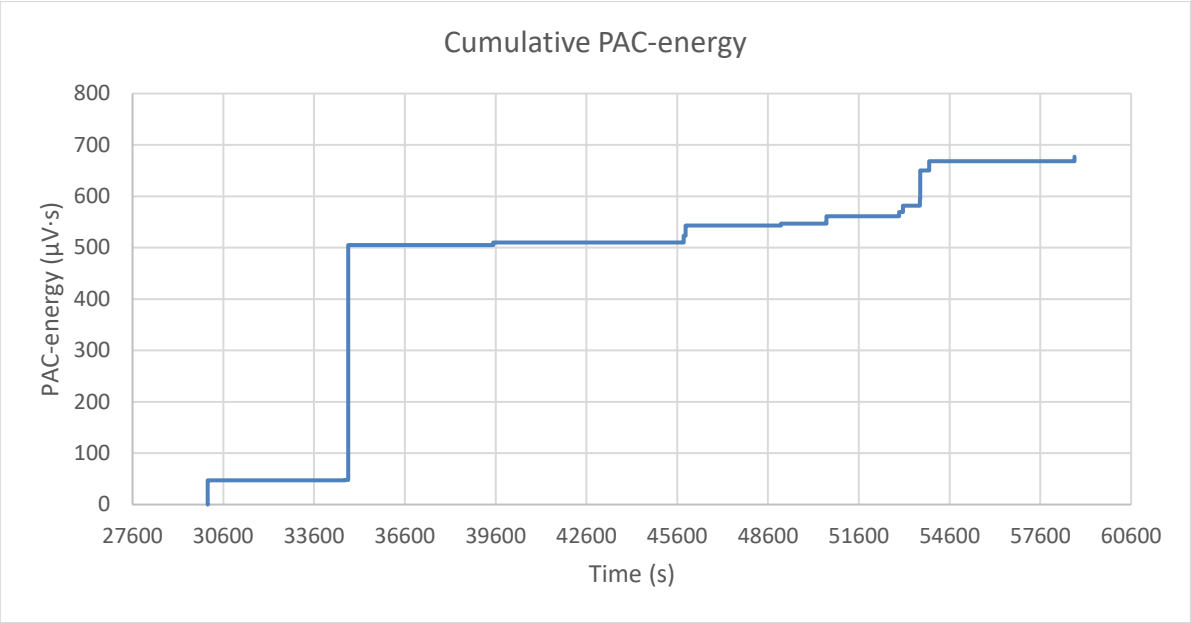

Figure 5.3-15 The cumulative PAC-energy of the AE hits detected from untreated EN40BT wheel in the 3rd period of Test 2

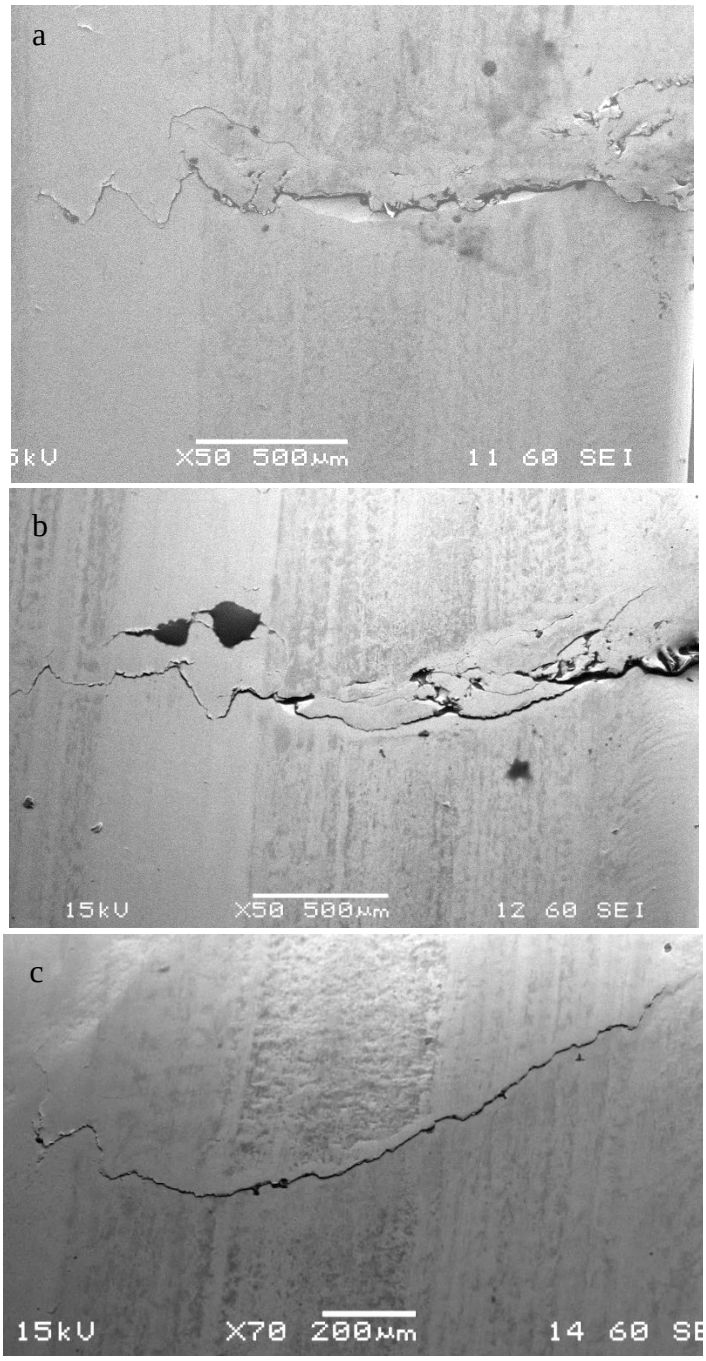

Figure 5.3-16 SEM images of big cracks in untreated EN40BT wheel surface after the 3rd period of Test 2

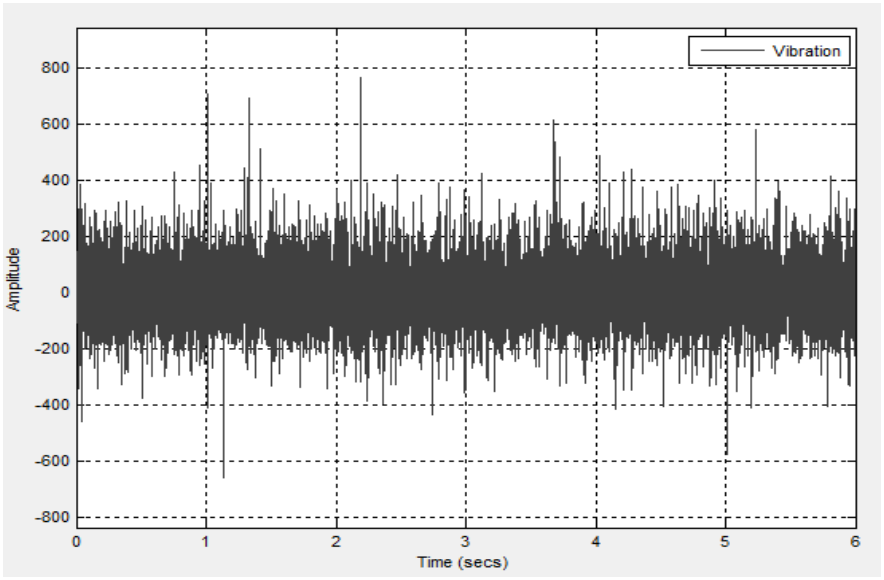

(a)

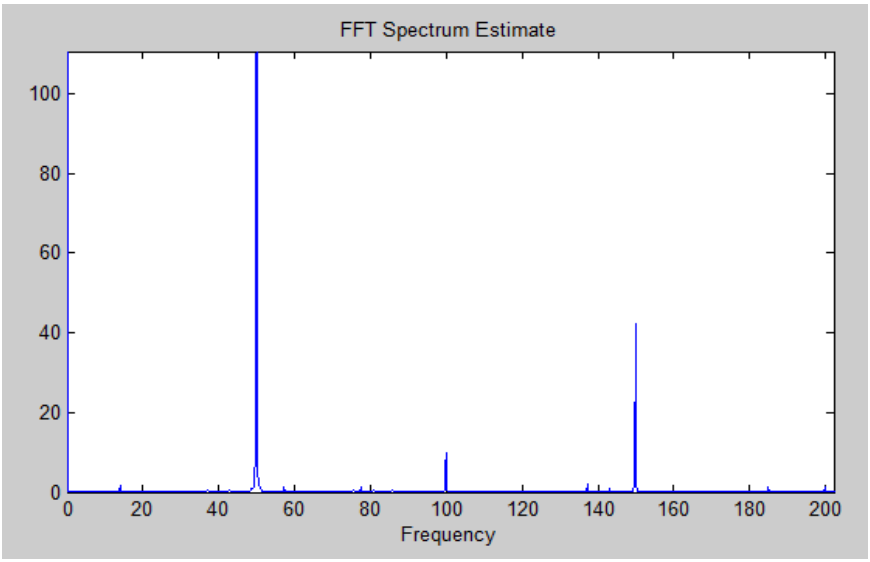

(b)

Figure 5.3-17 (a) Raw vibration signal, and (b) the FFT spectrum, after the 3rd period of Test 2

(4) Fourth period (60,000-80,700 sec)

At the end of the first 1,800 seconds of this period, a cluster of 10 AE signals were collected. Then another 22 defect-related AE hits were detected at irregular intervals during the rest of this period. The amplitude and PAC-energy of detected AE signals are shown in Figure 5.3-18 and Figure 5.3-19 respectively. The maximum amplitude was 62 dB and the maximum

PAC-energy was 64 μV·s. The cumulative PAC-energy was 200 μV·s and increased significantly at the first half of this test period (as shown in Figure 5.3-20).

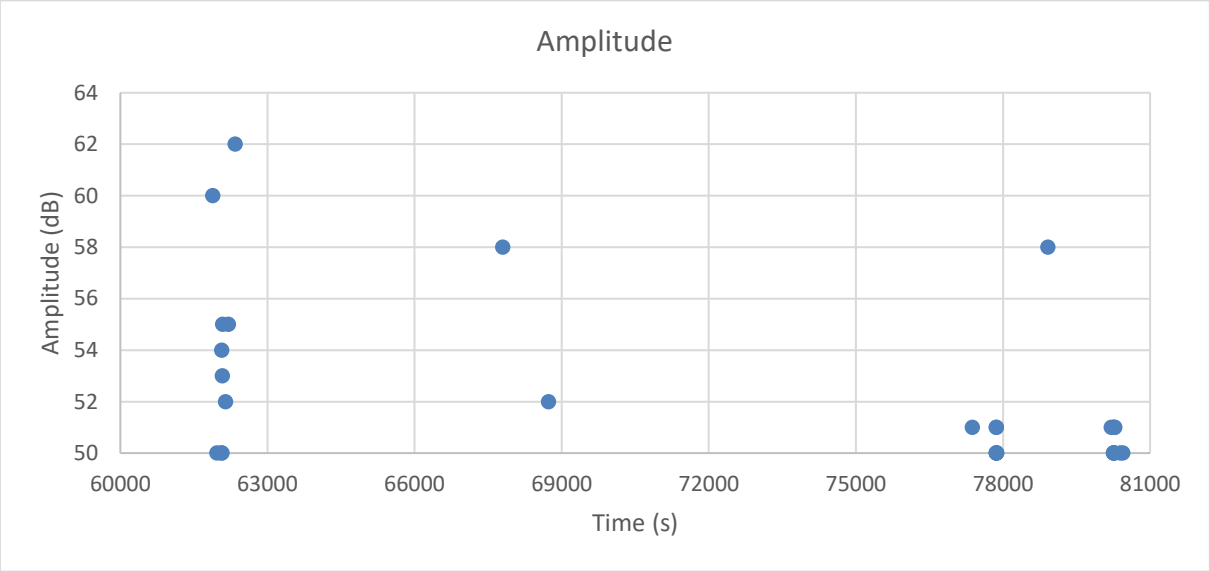

Figure 5.3-18 The AE hits detected from untreated EN40BT wheel in the 4th period of Test 2

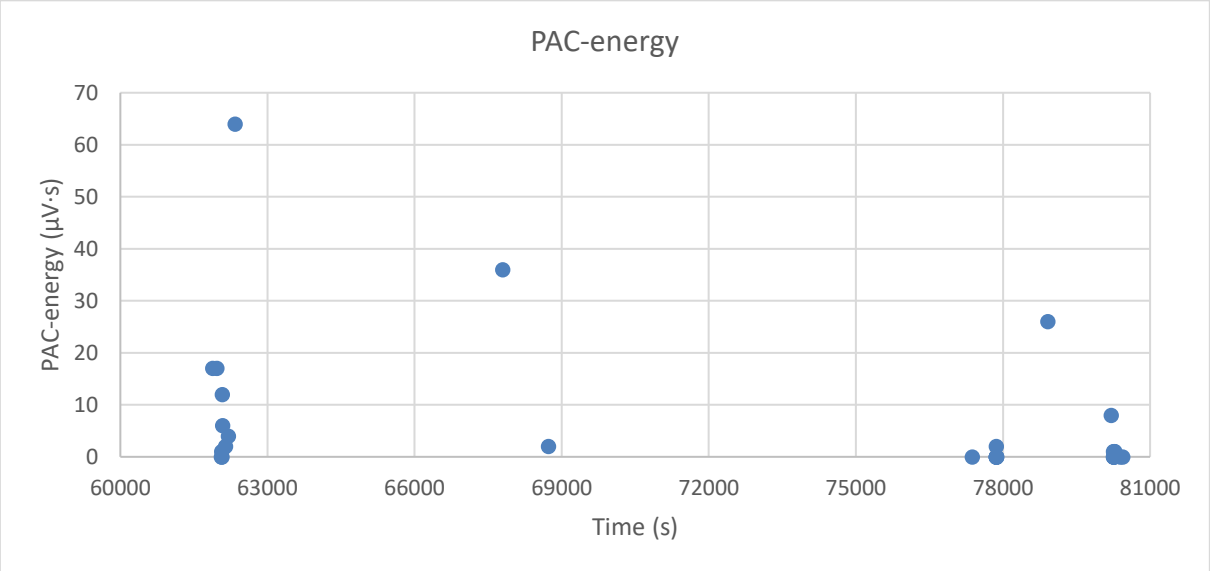

Figure 5.3-19 The PAC-energy of the AE hits detected from untreated EN40BT wheel in the 4th period of Test 2

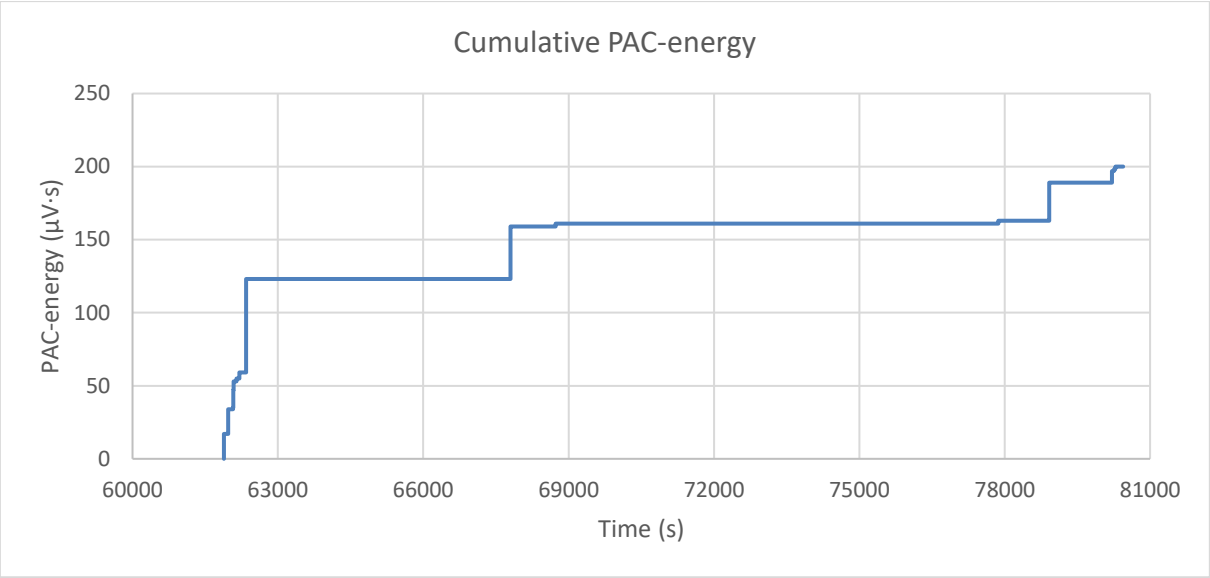

Figure 5.3-20 The cumulative PAC-energy of the AE hits detected from untreated EN40BT wheel in the 4th period of Test 2

Three visible major cracks with craters formed in the tested steel wheel sample during this period (as shown in Figure 5.3-21 and Figure 5.3-22). The length of the cracks was measured to be up to 4,000 μm, whilst the dimensions of the biggest crater was found to be approximately 0.5mm×1.75mm. There was no damage in the WC wheel (as shown in Figure 5.3-23).

At the end of the test, the weight of the EN40BT wheel was measured at 63.0286 g. Hence, the weight loss was 0.1679 g, indicating an average wear rate of 7.5 mg/hour, which are quite small values. The average wear rate is similar to that for the untreated EN36 sample (7.6 mg/hour). Side-bands of about 3 Hz clearly occurred around the fundamental 50 Hz and its 3rd harmonic 150 Hz peaks in the vibration spectrum (as shown in Figure 5.3-24). This sample was deemed to have failed at this point.

The damaged wheel was sectioned in order to conduct further failure analysis on its subsurface in the radial plane.

A plastically deformed area was observed at the top 180 μm using an optical microscope (as shown in Figure 5.3-25). The plastic flow can be identified from left to right, which indicates the friction direction. In addition to that, a subsurface crack more than 1,600 μm long was observed (as shown in Figure 5.3-26). It propagated along the boundary between the plastic deformed top area and the undeformed core area. The strong AE signals detected in the 2nd period were very probably generated from the rapid propagation of this long subsurface crack which was invisible from the surface.

The SEM micrograph of a typical large rolling contact fatigue crack in the untreated EN40BT wheel is shown in Figure 5.3-27. The main crack is about 45˚ to the wheel surface. It is so long that one end has reached the wheel surface and the other reached the unaffected from plastic deformation core area. Its rapid propagation may have resulted in the generation of strong AE signals. However, this crack did not modify the wheel profile, thus would not change the vibration pattern.

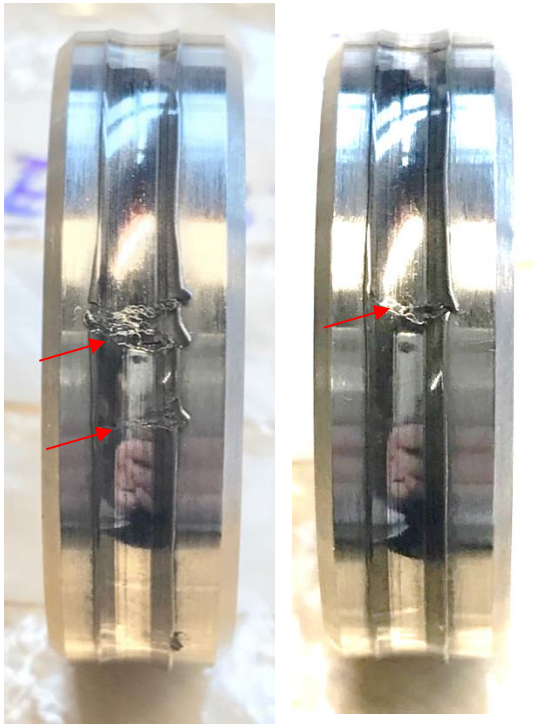

(a) (b)

Figure 5.3-21 Photos of visible surface damage in untreated EN40BT wheel surface after the 4th period of Test 2

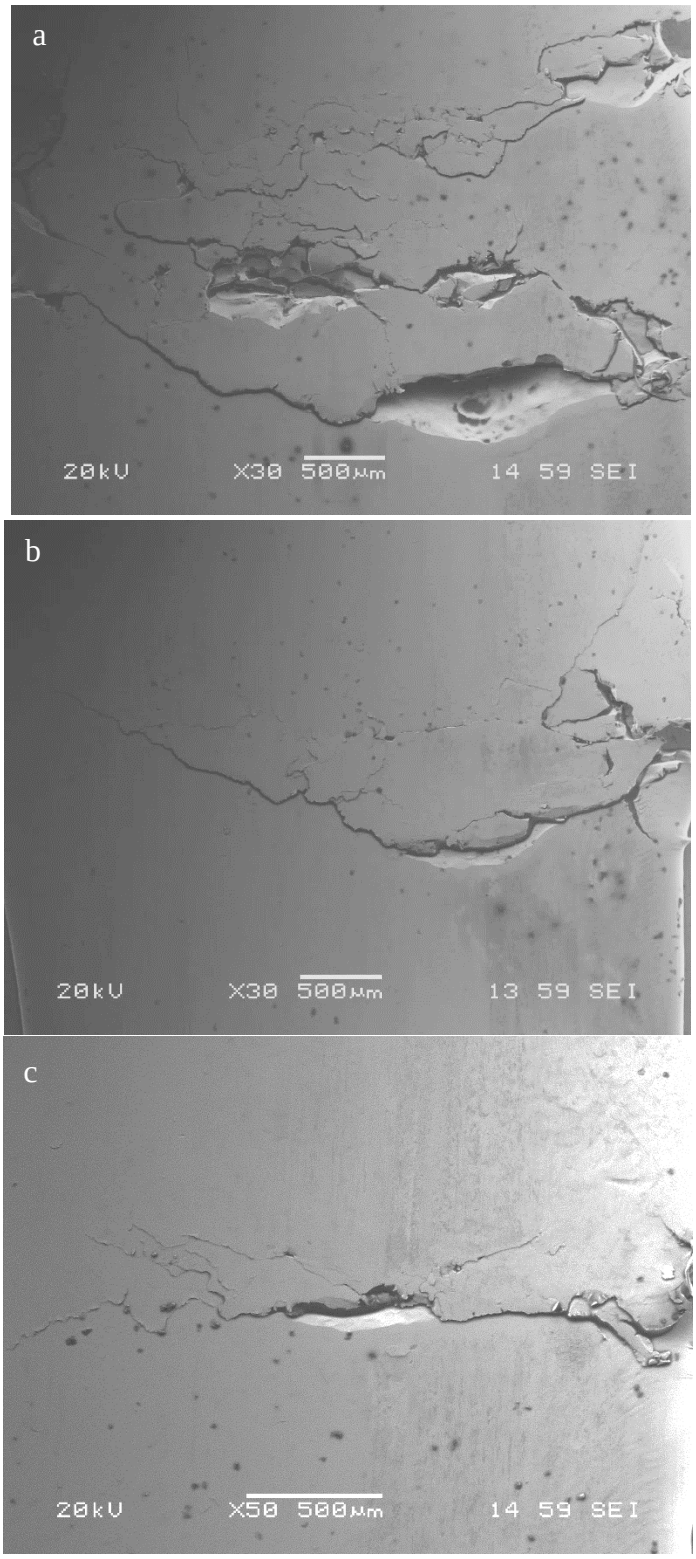

Figure 5.3-22 SEM images of long cracks and craters formed in untreated EN40BT wheel surface after the 4th period of Test 2

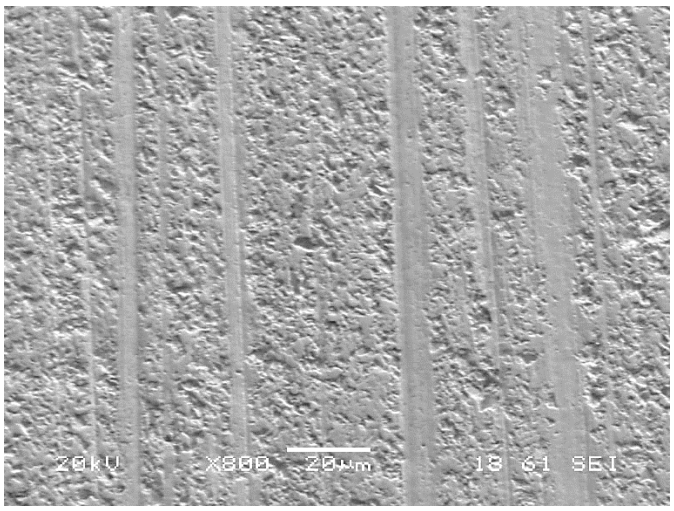

Figure 5.3-23 SEM image of the WC wheel contact surface after the 4th period of Test 2, indicating no severe damage formed in WC wheel surface.

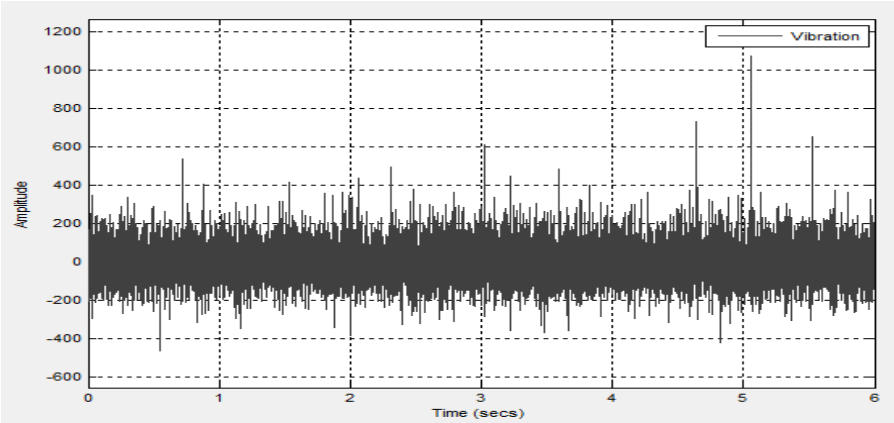

(a)

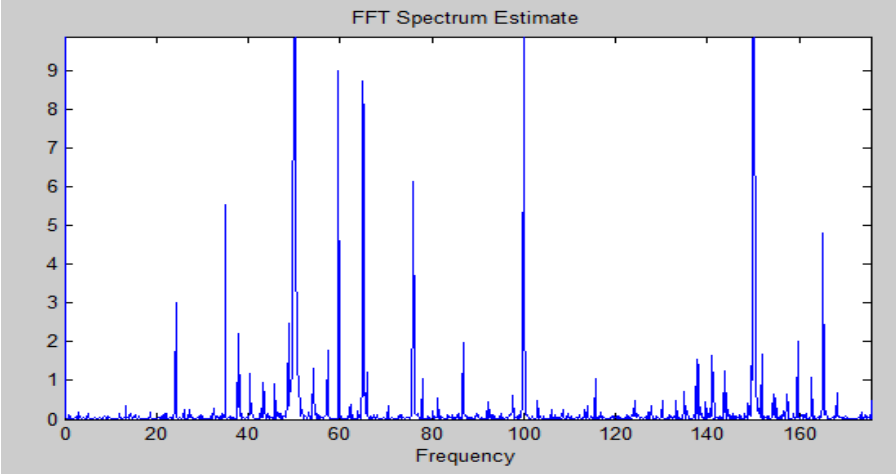

(b)

Figure 5.3-24 (a) Raw vibration signal, and (b) the FFT spectrum, after the 4th period of Test 2

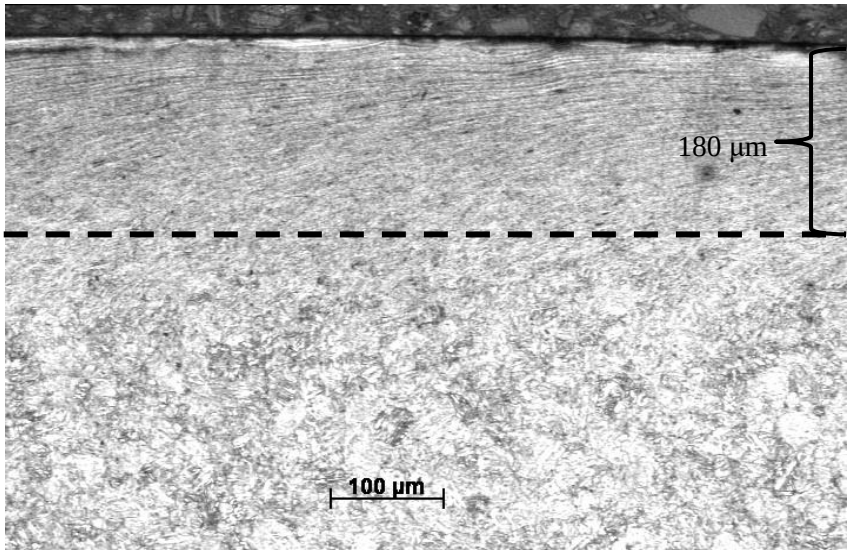

Figure 5.3-25 Plastic deformation area formed during Test 2 in the top 180 µm of untreated EN40BT sample

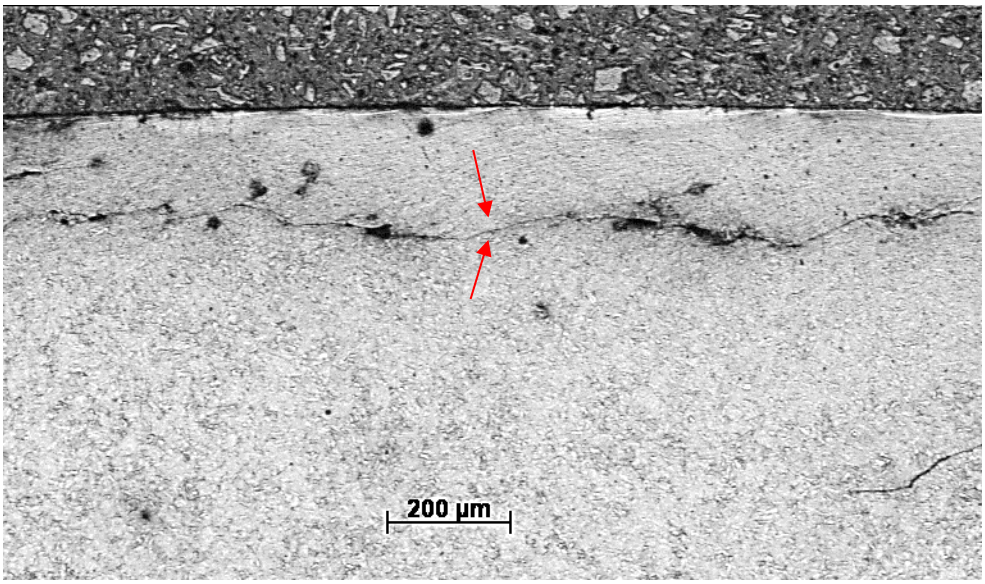

Figure 5.3-26 A long subsurface crack (longer than 1,600 µm) propagated along the boundary between the deformed area and the core area of untreated EN40BT of Test 2.

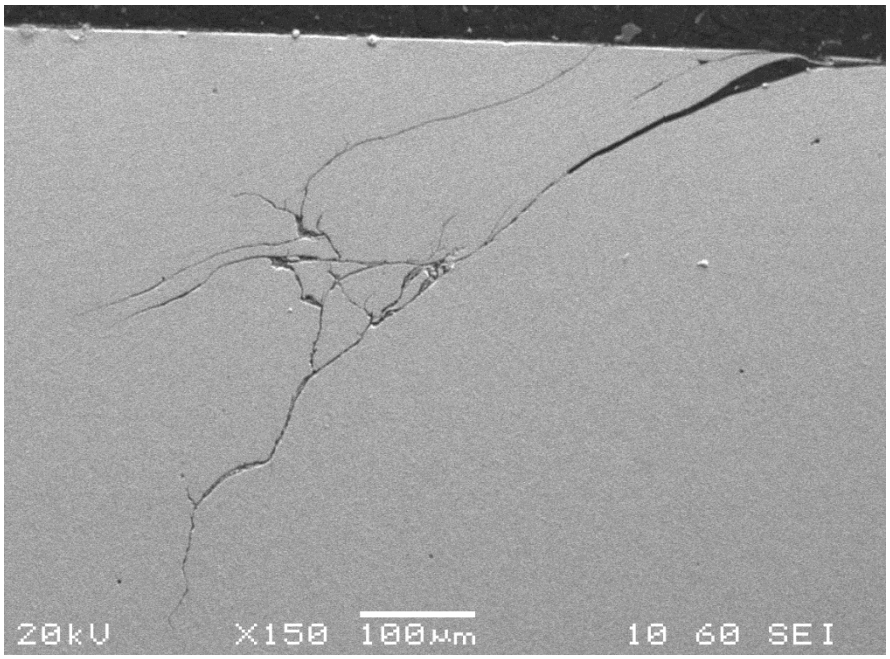

Figure 5.3-27 SEM image of a typical big rolling-contact-fatigue crack in untreated EN40BT wheel of Test 2

The cross-section of the large crater and the cracks producing it is clearly shown in Figure 5.3-28. The indicated long crack has already reached the deep undeformed core area, based on its distance from the surface. This large crater significantly modified the wheel profile and the contact condition of the wheel pair, causing impacts when the crater rotated to the contact point. Thus, the vibration spectrum significantly changed after the formation of the crater.

Several subsurface initiating long cracks and their branches (between 100 and 500 μm long) growing towards the wheel surface were also observed (as shown in Figure 5.3-29 and Figure 5.3-30). Although they were invisible from the wheel surface they may have generated detectable AE signals during the test. They would have broken to the surface if the test continued further. Some surface micro-cracks around 50 μm long were also observed (as shown in Figure 5.3-31). Some of the discrete AE signals may have also been generated from them, possibly resulting in the formation of micro-pits in the future.

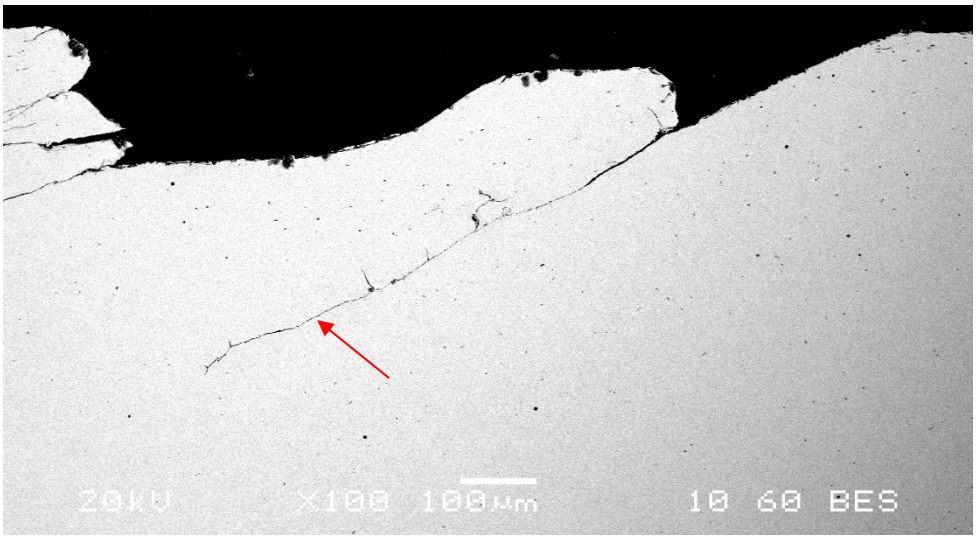

Figure 5.3-28 SEM image of the cross section of crater and the cracks formed during Test 2 which may make the crater bigger. The arrowed long crack has reached the undeformed core area.

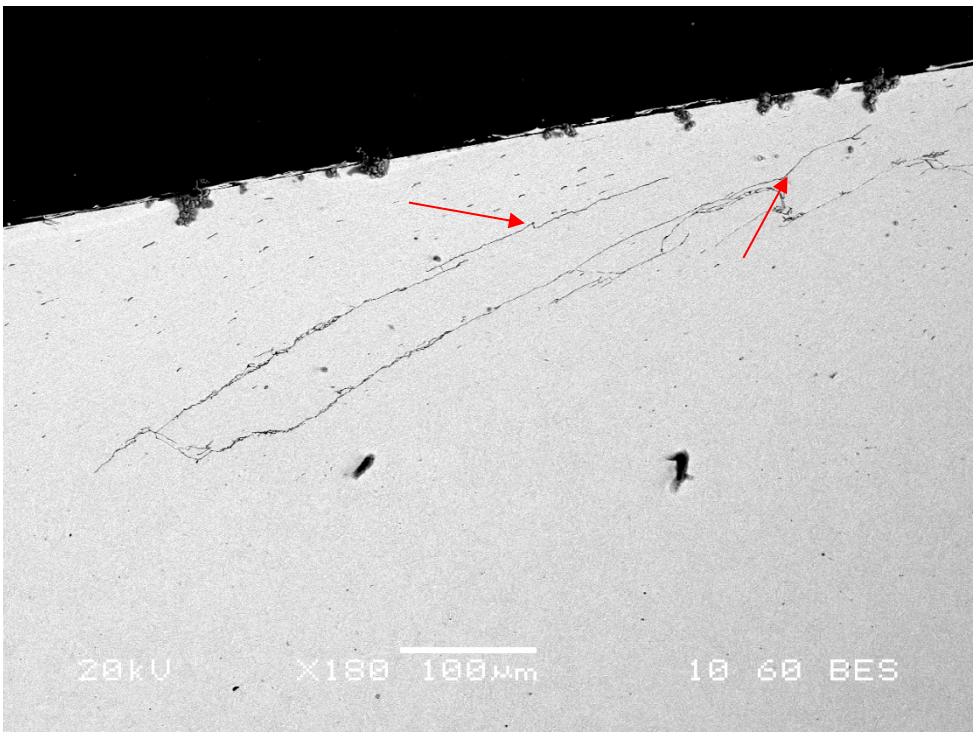

Figure 5.3-29 SEM image of two subsurface initiated long cracks growing towards the surface as arrowed (Test 2)

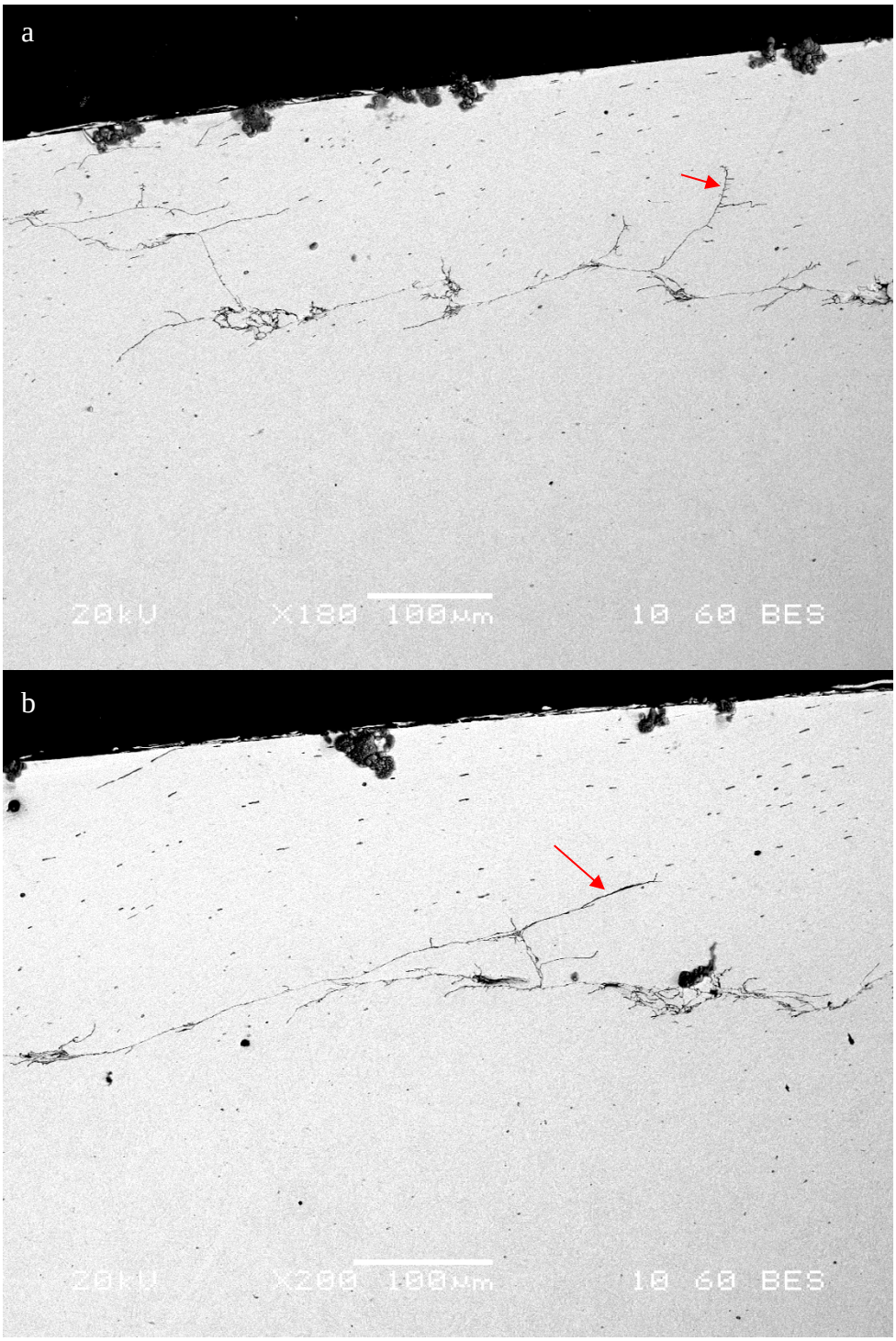

Figure 5.3-30 SEM images of subsurface initiated cracks mainly propagated parallel to surface, while the arrowed crack branches propagated towards the surface in Test 2

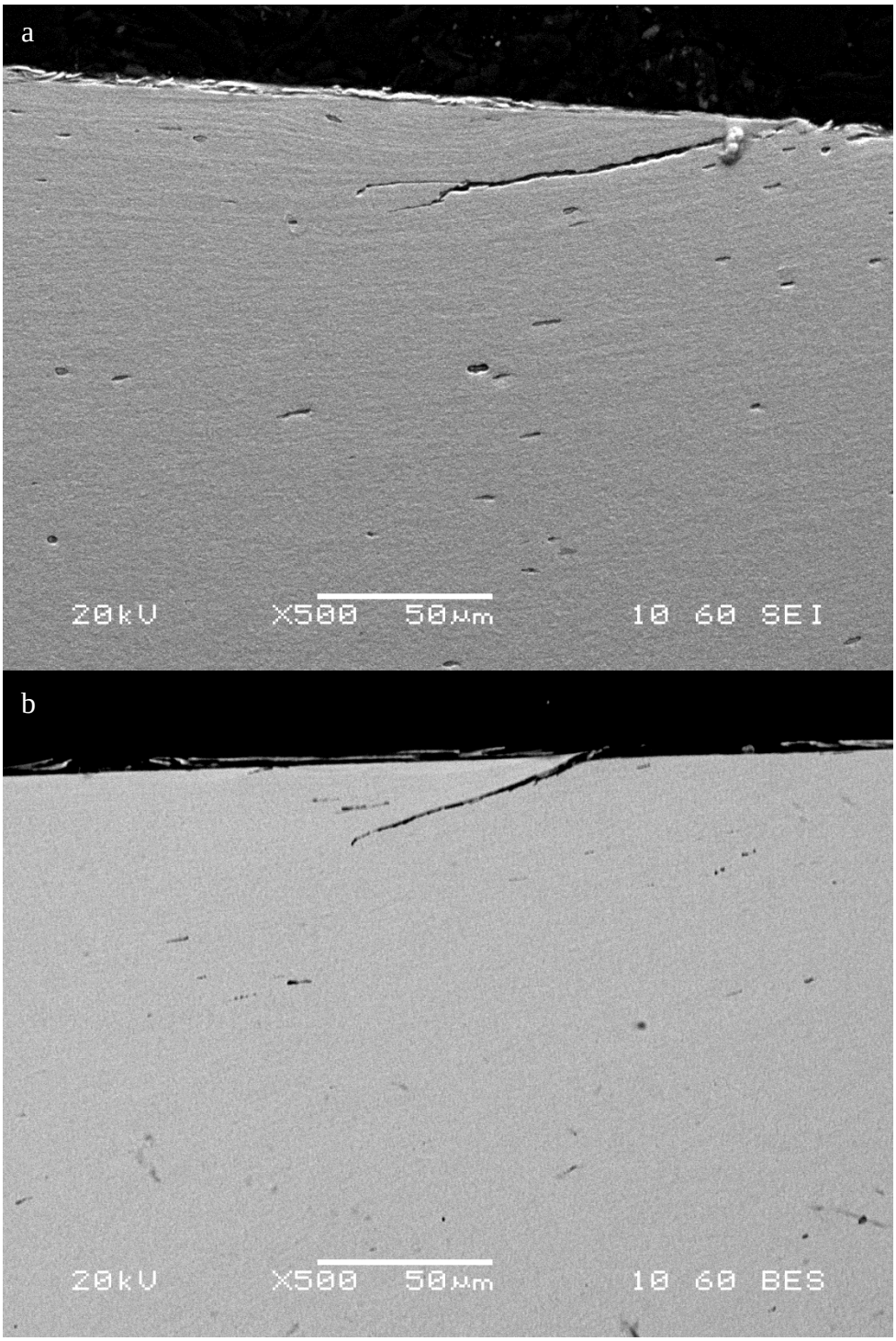

Figure 5.3-31 SEM images of surface minor cracks in untreated EN40BT wheel of Test 2

5.4 Test 3: Carburised EN36 wheel against WC wheel

Before testing, the measured weight of the carburised EN36 wheel was 63.3995g. At the end of the test, only micro-pits/craters formed in the steel wheel. The whole test of this wheel pair lasted about 19.5 hours and was divided into 2 periods.

(1) First period (0-1,500 seconds)

At the end of this period, a shallow and shiny concaved surface was observed in the carburised EN36 wheel (as shown in Figure 5.4-1). The weight loss was negligible. The relatively shallow concave surface is due to the hardened surface which has higher resistance to plastic deformation, comparing to the untreated wheels. The surface is shiny after this period due to the polishing effect. No AE hit beyond threshold was detected, and the FFT spectrum of vibration signal did not show any significant change from the beginning to the end of 1st period either.

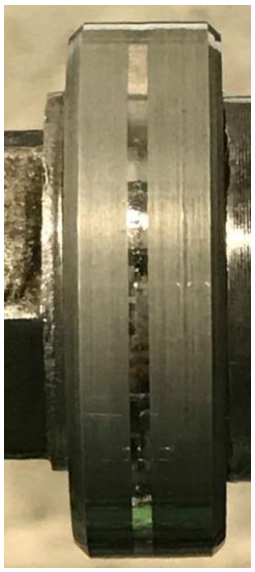

Figure 5.4-1 A shallow and shiny concave surface formed in the carburised EN36 wheel due to plastic deformation and polishing effect during the 1st period of Test 3

(2) Second period (1,500-70,200 seconds)

A total of 90 discrete AE signals were detected in this period (as shown in Figure 5.4-2). The maximum amplitude is 77 dB, and the PAC-energy of these AE hits is shown in Figure 5.4-3. The maximum PAC-energy of the AE signals recorded is 663 μV·s. The trend of the cumulative PAC-energy in this period is shown in Figure 5.4-4.

At the end of this period, only micro-pits with diameter between 50 and 100 μm (as shown in Figure 5.4-5) were observed in the carburised steel wheel using SEM. No damage was observed in the WC wheel (as shown in Figure 5.4-6). The formation of these micro-pits may be the source of the detected discrete AE signals. The formation of these micro-pits did not change the vibration pattern of wear tester (as shown in Figure 5.4-7).

After test, the wheel weight had been reduced to 63.3319 g, so the wear loss was 0.0676 g. The average wear rate of carburised EN36 wheel was 3.5 mg/hour, which is only 45.6% that of the untreated EN36 sample.

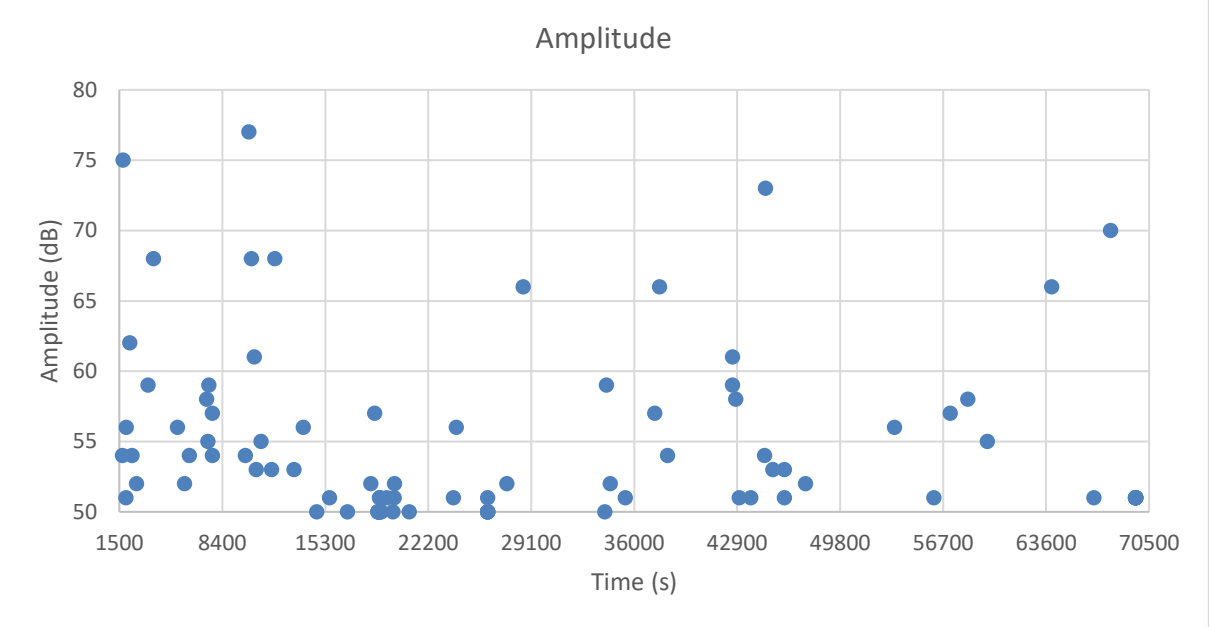

Figure 5.4-2 AE hits detected from carburised EN36 wheel in the 2nd period of Test 3

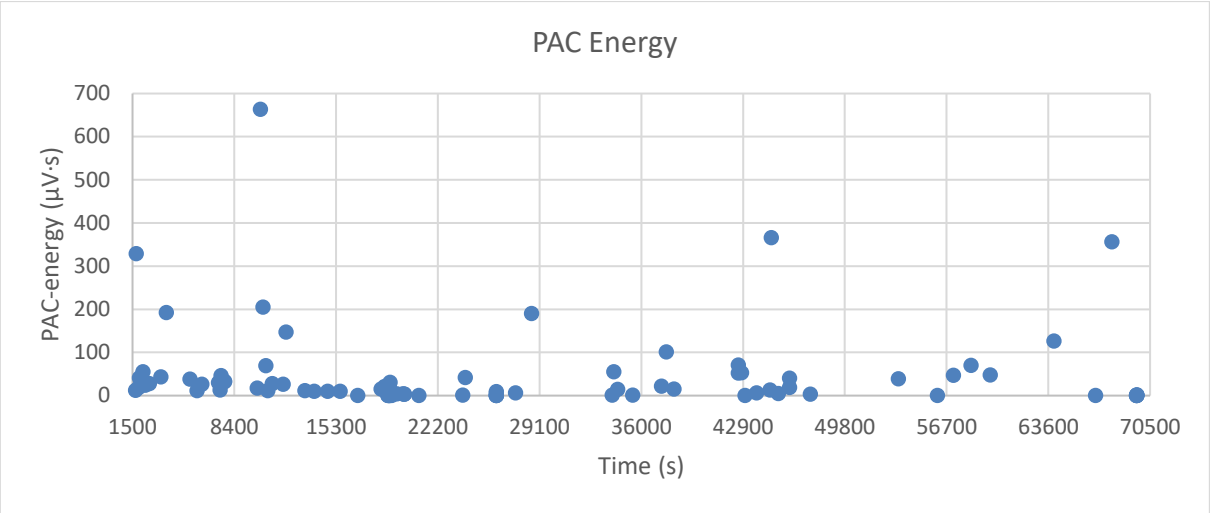

Figure 5.4-3 The PAC energy of AE hits detected from carburised EN36 wheel in the 2nd period of Test 3

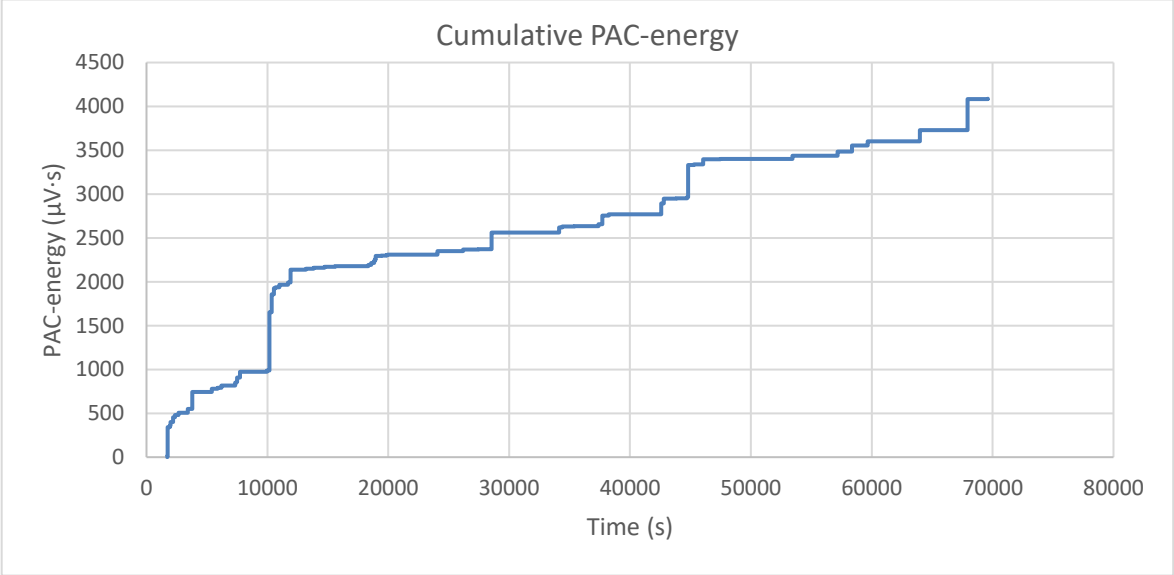

Figure 5.4-4 The cumulative PAC energy of AE hits detected from carburised EN36 wheel in the 2nd period of Test 3

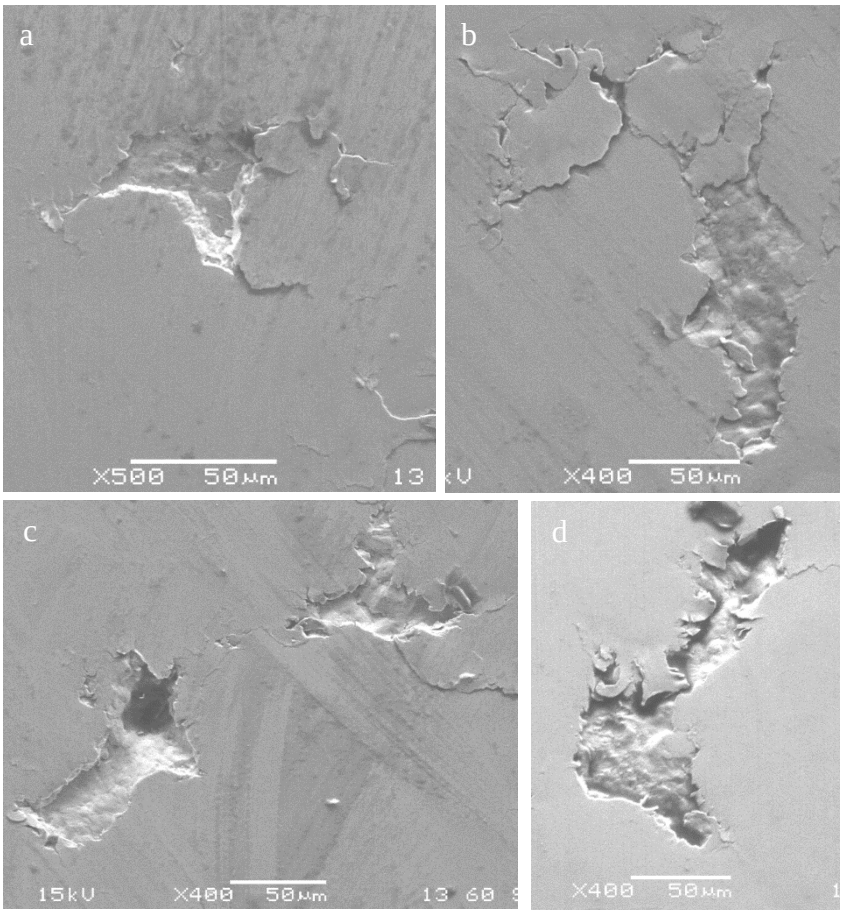

Figure 5.4-5 SEM images of the contact surface of carburised wheel after the 2nd period of Test 3, micro-pits can be observed

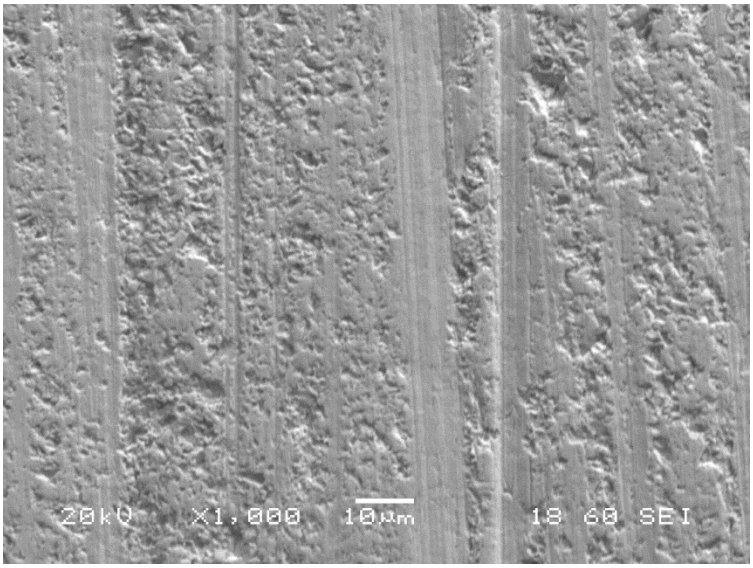

Figure 5.4-6 SEM image of WC wheel surface at the end of Test 3

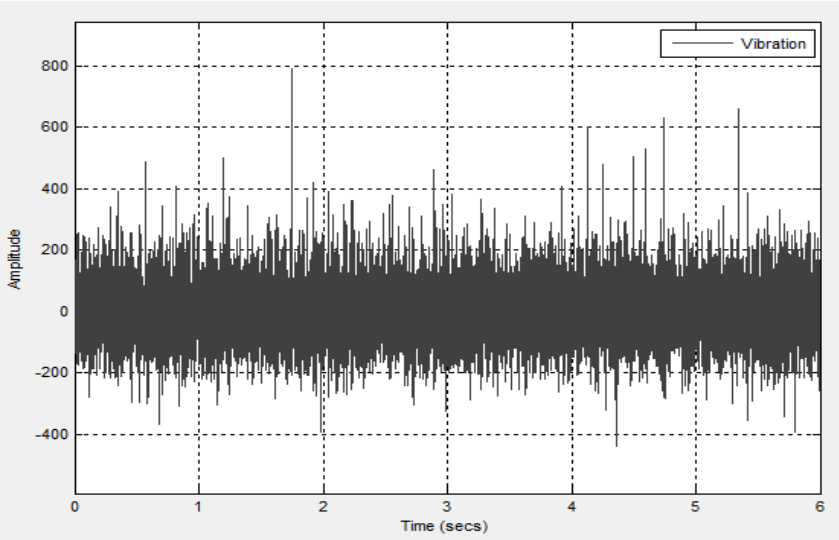

(a)

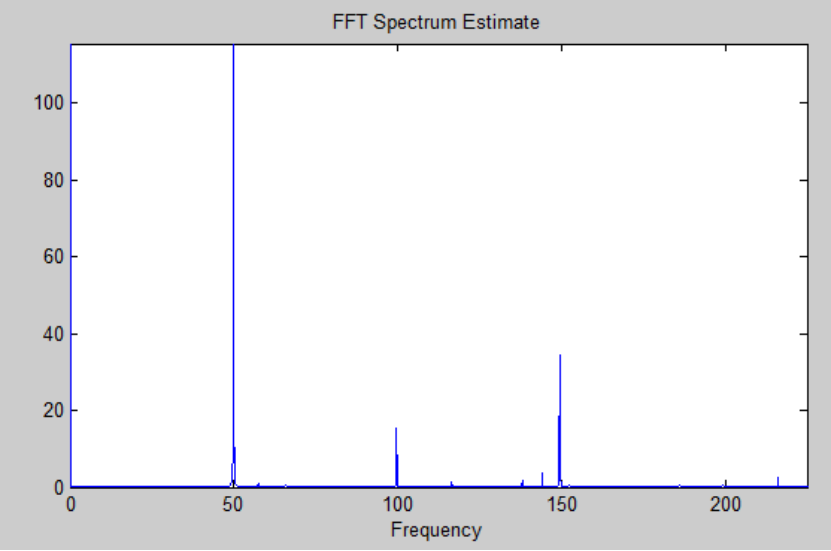

(b)

Figure 5.4-7 (a) Raw vibration signal, and (b) the vibration spectrum, of carburised EN36 wheel at the end of the 2nd period of Test 3

5.5 Test 4: Direct-current plasma nitrided (DCPN) EN40BT wheel against WC wheel

Before testing, the direct-current plasma nitrided EN40BT wheel was measured to have a total weight of 63.2035g. At the end of the test, only micro-pits/craters formed in the steel wheel. The whole test of this wheel pair lasted about 27.5 hours, and it was divided into 2 periods.

(1) First period (0-3,000 seconds)

At the end of this period, a shallow and shiny concaved surface was observed in the plasma nitrided EN40BT wheel (as shown in Figure 5.5-1). The weight loss was negligible. The relatively shallow concave surface is due to the hardened surface which has higher resistance to plastic deformation, comparing with the untreated wheels as for the sample discussed earlier. No AE hits beyond the threshold were detected. Moreover, the FFT spectrum of vibration did not change from the beginning to the end of the 1st period either.

Figure 5.5-1 A shallow and shiny concave surface formed in the direct-current plasma nitrided EN40BT wheel during the 1st period of Test 4

(2) Second period (3,000-9,9000 seconds)

Only 18 damage-related discrete AE signals were detected in this long period (as shown in Figure 5.5-2), hinting infrequent propagations of cracks. The maximum amplitude is 75 dB, and the PAC-energy of these AE hits is shown in Figure 5.5-3, in which the maximum PAC-energy is 606 μV·s. The trend of the cumulative PAC-energy in this period is shown in Figure 5.5-4, which is a step-like pattern.

At the end of this period, only micro-pits with diameter between 30 and 50 μm (as shown in Figure 5.5-5) were observed in the DCPN steel wheel using SEM. No damage was observed in the WC wheel (as shown in Figure 5.5-6). The formation of these micro-pits may be the

source of the detected discrete AE signals. The formation of these micro-pits did not change the vibration pattern of wear tester (as shown in Figure 5.5-7).

After testing, the wheel weight was measured to have been reduced to 63.1216 g, so the total wear loss was 0.0819 g. The average wear rate of direct-current plasma nitrided EN40BT wheel was 3.0 mg/hour, which is only approximately 33% of that of the untreated EN40BT sample.

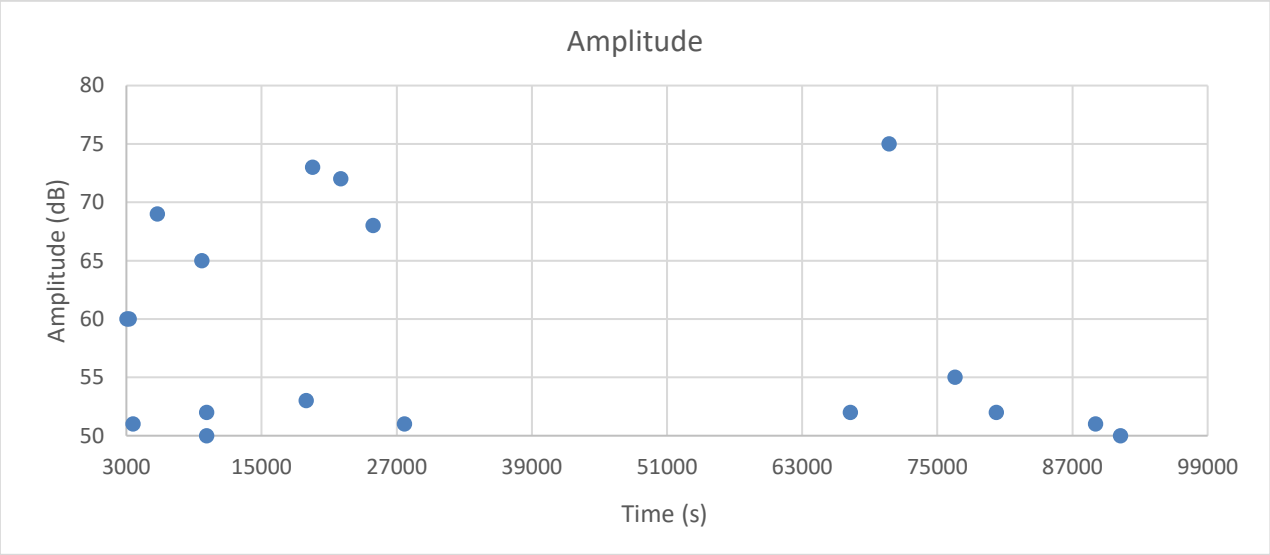

Figure 5.5-2 The AE hits detected from DCPN wheel in the 2nd period of Test 4

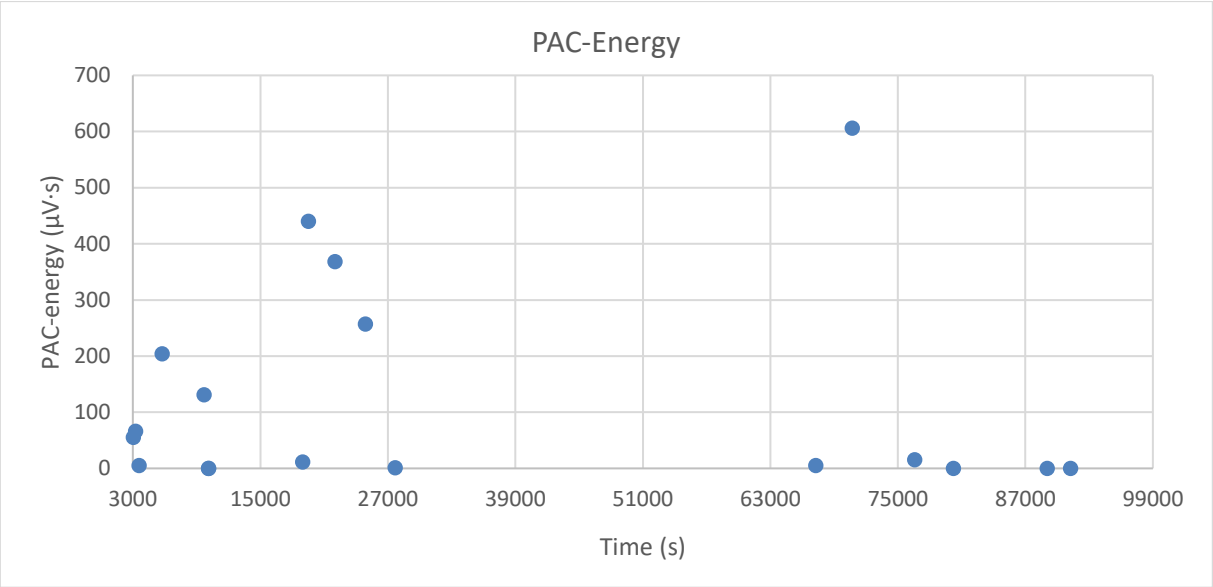

Figure 5.5-3 The PAC-energy of the AE hits detected from DCPN wheel in the 2nd period of Test 4

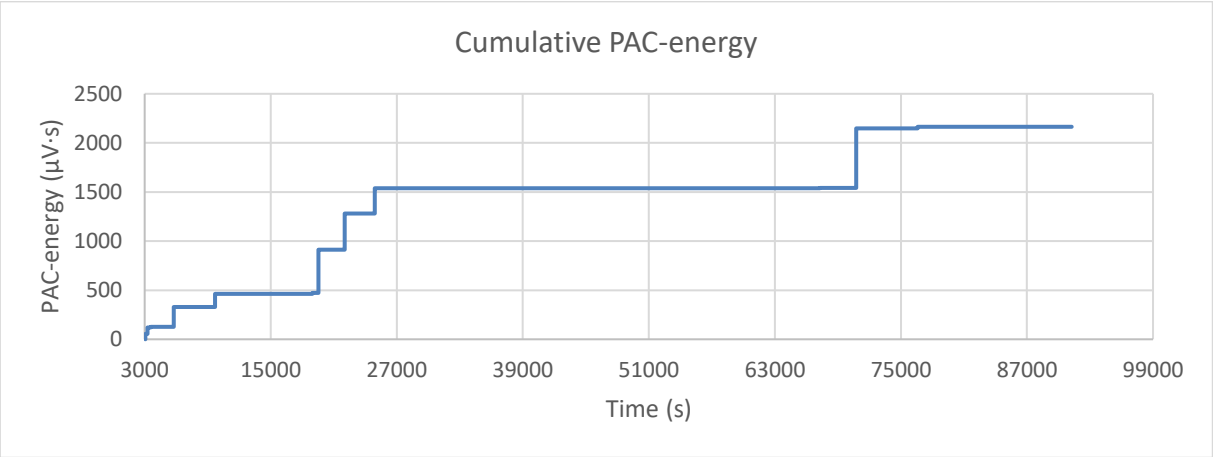

Figure 5.5-4 The cumulative PAC-energy of the AE hits detected from DCPN wheel in the 2nd period of Test 4

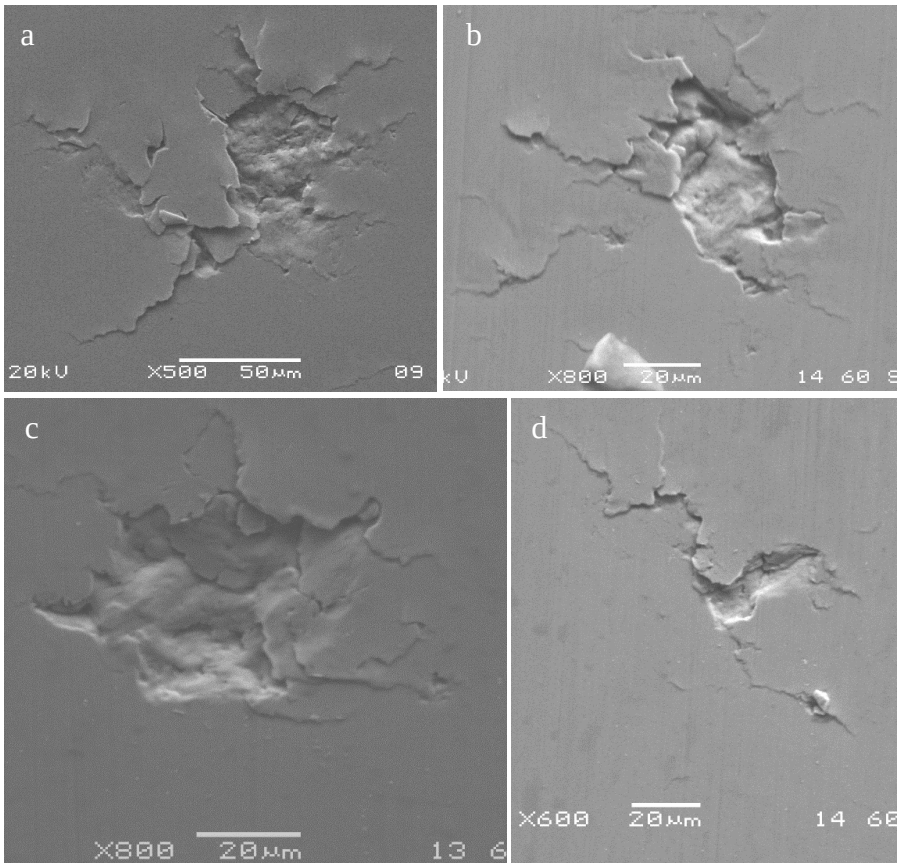

Figure 5.5-5 SEM images of the contact surface of DCPN sample after the 2nd period of Test 4, micro-pits can be observed

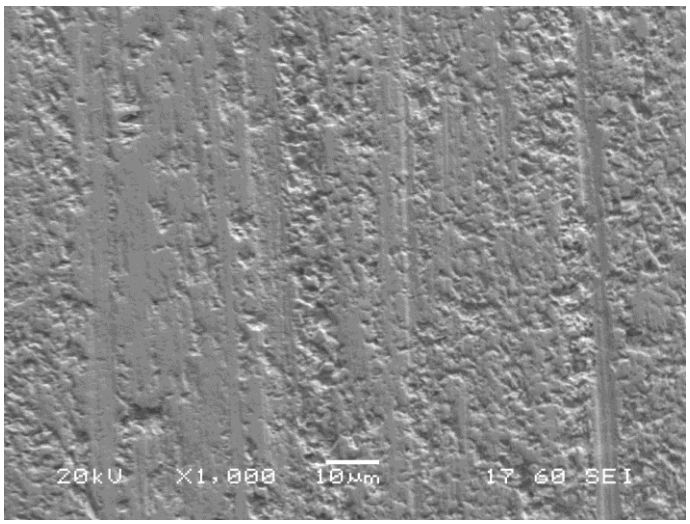

Figure 5.5-6 SEM image of WC wheel surface at the end of Test 4

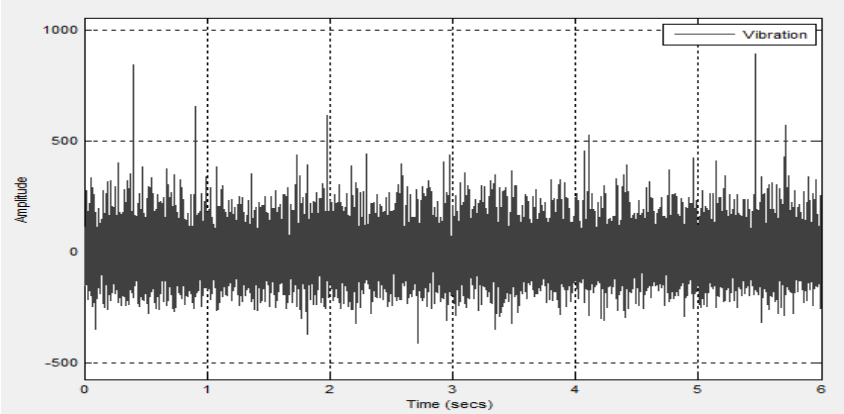

(a)

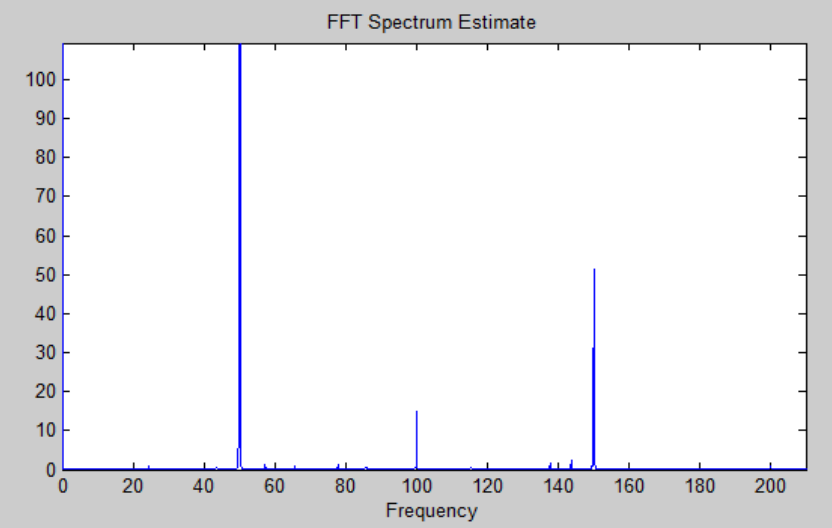

(b)

Figure 5.5-7 (a) Raw vibration signal, and (b) vibration spectrum, at the end of the 2nd period of Test 4

5.6 Summary

Pencil-lead break testing was conducted before the wear test showing that there is a transmission path between the wheel sample and the sensor. In the trial, two noise sources were identified. One was the frictional noise arising from the rubbing between the wheels rolling surfaces. The other noise source was due to oil splash. Both noise sources generated a large number of unwanted AE signals. Appropriate methods were used to prevent noise signals from affecting the collection of AE data.

Four wheels made of as-received EN36 and EN40BT steel grades, carburised EN36 and nitrided EN40BT were tested against WC wheel using an Amsler rolling-sliding wear tester. The AE and vibration signals generated during the tests were recorded and analysed. After each test, the wheel samples were examined carefully. Micro-pits, large cracks and craters were observed in the as-received EN36 and EN40BT wheels, while only micro-pits were observed in the wheels made of carburised EN36 and nitrided EN40BT. Correspondingly, it was found that the irregular propagation of cracks (e.g. the formation of micro-pits) only generated discrete AE signals. The rapid propagation of cracks (e.g. the formation of large cracks and craters) generated AE cluster signals. Based on the results obtained, it can be concluded that the development of material damage (including invisible subsurface cracks) was closely interrelated with the detected AE signals. Nevertheless, the vibration spectrum only significantly changed after severe and visible damage formed on the surface of the tested wheel samples due to its lower sensitivity in comparison with AE.

CHAPTER 6: CONCLUSIONS AND FUTURE WORK

6.1 Conclusions on root failure cause analysis of field samples (section 4.1)

One failed bearing, a spherical roller, several broken gear teeth and gear-related debris particles from various wind turbine gearbox stages have been retrieved from the field. Observation, investigation and metallurgical failure analysis were carried out on the materials of these failed gearbox components. In the end, the root failure causes of these components were deduced to be the high stresses due to the combined effects of misalignment, coarse non-metallic inclusions, and inadequate or inconsistent lubrication.

6.2 Conclusions on Finite Element Simulations using ABAQUS (section 4.2)

In order to validate the identified failure causes of wind turbine gearbox components presented in section 4.1, finite element analysis was carried out simulating the stress field. The simulation results present that when the input torque increased from 8 kN·m to 80 kN·m, the contact stress increased from 372 MPa to 1.22 GPa, by 227.96 %. When the friction coefficient increased from 0 to 0.5, the contact stress grew from 309.3 MPa to 442.8 MPa, by 43.16%. In addition, higher friction coefficient moves the maximum stress to the position closer to the surface. Moreover, when the angular misalignment is 1°, the contact stress achieving 3.10 GPa can be almost 8.3 times higher than the contact stress at perfect alignment. It can be concluded that extreme high input torque, poor lubrication quality and misalignment would significantly increase the contact stress level of wind turbine gearbox components prompting the initiation and subsequent rapid damage evolution which result in premature catastrophic failure of the wind turbine gearbox. In addition, crack initiation caused by the coarse inclusions and subsequent propagation was also successfully simulated indicating the number of coarse inclusions present in the material need to be reduced further.

6.3 Conclusions on surface engineering of wind turbine gearbox materials (section 4.3)

Duplex surface systems for wind turbine gearbox components were designed as low friction DLC coating deposited on surface hardened EN36 and EN40BT steel, which aim to solve the life-limiting problems of gearbox by increasing the resistance to the high contact stresses due to high input torque, poor lubrication quality and unavoidable misalignment. The as-received EN36 and EN40BT were characterised firstly. Then, EN36 samples were carburised and EN40BT were nitrided successfully. After plasma nitriding, the surface hardness of EN40BT increased from 321 HV0.05 to about 920 HV0.05 (DCPN550-20) and 816 HV0.05 (ASPN550-20). The carburising process increased the surface hardness of EN36 from 356 HV0.05 to about 850 HV0.05. Nitrided samples possess similar or higher hardness at much lower treating temperature than the carburised samples. For the purpose of comparison, single surface systems, i.e. DLC coating deposited on as-received steel samples, were also produced. The duplex surface systems exhibited superior properties and performance than single coating systems and traditional carburised surface, i.e. low friction coefficient of about 0.16, high surface hardness of 11.43 GPa, higher load bearing capacity and higher resistance to scratch and rolling-sliding wear. These properties of duplex surface systems could mitigate the effect of higher contact stresses due to high input torque, poor lubrication quality and unavoidable misalignment and prevent the premature failures of wind turbine gearbox components.

6.4 Conclusions on rolling-sliding wear tester combined with condition monitoring systems (chapter 5)

Four wheels made of as-received EN36 and EN40BT steel grades, carburised EN36 and nitrided EN40BT were tested against WC wheel using an Amsler rolling-sliding wear tester. The acoustic emission and vibration signals generated during the tests were recorded and analysed. After each test, the wheel samples were examined carefully. Based on the results, it can be concluded that the development of material damage (including invisible subsurface damage) was closely interrelated with the detected AE signals. Nevertheless, vibration spectrum only significantly changed after severe and visible damage formed on the surface of the tested wheel samples. It indicates that AE test system is better than vibration-based system in the aspect of sensitivity.

6.5 Future work

Through the examination of failed wind turbine gearbox components retrieved from field, some common failures have been identified, for instance, the rolling contact fatigue (e.g. micro/macro-pitting and micro/macro-spalling) and scuffing. However, another important and frequently reported failure, the microstructural alteration (i.e. white etching crack), has not been observed in the currently available field samples. It is worth obtaining more field samples potentially containing white etching cracks (WEC) to conduct root cause analysis on these samples, in order to better understand the mechanisms of WEC.

In this study, the effect of friction coefficient and misalignment on stress distribution of meshing gear pair, and the effect of coarse inclusions on crack initiation and propagation were simulated using FEA software. More FEA simulations of wind turbine gearbox components

and the related failures are suggested for a systematic study. For instance, to simulate the initiation and development of fatigue cracking in gear teeth.

To eliminate the life-limiting problems occurring in wind turbine gearboxes, duplex surface systems combined DLC coating with surface hardening have been designed in this study. The samples demonstrated superior properties and performance in laboratory conditions. Field trials of surface engineered gears or bearings are suggested to prove the feasibility of the designed surface systems in the future.

During the rolling-sliding wear tests coupled with condition monitoring systems (CMS), AE signals have clearly shown close correlation with the development of test samples in this study, especially for the untreated steels. It is suggested that more tests could be carried out on other samples, such as coating samples, and various load/speed conditions to find ways of mitigating the effect of variable loading conditions on the AE signals.

LIST OF TABLES

LIST OF FIGURES

REFERENCES

1. O. Adaba 2015. Formation and evolution of Spinel in aluminum killed calcium treated linepipe steels.

2. P. S. Addison 2017. *The Illustrated Wavelet Transform Handbook: Introductory Theory and Applications in Science, Engineering, Medicine and Finance, Second Edition*, CRC Press.

3. H. Aghajani & S. Behrangi 2016. *Plasma Nitriding of Steels*, Springer International Publishing.

4. X. Ai & C. Moyer 2001. Rolling Element Bearings. *In:* BHUSHAN, B. (ed.) *Modern tribology handbook. 2. Materials, coatings, and industrial applications.* CRC Press.

5. S. K. Al-Arbi. 2012. *Condition Monitoring of Gear Systems using Vibration Analysis.* University of Huddersfield.

6. E. S. Alley & R. W. Neu 2010. Microstructure-sensitive modeling of rolling contact fatigue. *International Journal of Fatigue,* 32**,** 841-850.

7. A. Almasi & R. M. Consultant 2014. Oil analysis methods and lubrication monitoring. *Plant Services*.

8. R. Amavis 1990. *Refractories for the Steel Industry*, Springer Netherlands.

9. ANSI/AGMA 2004. AMERICAN NATIONAL STANDARD ANSI/AGMA 2001- D04 *Fundamental Rating Factors and Calculation Methods for Involute Spur and Helical Gear Teeth*.

10. ANSI/AGMA/AWEA 2004. AMERICAN NATIONAL STANDARD ANSI/AGMA/AWEA 6006-A03. *Standard for Design and Specification of Gearboxes for Wind Turbines.*

11. J. Antoni 2006. The spectral kurtosis: a useful tool for characterising non-stationary signals. *Mechanical Systems and Signal Processing,* 20**,** 282-307.

12. M. Arbak, A. E. Tekkaya & F. Özhan 2005. Comparison of various preforms for hot forging of bearing rings. *Journal of materials processing technology,* 169**,** 72-82.

13. J. C. Avelar-Batista, E. Spain, G. G. Fuentes, A. Sola, R. Rodriguez & J. Housden 2006. Triode plasma nitriding and PVD coating: A successful pre-treatment combination to

improve the wear resistance of DLC coatings on Ti6Al4V alloy. *Surface and Coatings Technology,* 201**,** 4335-4340.

14. R. Barron 1996. *Engineering condition monitoring: practice, methods and applications*, Longman.

15. J. Batista, C. Godoy & A. Matthews 2003. Impact testing of duplex and non-duplex (Ti, Al) N and Cr–N PVD coatings. *Surface and Coatings Technology,* 163**,** 353-361.

16. J. C. A. Batista, C. Godoy & A. Matthews 2003. Impact testing of duplex and non-duplex (Ti,Al)N and Cr–N PVD coatings. *Surface and Coatings Technology,* 163–164**,** 353-361.

17. H. S. Bawa 2004. *Manufacturing Processes - Ii*, McGraw-Hill Education (India) Pvt Limited.

18. R. Beardmore. 2013. *Friction Factors* [Online]. Available: http://www.roymech.co.uk/Useful_Tables/Tribology/co_of_frict.htm#method [Accessed 2017].

19. E. Becker & P. Poste 2006. Keeping the blades turning: Condition monitoring of wind turbine gears. *Refocus,* 7**,** 26-32.

20. T. Bell 1987. Surface engineering: a rapidly developing discipline. *European Journal of Engineering Education,* 12**,** 27-32.

21. T. Bell, H. Dong & Y. Sun 1998. Realising the potential of duplex surface engineering. *Tribology International,* 31**,** 127-137.

22. H. Berger, L. Mordfin, A. S. f. Testing & M. C. E.-o. N. Testing 1992. *Nondestructive Testing Standards--present and Future*, ASTM.

23. H. Bhadeshia 2012. Steels for bearings. *Progress in materials Science,* 57**,** 268-435.

24. P. J. Blau, L. R. Walker, H. Xu, R. Parten, J. Qu & T. Geer 2010. Wear Analysis of Wind Turbine Gearbox Bearings. *ORNL/TM-2010/59*.

25. M. Boniardi, F. D'Errico & C. Tagliabue 2006. Influence of carburizing and nitriding on failure of gears–A case study. *Engineering Failure Analysis,* 13**,** 312-339.

26. A. Brandt 2011. *Noise and Vibration Analysis: Signal Analysis and Experimental Procedures*, Wiley.

27. T. Bruce, H. Long, T. Slatter & R. Dwyer-Joyce 2016. Formation of white etching cracks at manganese sulfide (MnS) inclusions in bearing steel due to hammering impact loading. *Wind Energy*.

28. T. Burton, N. Jenkins, D. Sharpe & E. Bossanyi 2011. *Wind energy handbook*, Chichester, West Sussex, Wiley.

29. R. T. Buscarello 1985. *Practical Solutions to Machinery and Maintenance Vibration Problems [videocassette]*, Update International.

30. G. Bywaters, V. John, J. Lynch, P. Mattila, G. Norton, J. Stowell, M. Salata, O. Labath, A. Chertok & D. Hablanian 2004. Northern Power Systems WindPACT drive train alternative design study report. *NREL, Golden, Colorado, Report no. NREL/SR-500-35524*.

31. P.-M. Cabanne 2006. USE OF SILICON CARBIDE IN THE INDUCTION FURNACE. *Sorelmetal Technical Services*.

32. S. Chattopadhyay & C. Sellars 1982. Kinetics of pearlite spheroidisation during static annealing and during hot deformation. *Acta Metallurgica,* 30**,** 157-170.

33. B. H. Chudnovsky 2017. *Transmission, Distribution, and Renewable Energy Generation Power Equipment: Aging and Life Extension Techniques, Second Edition*, CRC Press.

34. E. Claesson. 2014. *Modelling of roller bearings in ABAQUS.* Master, CHALMERS UNIVERSITY OF TECHNOLOGY.

35. S. Corujeira Gallo & H. Dong 2009. Study of active screen plasma processing conditions for carburising and nitriding austenitic stainless steel. *Surface and Coatings Technology,* 203**,** 3669-3675.

36. C. J. Crabtree, D. Zappalá & P. J. Tavner 2014. Survey of commercially available condition monitoring systems for wind turbines.

37. Dassault-Systèmes. 2015. *Abaqus Analysis User's Guide (2016)* [Online]. Available: http://130.149.89.49:2080/v2016/books/usb/default.htm?startat=pt04ch10s07at36.html [Accessed 02/11 2016].

38. D. H. Dave Heidenreich 2012. Why gearboxes fail and a solution to lower drivetrain costs. *Windpower engineering and development.*

39. T. Davidson 1999. An Introduction to Failure Analysis for Metallurgical Engineers. *TMS Outstanding Student Paper Contest Winner–1999 Undergraduate Division*.

40. A. Davies 1998. *Handbook of Condition Monitoring:: Techniques and Methodology*, Springer.

41. P. Davoli, E. Conrado & K. Michaelis 2007. Recognizing gear failures. *Machine Design,* 63**,** 64-67.

42. L. de Campos Franceschini Canale 2008. *Failure Analysis of Heat Treated Steel Components,* ASM International.

43. F. De Lorenzo & M. Calabro. Kurtosis: a statistical approach to identify defect in rolling bearings. Proceedings of 2nd International Conference on Marine Research and Transportation, Naples, 2007. 17-24.

44. E. Dehner & F. Weber 2007. Experience with Large, High-Speed Load Gears. *Gear Technology***,** 42-52.

45. S. K. Dhua, A. Ray, S. K. Sen, M. S. Prasad, K. B. Mishra & S. Jha 2000. Influence of nonmetallic inclusion characteristics on the mechanical properties of rail steel. *Journal of Materials Engineering and Performance,* 9**,** 700-709.

46. G. E. Dieter 1976. *Mechanical metallurgy*, McGraw-Hill New York.

47. J. Dlouhy, D. Hauserova & Z. Novy 2014. Carbide spheroidisation in 100CrMnSi6-4 bearing steel by controlled rolling. *Archives of Materials Science and Engineering,* 68**,** 87--92.

48. E. DOE 2010. Advanced Wind Turbine Drivetrain Concepts: Workshop Report, June 29-30, 2010.

49. N. Dogan, R. Longbottom, M. H. Reid, M. Chapman, P. Wilson, L. Moore & B. J. Monaghan 2015. Morphology and composition changes of spinel (MgAl2O4) inclusions in steel. *Ironmaking & Steelmaking,* 42**,** 185-193.

50. G. Doll. Tribological Challenges in Wind Turbine Technology. National renewable energy laboratory wind turbine tribology seminar, 2011.

51. G. L. Doll, M. N. Kotzalas & Y. S. Kang. Life-limiting wear of wind turbine gearbox bearings: Origins and solutions. European Wind Energy Conference and Exhibition 2010, EWEC 2010, April 20, 2010 - April 23, 2010, 2010 Warsaw, Poland. European Wind Energy Association, 2559-2568.

52. G. Doyon, D. Brown, V. Rudnev, F. Andgea, C. Stilwala & E. Almeida 2009. Induction heating helps to put wind turbines in high gear. *Heat Treating Progress***,** 55-58.

53. R. S. Dwyer-Joyce 1997. Contact Mechanics. *Tribological Design Data.* 1st ed. London: Institution of Mechanical Engineers.

54. R. Dwyer. Detection of non-Gaussian signals by frequency domain kurtosis estimation. Acoustics, Speech, and Signal Processing, IEEE International Conference on ICASSP'83., 1983. IEEE, 607-610.

55. B. Eftekharnejad & D. Mba 2009. Seeded fault detection on helical gears with acoustic emission. *Applied acoustics,* 70**,** 547-555.

56. P. EG 1982. Fretting corrosion in rolling bearings – cause and avoidance. UK: INA Bearing Company Ltd.

57. F. Elasha, M. Greaves, D. Mba & A. Addali 2015. Application of Acoustic Emission in Diagnostic of Bearing Faults within a Helicopter Gearbox. *Procedia CIRP,* 38**,** 30-36.

58. Electro-Abrasives. 2015. *Metallurgical Silicon Carbide* [Online]. Available: http://www.electroabrasives.com/Products/Metallurgical_Silicon_Carbide/ [Accessed 2017].

59. J. Endrino, R. Escobar Galindo, H. S. Zhang, M. Allen, R. Gago, A. Espinosa & A. Anders 2008. Structure and properties of silver-containing aC (H) films deposited by plasma immersion ion implantation. *Surface and Coatings Technology,* 202**,** 3675-3682.

60. O. o. E. E. a. R. Energy 2006. Schematic diagram of a modern horizontal-axis, three-bladed wind turbine.

61. A. Erdemir, C. Bindal, J. Pagan & P. Wilbur 1995. Characterization of transfer layers on steel surfaces sliding against diamond-like hydrocarbon films in dry nitrogen. *Surface and Coatings Technology,* 76**,** 559-563.

62. A. Erdemir, O. Eryillmaz & V. Sista 2012. Ultra-fast boriding for improved efficiency and reduced emissions in materials processing industries. Argonne National Laboratory (ANL).

63. R. Errichello 2004. Another perspective: false brinelling and fretting corrosion. *Tribology and Lubrication Technology,* 60**,** 34-37.

64. R. Errichello 2012. Morphology of micropitting. *Gear Technology,* 4**,** 74-81.

65. R. Errichello, R. Budny & R. Eckert 2013. Investigations of bearing failures associated with white etching areas (WEAs) in wind turbine gearboxes. *Tribology Transactions,* 56**,** 1069-1076.

66. R. Errichello, J. Muller, Geartech, N. R. E. Laboratory & U. S. D. o. Energy 1994. *Application Requirements for Wind Turbine Gearboxes,* National Renewable Energy Laboratory.

67. M.-H. Evans, A. Richardson, L. Wang & R. Wood 2013. Serial sectioning investigation of butterfly and white etching crack (WEC) formation in wind turbine gearbox bearings. *Wear,* 302**,** 1573-1582.

68. M. Evans 2012. White structure flaking (WSF) in wind turbine gearbox bearings: effects of'butterflies' and white etching cracks (WECs). *Materials Science and Technology,* 28**,** 3-22.

69. R. D. Evans, C. H. Hager & R. D. Logsdon 2009. Friction and wear performance of candidate surface treatments for wind turbine gearbox bearings in high slip contacts.

70. FAG 2001. Rolling Bearing Damage Recognition of damage and bearing inspection.

71. S. Field, M. Jarratt & D. Teer 2004. Tribological properties of graphite-like and diamond-like carbon coatings. *Tribology International,* 37**,** 949-956.

72. S. K. Field, M. Jarratt & D. G. Teer 2004. Tribological properties of graphite-like and diamond-like carbon coatings. *Tribology International,* 37**,** 949-956.

73. D. Fletcher, F. Franklin, J. Garnham, E. Muyupa, M. Papaelias, C. Davis, A. Kapoor, M. Widiyarta & G. Vasic 2008. Three-dimensional microstructural modelling of wear, crack initiation and growth in rail steel. *International Journal of Railway,* 1**,** 106-112.

74. A. Fraser. 2002. *horizontal axis wind turbine (HAWT)* [Online]. Available: http://www.formfonts.com/3D-Model/3674/1/d5010-electrical-service-distribution/d50-electrical/services/wind-turbine/ [Accessed 11 March 2014].

75. H. Fu, E. Galindo-Nava & P. Rivera-Díaz-del-Castillo 2017. Modelling and characterisation of stress-induced carbide precipitation in bearing steels under rolling contact fatigue. *Acta Materialia,* 128**,** 176-187.

76. P. Fu, K. Zhan & C. Jiang 2013. Micro-structure and surface layer properties of 18CrNiMo7-6 steel after multistep shot peening. *Materials & Design,* 51**,** 309-314.

77. F. P. García Márquez, A. M. Tobias, J. M. Pinar Pérez & M. Papaelias 2012. Condition monitoring of wind turbines: Techniques and methods. *Renewable Energy,* 46**,** 169-178.

78. T. K. Garrett, K. Newton & W. Steeds 2000. *Motor Vehicle*, Butterworth-Heinemann.

79. J. Gegner 2011. *Tribological aspects of rolling bearing failures*, INTECH Open Access Publisher.

80. P. Gembalova, J. Boruta, E. Grycz & K. M. Cmiel 2007. Hot forming parameters research of bearing steel. *Archives of Civil and Mechanical Engineering,* 7**,** 21-28.

81. A. J. Gentile & A. D. Martin. Effects of prior metallurgically induced compressive residual stress on metallurgical and endurance properties of overload tested ball bearings. ASME Meeting WA/CF-7, Nov 7-11 1965, 1965 New York, NY, United States. American Society of Mechanical Engineers (ASME), 8.

82. D. Gielen 2012. Renewable energy technologies: cost analysis series. *Wind Power.*

83. W. Glaeser 1996. Contact fatigue. *ASM International, Member/Customer Service Center, Materials Park, OH 44073-0002, USA, 1996.***,** 331-336.

84. R. Grange, C. Hribal & L. Porter 1977. Hardness of tempered martensite in carbon and low-alloy steels. *Metallurgical Transactions A,* 8**,** 1775-1785.

85. A. Greco, K. Mistry, V. Sista, O. Eryilmaz & A. Erdemir 2011. Friction and wear behaviour of boron based surface treatment and nano-particle lubricant additives for wind turbine gearbox applications. *Wear,* 271**,** 1754-1760.

86. A. Greco, S. Sheng, J. Keller & A. Erdemir 2013. Material Wear and Fatigue in Wind Turbine Systems. *Wear*.

87. K. Gröchenig 2013. *Foundations of Time-Frequency Analysis*, Birkhäuser Boston.

88. C. U. Grosse & L. M. Linzer 2008. Signal-based AE analysis. *Acoustic emission testing.* Springer.

89. Y. Guo & R. G. Parker 2010. Dynamic modeling and analysis of a spur planetary gear involving tooth wedging and bearing clearance nonlinearity. *European Journal of Mechanics-A/Solids,* 29**,** 1022-1033.

90. G. W. E. C. GWEC 2017. GLOBAL WIND STATISTICS 2016.

91. B. Hafner 2007. Scanning electron microscopy primer. *Characterization Facility, University of Minnesota-Twin Cities***,** 1-29.

92. J. F. Hall, C. A. Mecklenborg, D. Chen & S. B. Pratap 2011. Wind energy conversion with a variable-ratio gearbox: design and analysis. *Renewable Energy,* 36**,** 1075-1080.

93. Z. Hameed, Y. S. Hong, Y. M. Cho, S. H. Ahn & C. K. Song 2009. Condition monitoring and fault detection of wind turbines and related algorithms: A review. *Renewable and Sustainable Energy Reviews,* 13**,** 1-39.

94. A. Harnoy 2002. *Bearing design in machinery: engineering tribology and lubrication*, CRC press.

95. D. C. Harris, M. Baronowski, L. Henneman, L. LaCroix, C. Wilson, S. Kurzius, B. Burns, K. Kitagawa, J. Gembarovic & S. M. Goodrich 2008. Thermal, structural, and optical properties of Cleartran® multispectral zinc sulfide. *Optical Engineering,* 47**,** 114001-114001-15.

96. C. Hatch 2004. Improved wind turbine condition monitoring using acceleration enveloping. *Orbit,* 61**,** 58-61.

97. C. Hellier & M. Shakinovsky 2003. Acoustic emission testing. *Handbook of Nondestructive Evaluation.* 2 ed. USA: The McGraw-Hill Companies, Inc.

98. J. Helsen, F. Vanhollebeke, F. De Coninck, D. Vandepitte & W. Desmet 2011. Insights in wind turbine drive train dynamics gathered by validating advanced models on a newly developed 13.2 MW dynamically controlled test-rig. *Mechatronics,* 21**,** 737-752.

99. R. A. Higgins & W. Bolton 2010. *Materials for Engineers and Technicians*, Newnes.

100. J. P. Hirvonen, J. Koskinen, J. Jervis & M. Nastasi 1996. Present progress in the development of low friction coatings. *Surface and Coatings Technology,* 80**,** 139-150.

101. Hong-Kong-Bearing-Company. 2017. *FAG (Schaeffler) NU222-E-M1 Cylindrical Roller Bearings* [Online]. Available: http://kondisa.org/15963/FAG-(Schaeffler)-NU222-E-M1/ [Accessed March 2017].

102. M. Hotait, D. Talbot & A. Kahraman. An Investigation of the Influence of Shaft Misalignments on Bending Stresses of Helical Gear with Lead Crown. Proceedings of the 10th International Power Transmission and Gearing Conference, Las Vegas, 2007.

103. M. Huang, L. Jiang, P. K. Liaw, C. R. Brooks, R. Seeley & D. L. Klarstrom 1998. Using acoustic emission in fatigue and fracture materials research. *JOM,* 50**,** 1-14.

104. P. Hubbard, S. Dowey, J. Partridge, E. Doyle & D. McCulloch 2010a. Investigation of nitrogen mass transfer within an industrial plasma nitriding system II: Application of a biased screen. *Surface and Coatings Technology,* 204**,** 1151-1157.

105. P. Hubbard, J. Partridge, E. Doyle, D. McCulloch, M. Taylor & S. Dowey 2010b. Investigation of nitrogen mass transfer within an industrial plasma nitriding system I: The role of surface deposits. *Surface and Coatings Technology,* 204**,** 1145-1150.

106. R. Hyers, J. McGowan, K. Sullivan, J. Manwell & B. Syrett 2006. Condition monitoring and prognosis of utility scale wind turbines. *Energy Materials: Materials Science and Engineering for Energy Systems,* 1**,** 187-203.

107. IEA-ETSAP & IRENA 2016. Wind Power-Technology Brief. *In:* SIMBOLOTTI, G. & TOSATO, G. (eds.).

108. IEC 2012. INTERNATIONAL STANDARD IEC 61400-4. *Wind Turbines - Part 4: Design requirements for wind trubine gearboxes, Edition 1.0 2012-12.*

109. M. G. Inc. 2009. AEwin Software User's Manual. 3 ed.

110. M. Irfan 2013. Meta Modeling of Transmission Error for Spur, Helical and Planetary Gears for Wind Turbine Application. Chalmers University of Technology.

111. ISO 2003. INTERNATIONAL STANDARD ISO 6336-5:2003. *Calculation of load capacity of spur and helical gears - Part 5: Strength and quality of materials.*

112. S. Jain. 2013. *Skidding and fault detection in the bearings of wind-turbine gearboxes.* University of Cambridge.

113. D. Jeddi & H.-P. Lieurade 2010. Effect of retained austenite on high cycle fatigue behavior of carburized 14NiCr11 steel. *Procedia Engineering,* 2**,** 1927-1936.

114. P. Kaestner, J. Olfe, J. W. He & K. T. Rie 2001. Improvement in the load-bearing capacity and adhesion of TiC coatings on TiAl6V4 by duplex treatment. *Surface and Coatings Technology,* 142–144**,** 928-933.

115. Karlebo-Handbok 1992. Maskinelement. Kuggväxlar. Stockholm. Stockholm: Liber AB. *Karlebo Handbok. Utgåva 14*.

116. E. Kečkováa, P. Fabiana & E. Jarabicováb 2008. Selctive heat treatment of the gearbox component. *Archives of Foundry,* 8.

117. F. Khalid, M. Farooque, A. Ul Haq & A. Khan 1999. Role of ferrite/pearlite banded structure and segregation on mechanical properties of microalloyed hot rolled steel. *Materials science and technology,* 15**,** 1209-1215.

118. M. Kharrat, E. Ramasso, V. Placet & M. Boubakar 2016. A signal processing approach for enhanced acoustic emission data analysis in high activity systems: application to organic matrix composites. *Mechanical Systems and Signal Processing,* 70**,** 1038-1055.

119. R. Kiessling & N. Lange 1968. Non-metallic inclusions in steel.

120. J. G. Kim, G. H. Lee, Y. J. Park, Y. Y. Nam & T. H. Chong 2011. Study of Load Distribution and Sharing Characteristics of Planetary Geartrain for Wind Turbines. *Applied Mechanics and Materials,* 86**,** 674-679.

121. J. A. Kleinhans, E. Jakubowitz, J. B. Seeger, C. Heisel & J. P. Kretzer 2009. Macroscopic third-body wear caused by porous metal surface fragments in total hip arthroplasty. *Orthopedics,* 32.

122. M. N. Kotzalas & G. L. Doll 2010. Tribological advancements for reliable wind turbine performance. *Philosophical Transactions of the Royal Society A: Mathematical, Physical and Engineering Sciences,* 368**,** 4829-4850.

123. M. Kulshreshtha 2013. Analysis of the Effect of Machining Parameters on Surface Roughness of EN 36 Nickel Steel. *International Journal Advanced Information Science and Technology (IJAIST),* 16.

124. M. LaPlante 2009. Carburizing Wind-Turbine Gears. *Gear Solutions.*

125. N. Lecis, G. La Vecchia, M. Boniardi & F. D'Errico 2006. Fatigue behavior of duplex-treated samples coated with Cr (C, N) film. *Surface and Coatings Technology,* 201**,** 2335-2340.

126. N. Lecis, G. M. La Vecchia, M. Boniardi & F. D'Errico 2006. Fatigue behavior of duplex-treated samples coated with Cr(C,N) film. *Surface and Coatings Technology,* 201**,** 2335-2340.

127. B. D. Leonard, F. Sadeghi, R. D. Evans, G. L. Doll & P. J. Shiller 2009. Fretting of WC/aC: H and Cr2N coatings under grease-lubricated and unlubricated conditions. *Tribology Transactions,* 53**,** 145-153.

128. W. Leslie 1983. Inclusions and mechanical properties. *SS Trans. 2***,** 1-24.

129. C. X. Li, J. Georges & X. Y. Li 2002. Active screen plasma nitriding of austenitic stainless steel. *Surface Engineering,* 18**,** 453-457.

130. G. D. Lindell, D. J. Breuer & D. H. Herring 2002. *Selecting the Best Carburizing Method for the Heat Treatment of Gears,* AGMA.

131. G. D. Lindell & D. H. Herring 2007. Heat Treating Heavy-Duty Gears.

132. W. Liu, B. Tang, J. Han, X. Lu, N. Hu & Z. He 2015. The structure healthy condition monitoring and fault diagnosis methods in wind turbines: A review. *Renewable and Sustainable Energy Reviews,* 44**,** 466-472.

133. Y. Liu, A. Erdemir & E. Meletis 1996a. An investigation of the relationship between graphitization and frictional behavior of DLC coatings. *Surface and Coatings Technology,* 86**,** 564-568.

134. Y. Liu, A. Erdemir & E. Meletis 1996b. A study of the wear mechanism of diamond-like carbon films. *Surface and Coatings Technology,* 82**,** 48-56.

135. M.-a.-C. LLC. 2015. *BRIQUETTES AND SILICON CARBIDE FOR THE STEEL INDUSTRY* [Online]. Available: http://www.millerandco.com/products/briquettes-and-silicon-carbide-for-the-steel-industry/ [Accessed 2017].

136. B. Lu, Y. Li, X. Wu & Z. Yang. A review of recent advances in wind turbine condition monitoring and fault diagnosis. Power Electronics and Machines in Wind Applications, 2009. PEMWA 2009. IEEE, 2009. IEEE, 1-7.

137. N. Luzginova, L. Zhao & J. Sietsma 2008. The cementite spheroidization process in high-carbon steels with different chromium contents. *Metallurgical and Materials Transactions A,* 39**,** 513-521.

138. J. Maciejewski 2015. The Effects of Sulfide Inclusions on Mechanical Properties and Failures of Steel Components. *Journal of Failure Analysis and Prevention,* 15**,** 169-178.

139. M. Mägi & K. Melkersson 2009. *Lärobok i maskinelement: Del A,* EcoDev International.

140. G. M. Maitra 1994. *Handbook of gear design,* Tata McGraw-Hill Education.

141. D. Mba & R. B. Rao 2006. Development of Acoustic Emission Technology for Condition Monitoring and Diagnosis of Rotating Machines; Bearings, Pumps, Gearboxes, Engines and Rotating Structures.

142. T. McNelley 1986. Porosity associated with insoluble carbides in VIM-VAR AISI M-50 steel and its probable effects on rolling contact fatigue.

143. M. Michaud, G. J. Sroka & R. E. Benson 2011. Refurbishing Wind Turbine Gears. *Gear Solutions,* 9.

144. T. Michler, M. Grischke, K. Bewilogua & H. Dimigen 1998. Properties of duplex coatings prepared by plasma nitriding and PVD Ti–C:H deposition on X20Cr13 ferritic stainless steel. *Thin Solid Films,* 322**,** 206-212.

145. J. Miettinen & P. Pataniitty 1999. Acoustic emission in monitoring extremely slowly rotating rolling bearing. *Proceedings of 12th international congress on condition monitoring and diagnostic engineering management, COMADEM.*

146. K. Miyachika, S. Oda & T. Koide 1995. Acoustic emission of bending fatigue process of spur gear teeth. *Journal of acoustic emission,* 13**,** S47-S53.

147. K. Monma, R. Maruta, T. Yamamoto & Y. Wakikado 1968. Effect of particle sizes of carbides and amounts of undissolved carbide on the fatigue life of bearing steel. *J. Jpn. Inst. Met.,* 32**,** 1198-1204.

148. S. Mridha & A. A. Khan 2008. The effects of process variables on the hardness of nitrided 3% chromium steel. *Journal of Materials Processing Technology,* 201**,** 325-330.

149. P. Musgrove 2010. *Wind power*, Cambridge, Cambridge University Press.

150. W. Musial, S. Butterfield & B. McNiff. Improving wind turbine gearbox reliability. Proceedings of the European Wind Energy Conference, 2007.

151. NDT-Resource-Center. 2012. *Introduction to Acoustic Emission Testing* [Online]. Available: https://www.nde-ed.org/EducationResources/CommunityCollege/Other%20Methods/AE/AE_Intro.htm [Accessed 23 March 2016].

152. M. J. Neale 1995. *The tribology handbook*, Butterworth-Heinemann.

153. D. Nélias, M. L. Dumont, F. Champiot, A. Vincent, D. Girodin, R. Fougéres & L. Flamand 1999. Role of Inclusions, Surface Roughness and Operating Conditions on Rolling Contact Fatigue. *Journal of Tribology,* 121**,** 240-251.

154. D. Nelias, C. Jacq, G. Lormand, G. Dudragne & A. Vincent 2005. New methodology to evaluate the rolling contact fatigue performance of bearing steels with surface dents: application to 32CrMoV13 (nitrided) and M50 steels. *Journal of tribology,* 127**,** 611-622.

155. M. P. Norton & D. G. Karczub 2003. *Fundamentals of Noise and Vibration Analysis for Engineers*, Cambridge University Press.

156. NOVEXA. 2017. *Defects treated* [Online]. Available: http://www.novexa.com/en/intervention/gears/defects-treated.html [Accessed].

157. Oerlikon-Balzers. 2017. *BALINIT C-Hard as metal – smooth as carbon* [Online]. Available: https://www.oerlikon.com/balzers/uk/en/portfolio/balzers-surface-solutions/pvd-and-pacvd-based-coatings/balinit/carbon-based/balinit-c/ [Accessed 2017].

158. T. Ohji, R. Kanakala, J. Maty??, N. J. Manjooran, G. Pickrell & W. K. Wong-Ng 2016. *Advances in Materials Science for Environmental and Energy Technologies V: Ceramic Transactions*, Wiley.

159. A. Oila & S. Bull 2005. Assessment of the factors influencing micropitting in rolling/sliding contacts. *Wear,* 258**,** 1510-1524.

160. M. Olzon-Dionysio, M. Campos, M. Kapp, S. de Souza & S. de Souza 2010. Influences of plasma nitriding edge effect on properties of 316L stainless steel. *Surface and Coatings Technology*, 204**,** 3623-3628.

161. C. Ottonello & S. Pagnan 1994. Modified frequency domain kurtosis for signal processing. *Electronics Letters,* 30**,** 1117-1118.

162. F. Oyague 2009. Gearbox Modeling and Load Simulation of a Baseline 750-kW Wind Turbine Using State-of-the-Art Simulation Codes.

163. S. Pagnan, C. Ottonello & G. Tacconi. Filtering of randomly occurring signals by kurtosis in the frequency domain. Pattern Recognition, 1994. Vol. 3-Conference C: Signal Processing, Proceedings of the 12th IAPR International Conference on, 1994. IEEE, 131-133.

164. J. H. Park 2007. Formation Mechanism of Spinel-Type Inclusions in High-Alloyed Stainless Steel Melts. *Metallurgical and Materials Transactions B,* 38**,** 657-663.

165. R. J. Parker & E. N. Bamberger 1983. Effect of carbide distribution on rolling-element fatigue life of AMS 5749.

166. P. K. Pearson & T. W. Dickinson 1988. The role of carbides in performance of high-alloy bearing steels. *Effect of Steel Manufacturing Processes on the Quality of Bearing Steels.* ASTM International.

167. S. Pehan, B. Zafosnik & J. Kramberger 2006. Crack Propagation in Gear Tooth Root. *Fracture of Nano and Engineering Materials and Structures.* Springer.

168. J. M. Pinar Pérez, F. P. García Márquez, A. Tobias & M. Papaelias 2013. Wind turbine reliability analysis. *Renewable and Sustainable Energy Reviews,* 23**,** 463-472.

169. D. Pirro & A. Wessol 2013. *Lubrication fundamentals,* CRC Press.

170. C. Pistorius, N. Verma & R. Fruehan 2011. Calcium modification of alumina and spinel inclusions in aluminum-killed steel. *Center for Iron and Steel making Research, Carnegie Mellon University, Pittsburgh.*

171. B. Podgornik & J. Vižintin 2001. Influence of substrate treatment on the tribological properties of DLC coatings. *Diamond and Related Materials,* 10**,** 2232-2237.

172. B. Podgornik & J. Vižintin 2001. Sliding and pitting wear resistance of plasma and pulse plasma nitrided steel. *Surface engineering,* 17**,** 300-304.

173. R. P. Racher, R. W. McConnell & A. Buhr. Magnesium aluminate spinel raw materials for high performance refractories for steel ladles. 43rd Conference of Metallurgists, 2004.

174. B. Rao 1996. *Handbook of condition monitoring,* Access Online via Elsevier.

175. L. Reinhardt & J. Cordes. XFEM Modeling of Mixed-Mode Cracks in Thin Aluminum Panels. Proceedings of the 2010 Simulia Customer Conference, Providence, RI, 2010. 24-27.

176. REN21 2016. Renewables 2016 Global Status Report.

177. RETEGATE. 2017. *Continuous Acoustic Emission* [Online]. Available: http://www.retegate.com/Continuous_AE [Accessed 2017].

178. Rexnord-Industries. 1978. FAILURE ANALYSIS GEARS-SHAFTS-BEARINGS-SEALS.

179. J. Rosinski & D. Smurthwaite 2010. Troubleshooting wind gearbox problems. *Gear Solut,* 8**,** 22-33.

180. V. Rudnev, D. Loveless, R. Cook & M. Black 2003. Induction Hardening of Gears: a Review. *heat treatment of metals,* 30**,** 97-103.

181. S&T-Stainless. 2014. *CASE HARDENING STEEL–18CrNiMo7- 6 or 17CrNiMo6* [Online]. Available: http://stainless.steelandtube.co.nz/wp-content/uploads/2014/06/CaseHardeningSteel18CrNiMo7.pdf [Accessed 2017].

182. F. Sadeghi, B. Jalalahmadi, T. S. Slack, N. Raje & N. K. Arakere 2009. A review of rolling contact fatigue. *Journal of Tribology,* 131**,** 041403.

183. S. S. Santavirta, R. Lappalainen, P. Pekko, A. Anttila & Y. T. Konttinen 1999. The counterface, surface smoothness, tolerances, and coatings in total joint prostheses. *Clinical orthopaedics and related research,* 369**,** 92-102.

184. C. Scheffer & P. Girdhar 2004. *Practical Machinery Vibration Analysis and Predictive Maintenance*, Elsevier Science.

185. C. Scholz 2013. Low friction slip-rolling contacts. Influences of alternative steels, high performance thin film coatings and lubricants.

186. H. Sentoku 1998. AE in tooth surface failure process of spur gears. *Journal of acoustic emission,* 16**,** S19-S24.

187. J. Serrano-González & R. Lacal-Arántegui 2016. Technological evolution of onshore wind turbines—a market-based analysis. *Wind Energy*.

188. S. Sheng 2010. *Wind turbine micropitting workshop: a recap*, National Renewable Energy Laboratory.

189. J. E. Shigley 2011. *Shigley's mechanical engineering design*, Tata McGraw-Hill Education.

190. C. Sims & F. Dahle 1938. Effect of aluminum on the properties of medium carbon cast steel. *Trans. AFS,* 46**,** 65.

191. A. Singh, D. Houser & S. Vijayakar. Early detection of gear pitting. Power Transmission and Gearing Conference, ASME, 1996. 673-678.

192. A. Singh, D. Houser & S. Vijayakar 1999. Detecting gear tooth breakage using acoustic emission: a feasibility and sensor placement study. *Journal of Mechanical Design,* 121**,** 587-593.

193. E. Siores & A. Negro 1997. Condition monitoring of a gear box using acoustic emission testing. *Materials evaluation,* 55**,** 183-187.

194. M. SLOGÉN. 2013. *Contact Mechanics in Gears - A Computer-Aided Approach for Analyzing Contacts in Spur and Helical Gears.*, Chalmers University of Technology.

195. K. Smolders, H. Long, Y. Feng & P. Tavner. Reliability analysis and prediction of wind turbine gearboxes. European Wind Energy Conference and Exhibition 2010, EWEC 2010, 2010. Sheffield, 2660-2682.

196. W. Song, P.-P. Choi, G. Inden, U. Prahl, D. Raabe & W. Bleck 2014. On the spheroidized carbide dissolution and elemental partitioning in high carbon bearing steel 100Cr6. *Metallurgical and Materials Transactions A,* 45**,** 595-606.

197. D. A. Spera 2009. *Wind turbine technology : fundamental concepts of wind turbine engineering,* New York, ASME Press.

198. G. Stachowiak & A. W. Batchelor 2013. *Engineering Tribology,* Elsevier Science.

199. K. Stadler & A. Studenrauch 2013. Premature bearing failures in wind gearboxes and white etching cracks (WEC). *SKF Evol., March,* 7.

200. J. Stallard, D. Mercs, M. Jarratt, D. Teer & P. Shipway 2004. A study of the tribological behaviour of three carbon-based coatings, tested in air, water and oil environments at high loads. *Surface and Coatings Technology,* 177**,** 545-551.

201. C. Stickels 1974. Carbide refining heat treatments for 52100 bearing steel. *Metallurgical Transactions,* 5**,** 865-874.

202. K. N. Strafford, Datta, P. K. and Gray, J. S. 1989. *Surface engineering practice: Processes, fundamentals, and applications in corrosion and wear,* Ellis Horwood (New York).

203. C. Subramanian & K. N. Strafford 1993. Towards optimization in the selection of surface coatings and treatments to control wear in metal-forming dies and tools. *Materials & Design,* 14**,** 291-298.

204. T. E. Tallian 1992. The Failure Atlas For Hertz Contact Machine Elements. *Mechanical Engineering,* 114**,** 66.

205. C. K. Tan & D. Mba. The source of Acoustic Emission during meshing of spur gears. The 26 th European conference on Acoustic Emission testing, EWGAE, 2004. 559-565.

206. C. K. Tan & D. Mba 2005. Limitation of acoustic emission for identifying seeded defects in gearboxes. *Journal of Nondestructive Evaluation,* 24**,** 11-28.

207. N. Tandon & S. Mata 1999. Detection of defects in gears by acoustic emission measurements. *Journal of Acoustic Emission,* 17**,** 23-27.

208. P. Tavner, R. Gindele, S. Faulstich, B. Hahn, M. Whittle & D. Greenwood. Study of effects of weather & location on wind turbine failure rates. Proceedings of the European wind energy conference EWEC, 2010. 2010.

209. P. Tavner, G. Van Bussel & F. Spinato 2006. Machine and converter reliabilities in wind turbines.

210. D. Teer 2001. New solid lubricant coatings. *Wear,* 251**,** 1068-1074.

211. E. J. Terrell, W. M. Needelman & J. P. Kyle 2012. Wind Turbine Tribology. *Green Tribology*. Springer.

212. R. Tharmakulasingam 2009. Transmission Error in Spur Gears: Static and Dynamic. *Brunel University United Kingdom*.

213. P. Thornton 1971. The influence of nonmetallic inclusions on the mechanical properties of steel: A review. *Journal of Materials Science,* 6**,** 347-356.

214. T. E. ToolBox. 2017. *Friction and Friction Coefficients* [Online]. Available: http://www.engineeringtoolbox.com/friction-coefficients-d_778.html [Accessed 2017].

215. T. Toutountzakis & D. Mba 2003. Observations of acoustic emission activity during gear defect diagnosis. *NDT & E International,* 36**,** 471-477.

216. R. Unnþórsson 2013. *Hit detection and determination in AE bursts*, INTECH Open Access Publisher.

217. H. Vallen 2002. AE testing fundamentals, equipment, applications. *Journal of Nondestructive Testing(Germany),* 7**,** 1-30.

218. T. Verbruggen 2003. *Wind Turbine Operation & Maintenance based on Condition Monitoring WT-*Ω, April.

219. A. P. Verma 2012. *Performance monitoring of wind turbines: a data-mining approach*, The University of Iowa.

220. C. A. Walford 2006. *Wind turbine reliability: understanding and minimizing wind turbine operation and maintenance costs*, United States. Department of Energy.

221. C. Weaver, P. Rigg, J. Cordes & A. Haynes 2011. XFEM Analyses of Critical Cracks in a Pressure Tap for a 40mm Gun Breech.

222. S. Webzell 2009. Take cover. *Plant Engineer (London),* 53**,** 27-29.

223. N. Weller 2004. Acceleration Enveloping–Higher Sensitivity, Earlier Detection. *Orbit***,** 10-19.

224. D. C. Wen 2009. Plasma nitriding of plastic mold steel to increase wear-and corrosion properties. *Surface and Coatings Technology,* 204**,** 511-519.

225. S. Wen & P. Huang 2012. *Principles of tribology*, John Wiley & Sons.

226. West-Yorkshire-Steel-Ltd. 2012a. *EN36 Case Hardening Steel* [Online]. Available: http://www.westyorkssteel.com/alloy-steel/case-hardening-steel/en36/ [Accessed 1 July 2015].

227. West-Yorkshire-Steel-Ltd. 2012b. *EN40B Nitriding Steel* [Online]. Available: http://www.westyorkssteel.com/alloy-steel/nitriding-steel/en40b/ [Accessed 12 May 2014].

228. M. R. Wilkinson, F. Spinato & P. J. Tavner. Condition monitoring of generators & other subassemblies in wind turbine drive trains. Diagnostics for Electric Machines, Power Electronics and Drives, 2007. SDEMPED 2007. IEEE International Symposium on, 2007. IEEE, 388-392.

229. M. V. O. Wind. 2017. *World's most powerful wind turbine once again smashes 24 hour power generation record as 9 MW wind turbine is launched* [Online]. Available: http://www.mhivestasoffshore.com/new-24-hour-record/ [Accessed 2017].

230. L. Winkelmann. Surface roughness and micropitting. National renewable energy laboratory wind turbine tribology seminar, 2011.

231. L. Winkelmann, O. El-Saeed & M. Bell 2009. The effect of superfinishing on gear micropitting. *Gear technology,* 2**,** 60-65.

232. T. M. Wright & S. B. Goodman 2001. *Implant wear in total joint replacement: clinical and biologic issues, material and design considerations: Symposium, Oakbrook, Illinois, October 2000*, American Academy of Orthopaedic Surgeons.

233. S. Yang, D. Camino, A. Jones & D. Teer 2000. Deposition and tribological behaviour of sputtered carbon hard coatings. *Surface and Coatings Technology,* 124**,** 110-116.

234. S. Yang, J. Li, L. Zhang, K. Peaslee & Z. Wang 2010. Evolution of Mgo· Al2O3 Based Inclusions in Alloy Steel During the Refining Process. *Metallurgical and Mining Industry,* 2**,** 87-92.

235. Z. Yuan, Q. Dai, X. Cheng, K. Chen, L. Pan & A. Wang 2006. In situ SEM tensile test of high-nitrogen austenitic stainless steels. *Materials characterization,* 56**,** 79-83.

236. E. V. Zaretsky 1986. Selection of rolling-element bearing steels for long-life application.

237. E. V. Zaretsky 1992. STLE life factors for rolling bearings. *STLE SPECIAL PUBLICATION SP*.

238. E. V. Zaretsky 2012. Rolling bearing steels-a technical and historical perspective. *Materials Science and Technology,* 28**,** 58-69.

239. E. V. Zaretsky, R. J. Parker & W. J. Anderson 1981. NASA five-ball fatigue tester: Over 20 years of research.

240. P. Zhang, F. C. Zhang, Z. Yan, T. S. Wang & L. H. Qian. Rolling contact fatigue property of low-temperature bainite in surface layer of a low carbon steel. Materials Science Forum, 2011. Trans Tech Publ, 585-588.

241. Z. Zhang, H. Dong & T. Bell 2006. The load bearing capacity of hydrogen-free Cr-DLC coatings on deep-case oxygen hardened Ti6Al4V. *Surface and Coatings Technology,* 200**,** 5237-5244.

242. J. Zhou. 2014. *Towards the Designer Surface for Ceramic Injection Moulds.* Master of Philosophy, University of Birmingham.

243. M. Zlatanović, N. Popović & M. Mitrić 2007. Plasma processing in carbon containing atmosphere for possible treatment of wind turbine components. *Thin Solid Films,* 516**,** 228-232.